


SATELLITE TO MODEL COMPARISONS OF VOLCANIC ASH EMISSIONS
IN THE NORTH PACIFIC

By

Torge S. Steensen

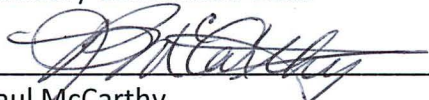
RECOMMENDED:


James Beget



Jonathan Dehn

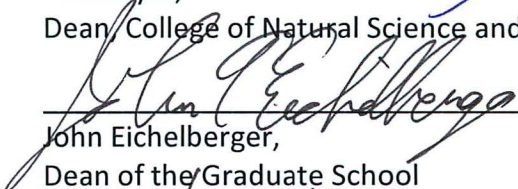

Martin Stuefer

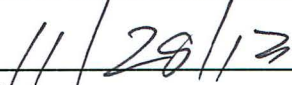

Peter Webley,
Advisory Committee Chair


Paul McCarthy,
Chair, Department of Geology and Geophysics

APPROVED:


Paul Layer,
Dean, College of Natural Science and Mathematics


John Eichelberger,
Dean of the Graduate School


Date

SATELLITE TO MODEL COMPARISONS OF VOLCANIC ASH EMISSIONS

IN THE NORTH PACIFIC

A

DISSERTATION

Presented to the Faculty
of the University of Alaska Fairbanks

in Partial Fulfillment of the Requirements
for the Degree of

DOCTOR OF PHILOSOPHY

By

Torge S. Steensen, M. Sc., B. Sc.

Fairbanks, Alaska

December 2013

Abstract

To detect, analyze and predict the movement of volcanic ash in real time, dispersion models and satellite remote sensing data are important. A combination of both approaches is discussed here to enhance the techniques currently used to quantify volcanic ash emissions, based on case studies of the eruptions of the Kasatochi (Alaska, USA, 2008), Mount Redoubt (Alaska, USA, 2009) and Sarychev Peak (Russia, 2009) volcanoes. Results suggest a quantitative approach determining masses from satellite images can be problematic due to uncertainties in knowledge of input values, most importantly the ground surface temperature required in the mass retrieval.

Furthermore, a volcanic ash transport and dispersion model simulation requires its own set of accurate input parameters to forecast an ash cloud's future location. Such input parameters are often difficult to assess, especially in real time volcano monitoring, and default values are often used for simplification. The objective of this dissertation is to find a quantitative comparison technique to apply to satellite and volcanic ash transport and dispersion models that reduces the inherent uncertainty in the results. The binary 'Ash – No Ash' approach focusing on spatial extent rather than absolute masses is suggested, where the ash extent in satellite data is quantitatively compared to that in the dispersion model's domain. In this technique, neither satellite data nor dispersion model results are regarded as the truth. The Critical Success Index (CSI) as well as Model and Satellite Excess values (ME and SE, respectively) are introduced as comparison tools. This approach reduces uncertainties in the analysis of airborne volcanic ash and, due to

the reduced list of input parameters and assumptions in satellite and model data, the results will be improved. This decreased complexity of the analysis, combined with a reduced error as the defined edge of ash cloud is compared in each method rather than defined threshold or mass loading, will have important implications for real time monitoring of volcanic ash emissions. It allows for simpler, more easily implemented operational monitoring of volcanic ash movements.

To the Loved Ones

To the Lost Ones

Table of Contents

	Page
Signature Page.....	i
Title Page.....	iii
Abstract.....	v
Dedication	vii
Table of Contents	ix
List of Figures	xiii
List of Tables.....	xvii
Chapter 1 Introduction	1
1.1 Volcanoes and Volcanic Emissions.....	4
1.2 Hazards due to Volcanic Ash Emissions	6
1.3 Case Studies.....	9
1.3.1 Kasatochi Volcano, 2008.....	9
1.3.2 Mount Redoubt Volcano, 2009.....	10
1.3.3 Sarychev Peak, 2009.....	11
1.4 Analysis Tools.....	12
1.4.1 Satellite Analyses	13
1.4.1.1 Reverse Absorption Method.....	16
1.4.1.2 Volcanic Ash Retrieval	18
1.4.2 Dispersion Model Analyses.....	22
1.4.2.1 Puff	23
1.4.2.2 WRF-Chem	29
1.4.2.3 WRF-Chem Output	30
1.4.2.4 Other Dispersion Models.....	31
1.4.3 Qualitative Comparison	33

1.5	Summary	34
1.6	References.....	36
1.7	Figures.....	44
1.8	Tables	51
Chapter 2 Qualitative comparison of Mount Redoubt 2009 volcanic clouds using the PUFF and WRF-Chem dispersion models and satellite remote sensing data ¹		59
2.1	Introduction	60
2.2	Methodology.....	62
2.3	Explosive Event 5: March 23, 2009	67
2.4	Explosive Event 19: April 14, 2009	68
2.5	Results.....	69
2.5.1	Satellite Data	69
2.5.2	Puff Model.....	70
2.5.3	WRF-Chem Model.....	71
2.5.3.1	Event 5.....	71
2.5.3.2	Event 19.....	72
2.6	Discussion.....	74
2.6.1	Event 5	74
2.6.2	Event 19	77
2.7	Conclusions	79
2.8	Acknowledgements	81
2.9	References.....	81
2.10	Figures.....	84
2.11	Tables	98
Chapter 3: Qualitative Analysis of Input Parameters for Satellite-Based Quantification of Airborne Volcanic Ash ¹		101
3.1	Introduction	102
3.2	Case Study.....	102
3.3	Results and Discussion.....	104
3.4	Conclusion.....	106

3.5	Acknowledgements.....	107
3.6	References	108
3.7	Figures	109
3.7	Tables	112
Chapter 4: Quantitative Comparison of Volcanic Ash Observations In Satellite-Based Remote Sensing Data and WRF-Chem Model Simulations ¹		113
4.1	Introduction	114
4.2	Sarychev Peak Volcano and its 2009 Eruption	116
4.3	Methods	117
4.3.1	Satellite Remote Sensing	117
4.3.2	Volcanic Ash Emission, Dispersion and Transport Model	121
4.3.3	Comparison Between Satellite Retrievals and Model Simulations	124
4.3.3.1	Quantitative Spatial Comparison	125
4.3.3.2	Qualitative Spatial Comparison.....	127
4.3.3.3	Point to Point Comparison.....	128
4.4	Results	129
4.4.1	Quantitative Spatial Comparison	130
4.4.2	Qualitative Spatial Comparison	133
4.4.3	Point to Point Comparison	135
4.5	Discussion	137
4.6	Conclusions	145
4.6.1	Input and Model/Retrieval Parameter.....	147
4.6.2	Model Limitations and Geometrical Setting.....	149
4.6.3	Future Work.....	152
4.7	Acknowledgements.....	153
4.8	References	153
4.9	Figures	158
4.10	Tables.....	177

Chapter 5: Improvements on Volcanic Ash Quantification in the Puff Volcanic Ash Tracking and Dispersion Model and Satellite Thermal Infrared Remote Sensing Data ¹	181
5.1 Introduction	182
5.1.1 Kasatochi Location and its 2008 Eruption.....	185
5.2 Methodology.....	185
5.2.1 Using Pixel-Specific Background Temperatures	186
5.2.2 Comparison techniques of binary ash detection in model and satellite data	190
5.2.3 Correction of the VATD model results to the satellite’s line-of-sight	191
5.3 Results.....	192
5.3.1 Satellite-Model Comparison 1: Mass Loading.....	192
5.3.2 Satellite-Model Comparison 2: Spatial Extent	193
5.3.3 Model Projections: Vertical vs. Corrected for Satellite Angle.....	195
5.4 Discussion.....	196
5.4.1 Satellite-Model Comparison 1: Mass Loading.....	196
5.4.2 Satellite-Model Comparison 2: Spatial Extent	197
5.4.3 Model Projections: Vertical vs. Corrected for Satellite Angle.....	199
5.5 Conclusions	200
5.6 Acknowledgements	203
5.7 References.....	204
5.8 Figures.....	206
5.9 Tables	215
Chapter 6: Conclusions.....	219
6.1 Necessity of Satellite – VATD Intercomparisons.....	222
6.2 Importance of Pixel-Based Values for the Surface Temperature in VAR	223
6.3 Improvements of LOS-Projections of VATD Model Data.....	224
6.4 Advantages Using a Binary ‘Ash – No Ash’ Approach as Opposed to a Quantitative Mass Estimate for two band Thermal Infrared data	225
6.5 Future Work	230
6.6 Final Thoughts	231
6.7 References.....	233

List of Figures

	Page
Figure 1.1: Map of the North Pacific region. The volcanoes focused on in this dissertation are highlighted in gray.	44
Figure 1.2: Location of Kasatochi volcano in the Aleutian Islands in relation to Alaska, Canada and the contiguous United States.....	45
Figure 1.3: Location of Mount Redoubt volcano in Cook Inlet close to Anchorage.	46
Figure 1.4: Location of Sarychev Peak volcano in the Kuril Islands, Russia.....	47
Figure 1.5: Transmission index of volcanic ash in the atmosphere.	48
Figure 1.6: Relationship between optical depth of the cloud and mean effective radii of the particles.....	49
Figure 1.7: Sensitivity of the Volcanic Ash Retrieval.	50
Figure 2.1: Location of Mount Redoubt volcano at the Cook Inlet.....	84
Figure 2.2: Advanced Very High Resolution Radiometer Thermal Infrared channel 4 image showing the ash clouds from Mount Redoubt volcano explosive event 5.. ..	85
Figure 2.3: Advanced Very High Resolution Radiometer Thermal Infrared image from April 4, 2009 at 16:23 UTC after event 19.....	86
Figure 2.4: Advanced Very High Resolution Radiometer Thermal Infrared and Brightness Temperature difference images with defined thresholds from 0 to -2 K.....	87
Figure 2.5: Advanced Very High Resolution Radiometer Thermal Infrared (TIR) (left) and Brightness temperature difference (BTD) images (right) with defined thresholds from 0 to -2 K according to Table 2.3.	88
Figure 2.6: Puff Volcanic Ash Transport and Dispersion model simulations show the predicted plume dispersion for explosive events 5 and 19.	89
Figure 2.7: Comparison between satellite data (A) and WRF-Chem runs with spatial resolutions of 2 km (B and E) and 5 km (C and F) for the timings 16:10 UTC and 18:00 UTC on March 23.....	90

Figure 2.8: Ash concentrations from WRF-Chem using 2 km grid resolution at 2, 8 and 14 km ASL on March 23, 2009, from event 5 at Mount Redoubt volcano 91

Figure 2.9: Vertical cross section of ash concentration from WRF-Chem through the cloud on March 23, 2009, at 16:10 UTC. 92

Figure 2. 10: WRF-Chem ash fallout compared to the sample-based isopach map adjusted to highlight event 5. 93

Figure 2.11: Comparison between satellite BTD images, WRF-Chem simulations 94

Figure 2.12: WRF-Chem ash concentrations using 5 km grid resolution at 2, 8 and 14 km ASL on April 4, 2009, from event 19 at Mount Redoubt volcano. 95

Figure 2.13: Vertical cross section of ash concentrations from WRF-Chem through the cloud on April 4, 2009, at 17:00 UTC. 96

Figure 2.14: WRF-Chem ash fallout compared to the sample-based isopach map adjusted to highlight event 19. 97

Figure 3.1: Location of Sarychev Peak in the Kuriles, eastern Russia. 109

Figure 3.2: Variation of derived masses with changing input parameters. 110

Figure 3.3: Possible combinations of surface and cloud top brightness temperature to derive the ‘true’ masses. 111

Figure 4.1: Location of Sarychev Peak volcano in the Kuril Islands, Eastern Russia..... 158

Figure 4.2: Spatial extent of the ash clouds on June 14, 2009, at 21:00 UTC. 159

Figure 4.3: Ash dispersion predicted by the Weather Research and Forecast model with online Chemistry using the Plumeria and Sparks-defined eruption rates and the particle size distribution S2/S3. 160

Figure 4.4: Ash dispersion predicted by the Weather Research and Forecast model with online Chemistry using the Plumeria and Sparks-defined eruption rates and the particle size distribution S1..... 161

Figure 4.5: Ash concentration and dispersion predicted by the Weather Research and Forecast Model with online Chemistry at different altitudes. 162

Figure 4.6: Qualitative spatial comparison of ash inundation between model and satellite results during June 13 - 16, 2009 over the domain studied..... 163

Figure 4.7: Selected timings of ash extent as derived by satellite data, calculated by WRF-Chem without a mass cutoff and the match of the two data sets.	164
Figure 4.8: Selected timings of ash extent as derived by satellite data, calculated by WRF-Chem with a mass cutoff of 50 tons and the match of the two data sets	165
Figure 4.9: Selected timings of ash masses calculated by the WRF-Chem model using the Plumeria eruption rate and the particle size distribution S2/S3.....	166
Figure 4.10: Selected timings of ash masses as calculated from satellite data.....	167
Figure 4.11: Quantitative spatial comparison of ash inundation between modeling and satellite retrieval results during June 13 (22:00 UTC) to 16 (00:00 UTC), 2009 over the domain studied.....	168
Figure 4.12A: For explanations see Figure 4.12E.	169
Figure 4.12B: For explanations see Figure 4.12E.	170
Figure 4.12C: For explanations see Figure 4.12E.	171
Figure 4.12D: For explanations see Figure 4.12E.	172
Figure 4.12E: Ash masses derived from satellite data and the WRF-Chem simulations at the five locations analyzed.....	173
Figure 4.13: Vertical slice through the plume on June 14, 2009 at 07:00 (UTC) ranging from location '1' to '4'.....	174
Figure 4.14: Vertical slice through the plume on June 14, 2009 at noon (UTC) ranging from location '1' to '4'.....	175
Figure 4. 15: Diagram illustrating potential discrepancies between model calculations and non-line-of-sight-corrected satellite retrievals.	176
Figure 5.1: Location of Kasatochi Volcano in relation to Alaska, Canada and the Contiguous United States.	206
Figure 5.2: Schematic illustrating potential discrepancies between model calculations and satellite retrievals.....	207
Figure 5.3: Maximum, mean and minimum ash mass loadings as calculated by the Puff model and as determined by satellite.	208

Figure 5.4: Extent and height analysis of the Puff ash dispersion for the first 74 hours after the eruption of Kasatochi. 209

Figure 5.5: Preliminary extent comparison between Puff VATD model results and satellite detected volcanic ash data during dispersion. 210

Figure 5.6: Direct comparison of the ash extent as identified in satellite data and calculated by Puff. 211

Figure 5.7: Critical Success Index, Model Excess and Satellite Excess values for the ash extent comparison between satellite data and Puff VATD model. 212

Figure 5.8: Direct comparison of the Puff VATD modeled ash extent using the default vertical summation versus the projection to the satellite’s line-of-sight. 213

Figure 5.9: Quantification of the comparison between default and adjusted model projections.. 214

List of Tables

	Page
Table 1.1: Criteria for determination of the Volcanic Explosivity Index (VEI).	51
Table 1.2: Eruption chronology for the Kasatochi volcanic eruptive events in August 2008.	52
Table 1.3: Eruption chronology for the Redoubt volcanic eruptive events in March and April 2009.	53
Table 1.4: Eruption chronology for the Sarychev Peak volcanic eruptive events in June 2009.	54
Table 1.5: Specification of the four types of sensors and their satellites used for this project.	55
Table 1.6: Relevant infrared bands used for the Reverse Absorption Method.....	56
Table 1.7: Particle size bins used in WRF-Chem simulations and adapted in current version of WRF-Chem.	57
Table 2.1: Parameters used for each analysis and each event.....	98
Table 2.2: Volcanic Ash Particle bins and their respective masses used for the Mount Redoubt eruption.	99
Table 2.3: Advanced Very High Resolution Radiometer images analyzed and parameters used for the analysis of event 5 and 19 of the 2009 unrest of Mount Redoubt volcano, Alaska..	100
Table 3.1: Parameters used for the Volcanic Ash Retrieval and their average error.	112
Table 4.1: Timings and heights of the 23 explosive events of the Sarychev Peak eruption of 2009.	177
Table 4.2: Parameters used for satellite and volcanic ash transport and dispersion analyses for the Sarychev Peak events 13 to 16.	178
Table 4.3: Particle size distributions based on the classification of Mastin et al. (2009).	179

Table 5.1: Volcano and eruption specifics as determined by seismic and satellite observations of the 2008 Kasatochi eruption.....	215
Table 5.2: Relevant characteristics for calculation of ash properties.....	216
Table 5.3: Input parameter for the Puff Volcanic Ash Transport and Dispersion runs. .	217

Chapter 1 Introduction

Operational monitoring of volcanic ash emissions is crucial for aviation safety (Casadevall, 1994). To achieve accurate knowledge of the ash location, as well as its properties (such as concentration, mass loading, and optical depth), a combination of satellite data and model analyses is required. This will determine the spatial extent of the plume/cloud in real time, through the use of satellite data, and the dispersing emission and its future location through the use of volcanic ash transport and dispersion (VATD) modeling.

VATD model calculations are available in custom-designed time steps. For research purposes, finer temporal and spatial resolutions are often chosen, that can resolve the changing atmospheric patterns more precisely, but are also more time-intensive to generate. For operational purposes, larger time outputs and spatial resolutions are more feasible, as computed results are needed in a time-sensitive manner. Due to this, satellite product timings, which come in pre-defined intervals, don't always match the model output timings.

Infrared satellite measurements of volcanic ash are sensitive to many factors, including those related to the measured wavelengths used, and ash retrievals applied (see work of Wen and Rose, 1994 and Pavolonis et al., 2006). VATD models forecast all parts of the plume and dispersing cloud, depending on input parameters like numerical weather prediction (NWP) wind fields, and eruption source characteristics, such as plume top

height and particle size ranges (see Searcy et al., 1998, Grell et al., 2005 for example VATD models). To accurately analyze the current location of the volcanic ash, satellite imagery needs to be acquired and compared to operationally running VATD models. This satellite data, in turn will validate the model simulations and allow the models to accurately predict the movement of the ash cloud beyond the timing of the satellite acquisition.

In order to improve this forecast, research VATD model simulations need to be performed, which share the same modeling environment with operational models, but include more detailed input parameters, finer spatial resolution and smaller time intervals in their outputs. Such VATD model forecasts are often far more sophisticated than the operational ones and analyze more parameters, but can also take longer time to run, sometimes too much time for an operational setting (Peterson et al., 2013). By running these research VATD model simulations retrospectively and analyzing previous eruptions, the volcanic eruptions themselves can be better understood and the performance of the operational VATD models can be improved. As is the case with operational models, satellite remote sensing data needs to be acquired and examined to compare the research model results to observations.

The aims of this dissertation are: (1) the qualitative comparison between satellite remote sensing analyses and VATD model predictions as well as their contributions to each other while limiting the uncertainties; (2) an accuracy assessment of ash mass

quantifications; and (3) the uncertainty analysis accompanied with a correction for the satellite's line-of-sight as opposed to the vertical, default model projection. With example eruptions distributed across the North Pacific [Kasatochi, 2008 (Waythomas et al., 2010); Mount Redoubt, 2009 (Wallace and Schaefer, 2013); Sarychev Peak, 2009 (Rybin et al., 2011)] and two distinctively different dispersion models (using Eulerian and Lagrangian approaches), the research will retrieve characteristics from each eruption and evaluate the advantages and disadvantages of each approach, as well as the respective modifications needed for near real time monitoring situations.

As a result of this research, a quantitative, binary comparison of the spatial extent is developed that minimizes uncertainties due to incorrect input parameters and input parameters with high sensitivities assigned to them. In addition, a quantification of the offset with the line-of-sight adjusted to the respective satellite pass shows the importance to adjust the model output. With this knowledge, volcano observatories as well as other volcano-monitoring agencies, (such as the volcanic ash advisory centers) will be able to track and forecast volcanic cloud movement with improved accuracy and higher confidence. This will reflect to the aviation community being able to obtain better volcanic ash advisories and, therefore, allowing them to avoid any possible ash encounters.

1.1 Volcanoes and Volcanic Emissions

Volcanoes are a crucial part of the geological cycle on Earth. Forming at subduction zones, mid-ocean ridges and at intra-plate hot spots, their eruptions can produce large amounts of magma and gases, as well as pulverize ambient rocks. Over the last few hundred years, several massive eruptions have been recorded; most notably are the Superplinian explosions of Tambora (1815; see Oppenheimer, 2003) and Krakatau (1883; see Spicak et al., 2008) in Indonesia as well more recent examples of Pinatubo, Philippines (1991; see Holasek et al., 1996), Kasatochi, Alaska, USA (2008; see Waythomas et al., 2010) and Eyjafjallajökull, Iceland (2010; see Flentje et al., 2010). The total number of dormant volcanoes is estimated at about 550 worldwide with an additional 50 to 70 active volcanoes and related eruptions per year (Pichler and Pichler, 2007).

Volcanic eruption sizes are classified into different groups based on their explosivity, using the Volcanic Explosivity Index (VEI, Newhall and Self, 1982, Table 1.1). This system, generally depicted with eight indices, has no upper limit, and can be expanded for larger events. Small VEI numbers are generally associated with intra- plate hot spot volcanism as on Hawaii (USA) or mid-ocean ridge volcanism, while subduction zone volcanoes are generally listed with higher VEIs. However, some hot spot volcanoes have been assigned higher explosivity indices like Yellowstone (VEI = 10; Pichler and Pichler, 2007).

Depending on magma composition and supply, as well as the environment of the

volcano, eruptions can cause different kinds of hazards. The most widely known are lava flows, often observed in less explosive volcanoes like Kilauea, Hawaii (1983-recent; see Harris et al., 1998) or Etna, Italy (1991-1993, see Harris et al., 1997). Larger VEI events are characterized by pyroclastic flows and base surges as observed at Mount St. Helens, USA (1980; see Andrews and Gardner, 2009) and Pelée, Martinique (1902; see Burt et al., 2001).

Eruptions with larger plumes are classified as having higher VEIs (see definition of VEI in Table 1.1). These plumes are composed of different gases, with major constituents such as sulfur dioxide (SO_2), water (H_2O) and carbon dioxide (CO_2). Smaller components identified in volcanic plumes are hydrogen sulfide (H_2S), hydrogen chloride (HCl), hydrogen (H_2), carbon monoxide (CO), carbonyl sulfide (COS) and bromine monoxide (BrO) (see work by Shinohara, 2005; Mori and Notsu, 2008; Theys et al., 2009). Out of the major gases, H_2O and CO_2 are known to be major greenhouse gases (Forster et al., 2007) and therefore play a major role in current climate change discussions. In addition, SO_2 , often operationally detected as part of volcanic clouds (Carn et al., 2008), and H_2S in its conversion to sulfuric acid (H_2SO_4) form acid rain, which plays a direct role in the energy balance of the planet (Labitze et al., 1983, Pinto et al., 1989, Rose et al., 2000). A similarly important effect is induced by HCl injection into the stratosphere. Here, ozone depletion results in an increased flux of ultraviolet light to the

surface. However, this effect is limited as HCl often condenses on ash particles and falls out (Pinto et al., 1989).

1.2 Hazards due to Volcanic Ash Emissions

Explosive eruptions dominated by ash plumes that can extend many kilometers into the atmosphere are being classified with a high VEI (see VEI definitions in Table 1.1). The dispersing ash particles from these plumes and the drifting clouds can remain above atmospheric background levels for up to several years (McCormick et al., 1995) and have different ramifications on the environment, developing in potential volcanic hazards.

A wide range of hazards are associated with airborne volcanic ash. Globally, the largest effect lies in the atmospheric forcing of volcanic dust (Forster et al., 2007). Forcing, described as “mechanisms by which aerosols scatter and absorb shortwave and long-wave radiation” (Forster et al., 2007), consists of a cooling of the surface temperature, when fine ash particles are injected in the stratosphere. With a residence time of two years and more, volcanic dust has been observed to cool Earth’s surface by 0.5 to 1°C for the years succeeding the Tambora eruption (Indonesia) of 1815 (Oppenheimer, 2003). Similarly, stratospheric temperature increases have been correlated to injected ash (Labitzke et al., 1983).

Ash fallout, despite being very fertile (e.g. Pichler and Pichler, 2007), also has the ability to destroy vegetation and impact road conditions as seen during the Krakatau (Indonesia, 1883) and Mt. St. Helens (USA, 1980) eruptions (Prabaharan, 2002). In addition, the tephra can contain toxic fluoride compounds that can be poisonous to animals (Blong, 1984). Such effects caused 80,000 secondary casualties in the years following Krakatau's eruption. Another example is Iceland's 'haze famine' of 1784 following the eruption of the Laki volcano in the previous year (Vasey, 1991).

The most prominent examples of airborne ash hazards, however, are the ramifications on air traffic. An early example was in 1982, when a British Airways Boeing 747 plane on route from Kuala Lumpur, Malaysia, to Perth, Australia, encountered an ash cloud from the erupting Galunggung volcano, Indonesia. The silica-bearing tephra melted in the jet engines and fused onto internal surfaces limiting the air flow (Hanstrum and Watson, 1983; Prata et al., 1991). All four engines cut out causing the plane to descend from 11.3 to 7.3 km above sea level (ASL) for 13 minutes, after which the pilot was able to restart three engines. Due to abrasion, the windscreen turned opaque forcing the pilot to use the side windows to land the plane in Jakarta with considerable damage to wings, fuselage and engines (Hanstrum and Watson, 1983; Diamond, 1986; Prabaharan, 2002). Two weeks later, a Singapore Airlines 747 flew into another plume on route from Singapore to Melbourne and dropped 2.5 km in altitude. Only after this incident, a warning was issued to avoid the area (Hanstrum and Watson, 1983).

Over the last few decades, aircraft-plume encounters have been noted on several occasions at different distances to the volcanic vent from 150 km (Mount Redoubt, Alaska, 1989) to over 1200 km (Mt. Spurr, Alaska, 1992) and up to 1740 km (Mt. Pinatubo, Philippines, 1991, see Prabakaran, 2002). The largest costs were incurred during 20 separate incidents during the Pinatubo eruption, when commercial planes flew into the plume and caused a total damage of \$US100 million (Prata et al., 1991; Prabakaran, 2002). One of the most prominent encounters happened during the eruption of Redoubt Volcano, 1989-1990, when KLM flight 867, on route from Amsterdam to Tokyo, flew into a cloud at about 7.6 km ASL. All four engines stalled and subsequently restarted after the plane dropped to about 4 km in altitude, less than 1 km above the highest peaks of the Alaska Range (Casadevall, 1994). Damage to the aircraft included ash deposits in engines, disruptions in the electrical systems and abrasion of multiple parts of the plane's exterior including windshield, wings and tail rudder accumulating to an initial estimate of \$US50 to \$US80 million. As a precaution, the International Civil Aviation Organization (ICAO) formed Volcanic Ash Advisory Centers (VAACs) around the globe in the late 1980s, which are responsible for producing advisories for volcanic ash within (ICAO, 2004) for a defined region. In practice, air space is often closed when volcanic ash is present based upon a 'zero tolerance' guideline, recently seen in the 2010 eruption of Eyjafjallajökull in Iceland (Flentje et al., 2010; Petersen, 2010), often causing expenses in the range of billions of dollars in economy

and repairs. Due to such costs, it is vital to observe and predict the movements of ash clouds accurately.

1.3 Case Studies

For this proposed project, three different volcanic eruptions across the North Pacific are used as case studies. With more than 100 volcanoes stretching from the southern tip of the Kurile Islands to Alaska's Canadian border and located on the major air traffic corridor between North America and Asia, this region has the potential to severely disrupt air traffic as highlighted by the KLM 867 ash encounter during the Mount Redoubt eruption in 1989 (Casadevall, 1994). During 2008 and 2009, three volcanoes in this region erupted violently: Kasatochi (August 2008), Mount Redoubt (March to April 2009) and Sarychev Peak (June 2009) (see locations in Fig. 1.1). These three eruptions will form the basis for this study.

1.3.1 Kasatochi Volcano, 2008

Kasatochi is a small volcano of 3 km diameter located on Kasatochi Island in the Central Aleutian Islands (Figs. 1.1 and 1.2). Without recorded historical eruptions, the volcano erupted on August 7 and 8, 2008, with three distinctive pulses producing ash plumes up to 18 km ASL. These ash clouds travelled long distances and were responsible for significant interferences to airborne traffic over that region (Waythomas et al., 2010). A concise chronology of the eruption is listed in Table 1.2. The time period of the eruption

had good satellite coverage with different instruments including the National Oceanic and Atmospheric Administration (NOAA) Advanced Very High Resolution Radiometer (AVHRR), the National Aeronautical and Space Administration (NASA) Moderate Resolution Imaging Spectroradiometer (MODIS) and the NOAA Geostationary Operational Environmental Satellite (GOES).

In this study, data from the GOES satellite is used, with a geostationary view, that allows the whole extent of the ash emission and subsequent dispersing cloud to be mapped. The temporal domain will start with the onset of the eruption and allow for dispersion of the ash cloud over the course of 75 hours.

1.3.2 Mount Redoubt Volcano, 2009

Mount Redoubt, located in the Gulf of Alaska (Fig 1.1 and Fig. 1.3), previously erupted in 1989/ 1990 (Scott and McGimsey, 1994), with an associated ash-encounter by a KLM jet (Casadevall, 1994). Situated about 170 km southwest of Anchorage, the largest city in Alaska, and positioned on the main flight corridor between North America and Asia, this volcano is a special threat to aviation and the environment. The eruption of 2009 consisted of 19 distinctive events analyzed by the Alaska Volcano Observatory (AVO) with durations up to 38 minutes and maximum heights of 18.9 km ASL (Table 1.3). Changing wind patterns over the course of the eruption distributed the ash over different parts of Alaska (see Wallace and Schaefer, 2013).

The available satellite coverage for ash cloud detection was very sparse as meteorological cloud cover was present during most obtained satellite scenes hindering the detection of the ash cloud (Steensen et al., 2013). For this project, events 5 and 19 are the focus. The dispersing ash cloud of event 5 (March 23, 12:30 UTC), from an explosive event, was partly obscured, due to meteorological clouds, and also showed parts that were opaque and semi-translucent in the thermal infrared, the wavelengths used to analyze the ash (see Chapter 1.4.1 for details). Event 19 (April 4, 13:59 UTC) produced a large and high altitude plume, from a dome collapse, under cloud-free skies, while other events only had small plumes, mostly underneath or hardly distinguishable from weather clouds.

1.3.3 Sarychev Peak, 2009

Sarychev Peak located on Matua Island (Fig. 1.4) is one of the Kurile Island's most active volcanoes (Rybin et al., 2011). After 33 years of quiescence, it erupted violently several times from June 11, 2009 for 9 days. This eruption was among the largest of the recent historical eruptions in that area. 23 events were recorded with different satellites, mostly the Japanese Meteorological Agency (JMA) Meteorological Agency Multifunctional Transport Satellite (MTSAT), with plumes reaching altitudes up to 21 km ASL and drifting 1500 km to the north and over 3000 km to the southeast (Table 1.4). The proximity of air routes to the volcano caused a severe disruption in airborne traffic to and from East Asia (Rybin et al., 2011).

Due to a lack of seismic stations on and near Matua Island, the duration of the different events could not be determined easily. However, Matoza et al. (2011) reported infrasound observations correlated to the explosions of Sarychev Peak. With this data, it is possible to estimate the durations of those events, whose onsets match with the collected satellite and infrasound data (Table 1.4). Events 13 to 16 were chosen for study as the timing of the events can be associated with infrasound signals and hence defined durations and start times can be measured. Many earlier and later events have unknown durations, making it harder to perform the model simulations of the ash dispersion.

1.4 Analysis Tools

To analyze these volcanic events, a combination of satellite-based algorithms and dispersion model calculations will be used. Satellite remote sensing data provides information on the ash clouds at a specific moment in time, subject to sensibility ranges and cloud cover. VATD model results, on the other hand, show the complete predicted plume and cloud with all particle sizes at all altitudes, as long as reasonable input parameters have been used. In combining these two approaches, a more thorough analysis and prediction of current events can be achieved.

1.4.1 Satellite Analyses

There have been many different approaches to characterize volcanic ash emissions from volcanoes, as partially summarized by Oppenheimer (1998). A common difficulty is the diverse nature of plumes. A small-scale event can't always be detected with space-borne instruments due to their sensors' spatial resolutions in the infrared, which is the most common wavelength range used for plume observations (Prata, 1989a, b). Polar-orbiting satellites (with sensors AVHRR, and MODIS) at altitudes between 700 and 900 km (see specifications in Table 1.5) have an improved opportunity to resolve smaller details in ash clouds with a nadir spatial resolution of 1.09 x 1.09 (AVHRR) and 1 x 1 km (MODIS) compared to geostationary satellites at much higher altitude (35,790 km, GOES, and MTSAT) that only have spatial resolutions of 4 x 4 km at nadir in the thermal infrared (TIR). The further the volcanic event and dispersing cloud is away from the equator, the larger the geostationary pixels are (Prata et al., 2011). Especially for observations at high latitudes, the pixels are often too large to show any sign of the plume and dispersing cloud. However, the different geometry can allow geostationary satellites to detect some plumes that polar-orbiting ones can't. This is the case if an elongated plume is too thin to cause a significant signature when observed from directly above but has more material in the path when analyzed from an equatorial position (see work of Gu et al., 2005). Oblique viewing has also been shown to cause the ash signal to disappear due to increasing opacity (Prata and Barton, 1994).

The size of the interval between satellite passes, known as temporal resolution, is another often-encountered problem. While polar-orbiting sensors have a comparably good spatial resolution, their temporal resolution ranges from an hour (AVHRR in Polar Regions) to half a day (MODIS) and longer (e.g. the NASA Advanced Spaceborne Thermal Emission and Reflection Radiometer (ASTER), 6 days). Here, geostationary satellites are able to provide a much better time series with an image every 15 to 30 minutes (Prata et al., 2011).

As satellite passes of polar-orbiting devices converge at high latitudes, the temporal coverage increases in Polar Regions. AVHRR, being on board of a set of different satellites (Table 1.5), reduces the revisiting time of an identical instrument to 1 hour compared to 6 hours in the tropics (Prata et al., 2011). While this approaches the temporal resolution of geostationary sensors, quick changes in eruptive behavior can still go unnoticed. Here, a fusion of geostationary and polar-orbiting data provides the best tool for monitoring.

A third resolution that needs to be considered in satellite analysis is the spectral resolution. Here, the importance lies in the regions of the electromagnetic spectrum resolved in the satellite channels. This has been a problem since the first use of satellite remote sensing, when satellites had a limited number of atmosphere-penetrating bands and a large spectral resolution (e.g. the NASA Television Infrared Observation Satellite [TIROS]; Smith et al., 1979). Today, with multi- and hyper-spectral satellites and their

sensors (e.g. ASTER, the European Organisation for the Exploitation of Meteorological Satellites (Eumetsat) Spinning Enhanced Visible and Infrared Imager (SEVIRI) or the upcoming NOAA/NASA GOES-R) this is rarely a problem (e.g. Jin et al., 2008; Pavolonis and Sieglaff, 2010). However, with 5-channel-sensors like AVHRR, GOES or MTSAT still operational, the spectral resolution needs to be addressed for each specific target.

In terms of volcanic ash emissions, such an evaluation will yield a combination of different instruments for best coverage of the feature. The comparably high resolution of polar-orbiting satellites is necessary to capture the events in improved detail, while a high temporal coverage is useful to monitor their development. In Polar Regions, due to the higher temporal convergence of AVHRR passes, volcanic eruptions can sometimes solely be monitored with these instruments (e.g. Steensen et al., 2013). While AVHRR's spectral resolution is limited, it does include visible and thermal infrared channels, including those needed for the detection of volcanic clouds (see section 1.4.1.1). Tropical regions, on the other hand, need a more developed combination between geostationary and polar-orbiting instruments. Regardless of region, measurements should, if possible, be conducted with multiple sensors to achieve the highest possible temporal coverage while not neglecting the spatial accuracy.

Besides the different resolutions and their improvements over time, cloud coverage remains a general problem (Prata et al., 2011). If an ash cloud is too low in altitude and covered by thick meteorological clouds, the satellite can't detect it. Even if cloud cover is

limited, an ambiguity between volcanic and meteorological cloud remains. This is especially true at high volcanic summits where orographic clouds often mimic an eruption (Oppenheimer, 1998). Due to their content, plumes appear brownish as opposed to white meteorological clouds in visible wavelengths but detecting that requires day-time imagery, as well as an opportunistic viewing angle based on the sun's location and the scattering properties of the aerosols. A clear distinction is the wedge shape of meteorological clouds due to strong winds in the upper atmosphere and the initial umbrella cloud in major volcanic explosions (e.g. ash occurred during Redoubt's 1990 activity, see Scott and McGimsey, 1994). Generally, meteorological clouds can be distinguished from volcanic clouds due to inverse signals in the Reverse Absorption Method (see 1.4.1.1) but ambiguities can remain on cloud edges (Pavolonis et al., 2006).

1.4.1.1 Reverse Absorption Method

To facilitate the detection of volcanic clouds at any time, Prata (1989a, b) proposed the Reverse Absorption Method. This technique is based on emissivity differences between volcanic ash and meteorological clouds in the thermal infrared. In the infrared part of the electromagnetic spectrum, more precisely between 10 and 13 μm , volcanic ash, as well as other silica bearing substances like desert dust, emits more energy at relatively lower wavelengths than it does at relatively higher ones (Volz, 1973; Watson et al., 2004; see Fig. 1.5), as opposed to ice and water (Downing and Williams, 1975).

The difference of the radiative transmission results in more energy reaching the sensor at higher wavelengths in the 10 to 13 μm window as less radiation is scattered or absorbed. This can be exploited using different satellites and their sensors. Originally published by Prata (1989a, b) for AVHRR data, the retrieved brightness temperatures in two bands, converted from thermal radiance, (T_{10} and T_{12} for the respective wavelengths) show a negative difference at the sensor (the brightness temperature difference [BTD], $T_{10} - T_{12}$) as opposed to meteorological clouds ($T_{10} - T_{12} > 0 \text{ K}$). Later, this approach has been applied to different satellites including those used in this study (Table 1.6; Schneider et al., 1999; Dean et al., 2002; Tupper et al., 2004; Andronico et al., 2009). However, this simplified approach bears uncertainties in terms of ambiguities between volcanic ash and other silica-bearing minerals, like desert dust, that is also frequently analyzed with this method (Gu et al., 2003). In addition, the threshold of 0 K is generally adapted to match the respective situation and to avoid artifacts caused by cloud edges and soil (Pavolonis et al., 2006).

The reverse effect of water vapor compared to volcanic ash in the 10 – 13 μm spectral range, can result in a masking of the signal (Prata et al., 2011). Water present in the ash cloud affects the penetrating radiation differently than a pure ash cloud does. Both signals can cancel each other out, resulting in a zero difference in the BTD data, or in extreme cases the water vapor signal can dominate, masking the ash signal in the BTD data. This often happens in phreatomagmatic eruption where water is involved. Prata

and Barton (1994) also showed that this can cause geostationary satellites to be unable to detect an eruption cloud, when it is still possible from polar-orbiting ones due to less water vapor interference.

General criticism of this method has been voiced by Simpson et al. (2000; 2001). They state that the Reverse Absorption Method does not emphasize the 'dynamical interaction between the erupting volcano and the effects of overlying atmosphere water vapor, phreatic and phreatomagmatic water sources'. Prata et al. (2001) challenged this view by referring to the well-known and described ambiguities in previous literature (Rose et al., 1995). As pointed out, the Reverse Absorption Method does face certain limitations but being aware of those restrictions, it provides a solid approach to quantify the presence and extent of volcanic ash in the atmosphere.

1.4.1.2 Volcanic Ash Retrieval

To qualitatively analyze volcanic clouds, Wen and Rose (1994) expanded upon the Reverse Absorption Method by developing the Volcanic Ash Retrieval (VAR) to retrieve total ash masses, optical depths and effective particle radii of the respective pixels.

Optical depth is a measure of transparency of the cloud. It is defined as the negative natural logarithm of the fraction of radiation that reaches the sensor, i.e. the radiation that is not scattered or absorbed by aerosols on its path. If all radiation reaches the sensor, the optical depth is 0 ($-\ln(1)=0$). This is the case when an object is nearby or the

matter between the sensor and the object is minimal. The further the object is away and the more matter there is between it and the sensor, the higher the optical depth. If only 0.5% of the emitted radiation reaches the sensor, then the optical depth is about 5.3 ($-\log(0.005)=5.3$). The VAR method uses the surface and cloud top temperatures (representing the ground-based leaving radiance and the cloud top leaving radiance, respectively) to determine the optical depth per pixel. The effective radius of a particle distribution is a measure of the dominant particle radius. It is defined as the ratio of the skewness to the variance of a log normal distribution. Ash clouds dominated by larger particles therefore have a larger effective radius, as opposed to those dominated by smaller particles.

By analyzing the previously described temperature difference ($T_{10} - T_{12}$) against the temperature of the smaller wavelength channel (T_{10}), Wen and Rose (1994) found a correlation between optical depth of the ash cloud and its mean effective radii for each satellite pixel covering the cloud (Fig. 1.6). Here, a higher optical depth occurs at lower values on the abscissa, while higher ordinate number resembles larger effective radii. As seen in Figure 1.6, there is a limit on all sides of the resulting figure: When the effective radius approaches $5.0 \mu\text{m}$ or the optical depth approaches 4.0, the respective lines start to merge together reducing the sensitivity in this portion of the cloud/plume. Additionally, low optical depths and effective radii originate in one location limiting the expansion to the right.

Based on the area between the O K line (T_{10} - T_{12}) and different effective radii values, the sensitivity of the retrieval can be determined (Fig. 1.7). The converging lines at higher effective radii (5.0 μm and above) represent a lower sensitivity in this region compared to smaller values (1.0 to 4.0 μm). The maximum sensitivity occurs with an effective radius of 0.8 μm . All larger values decrease the sensitivity monotonically up to 4.3 μm . This monotony results in an unambiguous identification of effective radii and optical depth pairs for effective radii between 0.8 and 4.3 μm . The largest effective radii observable with the wavelength range are 12 μm . Larger effective radii represent a domination of larger particles that effectively turn the cloud opaque for the retrieval.

Such opaqueness in the infrared is often observed in satellite images during initial volcanic eruptions, when the plume is dominated by very large particles (e.g. Mt. Spurr, 1992; Rose et al., 2001). However, besides the particle size, their density, mass, concentration and refractive indices are also important to determine the optical opacity (Sparks et al., 1997). The Reverse Absorption Method, as well as the Volcanic Ash Retrieval does not provide volcanic ash detection and total masses in this scenario. Due to this necessity of the plume being translucent, every pixel-retrieved temperature is a combination of cloud top temperature (T_c) and surface temperature (T_s), assuming no other interfering aerosols are present (e.g. meteorological clouds), T_s doesn't change (i.e. the surface remains the same and there is no land to ocean transition) and the plume itself is homogenous. In order to accurately calculate the penetration of surface

and cloud radiances, those two parameters as well as the refractive index of the volcanic ash are necessary.

To estimate masses, a uniform density (ρ) has to be assumed and the pixel size (S) has to be known. Those two factors, along with the previously calculated effective radius (r_e) and the optical depth (OD) are used to define the mass for each pixel based on equation 1.1 (Wen and Rose, 1994):

$$\text{Pixel Mass} = \frac{S \frac{4}{3} \rho r_e \text{OD}}{Q_{\text{ext}}} \quad (1.1)$$

where Q_{ext} is the efficiency extinction factor calculated by the Mie theory in the assumption of a spherical particle size (Mie, 1908). The total ash mass in the image is therefore the sum of all pixel masses.

In these calculations, a correct estimate of T_c and T_s is crucial as a comparable small deviation of a few degrees can result in a large increase in the derived masses, as shown by Steensen and Webley (2012). In an operational or research setting, the accuracy of these parameters needs to be addressed to avoid large error bars in the total mass and pixel-based mass loading. While the cloud top temperature can be estimated from opaque clouds or using wind shear effects, a correct determination of the surface temperature is more complicated. Besides diurnal and topographic effects, changing background surfaces can further complicate the measurement. Ultimately, a pixel-

specific surface temperature is desired but as of now most studies use one generalized value.

1.4.2 Dispersion Model Analyses

VATD models have repeatedly been used to simulate historic eruptions (see work by Aloisi et al., 2002; Witham et al., 2007; Peterson et al., 2013) and to forecast hypothetical eruptions to support aircraft flight safety operations (Stunder et al., 2007). The advantage of VATD model analyses, in terms of volcanic plume and cloud forecasting, is their ability to simulate the cloud movement without dependence on clear-sky conditions, satellite revisiting times and retrieval sensitivities. However, without the real-time comparison to 'detected' ash clouds, VATD models alone cannot succeed in a mitigation, forecast and research environment. Regardless of the model used, input parameters with high levels of accuracy are required. Mastin et al. (2009) provide a detailed description of these 'eruption source parameters'. The critical ones are start/end time of the eruption and ash column height. With more sophisticated models, such as the Weather Research and Forecasting Model with coupled Chemistry (WRF-Chem; Grell et al., 2005), vertical distribution, eruption rate, erupted mass and mass fraction of fine ash ($< 63 \mu\text{m}$) are also important. Especially with remote volcanoes, acquisition of some of these parameters can prove complicated.

Eruption times and heights can often be determined from analyses of satellite and

seismic data (see work by Aloisi et al., 2002; Prejean and Brodsky, 2011; Waythomas et al., 2010; Rybin et al., 2011; Buurman et al., 2013) but if no seismic network is in the vicinity and cloud cover obscures a satellite analysis, infrasound data has successfully been used to estimate onsets of eruptions (such as Matoza et al., 2011). Field work is necessary to estimate density and volume of erupted tephra, and therefore the eruption rate. However, Mastin et al. (2009) developed formulas, partly based on Sparks et al. (1997) and Wilson and Walker (1987), to empirically derive parameters like eruption rate, plume height, volume and duration as well as the mass fraction of fine ash from known values. Based on different definitions of height, duration and volume as well as different initial retrieval methods with associated errors, uncertainties of up to a factor of four occurred for height estimates.

A general trade-off, while working with dispersion models, is a thoroughly detailed analysis versus processing time. Better spatial resolution or more incorporated parameters or particles requires more processing (Searcy et al., 1998). Depending on model type, this can be a few minutes for operational VATDs or up to multiple days for research models that analyze the eruption retrospectively in more detail.

1.4.2.1 Puff

Puff is a Lagrangian-based VATD model specifically designed for volcanic ash cloud modeling (Searcy et al., 1998). The model can be used to simulate ash clouds through a

command-line system and/or a web-based program. The model uses numerical weather prediction data as its atmospheric parameters and as such can be used to analyze past volcanic events. Additionally, it can be used to simulate airborne ash movement in near-real time to aid in hazard warning (Searcy et al., 1998). Originally developed by Tanaka (1991), Puff was designed for emergency responses limiting its mandatory input parameters by setting default values for most inputs variables except for volcano location and eruption time (Searcy et al., 1998). Other parameters like run-length, output interval, eruption duration, plume height, vertical distribution and number of ash particles are desired but not mandatory.

Puff forecasts the motion of individual particles positioned above the vent in a default linear vertical distribution using a uniform random-number generator (Tanaka, 1991; Searcy et al., 1998). This vertical distribution can be changed to exponential or poisson distributions to better match the satellite images or reports of the initial plume shape. The number of particles can be amended to better comply with computational resources. Studies by Aloisi et al. (2002) show that a larger number of particles (>5000) does not significantly alter the results in terms of dispersal extent (case study: Etna, 1998).

During the Puff model simulations, particles are released independently over the given duration of the event or, per default, the duration of the run. These particles' distribution shapes follow a Gaussian form on a logarithmic scale with a changeable

standard deviation. The mean particle size is an important factor to control the form of the distribution as well as the weighting in the larger particle sizes, as Searcy et al. (1998) showed that all particles greater than about 10^{-4} m (100 μ m) are removed from the plume after the first few time steps. As most ash cloud simulations are interested in the long-term behavior of the cloud, the default option is a mean particle size of 10^{-5} m (10 μ m) with a logarithmic standard deviation of 1.5, shifting the mean particle size to the longer-lived particles, where vertical motion effectively overwhelms fallout causing them to be suspended for long distances. This behavior can lead to the manipulation of Puff to create trajectories by setting the mean ash size to a very small value, i.e. virtually eliminating any fall out, and setting the turbulent diffusivity to zero (Searcy et al., 1998).

To calculate the dispersion, the Puff VATD model uses a three-dimensional Lagrangian formulation. Transport, turbulent dispersion and fallout are determined for a pre-defined number of discrete particles based on equation 1.2 (Searcy et al., 1998):

$$R_i(t + \Delta t) = R_i(t) + W(t) \Delta t + Z(t) \Delta t + S_i(t) \Delta t \quad (1.2)$$

where ' R_i ' is the position vector of particle ' i ' at time ' t ', ' W ' stands for the local wind velocity, ' Z ' is the turbulent dispersion vector and ' S ' represents the terminal gravitational fall-out vector. An estimate of the mass distribution is not required.

Wind data, $W(t)$, is interpolated from a four-dimensional mesoscale NWP model to each particle's position and time (Searcy et al., 1998). The default source for these wind fields

is the North American Mesoscale Model Grid 216 (NAM 216) and the Global Forecast System (GFS) and includes zonal and meridional wind speeds (ms^{-1}), and geopotential height (m) (Tanaka, 1991; Peterson et al., 2013). Their spatial resolutions are 45 x 45 km for NAM 216 and $1.25^\circ \times 1.25^\circ$ for GFS. However, a higher spatial resolution is achieved within Puff firstly through a cubic spline interpolation (up to three hours) and secondly with a linear interpolation (up to five minutes). For slowly varying winds, though, a nearest-neighbor interpolation reduces the computational time while still being sufficiently accurate (Searcy et al., 1998).

Every new NAM 216 data set includes the present conditions as well as forecasted values for 28 three-hourly time-steps (NOAA, 2013a). The global GFS forecast consists of six-hourly time-steps for six days (NOAA, 2013b). Therefore, the database of NWP for Puff always comprises the observed data as well as the short-term prediction of up to 3.5 days. This can be used to estimate near-real time dispersion of the plume.

Differences between the forecasted data and the observed values are minor depending on weather situation (Tanaka, 1991). However, any dataset and grid resolution can be used for Puff, as long as it can be mapped into the required four-dimensional grid (Searcy et al., 1998). If the NWP data set and subsequent model simulation does not consider topography, Puff will map the particle distribution to a 0 m ASL boundary layer and particles with a height of ≤ 0 m are considered as fallen out.

For the turbulent dispersion, $Z(t)$, a random walk, or Brownian motion, is superimposed

on the wind transport term for each particle (Tanaka, 1991) to account for small-scale fluctuations in the field. The components of Z are Gaussian random numbers with a zero mean and a standard deviation related to the diffusion rate. Each of these time steps is independent of the others and attributed by new random numbers. To calculate this diffusion rate, the diffusivity (K) is derived independently to particle size and local wind dynamics (Searcy et al., 1998). The value of the diffusivity is related to the plume's areal extent and previous studies have shown that a modification of its value is necessary depending on local conditions to accurately match the satellite-observed dispersion (Searcy et al., 1998; Aloisi et al., 2002).

The final term of the simulation is the fallout, $S_i(t)=(0,0,s)$. The terminal velocity (s) in this vector is described by Stoke's Law as a function of particle size. This value depends on the density (ρ), the dynamic viscosity (η), the gravitational acceleration (g) and the particle's size (d), see equation 1.3:

$$S = \frac{2 \rho g d^2}{9 \eta} \quad (1.3)$$

For simplicity, the model assumes the term $\rho g/\eta = 1.08 \times 10^9 \text{ m}^{-1} \text{ s}^{-1}$, leaving the terminal velocity only directly proportional to the squared particle size (Searcy et al., 1998). The addition of shape factors to include non-spherical particles is possible (Aloisi et al., 2002).

As Puff uses a Lagrangian framework, it models the behavior of discrete particles in time and space without operating on a pre-defined grid. This has the advantage that the plume direction and maximum distance does not need to be known *a priori*, therefore allowing it to act as an operational tool. However, this comes with the disadvantage of a non-continuous plot of the ash extent. Particle sizes, absolute concentrations and derived values, like the optical depth and the effective radius, can be estimated given the accurate particle size distribution and enough discrete particles. Adding more particles will improve those numbers but will also slow down the model; making it of less use in an operational setting.

Puff is an operational tool used by the Alaska Volcano Observatory (AVO), the Air Force Weather Agency (AFWA) and the Volcanic Ash Advisory Centers (VAAC) in Anchorage and Washington D.C. (Peterson et al., 2013). This dissertation will involve using the Puff VATD model and evaluating its performance in accurately simulating volcanic clouds compared to the satellite images and their parameter retrievals. In addition, a second VATD model based, on an Eulerian framework, will be used as described in section 1.4.2.2. This Eulerian-based VATD model will have the advantage of a more accurate dispersion (given accurate NWP data) since it is not based on individual tracer particles but on pre-defined grid cells with attributed values. This, on the other hand, requires a pre-defined spatial domain unlike Puff where the maximum dispersion extent sets the domain size, unless otherwise specified.

1.4.2.2 WRF-Chem

The Weather Research and Forecasting Model with online Chemistry (WRF-Chem) combines a numerical weather model with air chemistry (Grell et al., 2005). The online chemistry is fully integrated in the WRF model using the same grid, time step and transport scheme, and accounts for chemical and radiative feedback with the atmospheric state variables. With this concatenation of two previously independent approaches chemical effects on meteorological conditions, such as radiation budget, can be modeled with less potential error. The separate treatment of chemical and meteorological processes causes a loss of information on short-lived phenomena (such as cloud formation and rainfall) as an, at best, half-hourly meteorology output is often used to calculate the chemistry (Grell et al., 2005). Especially in hazard monitoring, such as volcanic plumes and dispersing clouds, a coupled approach is desirable to resolve small-scale features temporally and spatially.

Recently, a volcano application for WRF has been developed to predict plume/cloud dispersion (see Stuefer et al., 2013). Because it is a more complex modeling program when compared to Puff, WRF-Chem requires more input parameters like eruption rate and volume/mass besides the general parameters like initial volcanic plume height, eruption time, and duration. Other input options include the range of particle sizes (see Table 1.7 for WRF-Chem bins with their size ranges) and their individual weighting as percentage of the total mass. As opposed to Puff, there is currently no option for

varying the shape of the vertical distribution. As many large eruptions produce an umbrella-shaped plume, this poisson-based shape is used as a default setting for WRF-Chem (75% of erupted mass in umbrella, Freitas et al., 2011). The output concentrations of WRF-Chem include ash concentration at the chosen time steps.

As an Eulerian-based model, WRF-Chem uses differential equations to calculate different fields (such as concentration and wind vectors) and the plume/cloud development. Advantages of WRF-Chem over Puff are: (1) combining meteorological and volcanic chemical and physical processes; and (2) their plotting on a contiguous field as opposed to discrete Lagrangian particles. However, the model grid has to be defined *a priori* and cannot be changed during the model run. If the volcanic cloud drifts outside these boundaries, its track is effectively lost. Running WRF-Chem involves three steps in the WRF Preprocessing System and the WRF main program (Skamarock and Klemp, 2008). These steps include setting up the environmental parameters (such as domain and meteorological source input), converting the data to the required format.

1.4.2.3 WRF-Chem Output

As meteorological conditions are modeled in-line with the volcanic ash dispersion, all values are derived on the same grid. Besides the ash masses of each bin at each time step and at each height, three-dimensional wind vectors and soil temperatures are defined, among other parameters (see Grell et al., 2005). This WRF-Chem output will be

used to analyze the plume and cloud formation over the time range in detail. As WRF-Chem offers many features Puff does not, it can be better used to compare current satellite and model retrieval techniques. A volcano application for WRF-Chem has been developed by Stuefer et al. (2013).

WRF-Chem is computer-intensive. An option to reduce the computational time is reduction of the spatial resolution. A retrospective analysis of an eruption, though, will also provide valuable information of the plume/cloud that can be incorporated into operational monitoring using satellites and models like Puff.

1.4.2.4 Other Dispersion Models

Besides Puff and WRF-Chem, there are several dispersion models in existence. Most notably and widely used is the Hybrid Single Particle Lagrangian Integrated Trajectory Model (HYSPLIT; see Draxler and Hess, 1997 and Prata et al., 2011). HYSPLIT can be used as a backward and a forward trajectory model as well as for creating air concentration contour patterns due to a combination of Lagrangian and Eulerian framework. It uses previously gridded meteorological data with either puff or particle dispersion. In the puff mode, the clouds expand until they reach the meteorological grid cell size when they split to two or more adjacent cells. The particle model is similar to the previously described Puff by initiating the dispersion of a finite number of discrete particles consecutively being advected over the model domain (Peterson et al., 2013).

HYSPLIT is used at the Anchorage, Darwin, Washington D.C. and Wellington VAACs (Prata et al., 2011). This makes it the most commonly used dispersion model followed by Puff, which is used in the Anchorage and Tokyo VAACs as well as by AVO. Other dispersion models include the Modèle Lagrangien de Dispersion de Particules d'ordre zéro (MLDPO: Montreal and Anchorage VAAC; D'Amours et al., 2010), the Numerical Atmospheric- dispersion Modeling Environment (NAME: London VAAC; Ryall and Maryon, 1998) and the Modélisation de la Chimie Atmosphérique Grande Echelle (MOCAGE: Toulouse VAAC; Bousserez et al., 2007).

All of these models, including Puff and WRF-Chem, run operationally. Alternative models for this project include MLDPO and HYSPLIT due to their usage in multiple VAACs in Polar Regions. However, none of them computes meteorological data on the same grid as WRF-Chem does. As Puff is one of the operational models being run at AVO and the Anchorage VAAC, it is chosen to compare to WRF-Chem results and the satellite data.

1.4.3 Qualitative Comparison

To compare model and satellite results qualitatively, the Critical Success Index (CSI) (as shown by Stunder et al., 2007) will be applied. This index combines the area the satellite sensor algorithms identify as ash (A), the area the model forecasts to be ash (B) and the region where both overlap (AB). With the satellite data set as the ‘truth’ data, the area A-B is then the “missed ash” and B-A are the “false alarms”. The CSI can then be calculated by equation 1.4:

$$\text{CSI} = \text{AB}/(\text{A}+\text{AB}+\text{B}) \quad (1.4)$$

A low CSI stands for less overlap between satellite data and model forecast. Previous analyses (Stunder et al., 2007) have set 0.25 as the critical threshold. Above this, the forecast is acceptable. A low ranking in the CSI can have different reasons. As it is essentially a comparison between satellite-detected and model-forecasted ash area, a larger area belonging to only one of the products and/or a small overlap will decrease the index. Furthermore, a shift of the entire plume due to miscalculated wind patterns will return a low value.

As satellite retrievals are most sensitive to the effective particle size range from 0.8 to 4.3 μm (Wen and Rose, 1994), they can be evaluated against appropriate WRF-Chem bins that show similar effective particle sizes. This effective radius is dependent on the initial particle size distribution, so that a specific bin number cannot always be taken to

retrieve comparable results. In addition, cloud coverage often masks ash from the satellite remote sensing detection (Pavolonis et al., 2006). This also has to be taken into account when applying the Critical Success Index.

Other possible qualitative comparisons include column integrated ash masses of satellite and WRF-Chem. The meteorological data in WRF-Chem can also help to better determine surface and cloud temperatures as input for VAR. A sensitivity analysis based on defined ranges for those variables allows an assessment of the possible variability in the volcanic ash masses caused by changes in temperature. This can then be compared to WRF-Chem derived masses to give an estimate on best input values for the ash retrieval. Similarly, BTM thresholds for the Reverse Absorption Method can be evaluated. All of these comparisons can ultimately lead to a better assessment of input parameters for VAR and to a better characterization of evolving volcanic clouds.

1.5 Summary

Such a quantitative error reduction through direct comparison between satellite data and VATD model calculations is crucial for near real time observations and analyses of airborne ash cloud distributions. Through the inter-comparison of different VATD models and remote sensing satellite data, ash cloud locations can be determined more accurately. These observations can then be used by the aviation community in their assessment of the volcanic ash hazard to aircrafts. The following chapters of this

dissertation deal with a qualitative comparison between Puff and WRF-Chem model outputs using the Mount Redoubt eruption as a case study (Chapter 2), the analysis of the importance of individual input parameters for VAR to improve a quantitative ash mass estimated using satellite remote sensing data (Chapter 3), the quantitative comparison between WRF-Chem model outputs and satellite data with a focus on an improved ash detection in satellite data using the case study of the Sarychev Peak eruption (Chapter 4) and the development of the 'Ash – No Ash' approach in Chapter 5 applied to the Kasatochi eruption, based on results from the previous Chapters.

The aims of this dissertation are:

- (1) To provide an approach that can compare satellite and VATD model data quantitatively while limiting the uncertainties
- (2) To assess the accuracy of input parameters for the Volcanic Ash Retrieval
- (3) To analyze the uncertainty introduced to comparison by not projecting the VATD model's calculation to the satellite's line-of-sight

The work in this dissertation has been done solely by me, except where otherwise noted. In co-authored papers, I received VATD model data and satellite imagery and wrote the analysis scripts as well as the papers. In case of WRF-Chem, I was also provided with visualizations of the model outputs, which I modified for Figures 2.7 to 2.14, 4.2A, 4.3 to 4.5, 4.13 and 4.14.

1.6 References

- Aloisi, M., M. D'Agostino, K. G. Dean, A. Mostaccio, and G. Neri (2002), Satellite analysis and PUFF simulation of the eruptive cloud generated by the Mount Etna paroxysm of 22 July 1998, *Journal of Geophysical Research-Solid Earth*, 107(B12).
- Andrews, B. J., and J. E. Gardner (2009), Turbulent dynamics of the 18 May 1980 Mount St. Helens eruption column, *Geology*, 37(10), 895-898.
- Andronico, D., C. Spinetti, A. Cristaldi, and M. F. Buongiorno (2009), Observations of Mt. Etna volcanic ash plumes in 2006: An integrated approach from ground-based and polar satellite NOAA-AVHRR monitoring system, *Journal of Volcanology and Geothermal Research*, 180(2-4), 135-147.
- Blong, R.J. (1984), *Volcanic Hazards: A Sourcebook on the Effects of Eruptions*. Academic Press, Sydney 424pp.
- Bousserez, N., Attí e, J.-L., Peuch, V.-H., Michou, M., Pfister, G., Edwards, D., Emmons, L., Mari, C., Barret, B., Arnold, S. R., Heckel, A., Richter, A., Shlager, H., Lewis, A., Avery, M., Sachse, G., Browell, E. V., and Hair, J. W. (2007), Evaluation of the MOCAGE chemistry transport model during the ICARTT/ITOP experiment, *J. Geophys. Res.*, 112, D10S42, doi:10.1029/2006JD007595.
- Burt, M. L., G. Wadge, and R. N. Curnow (2001), An objective method for mapping hazardous flow deposits from the stratigraphic record of stratovolcanoes: a case example from Montagne Pelee, *Bulletin of Volcanology*, 63(2-3), 98-111.
- Buurman, H., M. West, and G. Thompson, (2013), The Seismic Chronology of the 2009 Redoubt Eruption. Introduction to Redoubt Volcano, and overview of the 2009 eruption *Journal of Volcanology and Geothermal Research, Special Issue on the 2009 Redoubt Eruption*, 259, 16-30
- Carn, S. A., A. J. Krueger, N. A. Krotkov, K. Yang, and K. Evans (2008), Tracking Volcanic sulfur dioxide clouds for aviation hazard mitigation, *Natural Hazards*.
- Casadevall, T. J. (1994), THE 1989-1990 Eruption of Redoubt Volcano, Alaska - Impacts on Aircraft Operations, *Journal of Volcanology and Geothermal Research*, 62(1-4), 301-316.
- D'Amours, R., A. Malo, R. Servranckx, D. Bensimon, S. Trudel, and J.-P. Gauthier-Bilodeau (2010), Application of the atmospheric Lagrangian particle dispersion model MLDP0 to the 2008 eruptions of Okmok and Kasatochi volcanoes, *Journal of Geophysical Research-*

Atmospheres, 115.

Dean, K. G., J. Dehn, K. Engle, P. Izbekov, K. Papp, and M. Patrick (2002), Operational Satellite Monitoring of Volcanoes at the Alaska Volcano Observatory, *Advances in Environmental Monitoring and Modeling*, 1(1), 70-97.

Diamond, J. (1986), Down to a sunless sea - The anatomy of an incident, *The Log*, 13-16.

Downing, H. D., and D. Williams (1975), Optical Constants of Water in the Infrared, *Journal of Geophysical Research*, 80(12), 6.

Draxler, R. R., and G. D. Hess (1997), Description of the Hysplit_4 Modeling System, *NOAA Technical Memorandum ERL ARL-224*.

Flentje, H., H. Claude, T. Elste, S. Gilge, U. Köhler, C. Plass-Dülmer, W. Steinbrecht, W. Thomas, A. Werner, and W. Fricke (2010), The Eyjafjallajökull eruption in April 2010 - detection of volcanic plume using in-situ measurements, ozone sondes and a new generation ceilometer network, *Atmospheric Chemistry and Physics Discussions*, 10, 14947-14968.

Forster, P., P. Artaxo, T. Berntsen, R. Betts, D. W. Fahey, J. Haywood, J. Lean, D. C. Lowe, G. Myhre, J. Nganga, R. Prinn, G. Raga, M. Schulz and R. Van Dorland, (2007), Changes in Atmospheric Constituents and in Radiative Forcing, in *Climate Change 2007 The Physical Science Basis*, edited by S. Solomon, D. Qin, M. Manning, M. Marquis, K. Averyt, M. M. B. Tignow, H. L. Miller and Z. Chen, Cambridge University Press, Cambridge.

Freitas, S. R., K. M. Longo, M. F. Alonso, M. Pirre, V. Marecal, G. Grell, R. Stockler, R. F. Mello, and M. Sánchez Gácita, (2011), PREP-CHEM-SRC 1.0: a preprocessor of trace gas and aerosol emission fields for regional and global atmospheric chemistry models, *Geoscientific Model Development*, 4, 419-433.

Grell, G. A., S. E. Peckham, R. Schmitz, S. A. McKeen, G. Frost, W. C. Skamarock, and B. Eder (2005), Fully coupled "online" chemistry within the WRF model, *Atmospheric Environment*, 39(37), 6957-6975.

Gu, Y. X., W. I. Rose, and G. J. S. Bluth (2003), Retrieval of mass and sizes of particles in sandstorms using two MODIS IR bands: A case study of April 7, 2001 sandstorm in China, *Geophysical Research Letters*, 30(15).

Gu, Y. X., W. I. Rose, D. J. Schneider, G. J. S. Bluth, and I. M. Watson (2005), Advantageous GOES IR results for ash mapping at high latitudes: Cleveland eruptions 2001, *Geophysical Research Letters*, 32(2).

Hanstrum, B. N., and A. S. Watson (1983), A case study of two eruptions of Mount Galunggung and an investigation of volcanic eruption cloud characteristics using remote sensing techniques, *Australian Meteorological Magazine*, 31, 171-177.

Harris, A. J. L., S. Blake, D. A. Rothery, and N. F. Stevens (1997), A chronology of the 1991 to 1993 Mount Etna eruption using advanced very high resolution radiometer data: Implications for real-time thermal volcano monitoring, *Journal of Geophysical Research-Solid Earth*, 102(B4), 7985-8003.

Harris, A. J. L., L. P. Flynn, L. Keszthelyi, P. J. Mougini-Mark, S. K. Rowland, and J. A. Resing (1998), Calculation of lava effusion rates from Landsat TM data, *Bulletin of Volcanology*, 60(1), 52-71.

Holasek, R. E., S. Self, and A. W. Woods (1996), Satellite observations and interpretation of the 1991 Mount Pinatubo eruption plumes, *Journal of Geophysical Research-Solid Earth*, 101(B12), 27635-27655.

International Civil Aviation Organization (ICAO) (2004), Handbook on the International Airways Volcano Watch (IAVW), Doc 9766-AN/968, http://www.icao.int/publications/Documents/IAVW%20Handbook%20Doc%209766_en.pdf, last accessed August 1, 2013.

Jin, X., J. Li, T. J. Schmit, J. L. Li, M. D. Goldberg, and J. J. Gurka (2008), Retrieving clear-sky atmospheric parameters from SEVIRI and ABI infrared radiances, *Journal of Geophysical Research-Atmospheres*, 113(D15).

Labitzke, K., B. Naujokat, and M. P. McCormick (1983), Temperature Effects on the Stratosphere of the April 4, 1982 Eruption of el Chichon, Mexico, *Geophysical Research Letters*, 10(1), 24-26.

Mastin, L. G., M. Guffanti, R. Servranckx, P. Webley, S. Barsotti, K. Dean, A. Durant, J. W. Ewert, A. Neri, W. I. Rose, D. Schneider, L. Siebert, B. Stunder, G. Swanson, A. Tupper, A. Volentik and C. F. Waythomas (2009), A multidisciplinary effort to assign realistic source parameters to models of volcanic ash-cloud transport and dispersion during eruptions, *Journal of Volcanology and Geothermal Research*, 186(1-2), 10-21.

Matoza, R. S., A. Le Pichon, J. Vergoz, P. Herry, J.-M. Lalande, H. Lee, I.-Y. Che, and A. Rybin (2011), Infrasonic observations of the June 2009 Sarychev Peak eruption, Kuril Islands: Implications for infrasonic monitoring of remote explosive volcanism, *Journal of Volcanology and Geothermal Research*, 200, 35-48.

McCormick, P. M., L. W. Thomason, and C. R. Trepte (1995). Atmospheric Effects of the

Mt. Pinatubo eruption, *Nature*, 373, 399-404.

Mie, G. (1908), Beiträge zur Optik trüber Medien, speziell kolloidaler Metallösungen, *Annalen der Physik*, 4(25).

Mori, T., and K. Notsu (2008), Temporal variation in chemical composition of the volcanic plume from Aso volcano, Japan, measured by remote FT-IR spectroscopy, *Geochemical Journal*, 42(1), 133-140.

Newhall, C. G., and S. Self (1982), The Volcanic Explosivity Index (VEI) - An Estimate of Explosive Magnitude for Historical Volcanism, *Journal of Geophysical Research-Oceans and Atmospheres*, 87(NC2), 1231-1238.

National Oceanic and Atmospheric Administration (NOAA, 2013a), <http://www.nco.ncep.noaa.gov/pmb/products/nam/>, last accessed on July 25, 2013.

National Oceanic and Atmospheric Administration (NOAA, 2013b), <http://www.srh.noaa.gov/ssd/nwpmoel/html/nogover.htm>, last accessed on July 25, 2013.

Oppenheimer, C. (1998), Volcanological applications of meteorological satellites, *International Journal of Remote Sensing*, 19(15), 2829-2864.

Oppenheimer, C. (2003), Climatic, environmental and human consequences of the largest known historic eruption: Tambora volcano (Indonesia) 1815, *Progress in Physical Geography*, 27(2), 230-259.

Pavolonis, M. J., W. F. Feltz, A. K. Heidinger, and G. M. Gallina (2006), A daytime complement to the reverse absorption technique for improved automated detection of volcanic ash, *Journal of Atmospheric and Oceanic Technology*, 23(11), 1422-1444.

Pavolonis, M., and J. Sieglaff (2010), GOES-R Advanced Baseline Imager (ABI) Algorithm Theoretical Basis Document for Volcanic Ash (Detection and Height), *NOAA NESDIS Center for Satellite Applications and Research*.

Petersen, G. N. (2010), A short meteorological overview of the Eyjafjallajökull eruption 14 April-23 May 2010, *Weather*, 65(8), 203-207

Peterson, R., P. Webley, R. D'Amours, R. Servranckx, B. Stunder, and K. Papp (2013), Volcanic Ash Transport and Dispersion Models, in *Remote Sensing of Volcanic Eruptions*, edited by K. Dean, in press.

Pichler, H., and T. Pichler (2007), *Vulkangebiete der Erde. Elsevier Spektrum Akademischer Verlag, Munich, Germany, 261 pages.*

Pinto, J. P., R. P. Turco, and O. B. Toon (1989), Self-Limiting Physical and Chemical Effects in Volcanic Eruption Clouds, *Journal of Geophysical Research-Atmospheres*, 94(D8), 11165-11174.

Prabaharan, D. J. (2002), Fear of flying: Assessing the risks of volcanic ash clouds for aviation, *GIS User* 50, 22-23,

Prata, A. J. (1989a), Observations of Volcanic Ash Clouds in the 10-12 μm Window Using AVHRR/2 Data, *International Journal of Remote Sensing*, 10(4-5), 751-761.

Prata, A. J. (1989b), Infrared Radiative-Transfer Calculations for Volcanic Ash Clouds, *Geophysical Research Letters*, 16(11), 1293-1296.

Prata, A. J., I. J. Barton, R. W. Johnson, K. Kamo, and J. Kingwell (1991), HAZARD FROM VOLCANIC ASH, *Nature*, 354(6348), 25-25.

Prata, A. J., and I. J. Barton, (1994), Detection and discrimination of volcanic ash clouds by infrared radiometry – I: theory. In: Casadevall, T. J., editor. Volcanic Ash and aviation safety: proceedings of the first International Symposium on Volcanic Ash and Aviation Safety; Seattle, Washington, D.C.: U.S. G.P.O., *U.S. Geological Survey bulletin*, 2047, 305–311.

Prata, F., G. Bluth, B. Rose, D. Schneider, and A. Tupper (2001), Failures in detecting volcanic ash from a satellite-based technique - Comments, *Remote Sensing of Environment*, 78(3), 341-346.

Prata, A. J., G. Gangale, L. Clarisse, and F. Karagulian (2010), Ash and sulfur dioxide in the 2008 eruptions of Okmok and Kasatochi: Insights from high spectral resolution satellite measurements, *Journal of Geophysical Research-Atmospheres*, 115.

Prata, F., K. Dean, and M. Watson (2011), Volcanic Clouds, in *Remote Sensing of Volcanic Eruptions*, edited by K. Dean, in review.

Prejean, S. G., and E. E. Brodsky (2011), Volcanic plume height measured by seismic waves based on a mechanical model, *Journal of Geophysical Research-Solid Earth*, 116.

Rose, W. I., D. J. Delene, D. J. Schneider, G. J. S. Bluth, A. J. Krueger, I. Sprod, C. McKee, H. L. Davies, and G. G. J. Ernst (1995), Ice in the 1994 Rabaul Eruption Cloud – Implications for Volcano Hazard and Atmospheric Effects, *Nature*, 375(6531), 477-479.

Rose, W. I., G. J. S. Bluth, and G. G. J. Ernst (2000), Integrating retrievals of volcanic cloud characteristics from satellite remote sensors: a summary, *Philosophical Transactions of the Royal Society of London Series a-Mathematical Physical and Engineering Sciences*, 358(1770), 1585-1606.

Rose, W. I., G. J. S. Bluth, D. J. Schneider, G. G. J. Ernst, C. M. Riley, L. J. Henderson, and R. G. McGimsey (2001), Observations of volcanic clouds in their first few days of atmospheric residence: The 1992 eruptions of Crater Peak, Mount Spurr volcano, Alaska, *Journal of Geology*, 109(6), 677-694.

Ryall D.B., and Maryon R.H. (1998), Validation of the UK Met. Office's NAME model against the ETEX dataset, *Atmospheric Environment* 32(24), 4265-4276.

Rybin, A., M. Chibisova, P. Webley, T. Steensen, P. Izbekov, C. Neal, and V. Realmuto (2011), Satellite and ground observations of the June 2009 eruption of Sarychev Peak volcano, Matua Island, Central Kuriles, *Bulletin of Volcanology*, doi: 10.1007/s00445-011-0481-0.

Schneider, D. J., W. I. Rose, L. R. Coke, G. J. S. Bluth, I. E. Sprod, and A. J. Krueger (1999), Early evolution of a stratospheric volcanic eruption cloud as observed with TOMS and AVHRR, *Journal of Geophysical Research-Atmospheres*, 104(D4), 4037-4050.

Schneider, D.J., and R. P. Hoblitt, (2013), Doppler weather radar observations of the 2009 eruption of Redoubt Volcano, Alaska, *Journal of Volcanology and Geothermal Research, Special Issue on the 2009 Redoubt Eruption*, 259, 133-144.

Scott, W. E., and R. G. McGimsey (1994), Character, Mass, Distribution, and Origin of Tephra-Fall Deposits of the 1989-1990 Eruption of Redoubt Volcano, South-Central Alaska, *Journal of Volcanology and Geothermal Research*, 62(1-4), 251-272.

Searcy, C., K. Dean, and W. Stringer (1998), PUFF: A high-resolution volcanic ash tracking model, *Journal of Volcanology and Geothermal Research*, 80(1-2), 1-16.

Shinohara, H. (2005), A new technique to estimate volcanic gas composition: plume measurements with a portable multi-sensor system, *Journal of Volcanology and Geothermal Research*, 143(4), 319-333.

Simpson, J. J., G. Hufford, D. Pieri, and J. Berg (2000), Failures in detecting volcanic ash from satellite-based technique, *Remote Sensing of Environment*, 72(2), 191-217.

Simpson, J. J., G. L. Hufford, D. Pieri, and J. S. Berg (2001), Response to "Comments on 'Failures in detecting volcanic ash from a satellite-based technique'", *Remote Sensing of*

Environment, 78, 347-357.

Skamarock, W. C., and J. B. Klemp (2008), A time-split nonhydrostatic atmospheric model for weather research and forecasting applications, *J. Comput. Phys.*, 227(7), 3465-3485.

Smith, W. L., H. M. Woolf, C. M. Hayden, D. Q. Wark, and L. M. McMillin (1979), The TIROS-N Operational Vertical Sounder, *GARP Topics*, 60(10), 1177-1187.

Sparks, R.S.J., M. I. Bursik, S. N. Carey, R. S. Gilbert, L. S. Glaze, H. Sigurdsson, A. W. and Woods (1997). *Volcanic Plumes* New York, John Wiley and Sons, 574 pp.

Spicak, A., J. Kozak, J. Vanek, and V. Hanus (2008), The Krakatau volcano 125 years after the catastrophic eruption (August 27, 1883), *Studia Geophysica Et Geodaetica*, 52(3), 449-454.

Steensen, T. and Webley, P. (2012), Qualitative Analysis of Input Parameters for Satellite-Based Quantification of Airborne Volcanic Ash, *Geoscience and Remote Sensing Symposium (IGARSS), 2012 IEEE International* , Pages 2982 – 2985, 10.1109/IGARSS.2012.6350799.

Steensen, T., M. Stuefer, P. Webley, G. Grell, and S. Freitas, (2013), Plume Characteristics during the 2009 Mount Redoubt Eruption: A comparison between satellite data and dispersion models, *Journal of Volcanology and Geothermal Research, Special Issue on the 2009 Redoubt Eruption*, 259, 235-247.

Stuefer, M., S. R. Freitas, G. Grell, P. Webley, S. Peckham, S. A. McKeen, and S. D. Egan (2013), Inclusion of ash and SO₂ emissions from volcanic eruptions in WRF-Chem: development and some applications, *Geosci. Model Dev.*, 6(2).

Stunder, B. J. B., J. L. Heffter, and R. R. Draxler (2007), Airborne volcanic ash forecast area reliability, *Weather and Forecasting*, 22, 1132-1139.

Tanaka, H. (1991), Development of a Prediction Scheme for Volcanic Ash Fall From Redoubt Volcano, Alaska, *U. S. Geological Survey Bulletin*, 2047, 283-291.

Theys, N., M. Van Roozendaal, B. Dils, F. Hendrick, N. Hao, and M. De Maziere (2009), First satellite detection of volcanic bromine monoxide emission after the Kasatochi eruption, *Geophysical Research Letters*, 36.

Tupper, A., S. Carn, J. Davey, Y. Kamada, R. Potts, F. Prata, and M. Tokuna (2004), An evaluation of volcanic cloud detection techniques during recent significant eruptions in

the western 'Ring of Fire', *Remote Sensing of Environment*, 91, 27-46.

Vasey, D. E. (1991), Population, Agriculture, and famine – Iceland, 1784-1785, *Human Ecology*, 19(3), 323-350.

Volz, F. E. (1973), Infrared Optical Constants of Ammonium Sulfate, Sahara Dust, Volcanic Pumice, and Flyash, *Applied Optics*, 12(3), 564-568.

Wallace, K.L., and J. G. Schaefer, (2013), Event chronology, plume heights, and preliminary report of distribution, thickness, and mass of ash fall from the 2009 eruption of Redoubt volcano, *Alaska Journal of Volcanology and Geothermal Research, Special Issue on the 2009 Redoubt Eruption*, 250, 145-169.

Watson, I. M., V. J. Realmuto, W. I. Rose, A. J. Prata, G. J. S. Bluth, Y. Gu, C. E. Bader, and T. Yu (2004), Thermal infrared remote sensing of volcanic emissions using the moderate resolution imaging spectroradiometer, *Journal of Volcanology and Geothermal Research*, 135(1-2), 75-89.

Waythomas, C. F., W. E. Scott, S. G. Prejean, D. J. Schneider, P. Izbekov, and C. J. Nye (2010), The 7-8 August 2008 eruption of Kasatochi Volcano, central Aleutian Islands, Alaska, *Journal of Geophysical Research-Solid Earth*, 115.

Wen, S. M., and W. I. Rose (1994), Retrieval of sizes and total masses of particles in volcanic clouds using AVHRR bands 4 and 5, *Journal of Geophysical Research-Atmospheres*, 99(D3), 5421-5431.

Wilson, L., and G. P. L. Walker (1987), Explosive volcanic eruptions – VI. Ejecta dispersal in plinian eruptions: the control of eruption conditions and atmospheric properties, *Geophysical Journal of the Royal Astronomical Society*, 89.

Witham, C. S., M. C. Hort, R. Potts, R. Servranckx, P. Husson, and F. Bonnardot (2007), Comparison of VAAC atmospheric dispersion models using the 1 November 2004 Grimsvotn eruption, *Meteorological Applications*, 14(1), 27-38.

1.7 Figures

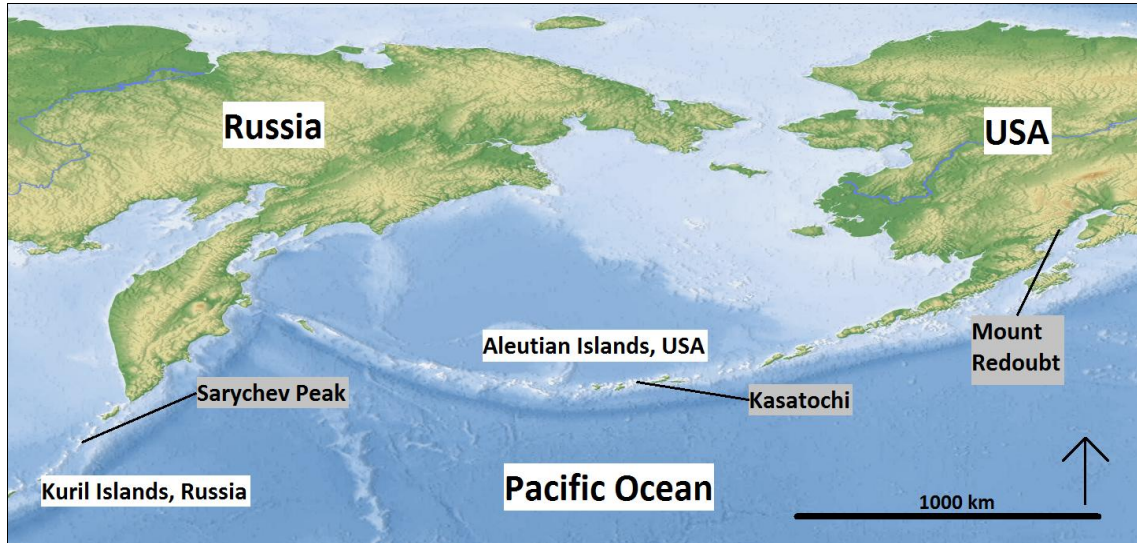


Figure 1.1: Map of the North Pacific region. The volcanoes focused on in this dissertation are highlighted in gray.

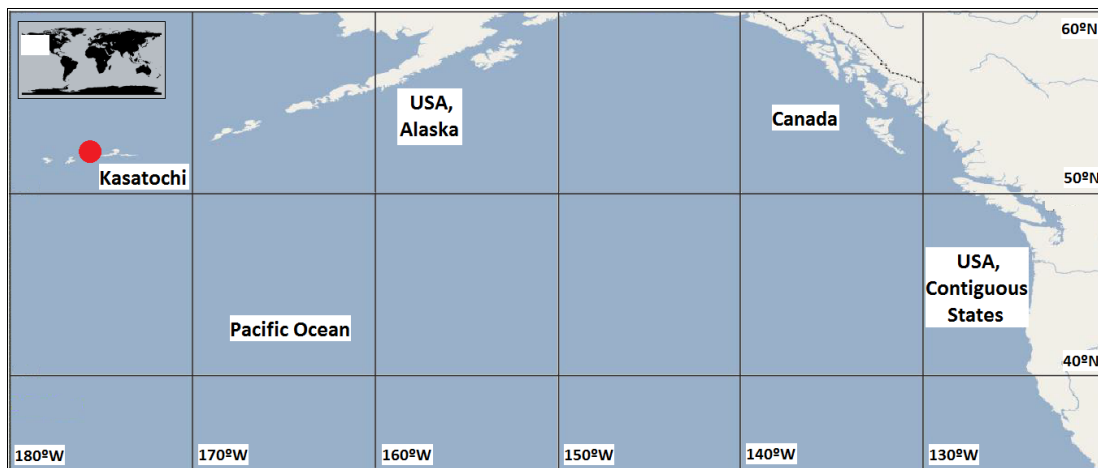


Figure 1.2: Location of Kasatochi volcano in the Aleutian Islands in relation to Alaska, Canada and the contiguous United States. For a bigger scale refer to Figure 1.1.

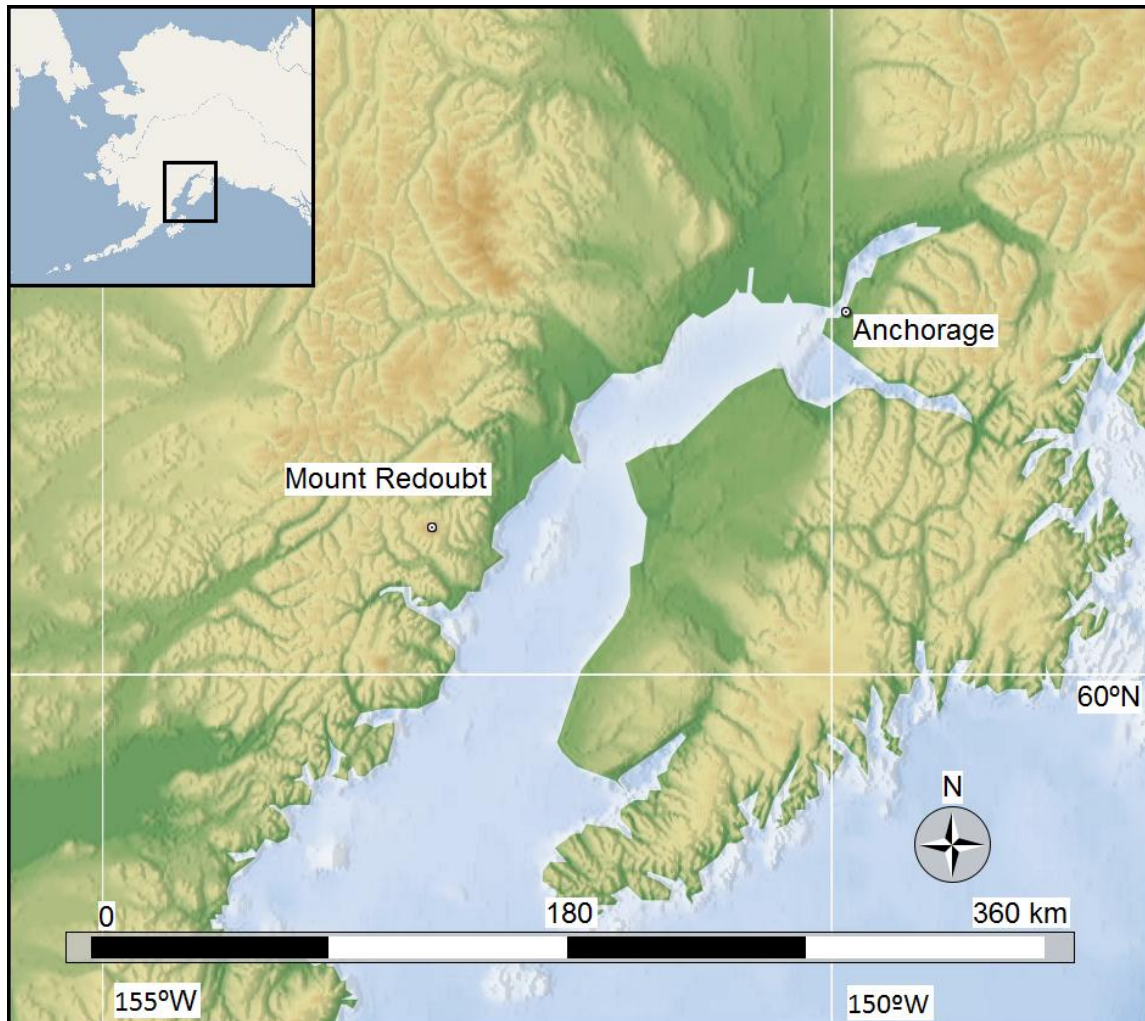


Figure 1.3: Location of Mount Redoubt volcano in Cook Inlet close to Anchorage. For a bigger scale refer to Figure 1.1.

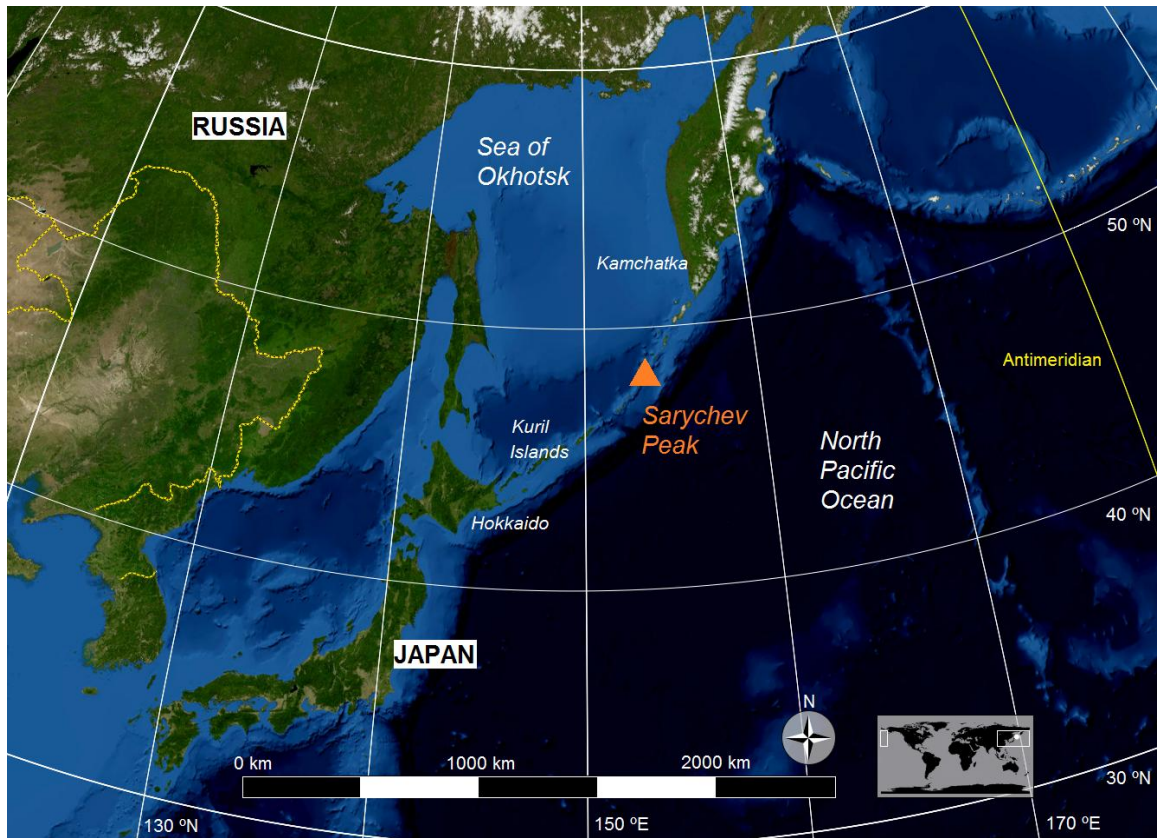


Figure 1.4: Location of Sarychev Peak volcano in the Kuril Islands, Russia. For a bigger scale refer to Figure 1.1.

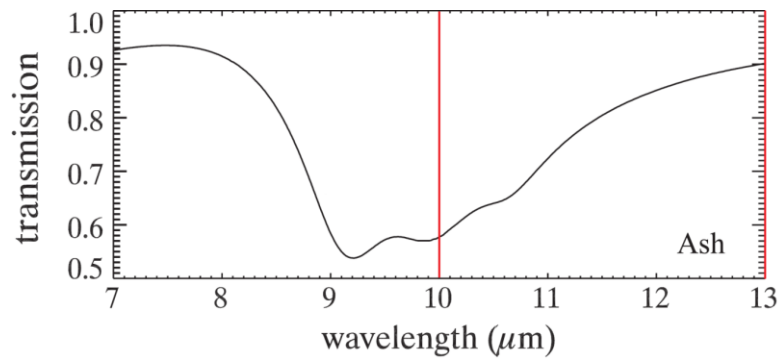


Figure 1.5: Transmission index (absorption and scattering) of volcanic ash in the atmosphere, modified after Watson et al. (2004). Between 10 and 13 μm , a continuous rise in the transmission is notable forming the basis of the Reverse Absorption Method.

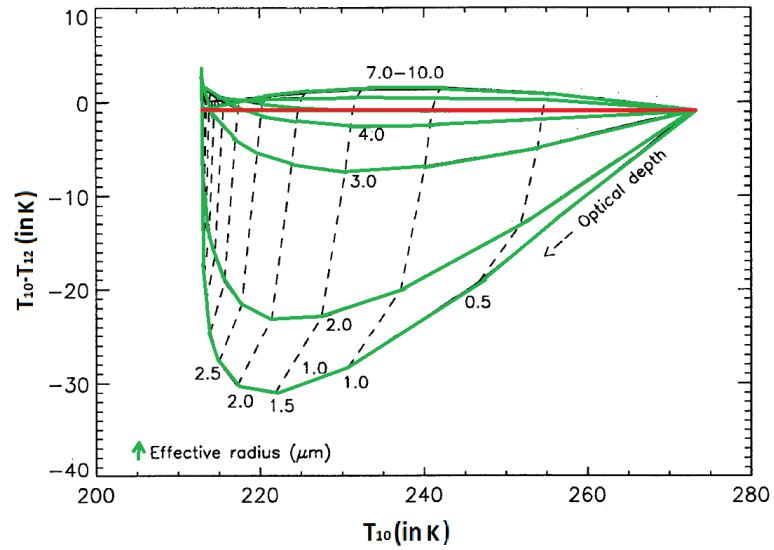


Figure 1.6: Relationship between optical depth of the cloud and mean effective radii of the particles in each covered satellite pixel revealed in a plot of the temperature difference ($T_{10}-T_{12}$) versus T_{10} , modified after Wen and Rose (1994).

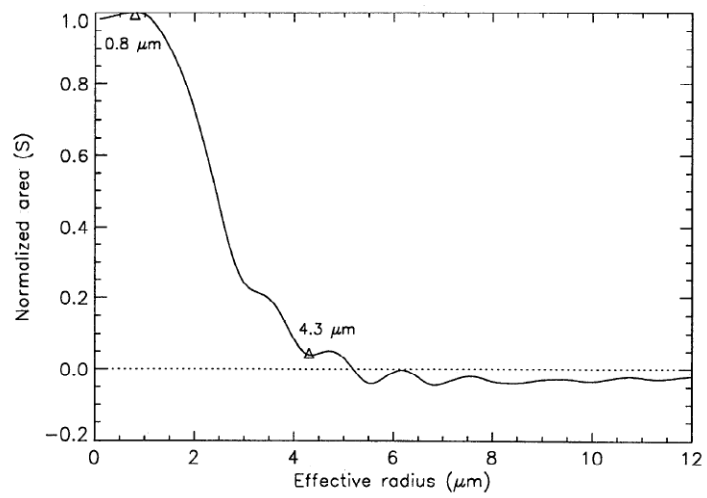


Figure 1.7: Sensitivity (S, normalized to represent a maximum of 1) of the Volcanic Ash Retrieval based on Figure 1.6. The retrieval is most sensitive to smaller effective radii with a monotonical decrease from 0.8 to 4.3 μm (from Wen and Rose, 1994).

Table 1.1: Criteria for determination of the Volcanic Explosivity Index (VEI). Modified after Newhall and Self, 1982, and Pichler and Pichler, 2007.

VEI	0	1	2	3	4	5	6	7	8
Explosivity	non-explosive	small	moderate	moderate-large	large (paroxysmal)	very large (superparoxysmal)			
Volume of Ejecta (m ³)	< 10 ⁴	10 ⁴ - 10 ⁶	10 ⁶ - 10 ⁷	10 ⁷ - 10 ⁸	10 ⁸ - 10 ⁹	10 ⁹ - 11 ¹⁰	10 ¹⁰ - 10 ¹¹	10 ¹¹ - 10 ¹²	> 10 ¹²
Column Height (km)	< 0.1	0.1-1	1-5	3-15	10-25	> 25	> 25	> 25	> 25
Classification	Hawaiian								
		Strombolian							
			Vulcanian						
				Plinian					
					Ultraplinian				
Example in documented history	Kilauea	Stromboli	Etna	Etna 1980	Pelée 1902	St. Helens 1980	Krakatau 1883	Tambora 1815	

Table 1.2: Eruption chronology for the Kasatochi volcanic eruptive events in August 2008. Three distinctive events have been recorded, with a continuous phase following afterwards (Waythomas et al., 2010).

Kasatochi, August 2008	Duration	Plume Height	Day	Time
Explosive event 1	1 hour	14 km	August 7	22:01 UTC
Explosive event 2	0.5 hours	14 km	August 8	01:50 UTC
Explosive event 3 initiates continuous phase with two more explosive pulses	0.5 hours 10 hours	18 km ≤ 10 km	August 8	04:35 UTC 07:12 UTC, 11:42 UTC
Waning Phase	8 hours		August 8	

Table 1.3: Eruption chronology for the Redoubt volcanic eruptive events in March and April 2009. 19 distinctive events have been recorded with duration from 1 to 38 minutes (Buurman et al., 2013) and a varying plume height between 5 and 19 km ASL (Schneider and Hoblitt, 2013).

Mount Redoubt, March - April 2009	Duration (mins)	Plume Height (km)	Day	Time (UTC)
1	2	5.5	March 23	06:34
2	7	13.4	March 23	07:02
3	20	13.1	March 23	08:14
4	38	13.1	March 23	09:39
5	20	14.9	March 23	12:30
6	15	18.3	March 24	03:41
7	1	6.7	March 26	16:34
8	14	18.9	March 26	17:24
9	1	11	March 27	07:48
10	7	14.9	March 27	08:29
11	8	15.5	March 27	16:39
12	2	11.9	March 28	01:35
13	4	15.2	March 28	03:24
14	2	11.9	March 28	07:20
15	4	13.1	March 28	09:20
16	6	5.2	March 28	21:40
17	6	12.2	March 28	23:30
18	11	12.5	March 28	03:24
19	31	15.2	April 4	13:59

Table 1.4: Eruption chronology for the Sarychev Peak volcanic eruptive events in June 2009. 23 distinctive events have been recorded with varying plume heights between 3 and 21 km (Matoza et al., 2011). Due to a lack of seismic stations around Sarychev Peak, the durations are inferred from infrasound measurements whenever the origin of the sound matches the onset of an event.

Sarychev Peak, June 2009	Duration (mins)	Plume Height (km)	Day	Time (UTC)
1		3 km	June 11	02:00 UTC
2		4 km	June 11	07:00 UTC
3		10 km	June 12	02:00 UTC
4	13 minutes	6 km	June 12	04:00 UTC
5		12 km	June 12	07:57 UTC
6	16 minutes	5 km	June 12	14:57 UTC
7	25 minutes	5 km	June 12	17:13 UTC
8		5 km	June 12	18:57 UTC
9	20 minutes	5 km	June 12	22:15 UTC
10		6 km	June 12	23:30 UTC
11		10 km	June 13	01:30 UTC
12		10 km	June 13	04:30 UTC
13	55 minutes	10 km	June 13	04:50 UTC
14	34 minutes	10 km	June 13	09:30 UTC
15	50 minutes	21 km	June 13	21:30 UTC
16	79 minutes	16 km	June 14	18:50 UTC
17		12 km	June 15	00:57 UTC
18		5 km	June 15	05:15 UTC
19	35 minutes	10 km	June 15	09:20 UTC
20		10 km	June 15	10:25 UTC
21		16 km	June 15	10:55 UTC
22	27 minutes	10 km	June 15	16:55 UTC
23		5 km	June 16	20:45 UTC

Table 1.5: Specification of the four types of sensors and their satellites used for this project. AVHRR and MODIS as examples for polar-orbiting sensors and satellites and GOES and MTSAT as geostationary.

Sensor	Type	Bands	Satellite	Agency	Devices	Altitude	Position	Launch Date
AVHRR	polar-orbiting	5	NOAA-10 and NOAA 14-19	NOAA ¹	7	833 km / 870 km	Variable	1986/1994/ 1998/2000/ 2002/2005/ 2009
			MetOp-A	EUMETSAT ²	1	817 km	Variable	2006
GOES	geostationary	5	GOES 11 and 13	NESDIS ³	2	35790 km	135°W/ 75°W	2000/2001
MODIS	polar-orbiting	36	Terra and Aqua	NASA ⁴	2	705 km	Variable	1999/2002
MTSAT	geostationary	5	MTSAT 2	JMA ⁵	1	35790 km	145°E	2006

- 1) National Oceanic and Atmospheric Administration
- 2) European Organisation for the Exploitation of Meteorological Satellites
- 3) National Environmental Satellite, Data, and Information Service
- 4) National Aeronautics and Space Administration
- 5) Japan Meteorological Agency

Table 1.6: Relevant infrared bands used for the Reverse Absorption Method, listed by the satellite-based instruments used in this project. AVHRR = Advanced Very High Resolution Radiometer, GOES = Geostationary Operational Environmental Satellite, MODIS = Moderate Resolution Imaging Spectroradiometer, MTSAT = Multifunctional Transport Satellite.

	Relevant Infrared Bands	Centered Wavelengths
AVHRR	4 and 5	10.8 and 12.0 μm
GOES	4 and 5	10.7 and 12.0 μm
MODIS	31 and 32	11.03 and 12.02 μm
MTSAT	IR1 and IR2	10.8 and 12.0 μm

Table 1.7: Particle size bins used in WRF-Chem simulations and adapted in current version of WRF-Chem (see Stuefer et al., 2013).

Bin	Particle size	Phi
1	1 - 2 mm	-1 - 0
2	0.5 - 1 mm	0 - 1
3	0.25 - 0.5 mm	1 - 2
4	125 - 250 μm	2 - 3
5	62.5 - 125 μm	3 - 4
6	31.25 - 62.5 μm	4 - 5
7	15.625 - 31.25 μm	5 - 6
8	7.8125 - 15.625 μm	6 - 7
9	3.9065 - 7.8125 μm	7 - 8
10	< 3.9065 μm	> 8

**Chapter 2 Qualitative comparison of Mount Redoubt 2009 volcanic clouds using
the PUFF and WRF-Chem dispersion models and satellite remote sensing data ¹**

Abstract

Satellite remote sensing data presents an important tool to map and analyze airborne volcanic ash, both spatially and temporally. However, such data only represents an instant in time. To supplement the satellite data and to forecast plume and cloud movement, volcanic ash transport and dispersion models are used. Mount Redoubt Volcano erupted in March and April 2009 with 19 detected events. By analyzing events 5 and 19, we show how satellite data can be used in combination with PUFF and the Weather Research and Forecast model with online Chemistry (WRF-Chem). WRF-Chem has been combined and initialized with a volcanic eruption model. PUFF as well as WRF-Chem show a good assessment of the plume characteristics compared to the satellite data. Especially for event 19, we observed a very close match between WRF-CHEM and satellite data, where PUFF showed an offset of the predicted plume.

¹ Steensen, T., M. Stuefer, P. Webley, G. Grell, and S. Freitas, (2013), Qualitative comparison of Mount Redoubt 2009 volcanic clouds using the PUFF and WRF-Chem dispersion models and satellite remote sensing data, *Journal of Volcanology and Geothermal Research, Special Issue on the 2009 Redoubt Eruption*, 259, 235-247.
(Changes have been made)

2.1 Introduction

After 20 years of quiescence, Mount Redoubt, Alaska (Fig. 2.1), erupted violently from March 22 to April 4, 2009 (Bull and Buurman, this issue). During this period, 19 large explosive events were recorded by the Alaska Volcano Observatory (AVO). As volcanic ash is a major hazard to aviation (Prata et al., 1991; Casadevall, 1994; Tupper et al., 2004), a precise determination of ash concentration and geographical position of the clouds and plumes were crucial for hazard avoidance in the heavily frequented flight corridors over the Anchorage area and the Gulf of Alaska. AVO uses brightness temperature differences (BTD) based around the reverse absorption method developed by Prata (1989a, b) to detect ash clouds. The satellite-derived data is then used for validation of volcanic ash dispersion models, such as Puff (Searcy et al., 1998) and the Hybrid Single-Particle Lagrangian Integrated Trajectory model (HYSPLIT, Draxler and Hess, 1998).

The WRF-Chem model (Grell et al., 2005) has been adapted and initialized with a volcanic eruption component (as described in section 2.2). A description of the model itself can be found in Freitas et al. (2011). In this Redoubt Volcano application, the first volcanic adaptation of WRF-Chem, the model simulated the volcanic clouds from several of the events from the 2009 Mount Redoubt eruption. Volcanic ash masses are simulated simultaneously, in space and time, with the model-internal numerical weather prediction (NWP) model. This approach of volcanic ash cloud prediction online

with the numerical weather prediction models will allow for examination of feedback processes between the ash and the weather at identical spatial increments and time steps. This approach is currently not used by any other operational volcanic ash transport and dispersion model, although it has been utilized to model air quality (Langmann et al., 2009).

In this study, WRF-Chem's capabilities to predict the characteristics of the Mount Redoubt eruption plumes and ash clouds are analyzed. The WRF-Chem simulations are compared with satellite remote sensing data, which were collected in near real-time, and with the volcanic ash simulations from the Puff volcanic ash transport and dispersion (VATD) model. Out of the 19 explosive events of the Redoubt Volcano eruption of 2009 described in Bull and Buurman (this issue), this analysis focuses on events 5 (March 23, 12:58 UTC) and 19 (April 4, 13:59 UTC) as these are the best documented events in terms of ash fall location and satellite coverage. Other events were not detected in satellite data or were largely obscured by surrounding meteorological clouds. A satellite to model comparison for these events was therefore not feasible.

2.2 Methodology

To retrieve volcanic ash plume and cloud characteristics, satellite remote sensing data has been extensively used across the North Pacific (Dean et al., 2004; Webley et al., 2009). For the Mount Redoubt 2009 events 5 and 19, the focus is on the use of Advanced Very High Resolution Radiometer (AVHRR) data due to a high spatial resolution of about 1.1 by 1.1 km at nadir and a temporal resolution of approximately 1 hour for the region (Dean et al., 2004). AVHRR channel 4 thermal infrared (TIR) data, centered at 10.8 μm , can be used to determine the cloud top temperature by comparing the temperature of an opaque cloud to a radiosonde-determined atmospheric profile (Sparks et al., 1997). Although with its limits, it requires a fully thermally heterogeneous atmosphere for best results, it provides a good approximation of volcanic plume and cloud heights. In addition, the BTD of the infrared AVHRR channels 4 and 5 (10.8 and 12 μm , respectively) reveals dry, fine volcanic ash (effective radii $< 4.3 \mu\text{m}$) entrained in the atmosphere as described by Prata (1989a, b) and Wen and Rose (1994). With the Volcanic Ash Retrieval (VAR) tool (Wen and Rose, 1994), the vertically-integrated volcanic ash masses, optical depths and the effective radii (the ratio of the skewness to the variance of a log-normal distribution of ash) were determined with input parameters described below for all observed translucent plumes and clouds from events 5 and 19. As the zero brightness temperature threshold of 0 K for the reverse absorption method (BT4-BT5, where 4 and 5 represent the respective AVHRR channels) can result in

high noise levels (Wen and Rose, 1994), especially in northern latitudes, the BTDR threshold has been customized for each AVHRR image.

For the VAR tool to be most effective, Wen and Rose (1994) stated that the ash cloud must be thin enough for surface radiation to penetrate it, homogenous and parallel to the surface to assume identical physical properties throughout. Such an assumption is necessary to compute the physical parameters of the ash as a detailed plume structure can't be known from satellite data alone and would be very time-consuming to compute. As these pre-requisites are unlikely the case in most ash clouds, a certain error is introduced into the measurements. Depending on the input parameters used for the computations, the results may vary greatly (Steensen et al., 2011).

The VAR tool fits a log-normal distribution of particle sizes within a pixel to estimate the effective radii. The effective radii are a representation of the distribution of ash particles within the AVHRR pixel. A lower effective radius equates to a higher proportion of the ash dominated by finer particles. Pavolonis and Sieglaff (2009) state that the measured radii will fit to a log normal distribution from 0 – 100 μm , and the effective radii represent the shape and width of the distribution.

To successfully determine the ash cloud characteristics, the VAR tool requires several initial input parameters; see Wen and Rose (1994). Two critical parameters are cloud top and surface or background temperature. The background temperature is required to

measure the radiant thermal signal absorbed by the ash cloud and the cloud top temperature is required to estimate the thickness to the cloud. For several of the satellite datasets, the volcanic plumes and clouds were optically opaque in the TIR, allowing the determination of the cloud top temperature directly from the satellite data but in most cases the dispersion seen over consecutive satellite passes was compared to the dominant wind direction measured from local radiosondes (Anchorage, Event 5, and Kodiak, Event 19) to determine the cloud height and hence its temperature. A uniform ground or surface temperature is unknown as an analysis of the image showed that it varies strongly between the land and ocean. In those cases for events 5 and 19, where the volcanic ash extends across the land and the ocean surface, an average value for the surface temperature, based on the percentage of the cloud covering the respective backgrounds, was used. Individual surface temperature analyses were performed under cloud-free conditions in the respective AVHRR images to obtain a true background radiant signal.

Puff was developed at the Geophysical Institute, University of Alaska Fairbanks (UAF) (Searcy et al., 1998). The model has been used for both research and as an operational tool (Peterson et al., 2013) such as during the 2006 eruption of Augustine Volcano (Webley et al., 2010). Puff generates automated volcanic ash forecasts for multiple volcanoes worldwide (<http://puff.images.alaska.edu/>) as well as being available as a web-based research tool (http://puff.images.alaska.edu/cgi-bin/login_agu.pl). As a

Lagrangian model, Puff uses NWP wind fields with a customized temporal resolution to simulate the movement of ash clouds throughout the atmosphere, including dry deposition but without aggregation. A major input for the Puff VATD model is the vertical plume shape (poisson-distributed, linear or exponential with height; see Searcy et al., [1998]). For the two events at Mount Redoubt Volcano, the sensitivity of plume shape on the modeled ash cloud provided a critical tool in the analysis of expected plume behavior and its comparison to AVHRR satellite data.

Important initial parameters to run the Eulerian WRF-Chem were the eruption time, initial plume heights, the erupted volume, eruption rate and the mass fraction below $63\mu\text{m}$. The meteorological fields from NOAA's Global Forecast System (GFS) numerical model served as meteorological initialization and boundary data for WRF-Chem. Model results may vary depending on the initial vertical distribution of the ash content and the spatial model resolution. With this input, ash masses were dispersed for each particle bin. Due to large processing times, the model was run without interaction between the bins or back to the NWP model. A finer spatial resolution will result in a smaller domain size if model simulations were to be computed within the same timeframe for operational capabilities. Table 2.1 shows the different model input parameters provided for the WRF-Chem model.

The volcanic ash volume is divided into 10 different particle size bins. The percentages of the total mass attributed to each of the ash bins are shown in Table 2.2. These

percentages are based on case studies of the Mount Spurr eruption in 1992 (Mastin et al., 2009; Durant and Rose, 2009). Based on historic events, Mount Redoubt has been classified as having medium silicic eruptions, S2 in Mastin et al. (2009), with plume heights between 6 and 12 km above sea level, a category in which Mount Spurr is the example case (Mastin et al., 2009) and in which events 5 and 19 fit as well. Using the Mount Spurr particle distribution is therefore likely to provide a close estimate for the physical parameters, like ash masses. WRF-Chem uses this distribution as a default first-order approximation of the particle distribution. For future runs, a customization of this parameter is planned. Results from WRF-Chem include the display of the whole plume/cloud at different time steps as well as the selection of the different particle bins. With this, dominant size ranges in different parts of the plume can be identified.

WRF-Chem includes wet and dry deposition but no aggregation processes. It was initialized with an umbrella vertical distribution of the ash cloud (poisson-distributed in the vertical). The base of the umbrella is defined as 73% of the maximum plume height with 25% of the total mass below the umbrella (Freitas et al., 2011). The domain sizes used were event-specific with spatial resolutions of 2 and 5 km (Table 2.1). The finer the spatial resolution, the closer to reality the topography (i.e. more grid points to represent the changing topography in the model) but the smaller the total domain size will be, as a result of the operational requirement and due to computational limitations. Vertical resolutions between model levels are increasing with height starting from about 15 m at

the model bottom surface to about 15.5 km ASL, at altitude differences per model level of 1.5 km (Grell et al., 2005).

The WRF-Chem results were qualitatively compared to the Puff results in addition to comparing both models to the AVHRR TIR and BTM satellite data. This will provide a critical analysis of the models ability to simulate the ash plumes and dispersing clouds of events 5 (March 23, 12:58 UTC) and 19 (April 4, 13:59 UTC) of the 2009 eruption of Mount Redoubt in Alaska. The potential of WRF-Chem as a real-time forecasting tool for future eruptions is demonstrated.

2.3 Explosive Event 5: March 23, 2009

Event 5 occurred on March 23, 2009 at 12:58 UTC. Based on seismic signals, AVO estimates its duration to be 20 minutes (Buurman et al., this issue). Radar measurements report an initial plume height of 14.9 km above sea level [ASL] (Schneider and Hoblitt, this issue). During event 5, cloud cover in the area around the volcano obscured portions of the plume and dispersed cloud so that they remained undetectable with satellite data. Using the TIR data and the Sparks et al. (1997) method, the cloud top temperature and local radiosondes suggest a weather cloud height between 6 and 7 km ASL.

TIR data from AVHRR, channel 4, showed the volcanic cloud drifting towards the northeast (Fig. 2.2). As most of this cloud remained opaque in the TIR data, the reverse

absorption method was only able to detect a weak BTM and the VAR method was unsuccessful for analyzing ash content. The only available AVHRR image that showed a semi-transparent cloud was obtained at 16:06 UTC (Table 2.3). From this data, the VAR input parameters of the cloud top temperature of the opaque cloud and the background temperature of a cloud-free portion of the image were determined. The VAR parameters used for the analyses are included in Tables 2.1 and 2.3.

2.4 Explosive Event 19: April 14, 2009

The last major event of the 2009 eruption occurred on April 4 at 13:59 UTC. The duration of the event was about 31 minutes (Buurman et al., this issue) and the ash plume had an initial height of 15.2 km ASL from ground-based radar (Schneider and Hoblitt, this issue). As opposed to event 5, no meteorological cloud cover was present. The TIR AVHRR data revealed the whole extent of the plume and subsequent cloud as it drifted to the southeast (Fig. 2.3). The initial cloud was opaque in the TIR, thus allowing determination of its cloud top temperature. The dispersing cloud became semi-transparent allowing the VAR algorithm to be used to determine the ash masses and, with thickness-assumption of the plume, the ash concentration from the following satellite passes (Table 2.3). This cloud drifted over Cook Inlet, the Kenai Peninsula and ultimately across the Gulf of Alaska, so that the background temperature used in the VAR tool changed over time.

In the first images showing the spatial event (at 16:23 and 17:03 UTC), the cloud passed over Cook Inlet and was largely located over Kenai Peninsula. For these, an averaged background TIR temperature of 269 K was used based on the measured temperatures of Cook Inlet (approximately 271K) and the Peninsula (approximately 263 K). In the later images (19:19 UTC onwards, see Table 2.3), the background temperature was set at 272 K as large parts of the cloud drifted over the relatively warm Gulf of Alaska (approximately 274 K).

2.5 Results

2.5.1 Satellite Data

The evolution of ash clouds from events 5 and 19 shows that each ash cloud was dispersed in a different direction (Figs. 2.4 and 2.5). The BTM imagery was analyzed to determine the volcanic ash load. The clouds became less defined in the TIR images but could still be seen in the BTM data as the cloud dispersed further, becoming more transparent and less spectrally opaque in the TIR. Additionally for event 5, the portions of the ash clouds were only detectable when they were above any surrounding tropospheric clouds. For those images with a detectable BTM signal, the total vertically-integrated volcanic mass was determined using the VAR tool (Table 2.3). Event 19 shows one portion of the plume drifting to the south-east above the Kenai Peninsula (P1 in Figs. 2.4 and 2.5) with another portion developing and dispersing above the southern tip

of the Peninsula (P2 in Fig. 2.5) The satellite data for event 5 resulted in a mass of approximately 15.7 kt, where the time series of clouds from event 19 shows a decline in mass from 37.6 kt at 16:06 UTC to 12.5 kt at 21:20 UTC. The associated error depends on the actual shape of the plume and the input parameters. In general, a change of 2% in the surface temperature can result in up to 40% error in the derived masses (Steensen et al., 2011). For event 5, the calculated optical depth is 1.23 with a mean effective radius of 4.7 μm . The range of images for event 19 shows a decline of optical depth from 0.75 to 0.34 and a mean effective radius between 5.5 and 7.2 μm . These values include only fine ash ($< 100 \mu\text{m}$) and are therefore not representative for the whole plume.

2.5.2 Puff Model

Puff simulations for events 5 and 19 (Fig. 2.6) showed a similar dispersion as the satellite data (Fig. 2.4 and 2.5). For event 5, the Puff model simulation showed the portion of the ash cloud that was traveling north. Parts of the cloud with altitudes of 7 km ASL and lower were not detected in the TIR satellite data, but were simulated by Puff and are colored blue through green in Figure 2.6. The time series analysis of the Puff output for event 19 illustrated the initial plume dispersed and drifted to the southeast at an altitude of 15.2 km ASL. The higher altitude portion predicted by Puff (green to red in Fig. 2.6 B-F) is in the same location as the one shown in the satellite imagery (P1 in Figs. 2.4 and 2.5).

2.5.3 WRF-Chem Model

2.5.3.1 Event 5

Using eruption source parameter from Mastin et al. (2009), a plume height of 14.9 km ASL (Schneider and Hoblitt, this issue) and an eruption duration of 20 minutes (Buurman et al., this issue), WRF-Chem was initialized with an eruption rate of 3.7×10^6 kg/s (using plume height to eruption rate from Sparks et al. (1997) and Mastin et al. (2009), see references for explanation) and a total eruptive mass of approximately 4.4×10^9 kg. The integrated volcanic ash loadings (g/m^2) for two timings (16:10 and 18:00 UTC) during the WRF-Chem simulation using a 2 and 5 km grid spacing, show the dispersing volcanic cloud to the northeast (Fig. 2.7). The highest ash loading occurs in the southeastern part of the ash cloud at elevations of about 14 km ASL, which is situated west of Anchorage (Figs. 2.7 and 2.8).

A cross section through the ash cloud at a spatial grid of 2 km at 16:10 UTC illustrates how the ash cloud top varied in altitude above sea level (Fig. 2.9). In the northwest portion of the cloud, the top was close to 9 km ASL from WRF-Chem ('1' in Fig. 2.9). The cloud top reached up to 13 – 14 km ASL at the southeastern end of the cloud ('2' in Fig. 2.9). Figure 2.9 additionally shows that, under the cloud top, there was significant variability in the ash cloud concentration. Within the modeled cross section, higher

concentrations can be seen at the left hand (northwestern) side around 6 km ASL, with the cloud top being around 8 km ASL.

WRF-Chem forecasted ash fall to the north of the volcano (Fig. 2.10) with mass loadings greater than 2 kg/m^2 at the summit. An extended region showing an ash deposition greater than 100 g/m^2 was found north of Mount Redoubt; this region represents approximately the higher topography to the north of the volcano.

2.5.3.2 Event 19

For the WRF-Chem simulation, a 15.2 km ASL initial plume height was used and, from the conversion of plume height to eruption rate, a total eruptive mass of about 8.3×10^9 kg was estimated. A 5 km spatial grid best was used for the WRF-Chem simulation. The column integrated ash loading (Fig. 2.11) shows the majority of the ash propagating to the southeast of the volcano.

Figure 2.12 shows the modeled volcanic ash at different altitude levels. A low pressure system was situated in the Gulf of Alaska during this event; the pressure system coincides with the low-level wind flow as shown in Figure 2.12. The ash concentrations at 2 km ASL at 17:00 and 19:30 UTC (Figs. 2.12A and D) show both the ash close to the volcano (E1) as well as a "pocket" of dispersed ash to the southeast (E2 in Fig. 2.12). At 8 km ASL (Fig. 2.12B and D), the ash cloud propagates further to the southeast. At the earlier stages (Figs. 2.12B), two distinct pockets of ash can be seen, whereas later (Fig.

2.12E), these regions have merged. Volcanic ash at 14 km ASL was advected further east (Figs. 2.12 C and F). The wind barbs shown in Figures 2.12B and 2.12C confirm that the wind shifted slightly from northwesterly at 8 km ASL to westerly at 14 km ASL.

Figure 2.13 shows vertical profiles of the ash concentration. At 17:00 UTC, the plume is shown in the vicinity of the vent at about 6 km ASL (Fig. 2.13A), while, at greater distance, a plume height of 13 km ASL was found (Fig. 2.13B). This profile view showed, similar to event 4, a complex plume structure that cannot be described as thin and homogenous. Different parts of the plume (dispersion maxima at different heights and fallout), as seen in Figure 2.12, can also be identified here. Fallout simulations showed the ash was deposited to the southeast (Fig. 2.14). The highest ash fallout (greater than 1000 g/m^2 or 1 kg/m^2) occurred close to the volcano and along a small region across the Cook Inlet.

The runs for event 19 on April 4, 2009, were only performed for the 5 km spatial resolution as the effect of low-altitudinal winds was negligible due to a lack of wind shear through the vertical (Fig. 2.12). A low pressure system, seen in the low level wind flow, was situated in the Gulf of Alaska. In these simulations, the main cloud was seen extending to the southeast for over several hundred kilometers (Fig. 2.11). A very low portion of the cloud was predicted drifting to the south of Mount Redoubt at a much slower speed than the main part (E2 in Fig. 2.12). This part roughly coincides with the secondary fallout maximum observed in Figure 2.14.

2.6 Discussion

2.6.1 Event 5

Satellite TIR, BTM and dispersion model data showed similar ash cloud extents for the two events analyzed from the 2009 eruption. The satellite data BTM retrieval is susceptible to fine, dry ash dominating the cloud. The cloud will stay spectrally opaque in the TIR until these finer particles dominate and the larger ones fall out. This transition is seen during event 5, when parts of the satellite BTM image reveal the plume, whereas others, that show the plume in the TIR image, have no sign of volcanic ash in the BTM image (Figs. 2.4A and B). Additionally, as the TIR data is from a passive sensor, the ash cloud has to be the highest layer in the atmosphere to be detected. This effect was more distinct in event 5, where both Puff and WRF-Chem simulated ash cloud movement to the north-east at 7 km ASL and below (Figs. 2.6 and 2.7). The satellite data was unable to detect parts of the ash as it was below the surrounding meteorological clouds. WRF-Chem identified these particles as ash bins 9 and 10, whose sizes are best identified using AVHRR channel 4 and the VAR tool (Wen and Rose, 1994). As lower portions of the cloud were dominated by larger particle sizes, these parts appear opaque (Fig. 2.2). Therefore, the estimated mass for event 5, 15.7 kt, is an underestimation of the total mass within the cloud. Comparison to the total cloud (Fig. 2.7) suggests that the volume of the cloud is roughly twice as large. As the ash in lower altitudes appears less concentrated than in higher altitudes (Fig. 2.9) but its effective

radii are increasing, the total mass was estimated between 25 and 40 kt, which is about twice the mass as derived from remote sensing data. A better estimate can only be achieved by quantitative comparison and evaluation of the model to satellite data.

Examination of the 2 km grid resolution simulation from WRF-Chem shows a similar pattern to that from the 5 km grid. With the topography being resolved in more detail in the 2 km grid spacing (Figs. 2.7B and 2.7E), less ash drifted to the west compared to the coarser resolution (Figs. 2.7C and 2.7F).

The effect of the degree of resolved topography on the ash cloud movement was more prevalent when examining the ash cloud concentrations at 2 km ASL (Fig. 2.8). In the lower portions of the ash clouds, the interaction of the cloud with the underlying topography occurs using a 2 km grid (Fig. 2.8A) causing lower amounts of ash to drift to the west than using the 5 km grid resolution (Fig. 2.8D). Examination of the ash loadings (Figs. 2.7B and 2.7C) show that there is a significant portion of the cloud propagating south-westerly using a 5 km grid, ash loadings exceeding 20 mg/m^2 , which is not evident using a 2 km grid spacing. This feature was not only prevalent at lower altitudes.

Comparing the ash concentrations at 14 km ASL (Figs. 2.8C and 2.8F) showed that the coarser spatial resolution predicts more ash present at higher altitudes towards the east compared to the finer spatial grid. The results illustrate the significance of the resolution on the propagation of the ash cloud. Either a finer model grid or an improved digital elevation model would resolve this.

Direct comparison between the spatial resolutions at different altitudes reveals more details of the cloud (Fig. 2.8), as predicted by WRF-Chem. Both spatial grid spacing simulations showed the lower altitude ash cloud propagating to the west, the 8 km ASL cloud propagated to the north and the 14 km ASL portion to the northeast. There was more detail in the cloud shape comparing the 2 and 5 km grid results as shown in the 14 km ASL portion (Fig. 2.8C and 2.8F). Comparing the 8 km ASL portion of the cloud, the wind was stronger in the 2 km grid and therefore the cloud has travelled slightly further north compared to the 5 km grid. This was a result of the finer grid spacing providing an improved wind field with more detail compared to the wind field resolved at 5 km grid spacing intervals.

The cross section of the cloud (Fig. 2.9) showed great detail in the cloud structure that cannot be obtained from the satellite thermal infrared signal and additionally it illustrated that, based on our estimate on the input parameters and without any direct observations, the ash cloud was not a thin layer propagating across the atmosphere, as needed for the VAR tool and used as basis for the satellite-derived ash mass calculations, and there can be considerable volcanic ash well below the cloud top. This is significant for aviation in defining concentration levels at set altitudes within the atmosphere.

WRF-Chem delineates the ash fall isopachs similarly to Wallace et al. (this issue) (Fig. 2.10). The main difference was the limited number of sampling locations that made the

sample-based isopach map requires greater approximations for the full ash extent when compared to the model output. To quantitatively evaluate the WRF-Chem ash fall predictions, however, a more detailed sample map is necessary.

2.6.2 Event 19

For event 19, the VAR tool was able to provide volcanic ash masses and cloud characteristics for a series of images. Effective radii of around 4 – 7 μm , as detected for these Mount Redoubt events, showed that the cloud was dominated by finer particles very quickly. Event 19 was the only event, a dome collapse, with a significant BTM signal. This correlates with the determination of Wallace et al. (this issue), that this event had the largest amount of fine ash deposits. As this event occurred under a cloud-free sky, the whole cloud was detected in the images. Still, as particles with effective radii lower than 4.3 μm have the largest impact on the estimated masses using the VAR tool (Wen and Rose, 1994) an underestimation of the masses was likely. The amount of underestimation depends on the particle distribution of the actual eruption as each effective radii influences the mass calculation differently, both positive and negative (Wen and Rose, 1994).

The dispersion in event 19 showed a hook-like structure in the model runs (Fig. 2.11). The eastern arm of this hook represented particles at higher altitudes (Figs. 2.11C, F and 2.12). This was also the portion of the cloud detected in the satellite BTM imagery (P1 in

Fig. 2.5), suggesting that these were the fine particles that were detected by VAR. Earlier satellite imagery (Fig. 2.4D and F) showed the lower altitude ash based on a comparison with the TIR signal (Fig. 2.4C) and the coinciding PUFF runs (Fig. 2.6B and C). This suggested that initially, the higher altitude portions were undetectable for the BTM signal until fallout caused the lower particle sizes to dominate the cloud, similar to event 5. The lower altitude portion became undetectable in later images, possibly due to ash fallout and an associated drop below the detection limit. In addition, a second maximum was seen at the southern tip of Kenai Peninsula (P2 in Fig. 2.5) which must also consist of fine particles. Its true height was not possible to determine through the satellite data alone, given the wavelengths used, but its location suggested that it was ash fallout from an earlier plume pass. Such fallout can also be seen in WRF-Chem model outputs where a secondary maximum (E2 in Figs. 2.12A and D) was attributed to ash fall based on evaluation of the vertical profile (Fig. 2.13A). Higher altitudes of the cloud also showed a similar pattern of ash fall (E3 in Figs. 2.12B and 2.13B). This ash fall must consist of large particles that cannot be identified in the satellite BTM images. However, none of these ash fall scenarios can be seen in the Puff model output (Fig. 2.6). In addition, Puff predictions showed an offset to the south by about 50 to 100 km (Figs. 2.5 and 2.6), which is not seen in WRF-Chem (Fig. 2.11). This was potentially due to the coarser spatial resolution of meteorological conditions used by Puff. Similar to event 5, the cross sections of event 19 (Fig. 2.13) showed a complex vertical structure of the

plume including ash fall. The thin, homogenous cloud expected by VAR is not reflected by the dispersion models and unlikely in reality so that a certain error will be included in the ash retrievals.

Comparisons between the WRF-Chem model (Fig. 2.14A) and the measured ash fall from Wallace et al. (this issue) (Fig. 2.14B) showed similar extents both in space and in terms of quantity. WRF-Chem was also able to simulate a secondary maximum in the ash fallout in the Gulf of Alaska, which was not observed in the fieldwork data due to lack of observations in this region.

2.7 Conclusions

Volcanic ash clouds are a major hazard to aviation and local communities and their detection is required to provide a full hazard assessment. Satellite remote sensing data sets are used for real-time detection of volcanic plumes and the subsequent dispersing volcanic clouds. However, the images capture only an instance in time. Volcanic Ash Transport and Dispersion models can forecast the future location of the ash cloud, but require validation and comparisons with the satellite data. This work has shown that the comparison of the WRF-Chem, Puff models and satellite TIR and BTM data can provide very valuable information for erupting plumes and dispersing clouds, such as lateral extent, likely vertical structure and ash densities. This analysis has shown that not all volcanic clouds will be detectable by the BTM data, such as the lower altitude portions of

the ash cloud associated with event 5. The clouds detectable in the TIR, and therefore observable in satellite data, still require input parameters for surface and cloud temperatures to be able to obtain volcanic ash retrievals. Similar inputs are necessary for the VATD models. Here, initial height, duration and wind pattern are most important factors.

WRF-Chem, applied for volcanic eruptions, allows for a more detailed analysis compared to pre-determined NWP and coarser spatial resolutions used by Puff. However, strong inaccuracies in modeling volcanic ash dispersion may arise due to a lack of eruption characteristics and an unknown initial spatial distribution of the volcanic tephra. An incorrect assessment of this will place inaccurate ash masses at respective altitudes, which will have direct ramifications on the successive distribution of that ash.

The Puff model showed a good correlation with the satellite data, despite small offsets, but does not show a detailed plume structure including fallout. As Puff runs quickly (within minutes) and is a web-based product, while WRF-Chem typically requires the use of a supercomputer, Puff is a good solution for a quick assessment of the likely spatial distribution of volcanic plumes and clouds. Still, for a more thorough analysis a more robust evaluation of ash dispersion is needed. By combining the analyses presented here, an improved understanding of the ash cloud and its potential hazard is possible. These tools will then give the means to provide the best volcanic ash advisory and most accurate hazard assessment.

2.8 Acknowledgements

We thank the American Recovery and Reinvestment Act grant (ARRA) for their support of this research. In addition, we thank the Alaska Volcano Observatory for providing the satellite data. The Alaska Volcano Observatory (AVO) is a joint program of the United States Geological Survey (USGS), the Geophysical Institute of the University of Alaska Fairbanks (UAFGI), and the State of Alaska Division of Geological and Geophysical Surveys (ADGGS). Finally, we thank the Arctic Region Supercomputing Center who provided the processing time and data storage space on their supercomputers for the WRF-Chem modeling.

2.9 References

- Bull, K.F., Buurman, H., An overview of the 2009 eruption of Redoubt Volcano, Alaska. *Journal of Volcanology and Geothermal Research*, this issue.
- Buurman, H., West, M., Thompson, G., The Seismic Chronology of the 2009 Redoubt Eruption. Introduction to Redoubt Volcano, and overview of the 2009 eruption. *Journal of Volcanology and Geothermal Research*, this issue.
- Casadevall, T. J., 1994. The 1989-1990 Eruption of Redoubt Volcano, Alaska – Impacts on Aircraft Operations. *Journal of Volcanology and Geothermal Research*, 62(1-4), 301-316.
- Dean, K. G., Dehn, J. , Papp, K. R., Smith, S., Izbekov, P., Peterson R. , Kearney, C., Steffke, A., 2004. Integrated satellite observations of the 2001 eruption of Mt. Cleveland, Alaska. *Journal of Volcanology and Geothermal Research*, 135(1-2), 51-73.
- Draxler, R. R., Hess, G. D., 1998. An overview of the Hysplit 4 modeling system for trajectories, dispersion and deposition. *Australian Meteorological Magazine*. 47, 295-308.

Durant, A. J., Rose, W. I., 2009. Sedimentological constraints on hydrometeor-enhanced particle deposition: 1992 Eruptions of Crater Peak, Alaska. *Journal of Volcanology and Geothermal Research*, 186, 40-59.

Fierstein, J., Nathenson, M., 1992. Another look at the calculation of fallout tephra volumes. *Bulletin of Volcanology*, 54, 156-167.

Freitas, S. R., Longo, K. M., Alonso, M. F., Pirre, M., Marecal, V., Grell, G., Stockler, R., Mello, R. F., Gacita, M. S., 2011. PREP-CHEM-SRC-1.0: a preprocessor of trace gas and aerosol emission fields for regional and global atmospheric chemistry models. *Geoscientific Model Development*, 4(2), 419-433.

Grell, G. A., Peckham, S. E., Schmitz, R., McKeen, S. A., Frost, G., Skamarock, W. C., Eder, B. 2005. Fully coupled "online" chemistry within the WRF model. *Atmospheric Environment*, 39(37), 6957-6975.

Langmann, B., Hort, M., Hansteen, T., 2009. Meteorological influence on the seasonal and diurnal variability of the dispersion of volcanic emissions in Nicaragua: A numerical model study. *Journal of Volcanology and Geothermal Research*, 182(1-2), 34-44.

Mastin, L. G., Guffanti, M., Servranckx, R., Webley, P., Barsotti, S., Dean, K., Durant, A., Ewert, J. W., Neri, A., Rose, W. I., Schneider, D., Siebert, L., Stunder, B., Swanson, G., Tupper, A., Volentik, A., Waythomas, C. F., 2009. A multidisciplinary effort to assign realistic source parameters to models of volcanic ash-cloud transport and dispersion during eruptions. *Journal of Volcanology and Geothermal Research*, 186(1-2), 10-21.

Pavolonis, M., Sieglaff, M., 2009. GOES-R Advanced Baseline Imager (ABI) Algorithm Theoretical Basis Document For Volcanic Ash (Detection and Height). NOAA CSTAR Tech. Doc: Ver. 2.0. June 30, 2009. 56 pp.

Peterson, R., Webley, P.W., D'Amours R., Servranckx, R., Stunder, B., Papp, K., 2013. Volcanic Ash Cloud Dispersion Models. In: Dean, K. G., Dehn, J. (Eds.), *Monitoring Volcanoes in the North Pacific: Observations from Space*. Springer, In Press.

Prata, A. J., 1989a. Observations of Volcanic Ash Clouds in the 10-12 μm Window using AVHRR/2 Data. *International Journal of Remote Sensing*, 10(4-5), 751-761.

Prata, A. J., 1989b. Infrared Radiative Transfer Calculations for Volcanic Ash Clouds. *Geophysical Research Letters*, 16(11), 1293-1296.

Prata, A. J., Barton, I. J., Johnson, R. W., Kamo, K., and Kingwell, J. 1991. Hazard from Volcanic Ash. *Nature*, 354(6348), 25-25.

- Pyle, D. M., 1989. The thickness, volume and grainsize of tephra fall deposits. *Bulletin of Volcanology*, 51, 1-15.
- Schneider, D.J., Hoblitt, R.P., Redoubt weather radar observations, 2009 Redoubt eruption. *Journal of Volcanology and Geothermal Research*, this issue.
- Searcy, C., Dean, K., Stringer, W. 1998. PUFF: A high-resolution volcanic ash tracking model. *Journal of Volcanology and Geothermal Research*, 80(1-2), 1-16.
- Sparks, R. S. J., Bursik, M. I., Carey, S. N., Gilbert, J. S., Glaze, L. S., Sigurdsson, H., Woods, A. W., 1997. *Volcanic Plumes*. John Wiley & Sons, Chichester.
- Steensen, T., Webley, P., Dehn, J., 2011. Sensitivity Analysis of Input Parameters for Near-Real-Time Monitoring of Volcanic Ash Emissions: A Satellite- and Model-Based Approach, Abstract V33A-2624 presented at 2011 Fall Meeting, AGU, San Francisco, California, 5-9 Dec.
- Tupper, A., Carn, S., Davey, J., Kamada, Y., Potts, R., Prata, F., Tokuna, M., 2004. An evaluation of volcanic cloud detection techniques during recent significant eruptions in the western 'Ring of Fire'. *Remote Sensing of Environment*, 91, 27-46.
- Wallace, K.L., Schaefer, J.G., Coombs, M.L., Event chronology, plume heights, and preliminary report of distribution, thickness, and mass of ash fall from the 2009 eruption of Redoubt volcano, Alaska. *Journal of Volcanology and Geothermal Research*, this issue.
- Webley, P.W., Dehn, J., Lovick, J., Dean, K.G., Bailey, J.E., Valcic, L., 2009. Near Real Time Volcanic Ash Cloud Detection: Experiences from the Alaska Volcano Observatory. *Journal of Volcanology and Geothermal Research*, 186 (1 – 2), 79 - 90.
- Webley, P.W., Dean, K.G., Dehn, J., Bailey, J.E., Peterson, R., 2010. Volcanic-ash dispersion modeling of the 2006 eruption of Augustine Volcano Using the Puff Model. In: Coombs, J.A., Freymueller, M.L., J.T., (Eds.), *The 2006 eruption of Augustine Volcano, Alaska*. U.S. Geological Survey Professional Paper 1769, pp. 507-526
- Wen, S. M., Rose, W. I., 1994. Retrieval of sizes and total masses of particles in volcanic clouds using AVHRR bands 4 and 5. *Journal of Geophysical Research-Atmospheres*, 99(D3), 5421-5431.

2.10 Figures

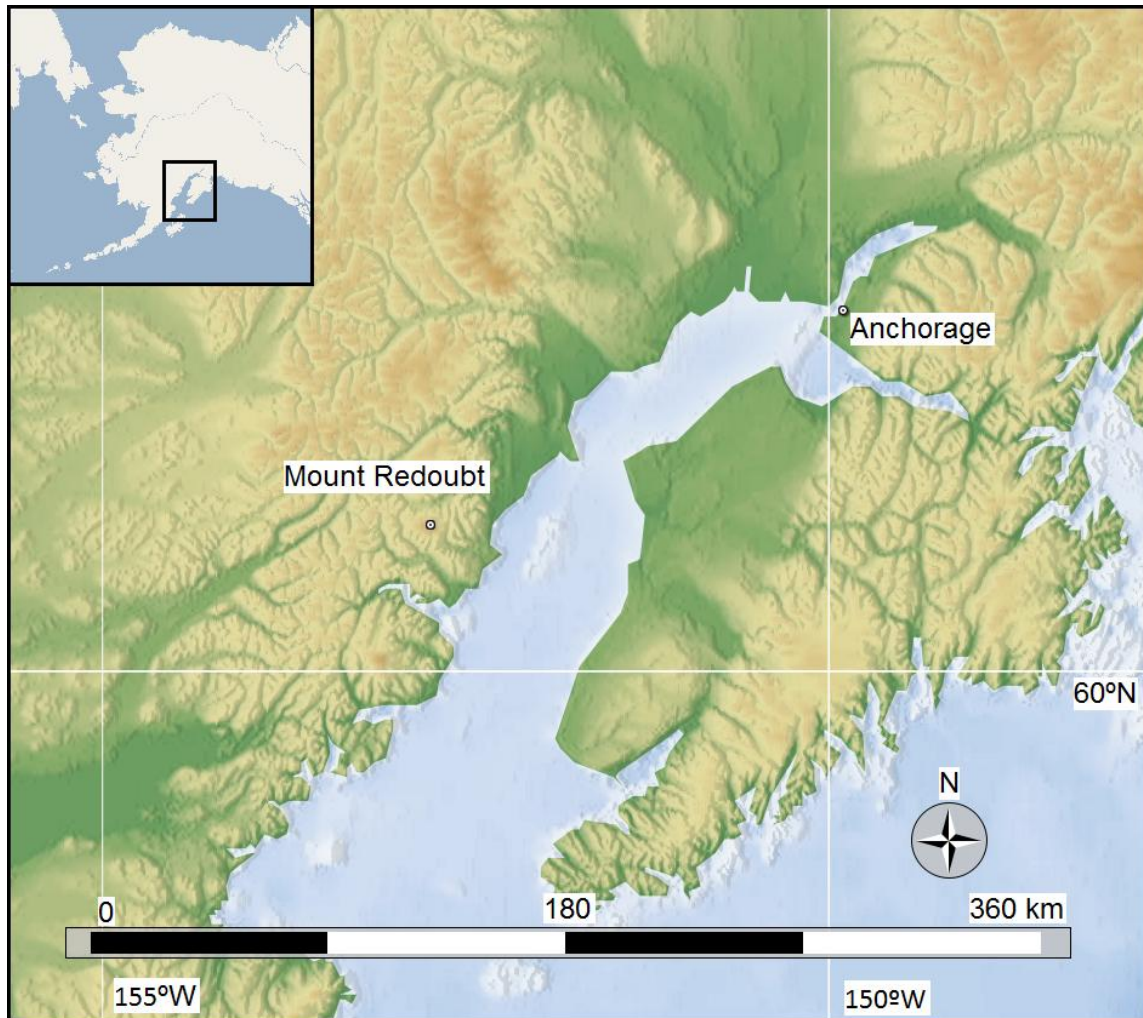


Figure 2.1: Location of Mount Redoubt volcano at the Cook Inlet, about 220 km southwest of Anchorage, courtesy of Marble, the KDE Education Project.

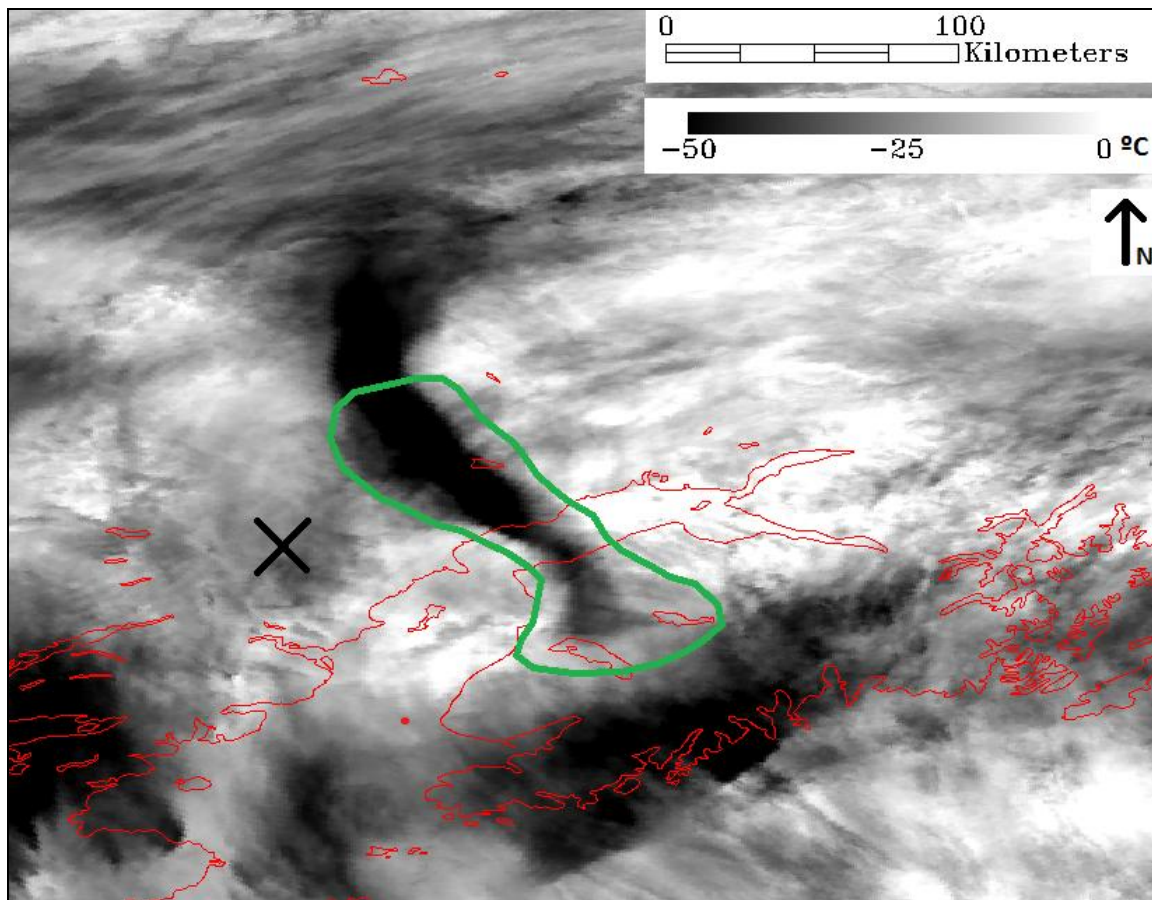


Figure 2.2: Advanced Very High Resolution Radiometer Thermal Infrared channel 4 image (March 23 2009 at 16:06 UTC) showing the ash clouds from Mount Redoubt volcano explosive event 5. Mount Redoubt volcano is marked by the black cross. The black ash cloud is seen to the northeast of the volcano. Brightness temperature difference images reveal the part of the cloud circled green as translucent with an increase in opacity towards the northwest.

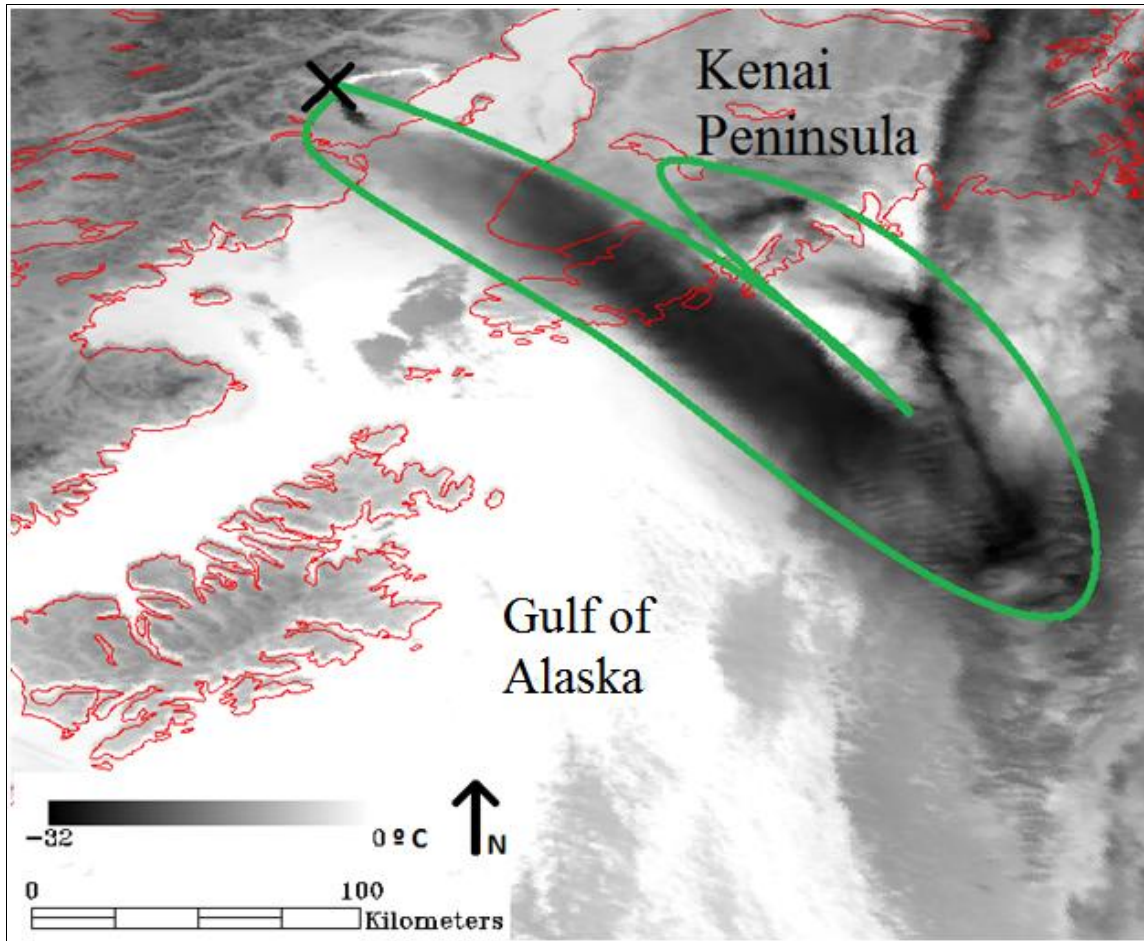


Figure 2.3: Advanced Very High Resolution Radiometer Thermal Infrared, channel 4, image from April 4, 2009 at 16:23 UTC after event 19. The cloud is drifting to the southeast passing the Kenai Peninsula heading towards the Gulf of Alaska. Mount Redoubt volcano is marked by the black cross, the plume is outlined for clarity using green polygon.

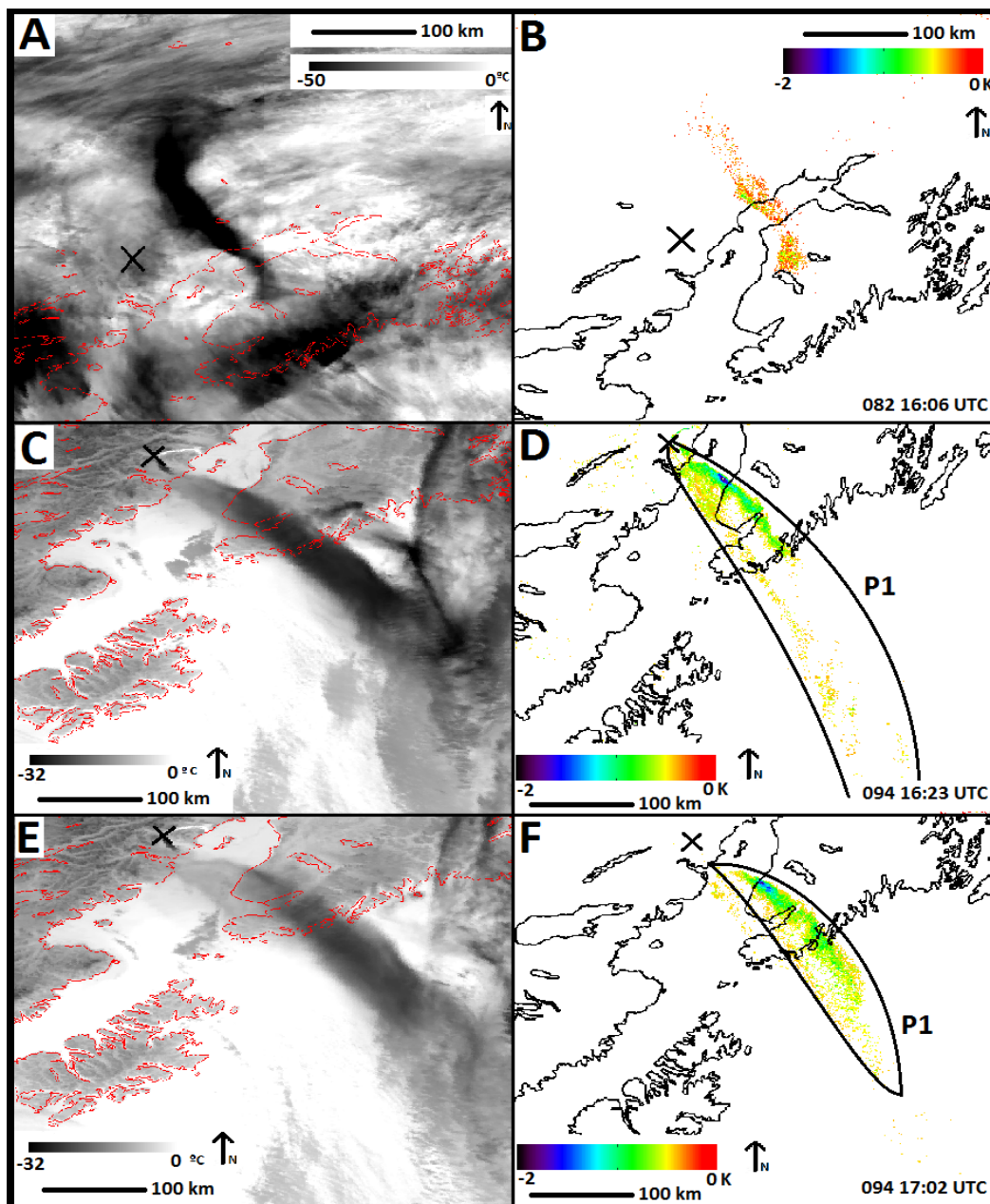


Figure 2.4: Advanced Very High Resolution Radiometer Thermal Infrared (left) and Brightness Temperature Difference (BTD) images (right) with defined thresholds from 0 to -2 K according to Table 2.3. The dispersing plume from events 5 and 19 from March 23, 2009 (Julian Day 082) at 16:06 UTC [A,B] and April 4, 2009 (Julian Day 094) at 16:23 [C,D] and 17:02 UTC is shown [D,E]. At these initial stages of the plume it can be well identified in both time series. Mount Redoubt volcano is indicated by the black cross. For the timings 16:23 UTC and 17:02 UTC, the plume is outlined as P1 in the BTD images (see also Fig. 2.5).

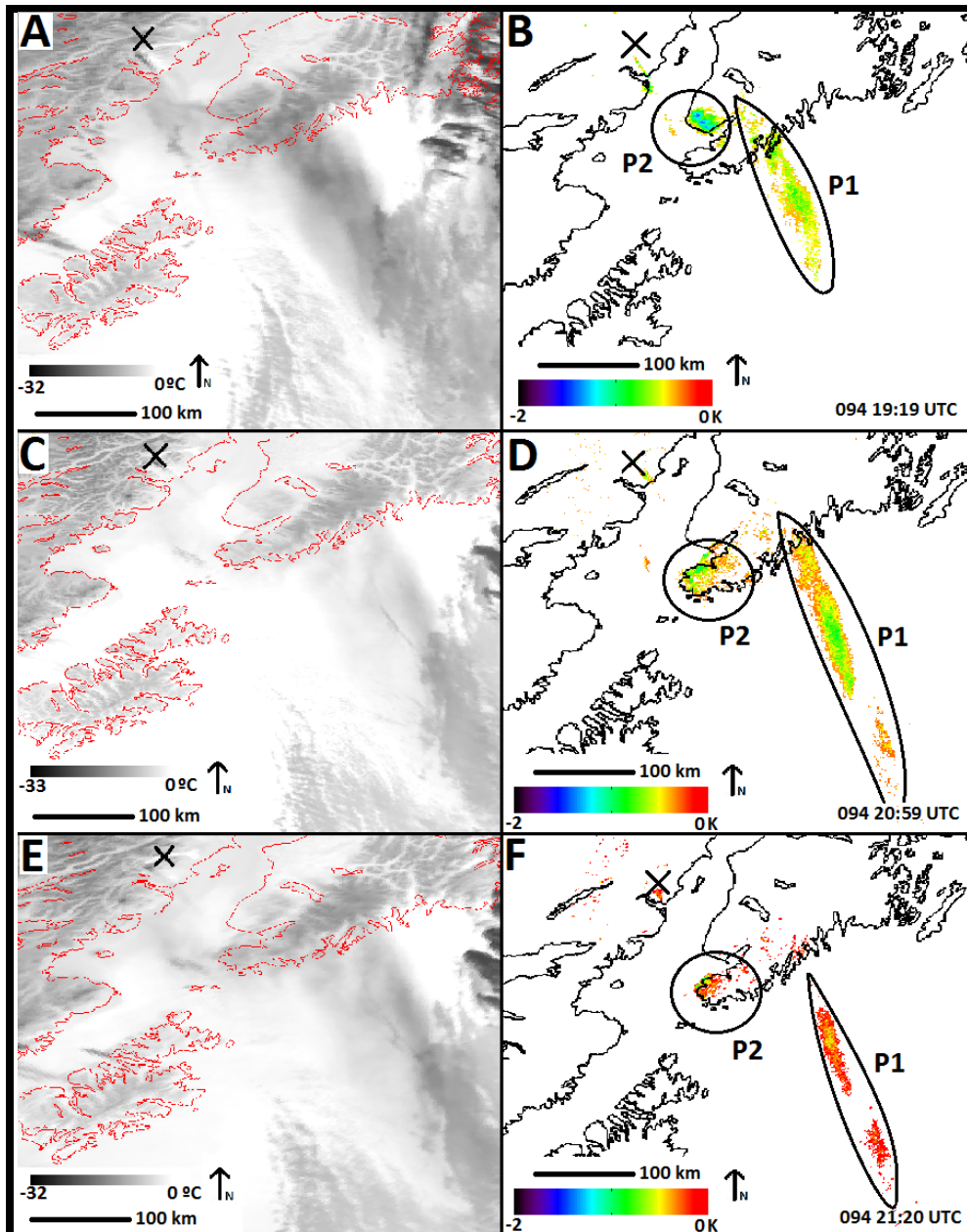


Figure 2.5: Advanced Very High Resolution Radiometer Thermal Infrared (TIR) (left) and Brightness temperature difference (BTD) images (right) with defined thresholds from 0 to -2 K according to Table 2.3. The dispersing cloud from event 19 from April 4, 2009 (Julian Day 094) at 19:19 [A,B], 20:59 [C,D] and 21:20 UTC [E,F] respectively is shown. The TIR images show an ambiguous ash signal as darker areas combined to the surrounding where the BTD images produce a distinct signal. In the BTD images, two different parts of the cloud are outlined as P1 and P2. Redoubt is indicated as a black cross.

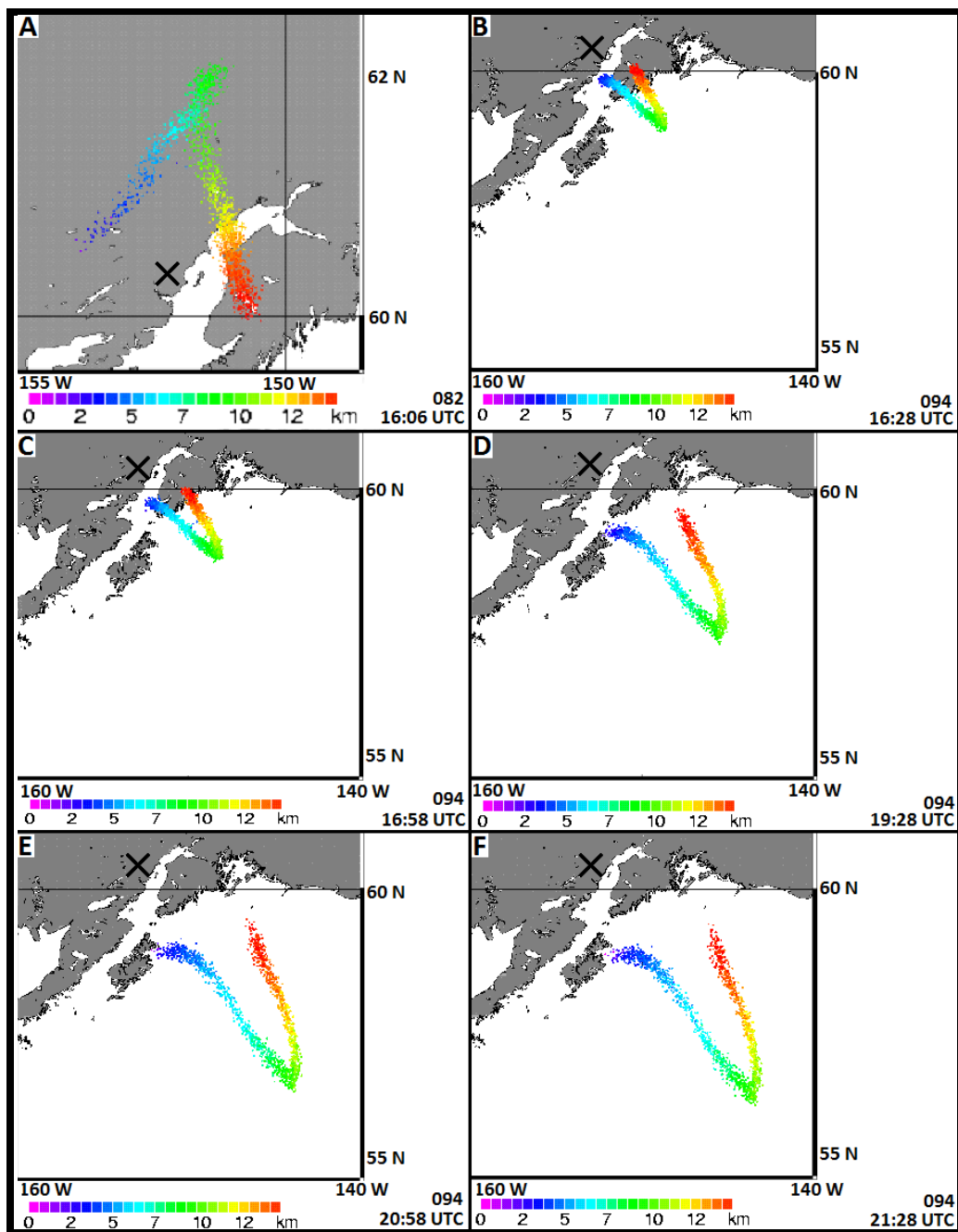


Figure 2.6: Puff Volcanic Ash Transport and Dispersion model simulations show the predicted plume dispersion for explosive events 5 and 19. Shown are the time steps that most closely match the satellite data acquisitions shown in Figures 2.3 and 2.4. Ash cloud altitudes are shown as color coded particles from 0 – 12 km ASL. Mount Redoubt volcano's location is marked by a black cross. A – 16:06 (March 23); and B – 16:28; C – 16:58; D – 19:28, E: 20:58 and F: 21:28 UTC on April 4.

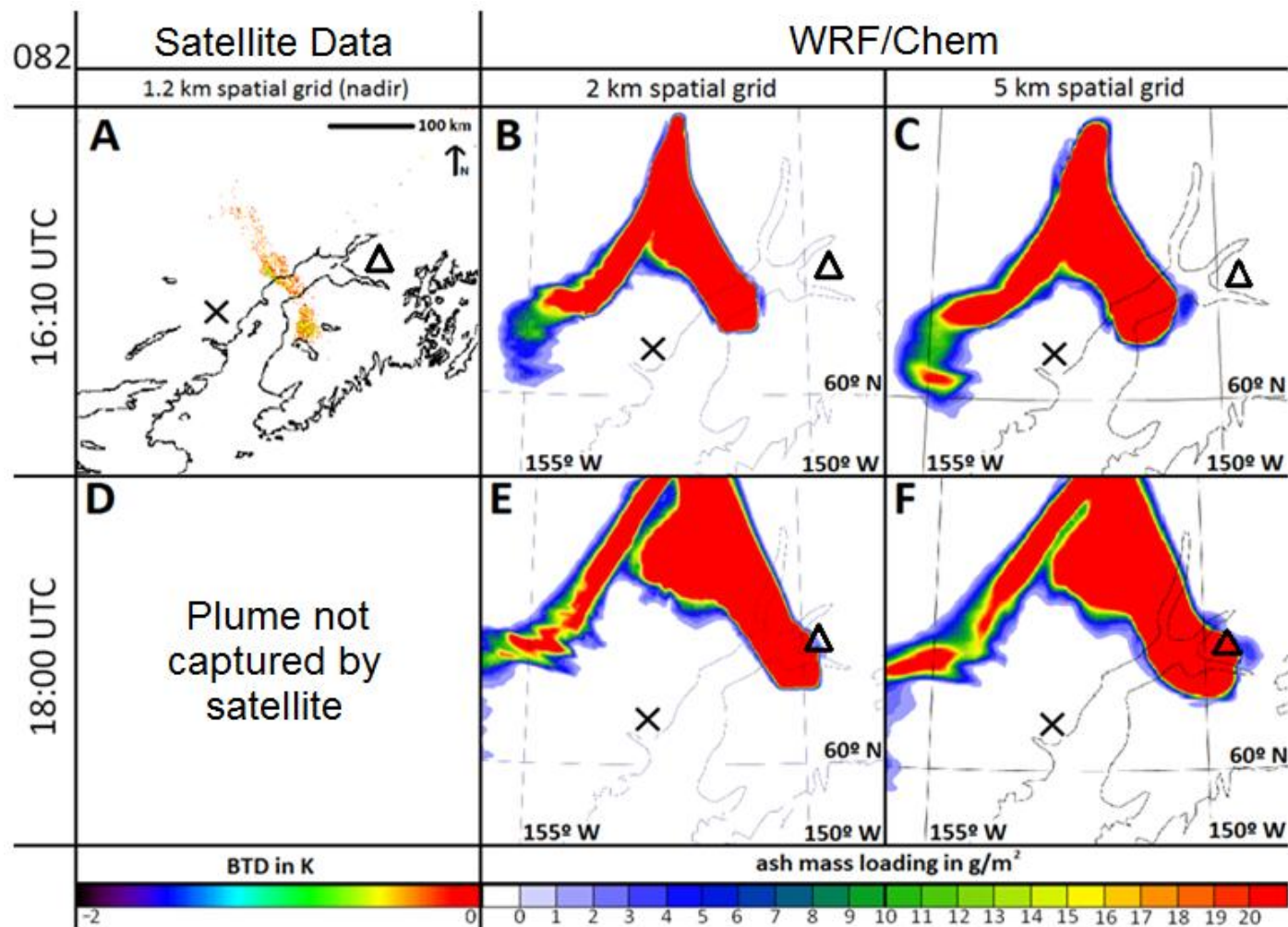


Figure 2.7: Comparison between satellite data (A) and WRF-Chem runs with spatial resolutions of 2 km (B and E) and 5 km (C and F) for the timings 16:10 UTC and 18:00 UTC on March 23 (Julian date 082). The satellite image used was dated at 16:06 UTC. Another satellite pass for this eruption was not available (D). See text for details. Mount Redoubt volcano's location is marked by a black cross, Anchorage is located at the black triangle.

WRF/Chem (16:10 UTC)

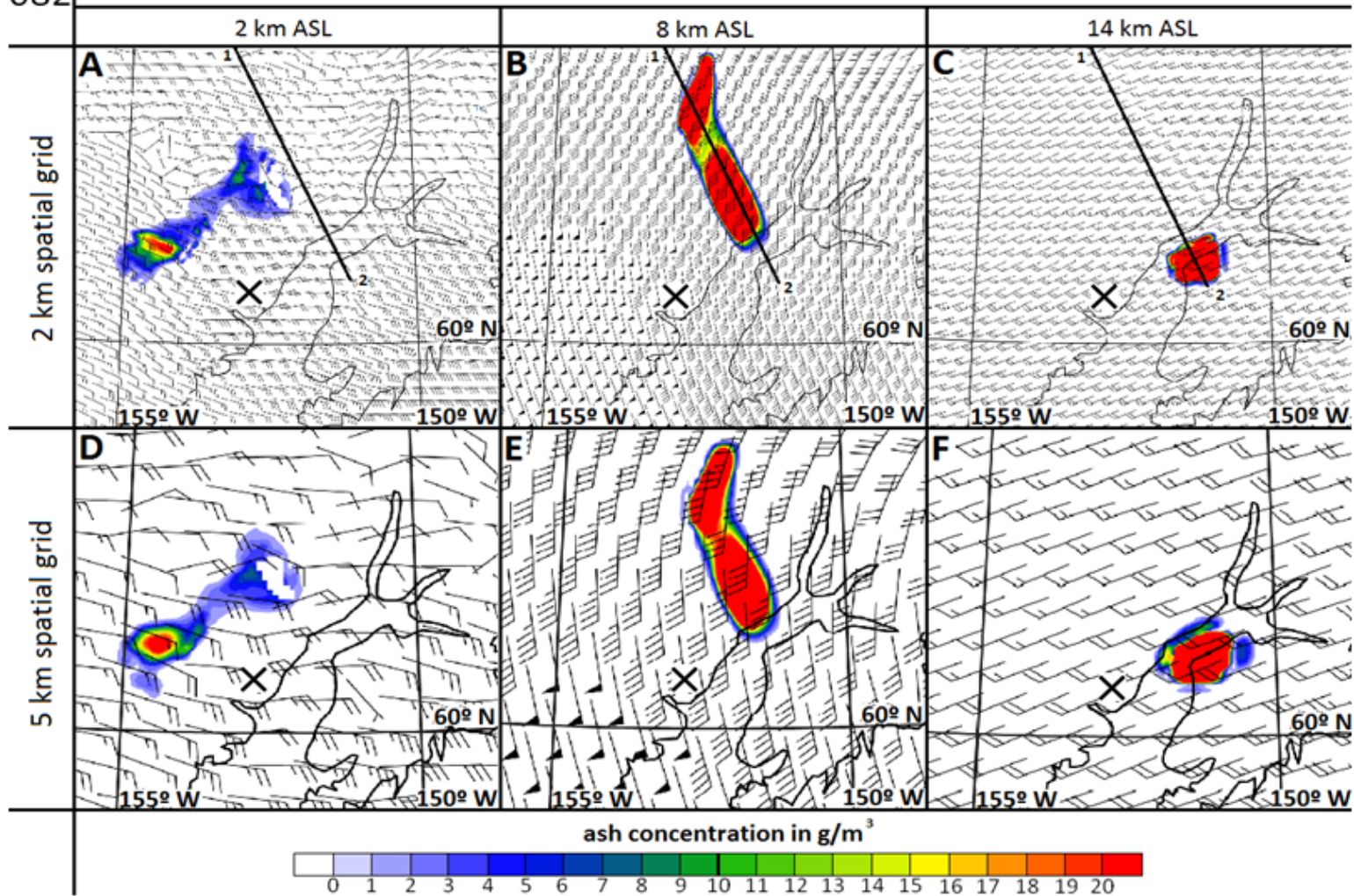


Figure 2.8: Ash concentrations (mg/m³) from WRF-Chem using 2 km grid resolution at 2, 8 and 14 km ASL on March 23, 2009, from event 5 at Mount Redoubt volcano (located at black cross). The line from '1' to '2' represents the location of the cross section (Fig. 2.9). Wind speeds at each grid point are shown as vectors/barbs.

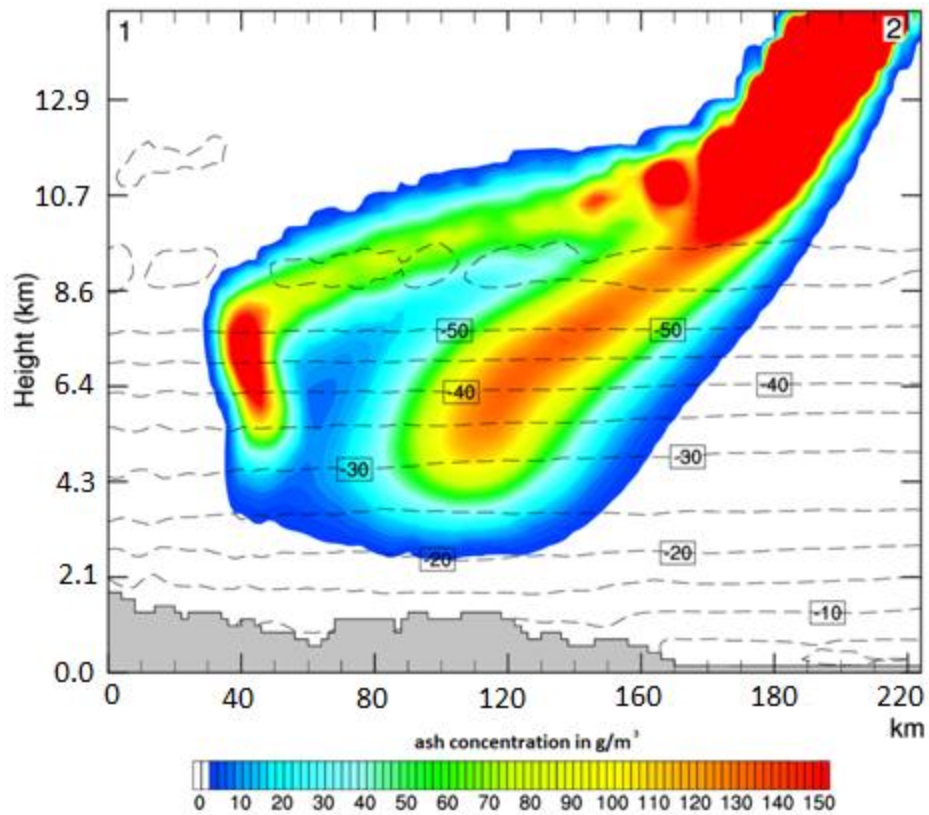


Figure 2.9: Vertical cross section of ash concentration (g/m^3) from WRF-Chem through the cloud on March 23, 2009, at 16:10 UTC at the location '1' to '2' (Fig. 2.8 A to C). The dashed lines represent isotherms in $^{\circ}\text{C}$.

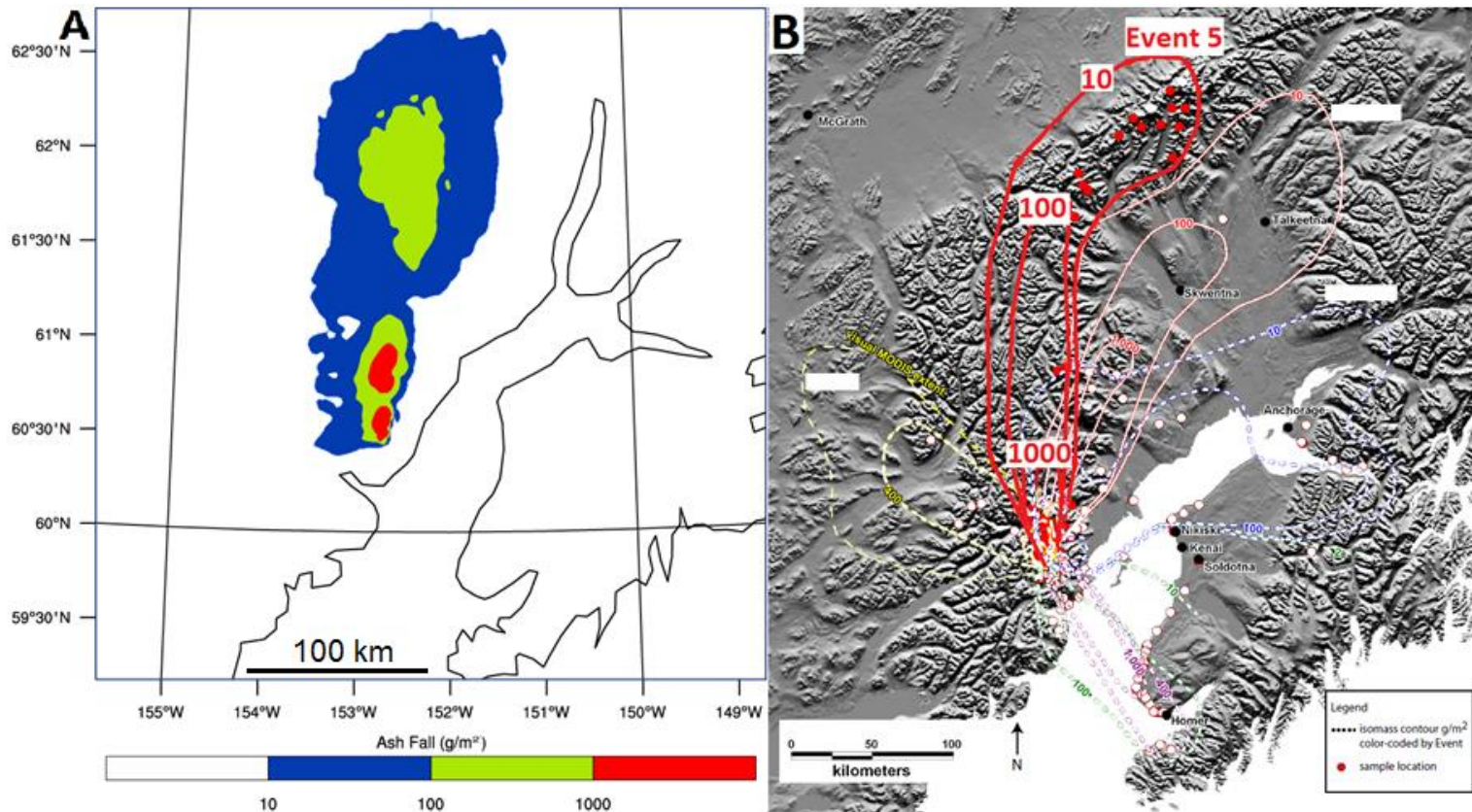


Figure 2.10: WRF-Chem ash fallout (g/m^2) compared to the sample-based isopach map by Wallace et al. (this issue), adjusted to highlight event 5 over the other events during the Mount Redoubt volcano's eruption of 2009.

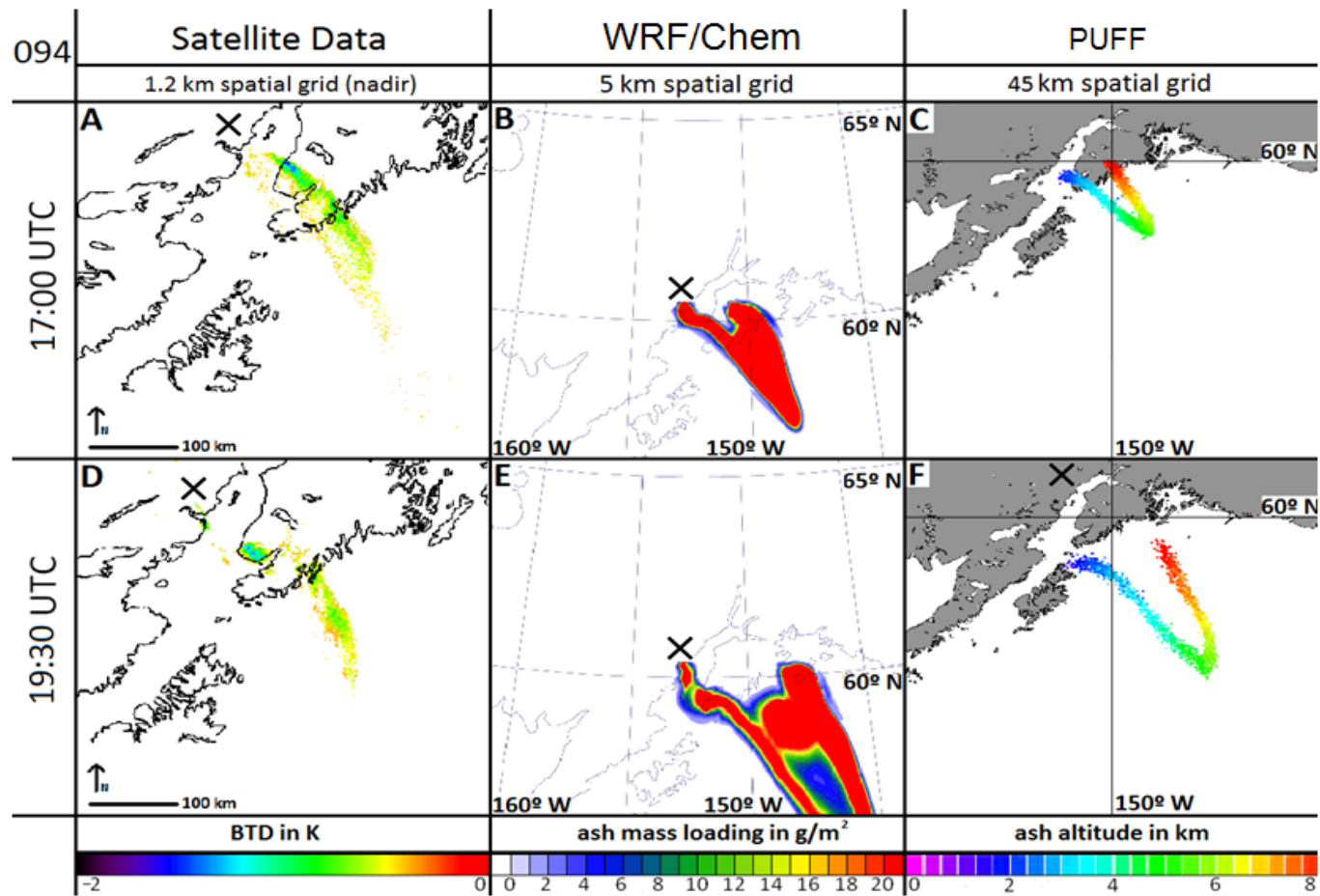


Figure 2.11: Comparison between satellite BTDR images (A and D), WRF-Chem simulations (B and E) and PUFF runs (C and F) at 17:00 UTC and 19:30 UTC for April 4, 2009. The satellite images are taken at 17:02 UTC and 19:19 UTC, Mount Redoubt volcano's location is marked by a black cross.

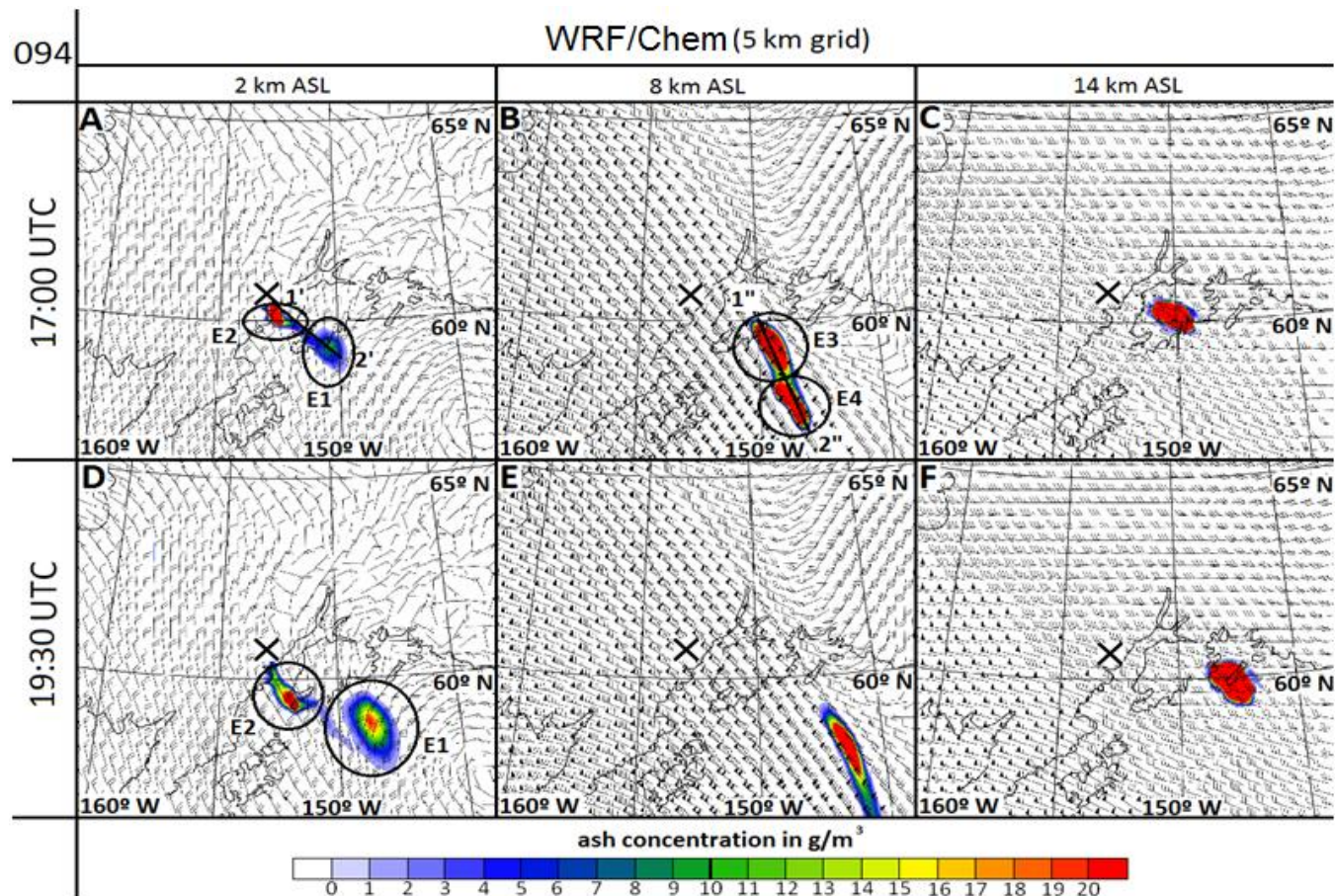


Figure 2.12: WRF-Chem ash concentrations (mg/m^3) using 5 km grid resolution at 2, 8 and 14 km ASL on April 4, 2009, from event 19 at Mount Redoubt volcano (black cross). The lines from '1' to '2' and from '1'' to '2'' represent the locations of the cross sections (Fig. 2.13). Different parts of the ash cloud can be identified at different altitudes with the highest part being at the eastern edge of the cloud. The parts are individually labeled E1 through E4, see text for discussion. Wind speed and direction at each grid point is highlighted by the wind bars.

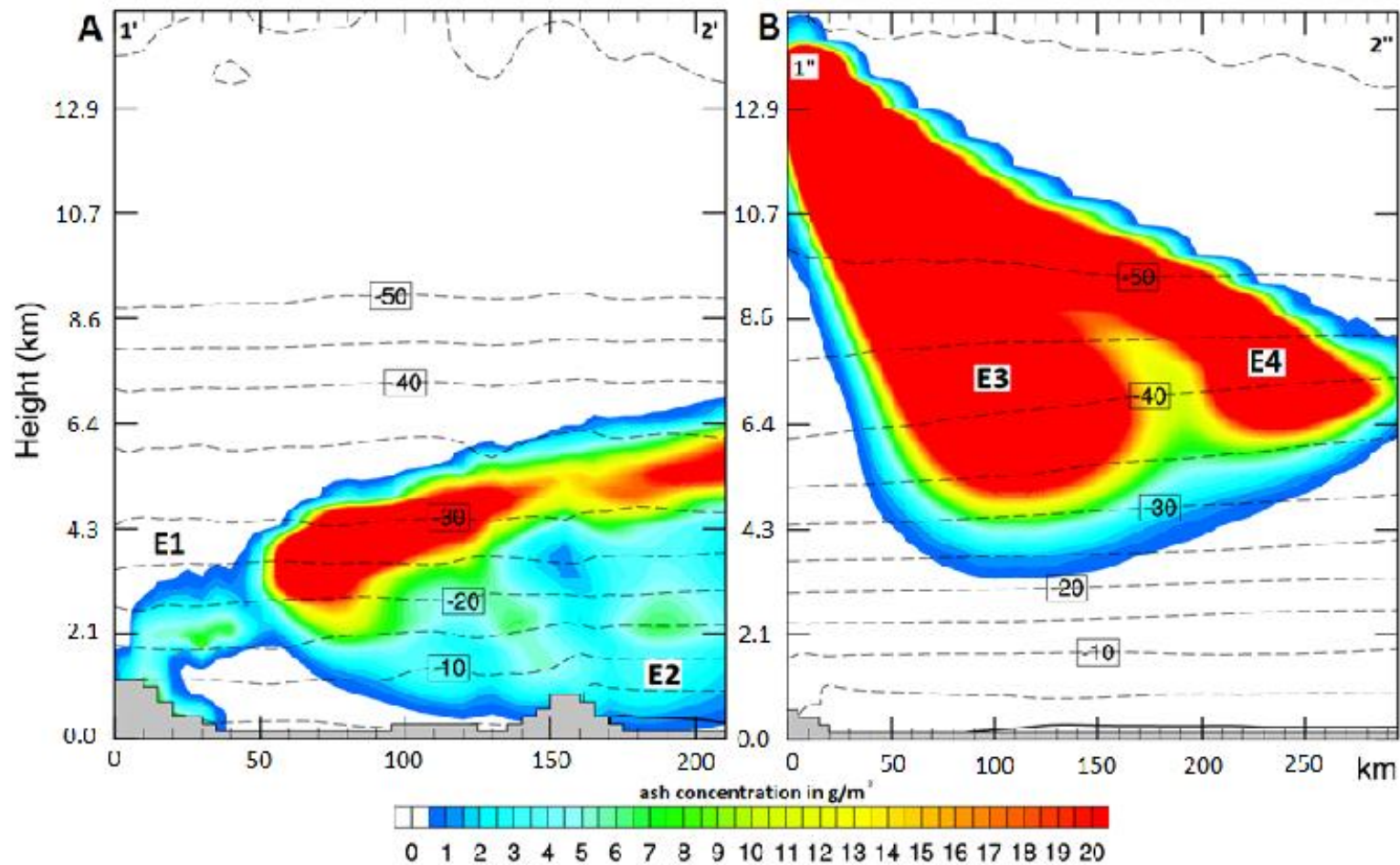


Figure 2.13: Vertical cross section of ash concentrations (g/m^3) from WRF-Chem through the cloud on April 4, 2009, at 17:00 UTC at the locations shown in Figures 2.12A and B. The dashed lines represent isotherms in °C. Different parts of the ash cloud are outlines as E1 through E4, see text for discussion.

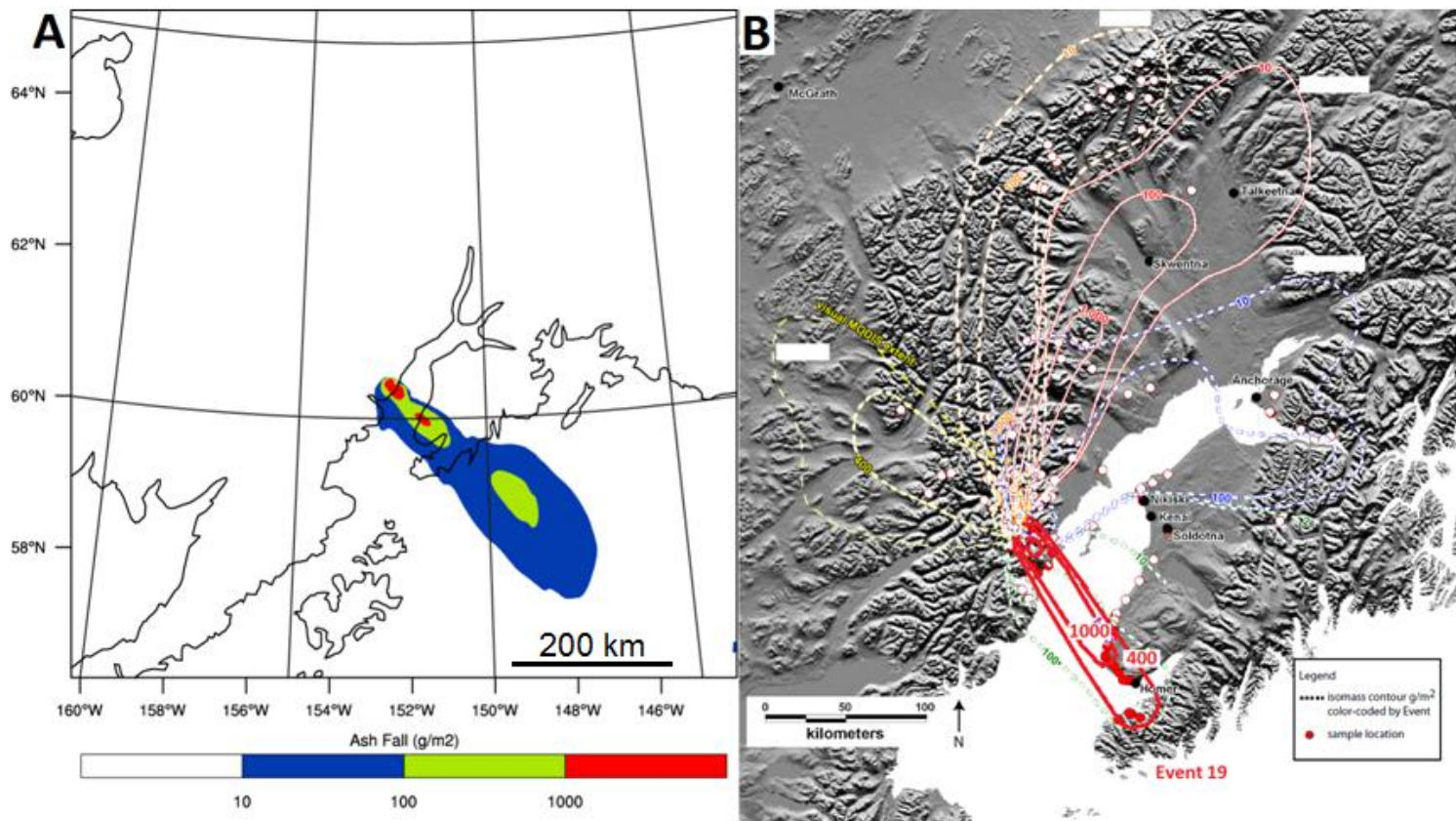


Figure 2.14: WRF-Chem ash fallout (g/m^2) compared to the sample-based isopach map by Wallace et al. (this issue), adjusted to highlight event 19 over the other events during the Mount Redoubt volcano's eruption of 2009.

2.11 Tables

Table 2.1: Parameters used for each analysis and each event. WRF-Chem = Weather Research and Forecasting model with online chemistry, VAR = Volcanic Ash Retrieval, NAM 216 = North American Mesoscale model Grid 216.

	Parameter	Unit	Event # 5	Event # 19
General	Julian Date		082	094
	Starting Time	UTC	12:58	13:59
	Duration	min	20	31
	Initial Height (ASL)	km	14.9	15.2
WRF-Chem	Erupted Volume ^(a)	km ³	0.0017	0.0032
	Eruption Rate ^(a)	kg s ⁻¹	3.7x10 ⁶	4.4x10 ⁶
	Mass Fraction <63μm	%	65	65
	Density	Kg m ⁻³	2600	2600
	Spatial Resolution	Km ²	2 and 5	5
Puff	Vertical Particle Distribution		exponential	exponential
	Wind model		NAM 216	NAM 216
VAR	Cloud Temperature	K	223	223
	Background Temp.	K	247	269 ^b 272 ^c
	Horizontal Resolution	km	2, 5	5

^a Based on AVO internal estimates for given density and duration, mass calculations using root-area method (Pyle, 1989, modified by Fierstein and Nathenson, 1992)

^b Valid for images acquired at 16:23 and 17:03 UTC

^c Valid for images acquired from 19:19 to 21:20 UTC

Table 2.2: Volcanic Ash Particle bins and their respective masses used for the Mount Redoubt eruption from the S2 type of the eruption source parameters specified by Mastin et al. (2009).

#	Particle size bin	Phi	Mass (% of total)
1	1 - 2 mm	-1 - 0	0
2	0.5 - 1 mm	0 - 1	6.6
3	0.25 - 0.5 mm	1 - 2	15.3
4	125 - 250 μm	2 - 3	19.3
5	62.5 - 125 μm	3 - 4	22.4
6	31.25 - 62.5 μm	4 - 5	14.3
7	15.625 - 31.25 μm	5 - 6	10.2
8	7.8125 - 15.625 μm	6 - 7	5.6
9	3.9065 - 7.8125 μm	7 - 8	3.8
10	< 3.9065 μm	> 8	2.5

Table 2.3: Advanced Very High Resolution Radiometer images analyzed for event 5 and 19 of the 2009 unrest of Mount Redoubt volcano, Alaska, thresholds used for the VAR model to determine ash masses, optical depths and effective radii of the volcanic clouds and the derived total masses of all particles in the plume smaller than about $4 \mu\text{m}$. Satellites are classed by their National Oceanic and Atmospheric Administration (NOAA) number, n15 = NOAA 15, n16 = NOAA 16, n17 = NOAA 17 and n18 = NOAA 18, BT = Brightness Temperature, UTC = Coordinated Universal Time.

Julian Day	Date	Time (UTC)	Satellite	Threshold (AVHRR BT4-BT5)	Total Mass (tons)
82	23-Mar-09	16:06	n16	-0.2	15694 ± 6000
94	4-Apr-09	16:23	n15	-0.4	37681 ± 15000
94	4-Apr-09	17:03	n16	-0.4	36685 ± 15000
94	4-Apr-09	19:19	n17	-0.4	20099 ± 8000
94	4-Apr-09	20:59	n17	-0.3	17694 ± 7000
94	4-Apr-09	21:20	n18	-0.1	12528 ± 5000

**Chapter 3: Qualitative Analysis of Input Parameters for Satellite-Based
Quantification of Airborne Volcanic Ash¹**

Abstract

Satellite remote sensing data is an important tool to analyze and quantify volcanic ash emissions. However, the algorithms used require a range of input parameters not always known accurately enough for precise calculations. Based on the eruption of Sarychev Peak in the Kuriles, eastern Russia, during June 2009, we analyzed the sensitivity of each of the variables used operationally to evaluate their contributions to the derived mass loading. It is shown that the derived cloud top and surface brightness temperatures, the refractive indices of air and ash, the particle density and the amount of water in the cloud are the dominant factors influencing the retrieval. It is further outlined, how a combination of over- and underestimates of different parameters can yield the same output.

¹ Steensen, T. and Webley, P. (2012), Qualitative Analysis of Input Parameters for Satellite-Based Quantification of Airborne Volcanic Ash, Geoscience and Remote Sensing Symposium (IGARSS), 2012 IEEE International , Pages 2982 – 2985, 10.1109/IGARSS.2012.6350799. (*Changes have been made*)

3.1 Introduction

Volcanic ash poses a major hazard to airborne traffic by melting in engines and blocking fuel nozzles resulting in possible failure of the engine [1]. To avoid exposure of planes to ash, satellite data is used to outline the spatial extent of recent ash emissions and to quantify their masses. However, such analysis requires a range of input parameters including surface and cloud radiance, the refractive indices of ash and air and the specific gravity of the particles. Not all of these inputs can be assessed qualitatively before or during the event, so the determination of the amount of ash has inherent variability. In this study, we analyze the importance of each variable independently to determine the variable with the largest impact on the result. In addition, we examine the interdependency of the parameters and the influence on the retrieved values by varying the input parameters simultaneously.

3.2 Case Study

This analysis is based on scenes of the Japanese Multifunctional Transport Satellite (MTSAT) geostationary located at 140° E taken between June 14 (1857 UTC) and June 15 (1130 UTC) 2009 of the erupting Sarychev Peak volcano in the Kuriles, Russia (Fig. 3.1). This eruption, the first at this volcano after a quiescence of over 30 years, consisted of at least 23 separate explosions between June 11 and 16, 2009. Altitudes of the ash

averaged between 8 and 16 km above sea level and the lateral extents were up to 1500 km to the northwest and over 3000 km to the east [2].

To quantify volcanic ash content in satellite imagery, Wen and Rose [3] developed the Volcanic Ash Retrieval (VAR). Based on several input parameters (Table 3.1) including relevant brightness temperatures and refractive indices, crucial quantities like ash mass and optical depth can be determined. Most of these parameters are set to default values in many applications with mainly surface and cloud top brightness temperatures changing on a case-by-case basis in operational and research settings.

To define the most important parameter for mass retrievals, we quantitatively analyzed the dependence of the final product on each input parameter by varying it individually by $\pm 25\%$ from its best-fit estimate, while leaving all other parameters constant. The variation by 25% has been chosen to be large enough to encompass possible assessment uncertainties, especially in variables with low quantitative values, and to allow sufficient computational time to process results.

After defining the contribution of each individual parameter to the estimated masses at different levels of uncertainty, we classified the interdependency of derived surface and cloud top brightness temperatures (T_s and T_c , respectively), the two variables most often changed during ash mass retrievals. Brightness temperatures do not equal absolute temperatures but are derived remotely from the received thermal radiance at each

satellite band under the assumption of a blackbody radiator. Again, we varied each parameter by $\pm 25\%$ and compared the calculated masses from each possible pair of brightness temperatures in that range.

3.3 Results and Discussion

Our results indicate that physical parameters like the surface brightness temperature and the refractive indices of ash and air have the strongest potential to influence the determined ash mass (Table 3.1, 1-7). Model variables like the number of radii level and the radii for the ash particle distribution tend to have a low tendency to alter the results, if assessed incorrectly (Table 3.1, 8-14).

Figure 3.2 shows the six parameters with the highest potential to affect the mass retrieval, with their errors and the resulting changes in the derived masses. The surface brightness temperature, T_s or ground-leaving radiance, shows the strongest influence on the retrieved values, doubling the estimated mass, if assessed 12% too high. However, it is also the best-known variable and generally associated with low error bars leaving the net average error at about $\pm 10\%$.

T_c is difficult to determine with current methods as meteorological profiles are comparably rare and only an optically opaque cloud can be precisely measured remotely. Derivations of $\pm 25\%$ of the actual value, as shown here, are possible. All other

parameters analyzed in this work are rarely assessed case-by-case. The standard value listed in Table 3.1 is chosen to facilitate the calculations, often because a precise estimate, like the refractive index of the ambient air or the particle coating, a dependency of the water ratio of the eruption, is, as of now, difficult to derive. Detailed assessment of the refractive index and specific gravity of the ash requires samples which can be hard to obtain, especially if the volcano, as in the case of Sarychev Peak, is on a comparably isolated island

The analysis of a simultaneous change of T_s and T_c shows that a change in T_c of $\pm 25\%$ can be buffered by an according change in T_s (Fig. 3.3). However, already a small overestimate of T_s ($> 5\%$) cannot be balanced by adjusting T_c in the range of $\pm 25\%$ to retrieve the same mass. Additionally, the relationship suggests that an underestimate of the surface brightness temperature of 4 to 15% can be counterbalanced by different overestimates of the cloud top brightness temperature.

These ambiguous values for T_c at the given T_s stem from the non-monotonically increasing graph in Figure 3.2. In the range of +15 to +25% of the optimal value for T_c , the respective graph shows different lows. Here, different values of T_c yield the same overestimate of masses and the same underestimate of T_s is required to balance this. This relationship is expressed in Figure 3.3 by the grouped data points at location A at the given intervals. The cloud-like structure of these points originates in the

concatenation of all used MTSAT scenes and their respective data. Individual scenes express slight variations to the overall shape.

An accuracy assessment of diversion from an optimal value for one parameter to balance an under- or overestimate of a different parameter was carried out for the surface and cloud top brightness temperatures. This yielded an error bar of $\pm 5\%$. These $\pm 5\%$ are variations in the T_c value with the inverse deviation of T_s in Figure 3.2 to the value needed based on Figure 3.3. Such a deviation equals an error in the derived masses between -10% to +5% (Fig. 3.2). This error analysis has been performed on an average of all used MTSAT scenes with the data points seen in Figure 3.3. An individual error analysis on single images will reduce this uncertainty. Further in-depth study on different volcanic eruptions is also needed to reduce this error bar and to assess whether this pattern is consistent for all remotely sensed volcanic ash clouds.

3.4 Conclusion

This study shows that different input parameters for the determination of airborne ash masses have a potentially large effect on the derived masses. In particular, the physical properties of the setting including surface and cloud top brightness temperature, relevant refractive indices and the specific gravity of the ash can realistically individually

influence the calculated ash masses by up to $\pm 30\%$, if associated with an error bar of only $\pm 5\%$.

This research further illustrates that the different parameters are directly correlated and an overestimate of one value can be buffered by an according underestimate of a different one. In some cases, multiple choices of parameters yield the same output. This is a direct result from a non-monotonical in- or decrease of their sensitivity with changing values.

An under- or overestimate of airborne ash masses has large impact on aviation safety, especially in highly frequented flight corridors like the North Pacific or Europe. Future work should therefore focus on determination of other key input factors like relevant refractive indices and specific gravities when actual sampling is hard to accomplish.

3.5 Acknowledgements

This publication is the result in part of research sponsored by the Cooperative Institute for Alaska Research with funds from the National Oceanic and Atmospheric Administration under cooperative agreement NA080AR4320751 with the University of Alaska. We also thank the Alaska Volcano Observatory (AVO) for providing the satellite data. AVO is a joint program of the United States Geological Survey (USGS), the

Geophysical Institute of the University of Alaska Fairbanks (UAFGI), and the State of Alaska Division of Geological and Geophysical Surveys (ADGGS).

3.6 References

[1] T. J. Casadevall, "The 1989 - 1990 eruption of Redoubt Volcano Alaska: impacts on aircraft operations", *Journal of Volcanology and Geothermal Research*, vol. 62, no. 30, pp. 301- 316, 1994.

[2] A. Rybin, M. Chibisova, P. W. Webley, T. Steensen, P. Izbekov, C. Neal and V. Realmuto, "The June 2009 eruption of Sarychev Peak volcano, Matua Island, Central Kuriles", *Bulletin of Volcanology*, vol. 73, no. 9, pp. 1377-1392, 2011.

[3] S. Wen and W. I. Rose, "Retrieval of sizes and total masses of particles in volcanic clouds using AVHRR bands 4 and 5", *Journal of Geophysical Research*, vol. 99, no. D3 pp. 5421-5432, 1994.

3.7 Figures



Figure 3.1: Location of Sarychev Peak in the Kuriles, eastern Russia.

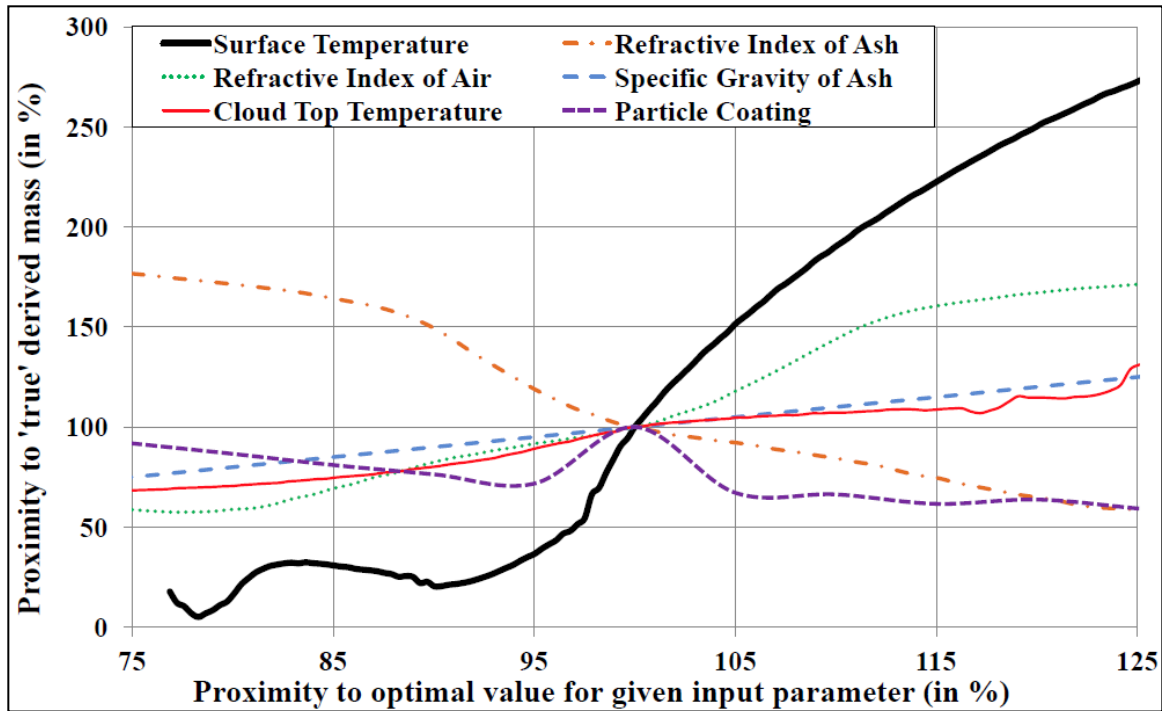


Figure 3.2: Variation of derived masses with changing input parameters. The six parameters here yield the highest variability in the estimated masses. The net effect of the surface temperature, although listed here as resulting in a high uncertainty, is around 10 to 15% as it is a well-known quantity with error bars of a few percent at most.

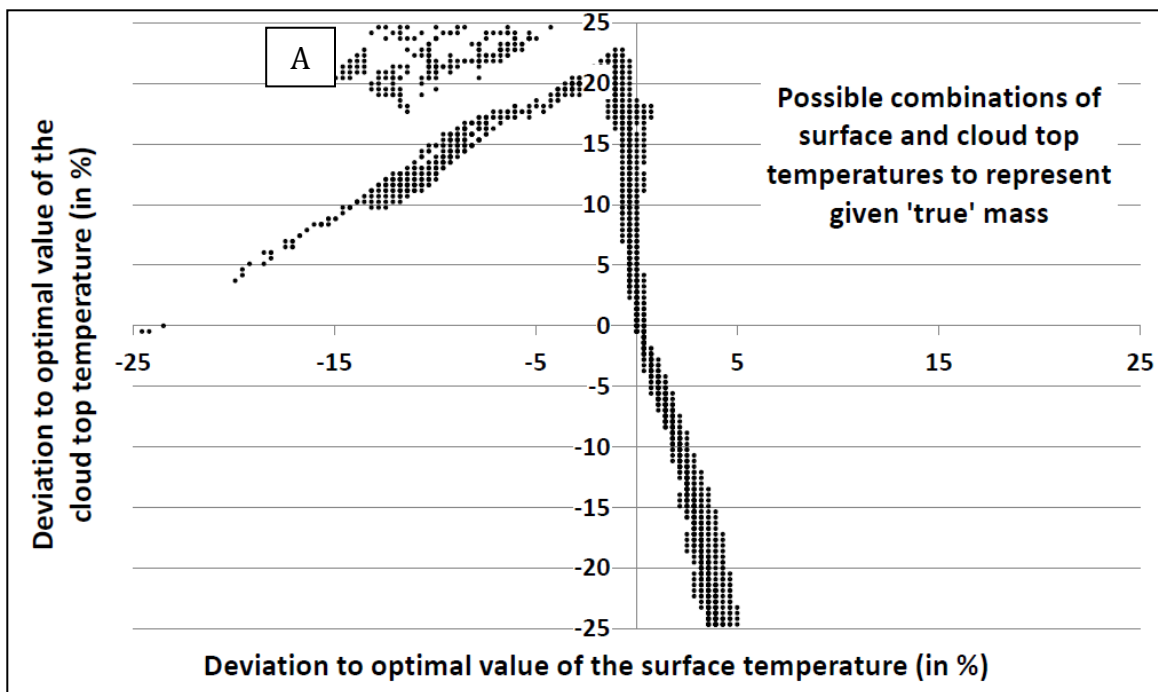


Figure 3.3: Possible combinations of surface and cloud top brightness temperature to derive the 'true' masses. This plot represents all values for the analyzed MTSAT scenes without averaging due to secondary data accumulation at location A. This feature is due to lows in the cloud top brightness temperature graph in Figure 2 where different values can be buffered by the same underestimate of the surface brightness temperature.

3.7 Tables

Table 3.1: Parameters used for the Volcanic Ash Retrieval (VAR), their best-fit estimates for this case study and their average error produced by independently varying each value by $\pm 25\%$. It can be seen that physical parameters of the scene (1-7) tend to have a larger influence on the retrieved mass than VAR model parameters do (8-14).

	Parameter	Best-Fit Estimate		Average Error at $\pm 25\%$
1	Surface Brightness Temperature	281 K		97.74 %
2	Refractive Index of Ash at 11 and 12 μm	11 μm :	2.14610 + 0.39891i	42.93 %
		12 μm :	1.82854 + 0.12953i	
3	Refractive Index of Air	1		42.49 %
4	Specific Gravity of Ash	2.6 kg m^{-3}		18.04 %
5	Cloud Top Brightness Temperature	215 K		17.86 %
6	Particle Coating	1		13.98 %
7	Shape of Particle Size Distribution	0.5		13.95 %
8	Optical Depth Step Size	0.1		5.36 %
9	Upper Radius for Ash Particle Distribution	50 μm		4.52 %
10	Number of Optical Depth Levels	30		3.03 %
11	Maximum Effective Radius	10 μm		0.48 %
12	Lower Radius for Ash Particle Distribution	0.1 μm		0.26 %
13	Number of Radii Levels	30		0.08 %
14	Minimum Effective Radius	0.01 μm		0.01 %

Chapter 4: Quantitative Comparison of Volcanic Ash Observations In Satellite-Based Remote Sensing Data and WRF-Chem Model Simulations¹

Abstract

Volcanic ash poses a significant hazard to air traffic. To accurately estimate masses and locations of volcanic ash, satellite remote sensing data and volcanic ash transport and dispersion (VATD) modeling results have repeatedly been used to detect and track the plumes and subsequent ash clouds. To further gain advantages of the simultaneous use of both approaches, a quantitative comparison is required to outline the strengths and weaknesses of each method. In this paper, an analysis with satellite-based remote sensing ash retrievals and the Weather Research and Forecast model with online Chemistry (WRF-Chem) have been performed, focusing on the 2009 eruptive events from Sarychev Peak volcano, Kurile Islands. This first-order comparison shows a good initial match between satellite data and model results but also outlines areas where future research is required to produce better quantitative and qualitative results. Results for WRF-Chem and for those combining the two datasets in real-time analysis are: (1) the necessity for the VATD model to use eruption source parameters and

¹ Steensen, T., Webley, P, and Stuefer, M. Quantitative Comparison of Volcano Ash Observations In Satellite-Based Remote Sensing Data and WRF-Chem Model Simulations, Submitted to *Natural Hazards*.

particle distributions not only tailored to a specific volcano but also to specific events during an eruption and corrected for aggregation; (2) the satellite-derived ash retrievals, with two-band brightness difference data, require a manually-outlined plume to produce the best results hence the definition of the edge of the cloud is critical; and (3) comparisons between the two datasets should be corrected for the satellite's line of sight and for differences in pixel size compared to the model grid cells. These results emphasize the need for more accurate eruption source parameters for volcanic ash models and that comparing and validating each method with the other is a difficult and taxing process.

4.1 Introduction

Volcanic ash poses a significant risk to aviation and human health (Blong, 1984; Casadevall, 1994). In the past, multiple aircraft have encountered ash from different volcanoes including Mount Galunggung, Indonesia, 1982 (Hanstrum and Watson, 1983), Mount Redoubt, USA, 1989 (Casadevall, 1994) and Mount Pinatubo, Philippines, 1990 (Prata et al., 1991). The total cost of such incidents can amount to \$100's US million in aircraft damage alone (Prabaharan, 2002). Historically, volcanic eruptions have been monitored with satellite-based remote sensing (Dehn et al., 2002), their plumes and subsequent clouds have been detected and tracked (Schneider et al., 1995) and analyzed in terms of particles sizes, heights and masses (Prata, 1989; Wen and Rose,

1994; Prata and Grant, 2001; Pavolonis and Sieglaff, 2010). Additionally, Volcanic Ash Transport and Dispersion (VATD) models like Puff (Searcy et al., 1998), the Hybrid Single-Particle Lagrangian Integrated Trajectory model (HYSPLIT, Draxler and Hess, 1997) and the Weather Research and Forecasting Model with online Chemistry (WRF-Chem, Grell et al., 2005) have been utilized to recreate past events and to predict the ash movement of current events in near real time (Kratzmann et al., 2010; Gangale et al., 2010; Webley et al., 2012; Steensen et al., 2013). The research presented herein aims to contribute to this developing community by assisting to improve the detection, analysis and forecasting of volcanic plumes and clouds in order to avoid aircraft-ash encounters and to reduce the associated risks and costs. This task is addressed by a qualitative and quantitative comparison of satellite remote sensing results with model predictions.

Previously, the WRF-Chem model (Grell et al., 2005; Freitas et al., 2011) has been expanded to include volcanic emissions (Stuefer et al., 2013). WRF-Chem is able to compute the dispersion of volcanic ash online with the numerical weather prediction (NWP) model. The online approach eliminates interpolation errors in space and time by using identical model grid-spacing and timing, as well as providing the chemistry component with temporally and spatially coincident atmospheric parameters and microphysical schemes. Similar to the analysis of the Mount Redoubt volcano eruption (Steensen et al., 2013), WRF-Chem is used to describe the 2009 Sarychev Peak eruption in the Kuril Islands, eastern Russia. The modeled ash masses are compared with mass

loading and total column ash masses derived from satellite remote sensing. In section 4.2, the Sarychev Peak eruption characteristics are described, and in section 4.3 the applied remote sensing and modeling methods, as well as the methods to compare the data. An evaluation of WRF-Chem and the satellite derived volcanic eruption characteristics is given in sections 4.4 and 4.5.

The objectives of this paper are: (1) to identify the sensitivity of different WRF-Chem input parameters; (2) to develop satellite-model comparison techniques for use in real-time; and (3) to show the dispersion and transport of the emitted ash in terms of (a) changing satellite derived particle size associated to WRF-Chem ash bins with time, (b) changes in the ability of the satellite to detect the ash over time and (c) subsequent consequences for the particle fallout.

4.2 Sarychev Peak Volcano and its 2009 Eruption

Sarychev Peak volcano (1.496 km above sea level [ASL]) is located on Matua Island in the Kuril Islands (48.1°N, 153.2°E), eastern Russia, that stretch over approximately 1300 km from Kamchatka, Russia, to Hokkaido, Japan, dividing the North Pacific Ocean from the Sea of Okhotsk (Fig. 4.1). Sarychev Peak is a stratovolcano and belongs to the most active volcanoes in the Kurile Islands (Rybin et al., 2011). After 33 years of quiescence, it erupted explosively with 23 events from June 11 to 23, 2009, sending ash up to 21 km ASL in a north westerly and south easterly direction (example image shown in Fig. 4.2B

and 4.2C and see in Rybin et al., 2011) and disrupting air travel significantly (Levin et al., 2010; Rybin et al., 2011). Infrasound data from stations around the volcano as well as stations located up to 60 °E (about 6400 km west of Sarychev Peak) show signals of the eruption (Matoza et al., 2011). Table 4.1 summarizes the explosive events with height and duration based on satellite and infrasound data, where available. Events where the satellite-derived onset was ± 5 minutes from the onset based on the observations of Levin et al. (2010) were considered for this study. Based on the availability of confirmed eruption characteristics, events 13 to 16 were chosen for analysis (June 13, 04:50 UTC, to June 14, 18:50 UTC 2009). These events comprise eruption columns of up to 21 km ASL and therefore form a central part of the whole eruption sequence.

4.3 Methods

4.3.1 Satellite Remote Sensing

For the satellite-based study of the Sarychev Peak eruption, data from the Japanese Multifunctional Transport Satellite (MTSAT) geostationary located at 140° east was used. MTSAT has a spatial resolution of 4 km in the infrared bands at nadir and a look angle that covers the whole plume series of the eruption (see details at University of Wisconsin, 2013). Located at a height of 36,000 km ASL, MTSAT has a foot-print of 4.3 x 4.3 km² at Matua Island. Other satellite instruments such as the Advanced Very High Resolution Radiometer (AVHRR) or the Moderate Resolution Imaging Spectroradiometer

(MODIS) have a better spatial resolution of up to 1.1 km (MODIS at nadir), but their temporal and spatial coverage was insufficient to fill a fixed spatial domain of the whole plume for a qualitative and quantitative comparison to VATD models. MTSAT data collected operationally by the Alaska Volcano Observatory in a 30 minute interval was available for this analysis.

MTSAT's infrared channels 1 and 2 (IR1 and IR2, centered at 10.8 and 12.0 μm , respectively) can be used to determine the ash mass in each of these images. For this, the Volcanic Ash Retrieval (VAR) algorithm was used, as developed by Wen and Rose (1994), based on the reverse absorption feature of silicate ash in the infrared first described by Prata (1989). This method states that the brightness temperature difference (BTD) between the infrared channels at 10.8 μm and 12.0 μm (IR1-IR2) is negative, when fine dry ash is present and certain assumptions are fulfilled (see Prata, 1989 and Wen and Rose, 1994, for a complete list). With a BTD threshold of zero, however, a large amount of low stratus clouds and other meteorological features are falsely classified as ash, so that the actual cutoff used is varied on a case-by-case basis or detailed algorithms are used (see Pavolonis and Sieglaff, 2010).

Based on visual image interpretation in the visible and infrared range with MTSAT's two band thermal IR (TIR) data, a threshold of -1.5 K was determined to best outline the ash, while cancelling out the majority of noise. However, such a cutoff results in the omission

of parts of the ash cloud that have a BTM value slightly below 0 K. This is especially significant as the initially opaque cloud becomes translucent and a large mass is associated with it despite the only slightly negative BTM value (Wen and Rose, 1994). To avoid the omission of ash-rich, weakly negative signal BTM pixels, while excluding also weakly negative BTM pixels originated by low stratus clouds and other background meteorological features, we manually outlined the ash as identifiable in the 0 K threshold BTM images, additionally using the visible and infrared satellite data. While this scenario is subjective based on experience in image interpretation, this route was chosen in addition to the standard universal BTM application to the whole scenes to analyze its potential in improving the ash detection and quantification. This approach aims to make the most of the two band TIR MTSAT data. The universal BTM value of -1.5 K and the manual ash outlines at a BTM value of 0 K were used in addition to a comparison of the ash detection areas using the BTM thresholds of 0 K, -0.5 K and -1 K of the whole scenes.

For VAR to be able to calculate the total ash mass within the atmospheric column, the surface and cloud top brightness temperatures (i.e. cloud top and ground based leaving radiances) are needed. They were both empirically measured in the satellite images at a cloud-free surface, for surface temperature, and an infrared-opaque part of the cloud, for cloud top temperature. In the next step, VAR derives physical parameters of the ash cloud including total mass in the vertical column, effective radii and optical depth based

on Mie scattering. The maximum effective radius possible in this VAR calculation is 10 μm (Wen and Rose, 1994).

The single value of the surface and cloud top brightness temperature for a whole scene is error-prone, as these temperatures can vary over small spatial scales and such changes can result in large uncertainties in the retrieval (Steensen and Webley, 2012). Additionally, using the cloud free surface temperature as the ground leaving radiance assumes that the ground surface is the only radiating feature below the ash cloud and removes the possibility of lower meteorological clouds contributing to the ground leaving radiance. Alternatives for the single values are using meteorological data for the pixel-based surface temperatures and alternative satellite bands for the cloud top temperature. Pavolonis et al. (2006) showed the use of satellite bands centered at 7.4 and 8.5 μm to help in the retrieval. However, in the case of MTSAT such bands do not exist.

Besides the brightness temperatures, VAR requires a range of input parameters including an assumed particle size distribution, the refractive indices of ash and ambient air as well as the water content of the plume (Wen and Rose, 1994). As most of these variables are hard to obtain, defined default settings are used for VAR as best estimates for the local conditions (see those listed in Table 4.2). The errors resulting from this simplification can cause a significant uncertainty of calculated masses (Steensen and

Webley, 2012). Additional limitations are caused by assumptions of a translucent ash cloud, as well as homogeneity for identical physical properties to exist throughout the ash-inundated area and a lack of other absorbing features in the radiation path.

4.3.2 Volcanic Ash Emission, Dispersion and Transport Model

WRF-Chem requires as input parameters: (1) the duration and altitude above sea level (ASL) for each eruptive event, both derived from satellite and infrasound data and listed in Table 4.1; (2) the mass eruption rate and (3) the initial ash particle size distribution. The onsets and initial plume heights of the events were observed in satellite data (Levin et al., 2010). Additionally, Matoza et al. (2011), used infrasound data to derive the duration of the events. Because this latter approach identified more events than were detectable in the satellite data and because the onsets differed, durations were only assigned to events detected in the satellite data, where the satellite-derived onsets were within the range of ± 5 minutes of the infrasound data.

There are different methods to calculate the mass eruption rate. For this study, the approach described by Sparks et al. (1997) was used, which bases the eruption rate solely on duration and height of many past eruptions, as well as on Plumeria, described by Mastin (2007), which takes into account the atmospheric conditions and determines the eruption rate required to reach a defined plume height. Sparks et al. (1997) analyzed the eruption rates (m^3s^{-1}) and column heights (km above vent) of 27 historic eruptions

and were able to infer an empirical relationship with a correlation coefficient of 0.921, equation 4.1, where H = Height above vent and Er = Mass eruption rate:

$$H = 1.67x(Er)^{0.259} \quad (4.1)$$

If the eruption produced a large amount of fine-grained tephra, uncertainties in other eruption parameters, including the atmospheric conditions, are of secondary nature and this formula can be used to define the eruption rate based on the column height above the vent. Only if there are a high proportion of coarse particles in the eruption, or a weak eruption is occurring in an atmosphere with high moisture content or strong horizontal winds, this relationship significantly deviates from observed values (Sparks et al., 1997).

A different approach was developed by Mastin (2007). His Plumeria model simulates a one-dimensional volcanic plume above the vent. As opposed to the Sparks et al. (1997) empirical approach, the Plumeria model is based on theoretical computations on plume behavior and also takes into account the atmospheric properties like temperature and relative humidity. Additional model parameters include the vent diameter, the magma temperature, the velocity and the mass fraction of gas in the magma and of external water. The eruption rate and, ultimately, the plume top height, are calculated from the input parameters under certain assumptions including water vapor being the only volcanic gas component and an ideal gas and the mixture being at the ambient

atmospheric pressure (Mastin, 2007). Using the empirical method of Sparks et al. (1997), eruption rates were determined from the satellite-derived plume top height and with the Plumeria approach, the recorded plume height is used and an iterative approach is carried out to determine the most likely eruption rate given the range of inputs to the Plumeria model, see Table 4.2 for the listed mass eruption rates from the two methods.

The particle size distribution (PSD) depends on the explosivity of the volcanic eruption, with more explosive eruptions having a larger amount of fine material as described by Mastin et al. (2009). They summarized different PSD classes for each volcano worldwide based on different eruption source parameter (ESP) types. This categorization is based on the magma type, the height of the eruption column and the Volcano Explosivity Index (VEI; Newhall and Self, 1982) of previous eruptions. For each type, a reference volcano is selected that fits the parameters and where the PSD of a previous event is known. In the case of Sarychev Peak, the classification assigned is S1 (case study: Mount Ruapehu, New Zealand, 1996; see Table 4.3 for associated PSD). However, this most recent eruption does not match the guidelines for the S1 type as inferred from previous volcanic eruptions. Events 13 and 14 both reach a height of 10 km ASL that is well above the maximum height of 6 km ASL associated with S1. The plumes of events 15 and 16 reach even higher with 21 and 16 km ASL, respectively (Table 4.1). In addition, the VEI has been set to 3 for most of the eruption with peak values of 4 (Urai and Ishizuka,

2011). With these parameters, the PSD for this study has been set to ESP type S2 (case study: Mount Spurr, USA, 1992) for events 13 and 14 and to ESP type S3 (case study: Mount St. Helens, USA, 1980) for events 15 and 16. Based on these PSD classes, percentages were assigned to the respective WRF-Chem bins for each run. The percentages for each particle size associated with the PSDs can be found in Table 4.3.

This range of input parameters results in four different WRF-Chem runs:

- 1) Sparks-determined eruption rate with the PSD of S1
- 2) Plumeria-determined eruption rate with the PSD of S1
- 3) Sparks-determined eruption rate with the PSD of S2 (Events 13, 14) and S3 (Events 15, 16)
- 4) Plumeria-determined eruption rate with the PSD of S2 (Events 13, 14) and S3 (Events 15, 16)

4.3.3 Comparison Between Satellite Retrievals and Model Simulations

Satellite data and WRF-Chem predictions deliver different information, which has to be processed for a comparison. While the MTSAT data in this study consists of two-dimensional pixel values for geographical coordinates and relevant brightness temperatures, the model predictions are presented in a three-dimensional grid with terrain-following coordinate system (Skamarock and Klemp, 2008). For the satellite

data, VAR results in an ash mass in tons per pixel (18.5 km^2). WRF-Chem data includes ash concentrations (g/m^3) of each ash bin per grid cell (25 km^2 for our runs), that are then converted to tons by vertically summing up respective concentrations. The WRF-Chem tonnages are then matched to the satellite's footprint. The data is not directly compared in terms of concentration as that involves estimating a thickness for the plume/cloud in the satellite-retrieved ash masses and is not always available in real time. The spatial and temporal match of satellite and model data is analyzed over chosen locations. For a vertical comparison with WRF-Chem, more information is needed about the plume/cloud based on satellite or other relevant data like radiosondes or *in-situ* measurements. Based on the model runs and the satellite-based analysis of the eruption, the spatial extent of the ash dispersion is compared quantitatively in different steps. Because of the large extent of the eruption clouds and the limited availability of full-ranged MTSAT data, the analyses focused on the center part of the sequence between 148 and 160°E and 46 and 51°N .

4.3.3.1 Quantitative Spatial Comparison

Firstly, the total spatial comparison is estimated, where the spatial extents of the ash clouds are calculated over time in both the WRF-Chem simulations and the MTSAT data. For the model results, the total ash inundation of all bins is used based on all four model runs listed in section 4.3.2, while the satellite data is analyzed with the BTM thresholds

of 0 K, -0.5 K, -1 K and -1.5 K on the whole satellite scenes over time, which represent automatic ash detection algorithms, as well as the manually-defined plume extent in each image with the BTM threshold of 0 K. The manually-defined outline is based on a negative BTM signal that can be associated to the volcanic ash (See Fig. 4.2C for an example). As the ash BTM signal is not always clearly differentiated from the background noise level, the signal to the ash identifiable in MTSAT's visible range (0.55 – 0.8 μ m, Fig. 4.2B) is identified, when visible data was available, as well as to the ash dispersion over time seen in consecutive passes. This step will provide the change of the ash area over our temporal range based on the nine different analyses. It will furthermore show the differences in WRF-Chem results caused by altering the PSDs and eruption rate models. In addition, mass cutoffs are analyzed in the WRF-Chem model results to discover the best spatial match to the satellite data. These cutoffs will eliminate areas of low tonnages which are harder for the satellite to identify (ICAO, 2011) and, hence, will likely not appear in the satellite-derived spatial extent. In the satellite data itself, the qualitative comparison will outline the changes in ash-classification based on the different thresholds and the inherent inclusion of more or less noise falsely classified as ash.

4.3.3.2 Qualitative Spatial Comparison

Following the calculation of the total ash extents in model results and satellite data, the degree of overlap between the two approaches has been computed. For this, the Critical Success Index (CSI) was used, as introduced by Stunder et al. (2007). The CSI describes the percentage of pixels correctly identified as containing ash in the model results based on the total number of pixels identified in model and satellite estimates. This states that the satellite-derived mass location is the truth. It is calculated taking into account the 'hits' (AF), the 'misses' (A) and the false alarms (F) (Equation 4.2). With this equation, a perfect match equals a CSI of '1' while a complete mismatch results in a CSI of '0'.

$$CSI = \frac{AF}{A + AF + F} \quad (4.2)$$

In a follow-up study to Stunder et al. (2007) by Webley et al. (2009), variations of this formula were used to calculate over- and underestimates of the match between model and satellite data. Here, an overestimate (OE) is defined as percentage of model area that does not correlate with satellite data (Equation 4.3) and underestimates (UE) as percentage of the satellite-derived ash extent that is not matched by the model (Equation 4.4). These calculations allow us to evaluate the accuracy of the model-satellite comparison.

$$OE = \frac{F}{AF + F} \quad (4.3)$$

$$UE = \frac{A}{AF + F} \quad (4.4)$$

4.3.3.3 Point to Point Comparison

The last step performed in this study is the point to point comparison. For this, five different locations were selected to include overhead the volcano and in the path of the plume and subsequent dispersion ash clouds (see Fig. 4.2B for location of points 1 – 4 and the Sarychev Peak, ‘SP’, location point). At these locations, the ash masses passing overhead were calculated as a function of time. In addition, the percentages that each WRF-Chem ash bin contributed to the total modeled ash mass were analyzed. This approach aims to provide evidence on the timing and the mass loadings of model and satellite data and to determine the dominant ash particle size range with time. Results are given in total tons in the vertical, mapped to be per satellite pixel. As the WRF-Chem grid cells are approximately 37% larger than the satellite pixels, the satellite data is linearly downscaled the model results. For clarity, we only focus on quantitative spatial comparisons for WRF-Chem results using the Plumeria S2/S3 runs.

4.4 Results

WRF-Chem simulations show the ash dispersing, during the four events analyzed in this study, to the north-west, crossing the Sea of Okhotsk reaching the Russian mainland on June 14, 2009. Another arm can be identified to the south-east drifting towards the Pacific Ocean, where it approaches the date line at noon on June 15, 2009 UTC (Figs. 4.3 and 4.4). The spatial extent of the dispersing cloud depends on the wind patterns, while the concentrations are influenced by the initial PSD and the eruption rate used. In the earlier hours of the simulations, the Sparks-determined eruption rate shows higher mass loadings than the Plumeria runs (June 13 and 14, 2009). However, in the later stages of the eruption (June 15, 2009), the mass loadings are much similar in both runs. Similarly, the difference in PSDs is also measureable in the downwind mass loadings. The spatial extent differences seen in Figures 4.3 and 4.4 stem from the scaling. Higher mass loadings down-wind in Figure 4.3 to 4.4 are caused by higher percentages in smaller bins (see PSDs in Table 4.3) and a higher eruption rate (see Table 4.2). These initial differences in the model situations result in a larger extent, when using the mass loading scale, $0 - 10 \text{ g/m}^2$, provided for the respective events.

Analysis of horizontal cross sections through the three-dimensional WRF-Chem ash distribution (Fig. 4.5) reveals parts of the lower altitude ash simulation (5 and 10 km ASL, Fig. 4.5A – 4.5F) being advected to the north-west due to a low pressure system moving from Japan towards the north-east. The remaining ash at 5 and 10 km ASL

heights, along with the ash at higher altitudes (15 km ASL, Fig. 4.5G- 4.5I), is caught in strong trans-Pacific winds causing it to move to the south-east.

4.4.1 Quantitative Spatial Comparison

Analyzing the spatial extent of the satellite data with BTD cutoffs between 0 K and -1.5 K shows a decreasing ash extent, with cutoffs at BTD signals of -1.0 K and -1.5 K producing less than 100,000 km² of ash coverage throughout the time series analyzed. The BTD data with a 0 K cutoff surpasses 650,000 km², Figure 4.6. Manually outlining the ash produces a time series of total area that lies between the cutoffs in the BTD of -0.5 K and -1.0 K.

The quantitative spatial comparison of the ash extent of the four model runs yields similar results for the data when no cutoff is applied. The results show a separation of ash extent between the different PSDs when the best-fitting threshold, as determined by the manual satellite cutoff, is applied (Figure 4.6). The combination runs of PSDs S2 and S3 yield a higher spatial extent throughout the eruption sequence than those with the standard distribution S1. The runs using the different eruption source models (Plumeria and Sparks) don't show a specific trend with the two Plumeria runs resulting, predominantly, in the highest and lowest model extent.

Direct comparison between model results and satellite data in Figure 4.6 shows a larger increase of ash inundation in the model results, without a tonnage cutoff, than in satellite data (dotted, non-blue lines). Comparing only WRF-Chem results with the summed ash masses above a certain threshold with those determined by using the manual cutoff in the satellite BTM images (solid, non-blue lines) results in a similar temporal shape to the time series. The selected cutoff, which shows a best-fit with the satellite ash based on the manually-defined outline, is lower for the S1 runs (10 tons per pixel; 0.54 g/m^2) than for the S2/S3 runs (50 tons per pixel; 2.7 g/m^2). In these scenarios, all WRF-Chem runs, as well as the satellite-determined masses (solid blue line in Fig. 4.6), decrease at approximately 03:00 UTC on June 15, 2009. All other satellite cutoffs (non-solids blue lines in Fig. 4.6) show a different trend throughout the temporal range.

Figure 4.7 shows snapshots of the satellite-derived and model-calculated ash extents at 5 timings from June 13 – 15 2009. These timings show the full extent from the satellite data and all the simulated volcanic ash masses from the modeling. Here, the rapid increase in the modeled ash extent is illustrated, when all ash mass loadings are considered. The spatial coverage increases in all model simulations as well as in the manually outlined ash data after each respective eruptive event.

When comparing the spatial ash extent in the satellite imagery to the WRF-Chem simulation data above the defined threshold, the S2/S3 runs show a closer match to the satellite data in terms of lateral extent than the S1 runs (Fig. 4.6). For simplicity, only the

S2/S3 runs were compared with the cutoffs used in Figure 4.6 to the satellite-derived ash extent (Fig. 4.8). While the satellite-derived ash extent is considerably higher than the WRF-Chem-defined ash extent in earlier snapshots, later scenes show a thin band of ash (about 200 to 400 km long) extending from the northwest of the spatial domain to the southeast in both the satellite- and model-derived ash burden. Specifically during June 14, 2009, a spatial offset can be seen, where the satellite projects the ash further north than the model does. The significance of this offset will be discussed later. At the end of the eruption sequence (June 15, 2009), a complex ash structure is shown to have developed in the satellite data and model results, where an improved spatial match occurs (Fig. 4.8E) than data sets in the previous snapshots (Figs. 4.8A – 4.8D).

In addition to the spatial extent of the ash seen in Figures 4.7 and 4.8, Figures 4.9 and 4.10 both show the extent, at the same time snapshots, with respect to the absolute masses as derived from the WRF-Chem output (Fig. 4.9) and satellite data (Fig. 4.10). The 8-bit color range of the images results in the masses below $(1/2^8)$ of the maximum in that scene not being represented. Due to this, no additional tonnage cutoff was applied. Initial masses over the vent after new events, as seen on June 13, 2009 (22:00 UTC) and June 14, 2009 (20:00 UTC), are very high (2.5 Mt and 261 kt, respectively) and thus the surrounding dispersing masses are not displayed in the 8-bit data. However, once the plume disperses and the maximum mass in the domain reduces significantly as the large ash particles settle out, the relatively low ash masses, that were not displayed

when the peak mass exceeded 2^8 times their amount, are now present once they breach the threshold. To visualize different mass loadings in the imagery on Figure 4.9 and 4.10, we chose not to show the maximum ash mass on the color scale, which would limit the spatial ash extent displayed in the images, but to scale the masses to a subset of the data. The highest ash masses for each scene are listed in the legend.

The satellite-derived masses (Fig. 4.10) show the onset of new eruptive events at June 13, 2009, 21:57 UTC (Event 15, Fig. 4.10A) and June 14, 2009, 19:57 UTC (Event 16, Fig. 4.10D). In addition, follow-up events 19 to 21 can be seen on June 15, 2009, 10:57 UTC (Fig. 4.10E). The majority of the ash is dispersing to the northwest while only a small amount can be seen drifting to the southeast. In the satellite data in Figure 4.10, no BTDC cutoff was applied.

4.4.2 Qualitative Spatial Comparison

The direct quantitative comparison with time of the CSI as well as the OE and UE values between satellite-derived and model-determined ash extents can be seen in Figure 4.11. As a representative model simulation for the comparison to the satellite data, the results from Plumeria with the changing PSD (S_2/S_3) are shown that corresponds to the event-specific PSD and the eruption rate incorporating atmospheric parameters. CSI values were derived for the cases with matching timings between model and satellite data (marked with 'x' in Fig. 4.11). The focus here is on the sequence covering the end of

June 13, 2009 to June 16, 2009, as this shows a better temporal match between satellite and model data due to less data gaps for the acquired satellite imagery. In addition to the absolute ash extent comparison (Fig. 4.11A), the CSI, OE and UE values are also computed for a mass cutoff of 50 tons/pixel for the WRF-Chem simulation (Fig 4.11B) that represents the closest match between the absolute values of the WRF-Chem modeled and MTSAT-based ash extents (Fig. 4.7).

The initial CSI value, evaluating the modeled ash cloud against the satellite-derived cloud without the mass threshold, is comparably high at approximately 60% on June 13, 2009 at 23:00 UTC (see blue line in Fig. 4.11A). This value declines to about 15% on June 15, 2009 at 03:00 UTC, shortly after event 16, before increasing again. At the same time intervals, the overestimates increase from 35% to 83% before declining again.

Meanwhile, the UE values range mostly below 10% with a few exceptions of up to 19% (June 14, 2009, 03:00 UTC). These exceptions mainly lie in the early sequence before event 16 occurs.

The time series analysis with the cutoff applied follow a different trend. With the UE starting at over 90%, decreases over the first 12 hours of this comparison, while the CSI and OE values increase simultaneously. At the time of event 16, the CSI hits a low at under 20%, while the UE and OE stand at about 75%. As event 16 disperses, UEs and OEs

decrease, with the CSI climbing up to 50% before those trends are reversed at the end of the time sequence.

4.4.3 Point to Point Comparison

The direct mass comparison between WRF-Chem results and the satellite data at the locations specified in Figure 4.2 and Table 4.2 can be seen in Figures 4.12A through 4.12E. Figure 4.12A, representing the location of Sarychev Peak volcano or 'SP' point, reveals the onsets of the different events. The satellite data shows ash masses peaking at around 200 Tons per pixel for the first three analyzed eruptive events, while WRF-Chem's results simulate event 15 to be most ash-rich (as defined by the input parameters), followed by event 16 and events 13 and 14 are significantly lower at about 500,000 tons. In addition, WRF-Chem returns values of up to 60×10^6 tons, whereas identically timed satellite measurements only get up to 190 tons per pixel. The WRF-Chem ash bins attributing most to this signal are bins 5 and 6 (31.25 - 125 μ m). Especially shortly after each event, bin 5 dominates the airborne ash masses, closely followed in time by bin 6 being the dominate particle size within the WRF-Chem ash simulated mass loadings (Fig 4.12A, bottom panel). In the later stages of the eruption, these peaks make up between 90 and 100% of the total modeled ash mass seen over location the volcano. After all events have occurred, bin 7 (15.625 - 31.25) increases its relative abundance,

constituting nearly all of the model ash masses from WRF-Chem at the end of the temporal range observed.

Figures 4.12B through 4.12E represent data from locations to the west and the east of the volcano (see Fig. 4.2 and Table 4.2 for their location information). The time series to the west shows the WRF-Chem modeled ash masses on average about 100-times larger than measured with the satellite data. Location '1' (Fig. 4.12B), to the far west, has similar onsets for both datasets. The peak retrieved ash mass in the satellite data (up to 55 tons) occurred over a 12 hour period, while WRF-Chem has a narrow peak of 4600 tons at 05:00 (UTC) on June 14, 2009 with an almost equal volcanic ash mass between the peaks (200-300 tons). Similar to location 'SP', WRF-Chem masses are considerably higher than satellite derived masses, about 100 to 200 times for the majority of the time series. Major contributors to this mass are WRF-Chem ash bins 6 and 7 (15.625 – 62.5 μm), Figure 4.12B bottom panel. The time series shows bin 7 representing the majority of the ash masses at this location between June 13 and 14, 2009 (UTC) and onwards from June 15, while bin 6 reaches between 90 and 100% contribution to the total mass during most of June 14 until early June 15, 2009.

A similar trend can be seen at location '2' (Fig. 4.12C). This location, also to the west of the vent, shows a similar time frame for ash masses to be detected by satellite and model data, although the initial model onset was about 8 hours later (June 14, 2009,

00:00 UTC). The peak masses calculated with WRF-Chem (41,000 tons, for event 15) consisted mostly of bins 6 to 8 (7.8125 - 15.625 μm) each bin with similar amounts, while bin 6 dominates the dispersing cloud between the onset of the events, especially during the later stages (June 14 and 15, 2009). Only the passing of event 16 at location '2' (June 15, 2009, 03:00 UTC) brings coarser ash from the bins 6 and 7.

At locations '3' and '4' (Figs. 4.12D and 4.12E), a different phenomenon is observed. While WRF-Chem predicts large peaks of 33 and 22 kt respectively, the satellite detects essentially no ash over the whole time series. These WRF-Chem peaks coincide with the dominance of bin 6. Snapshots coinciding with different phases of the eruption sequence can be seen in Figures 4.7 to 4.10. These timings are also highlighted in Figures 4.12A to 4.12E.

4.5 Discussion

The qualitative comparison between WRF-Chem and satellite data in terms of volcanic ash highlights strengths and weaknesses in this approach. The initial qualitative match between absolute ash extent in satellite-determined ash with a manual cutoff and total WRF-Chem ash extent shows that the majority of the volcanic ash as indicated by the satellite data falls in the total WRF-Chem extent (Fig. 4.7). However, once the mass cutoff in the model data, based on the best match between absolute extents in model and satellite data as shown in Figure 4.6, is applied, the satellite-derived ash shows a

similar shape to the model-calculated one, but with an offset to the north (Fig. 4.8). This change in the data, utilizing the mass cutoff, can also be seen in the CSI, OE and UE values (Fig. 4.11). In the data where the mass cutoff was used, the UEs are very high (> 50% for the majority of the temporal range) indicating that more than half of the ash determined by the satellite data was outside the region specified through WRF-Chem. This is especially true at the beginning, with the UE values reaching 90% but is expected, as ash from previous events will be detectable by satellite data but not seen in this WRF-Chem study, limiting WRF-Chem's accurateness and potential for operational purposes.

On the other hand, the OE values peak at the center of the time series (June 15, 2009, 00:00 UTC) at about 80% but are below 40% for most of the other time periods. This peak represents a large portion of the WRF-Chem ash extent being projected outside the satellite-defined region and can also be seen in Figure 4.8 on June 14, 2009, at 20:00 UTC. Towards the end of the time series, the CSI reaches approximately 50% showing a good match between model and satellite data (compared to other studies using the CSI like Webley et al., 2009). A factor that can cause such an offset, and that has not been included in this analysis, is the satellite's position and its line of sight. MTSAT is located geostationary at 140°E and therefore measures the radiant signal along its satellite zenith angle, rather than at a true nadir and hence, once mapped to the 2-dimensional plan view, it will offset the dispersing ash to the northeast. Hence, while the results

from the WRF-Chem simulations are shown as the ash vertically above the given locations, the satellite data will show an offset to the northeast.

The timings of the different events at the vent analyzed in this study match well (Fig. 4.12A) but despite correcting for the different pixel sizes, the masses derived by WRF-Chem are considerably higher than the satellite-derived ones. Especially in Figures 4.12D and 4.12E, this becomes obvious where WRF-Chem predicted a tonnage of up to 33,000 and 24,000 tons respectively but the satellite essentially detected no ash. There are, however, multiple factors that can result in this mismatch. Despite the previously mentioned satellite offset, the Kuriles and especially the domain chosen for this study was very cloudy during the course of the eruption (see Fig. 4.2B for an example) and meteorological cloud coverage will undermine the satellite ash retrievals resulting in a higher noise level (Pavolonis et al., 2006). This is also the case during the eruption. Figure 4.2B shows the cloud coverage for one defined timing and this phenomena was consistently the case throughout the eruption and so only the ash above these meteorological clouds is detectable from satellites. Still, the area of satellite-predicted ash in Figures 4.7 and 4.8 shows multiple gaps as a result of meteorological clouds overlying even the higher portions of the volcanic ash.

Another reason for the different mass retrievals is the sensitivity of VAR to different particle sizes. VAR can only correctly identify ash if the effective radius, the ratio between skewness and variance of a log normal distribution of ash where low values

indicate a high proportion of fine particles in a pixel, at that location is below $10\ \mu\text{m}$ (Wen and Rose, 1994). The majority of the WRF-Chem-predicted ash does not meet this criterion and hence the ash mass detected in the satellite data is likely lower than the actual amount. The ash results and calculated masses based on the satellite originates dominantly out of WRF-Chem bins 8 through 10 ($< 15.625\ \mu\text{m}$), bins that don't contribute greatly to the WRF-Chem signal (Figs. 4.12A to 4.12E). Especially at the volcano location (Fig. 4.12A), a large overestimate in WRF-Chem compared to the satellite can be seen. Here, the initial plume is emitted and the WRF-Chem bins attributed to it are those with large particles (Table 4.1). Consequently, the WRF-Chem masses are much higher than the masses measured in infrared satellite images. Given that the plume is dominated by larger particles, the satellite data will be an underestimation.

In addition, the ash in the satellite's line of sight must cover at least 500 m to cause a significant signal in the data (ICAO, 2011). In Figures 4.7 and 4.8, the last and the first two timings show satellite ash at location '3'. The total mass, based on WRF-Chem, consisted mainly of WRF-Chem bins 6, 7 and 8, with bin 6 having settled out by 07:00 UTC on June 15, 2009, leaving only the finer bins to contribute to the modeled cloud (Fig. 4.12D). The same effect is also seen in Figure 4.12A, where bin 5 has a spiked increased contribution after each event, closely followed by bins 6 and 7 contribution reaching their peaks, when the respective coarser bins have settled out. As the modeled

thickness of the cloud at 07:00 UTC on June 14, 2009 (UTC) at location '3' is greater than 500 m (Fig. 4.13) for the defined PSD and E_r used in these cases, this indicates that the bins still contributing to the dispersing cloud at this timing produce an effective radius too large to be identified with VAR. Additional ground-based data would be needed to confirm this.

A similar effect explains the narrow peak in WRF-Chem predicted ash in location '1' at 12:00 UTC on June 14, 2009, while the satellite shows a broader temporal range of ash (Fig. 4.12B). This location shows evidence of some meteorological cloud coverage above the volcanic ash clouds, as seen by the gaps in the satellite data in Figures 4.7 and 4.8. These gaps result in the 'saw-tooth' shaped time series for the satellite-determined ash in Figure 4.12B. The timings of satellite-detected and model-derived ash burden passing above location '2' are similar but the main increase for WRF-Chem is not detected in the satellite infrared data. The WRF-Chem bins contributing most to this increase in the ash masses are bins 6 and 7 (15.625 – 62.5 μ m). The dominant meteorological cloud cover will obscure some of the signal seen in the satellite data, but the effective radius, resulting from the particle sizes present, as seen in WRF-Chem modeled results, is likely too large to be detected by VAR. WRF-Chem shows the total thickness of the plume is greater than 500m (Fig. 4.14), given the PSD and E_r used in these cases, and as such is likely to provide a detectable signal in satellite images.

Figures 4.9 and 4.10 show a comparison between the mass distributions based on WRF-Chem modeled ash cloud and satellite data. Despite showing a relatively good match in absolute shape, although an offset, in Figure 4.8, Figures 4.9 and 4.10 do not compare well. WRF-Chem predicts the majority of the ash to be in the southeast, while satellite data shows it drifting mainly to the northwest. Based on the slices through the model domain of wind speed and direction (Fig. 4.5), the highest atmospheric layers can be seen distributing the ash to the southeast, while lower layers ≤ 10 km ASL showed a northwest transport. Based on this, the initial vertical structure of ash in the plume, assumed here to be poisson-distributed, attributed too much ash to the top layers, while underestimating the ash burden of the lower sections. Further work with uniform vertical distributions and varying the location of the dominant ash masses in the vertical distribution are needed to assess this dependency on the vertical distribution and dispersion pattern.

This offset, seen in Figure 4.8, stems from the satellite receiving radiation over its viewing angle as compared to the model that summarizes the ash vertically above each location. Figure 4.15 shows a simplification of this problem. When comparing the different paths through the ash plume and consequent ash cloud, different ash concentrations can be encountered based on viewing angle, as well as varying thicknesses. This will lead to a change in derived ash masses when comparing true vertical to satellite viewing-angle. While a simply shift of the satellite plume to the

south-west (in this study) can improve the spatial correlation the point-to-point comparison will still be inaccurate. For an overall improvement of the quantitative comparison, ray-tracing of the satellite's path has to be performed and at each vertical model level, the grid cells closest to the satellite's line of sight have to be summarized.

In addition, the VAR retrievals and WRF-Chem simulation both require a range of input parameters and case studies have shown that especially the brightness surface and cloud top temperatures are crucial values for VAR (Steensen and Webley, 2012). Using a default parameter for the whole satellite scene will introduce errors, but this is the only option if a more detailed analysis is not available. The sensitivity of the different WRF-Chem input parameters, such as vertical distribution, initial PSD and eruption rate, has not been studied to date but varying the eruption rates in this study shows only a small change in derived ash extent (Fig. 4.6). The main difference between these particle size distributions is the amount of ash in the finer bins (Table 4.3).

Figure 4.6 also shows the necessity of outlining the plume, illustrated here by a manual analysis from MTSAT's two band TIR data, to obtain the best estimate of the ash masses. The automatic delineations between the BTD threshold of 0 K (the standard default value) to the minimum value analyzed here (-1.5 K) all show peaks at similar locations. These are more pronounced at higher BTD cutoff values, but all occur at locations where the model data does not show a peak. This is due to cloud coverage (Fig. 4.2B), which can produce negative BTD values (Pavolonis et al., 2006). An automated outline on the

two band data, with a zero BTD cutoff, will classify those as ash, therefore introducing errors. The maximum extents of the manually outlined ash, however, coincide with the WRF-Chem calculated peaks.

Additional complications for the satellite to model comparison stem from the choice of the retrieval parameters in VAR. Figure 4.12A shows that the first three analyzed eruptive events reached approximately the same tonnage (190 tons in one MTSAT pixel) during the respective early stages which, based on plume heights and event durations (Table 4.1), cannot be the case. However, with constant surface and cloud top brightness temperatures/radiances, VAR has a maximum mass that can be retrieved (see discussion in Wen and Rose, 1994). There have been no concrete studies as to what this maximum tonnage is for different input parameter ranges but because of the similar tonnages, while changing heights and durations, it is likely that 190 tons per MTSAT pixel is the upper limit for the retrievable amount of ash using VAR with the parameters used in this study.

Another reason for the big difference is the penetration depth of the satellite retrievals, especially in cloudy regions like the Kuriles. If the ash is above a thick layer of meteorological clouds, the surface brightness temperature is sufficiently scattered and will not be detectable at the satellite (ICAO, 2011). The 'surface' brightness temperature to be used in this case is that of the highest layer of meteorological clouds

and not that of the actual surface. Lastly, if aggregation takes place, a feature not included within WRF-Chem, the particles would settle out at a faster rate as the particles aggregated. Without this process, the discrepancy between satellite and model data will therefore increase. Further work is needed to assess the effect of aggregation on the modeling results shown here.

4.6 Conclusions

Sarychev Peak Volcano erupted in June 2009 and had 23 separate explosions. Events 13 – 16 on June 13 – 14 2009 (see Table 4.1) were examined and compared the infrared satellite derived volcanic ash masses with those from an Eulerian VATD model, WRF-Chem. For the modeling, simulations were performed using two different particle size distributions and two different eruption rate models. For the eruption rate analysis, one used an empirical relationship of plume height and eruption rate (from Sparks et al., 1997) and the other using an atmospheric profile including temperatures and humidity above the vent to ascertain a likely eruption rate from the measured plume height (see Plumeria; Mastin, 2007). The model results were compared to the satellite measurements of volcanic ash over the same spatial and temporal domains.

The analysis results indicated that, with the input parameters chosen here, the eruption rate model is of negligible importance for a qualitative spatial comparison if a zero threshold in the model data is applied, while a change in the particle size distribution

can result in substantial changes to the predicted ash extent (Fig. 4.6). Those changes in spatial extent, however, represent the qualitative definition of boundary values based on the color bars. A change in actual extent of the plume does not occur as the ash will be advected based on the wind fields and only concentrations change with varying eruption rate and particle size distributions. A correct estimate of the particle size distribution, while taking account of aggregation, is crucial to predict masses that match with those derived from in the satellite data.

The ash masses calculated from the WRF-Chem model and satellite data over five different locations show a good temporal match but differ in the magnitude of the derived masses by a factor of 100 (Fig. 4.12B) up to 300,000 (Fig. 4.12A). These large differences occur as a result of sensitivity limitations in the satellite data, initial PSD and E_r chosen, meteorological cloud coverage and the geometric setting between satellite and dispersing ash. This is especially the case at locations '3' and '4' (Figs. 4.12D and 4.12E), where WRF-Chem predicts clouds with up to 33,000 tons but the satellite only shows background noise. There are different reasons that can cause this discrepancy, both in the WRF-Chem model and satellite input parameters as well in the geometrical setting of the scene.

4.6.1 Input and Model/Retrieval Parameter

The input parameters for VAR with the two band TIR data, as described in Steensen and Webley (2012), can result in strong over- or underestimates, if they are accessed incorrectly. This is especially true for the brightness temperatures of the surface and the cloud top, derived from the radiant signal of the satellite retrievals. In this study, these two variables were held constant due to a lack of detailed observations and access to multi-spectral data with sufficient temporal frequency. Other parameters including refractive indices of ash and air and the specific gravity of ash also have a significant influence on the retrieval (see Steensen and Webley, 2012) but often require in-situ measurements to be defined accurately.

Similarly, the BT_D threshold for the reverse absorption should be kept as 0 K to determine as much as possible the full ash cloud extent, but the cloud must be manually outlined in the two band TIR data to obtain best results if no further advanced algorithms (see Pavolonis and Sieglaff, 2010) can be used. Such advanced algorithms cannot be applied to MTSAT data and hence a manually determined ash spatial extent was used. An automatically determined 0 K BT_D threshold for the whole satellite dataset will drastically increase the calculated masses due to high noise levels, especially in a cloudy region like the Kuriles. Even an eruption-tailored cutoff will include a small amount of noise at the expense of missing parts of the ash cloud that are just below a 0

K BTD threshold, the part that often is associated with the largest masses (Wen and Rose, 1994) as the cloud starts to become translucent.

Similar sensitivities exist for the WRF-Chem model. A particle size distribution, generally assigned by consideration of the VEI and the top height of the initial plume (Mastin et al., 2009), can easily overestimate the finer particle fraction due to the missing aggregation in WRF-Chem. This causes the bin percentages to only change due to fallout and smaller particles will remain airborne longer than the actual ash transport from the eruption. In addition, Figures 4.12A to 4.12E show that the WRF-Chem bins with particle sizes of 15.625 μm or greater are not identified by VAR, likely because the larger particles were evident at those timings causing VAR to be unable to resolve the ash efficiently as the size range between 0 and 100 μm , the size range VAR analyzes in (Wen and Rose, 1994), did not dominate the signal. A careful consideration of the initial particle size distribution used in terms of initial and post-aggregation percentages as well as the range compared to satellite imagery is necessary for satellite to model comparisons.

For the eruption rate models used, this study does not show a clear advantage of one over the other, despite the fact that Plumeria takes account of the actual atmosphere.

For the spatial comparison (Fig. 4.6), no clear distinction between the models is noticeable for a zero cutoff in the WRF-Chem masses. In the case of Sarychev Peak

eruption and with our list of input parameters, a more detailed targeting of WRF-Chem bins and particle size distributions is necessary to be able to favor either Plumeria or the empirical relationship by Sparks et al. (1997). Another important factor to be considered is the vertical structure of the initial plume. As seen in Figures 4.9 and 4.10, WRF-Chem predicted much higher masses, relative to the satellite data, going to the southeast, which, in reality based on the satellite data, drifted to the northwest. Based on the wind profiles at different altitudes (Fig. 4.5), the overestimate in WRF-Chem lies in the higher altitudes, whereas lower levels are not attributed with sufficient ash mass. A correct vertical distribution, however, is hard to assume without in-situ data or previous model runs.

4.6.2 Model Limitations and Geometrical Setting

Besides the uncertainties associated with the input parameters, VAR has internal limitations that restrain the actual mass estimates as described in Wen and Rose (1994). These include the assumption of a thin, homogenous ash layer and an otherwise cloud-free atmosphere. Both cases represent an idealized atmosphere and therefore, in a realistic setting, it is very likely that the Volcanic Ash Retrieval will not take into account the full ash distribution from the respective event. If a spectrally opaque cloud layer is below the ash, the radiant signal from this layer causes the ash signal. In this case, the

'surface' brightness temperature of this layer needs to be taken into account for VAR and not that of the actual surface.

Multiple ash layers also complicate the retrieval and a radiative transfer model like MODTRAN5 (Moderate Resolution Atmospheric Transmission 5; Berk et al., 2003) needs to be run to estimate the scattering and absorption effect with altitude to outline the ash masses. Other limitations include different sensitivities for different size ranges depending on the wavelengths used and a limiting maximum value derived (see Fig. 4.12A). This results in a large overestimate of masses in WRF-Chem data, if compared to satellite estimates, especially in the case of early initial events. In addition, the satellite needs at least 500 m of volcanic ash in the line of sight (ICAO, 2011) and an effective radius of the ash particles less than 10 μm (Wen and Rose, 1994) to identify the ash. This was the case at locations '3' and '4' (Figs. 4.12D and 4.12E) and at the peak at location 'SP' (June 14, 07:00 UTC, Fig. 4.12A), where WRF-Chem showed a significant peak in the derived masses that the satellite didn't detect. Consequently, the ash masses calculated from the satellite data are an underrepresentation of the actual masses, whereas WRF-Chem treats all airborne particle sizes equally (through its defined size bins) and counts all of them in the final product and so is likely an overestimate.

Additional complications arise from the geometrical setting. Sarychev Peak volcano is located at about 48°N and 153.2°E, while the MTSAT is geostationary above the equator at 140°E. WRF-Chem calculations measured the mass vertically through the model domain, but the satellite records the thermal radiance at sensor and so the cloud will appear to be offset at an angle of over 56°, when mapped to a 2-dimensional plan view. Therefore, the satellite has a different line of sight than the model and the signal is potentially influenced by factors (and hence ash masses) out of the model's vertical view.

The difference between pixel sizes in the model and satellite outputs can also cause problems for the direct quantitative comparison at different locations. In this case study, the WRF-Chem simulations had a grid with had a pixel size of 25 km², while the satellite data at nadir was approximately 16 km². Based on the trigonometric settings described above, this results in an approximate pixel size of 18.23 km² at the volcano's location, about 73 % of the grid size in the WRF-Chem domain. A linear correction has been applied to the WRF-Chem data to match the satellite's footprint and to correct for this discrepancy in this study.

4.6.3 Future Work

This work has shown promising results for a direct, quantitative comparison between WRF-Chem and satellite data but also outlined areas to focus on in future studies. The major points to address in upcoming research should be:

- 1) Individual pixel-based estimates of surface brightness temperatures/radiant signals as VAR input
- 2) Calculation of effective radii in WRF-Chem results to compare only relevant data to VAR
- 3) Estimate of particle size distribution that includes aggregation and is not solely based on the VEI and initial plume height
- 4) Correction for line-of-sight in satellite measurements to calculate WRF-Chem masses
- 5) Determination of the eruption rate and vertical profile based on multiple atmospheric profiles and for different eruptions to estimate the importance of this input parameter

In addition, a deliberate overestimation of masses by changing the input parameters of VAR accordingly (for details see Steensen and Webley, 2012) should be evaluated on a case-by-case basis to balance VAR underestimates due to natural factors like cloud coverage. With these guidelines, a better spatial and temporal comparison between

satellite and model data can be achieved which, in turn, will result in a better performance of WRF-Chem to forecast volcanic ash distributions during an eruption.

4.7 Acknowledgements

This publication is the result in part of research sponsored by the Cooperative Institute for Alaska Research with funds from the National Oceanic and Atmospheric Administration under cooperative agreement NA080AR4320751 with the University of Alaska. In addition, we thank the Alaska Volcano Observatory for providing the satellite data. The Alaska Volcano Observatory (AVO) is a joint program of the United States Geological Survey (USGS), the Geophysical Institute of the University of Alaska Fairbanks (UAFGI), and the State of Alaska Division of Geological and Geophysical Surveys (ADGGS). Finally, we thank the Arctic Region Supercomputing Center for providing the processing time and data storage space on their supercomputers for the WRF-Chem modeling.

4.8 References

Berk, A., G. P. Anderson, P. K. Acharya, L. S. Bernstein, M. Fox, S. M. Adler-Golden, J. H. Chetwynd, M. L. Hoke, and P. E. Lewis (2003), MODTRAN5: A Reformed Atmospheric Band Model with Auxiliary Species and Practical Multiple Scattering Options, edited by A.F.R.L, p. 9, Hanscom Air Force Base, MA.

Blong, R.J. (1984), *Volcanic hazards: a sourcebook on the effects of eruptions*. Academic Press, Sydney, 424 p.

Casadevall, T. J. (1994), The 1989-1990 Eruption of Redoubt Volcano, Alaska - Impacts on Aircraft Operations, *Journal of Volcanology and Geothermal Research*, 62(1-4), 301-316.

Dehn, J., K. G. Dean, K. Engle, and P. Izbekov (2002), Thermal precursors in satellite images of the 1999 eruption of Shishaldin Volcano, *Bulletin of Volcanology*, 64, 525-534.

Draxler, R. R., and G. D. Hess (1997), Description of the Hysplit_4 Modeling System, *NOAA Technical Memorandum ERL ARL-224*.

Freitas, S. R., K. M. Longo, M. F. Alonso, M. Pirre, V. Marecal, G. Grell, R. Stockler, R. F. Mello, and M. S. Gacita (2011), PREP-CHEM-SRC-1.0: a preprocessor of trace gas and aerosol emission fields for regional and global atmospheric chemistry models, *Geoscientific Model Development*, 4(2), 419-433.

Gangale, G., A. J. Prata, and L. Clarisse (2010), The infrared spectral signature of volcanic ash determined from high-spectral resolution satellite measurements, *Remote Sensing of Environment*, 114(2), 414-425.

Grell, G. A., S. E. Peckham, R. Schmitz, S. A. McKeen, G. Frost, W. C. Skamarock, and B. Eder (2005), Fully coupled "online" chemistry within the WRF model, *Atmospheric Environment*, 39(37), 6957-6975.

Hanstrum, B. N., and A. S. Watson (1983), A case study of two eruptions of Mount Galunggung and an investigation of volcanic eruption cloud characteristics using remote sensing techniques, *Australian Meteorological Magazine*, 31, 171-177.

International Civil Aviation Organization [ICAO] (2011), International Volcanic Ash Task Force (IVATF), Second Meeting, Montréal, 11 to 15 July 2011.

Kratzmann, D. J., S. N. Carey, J. Fero, R. A. Scasso, and J. A. Naranjo (2010), Simulations of tephra dispersal from the 1991 explosive eruptions of Hudson volcano, Chile, *Journal of Volcanology and Geothermal Research*, 190 (3-4), 337-352.

Levin, B. W., A. V. Rybin, N. F. Vasilenko, A. S. Prytkov, M. V. Chibisova, M. G. Kogan, G. M. Steblov, and D. I. Frolov (2010), Monitoring of the Eruption of the Sarychev Peak Volcano in Matua Island in 2009 (Central Kurile Islands), *Dokl. Earth Sci.*, 435 (1), 1507-1510.

Mastin, L. G. (2007), A user-friendly one-dimensional model for wet volcanic plumes, *Geochemistry Geophysics Geosystems*, 8.

Mastin, L. G., M. Guffanti, R. Servranckx, P. Webley, S. Barsotti, K. Dean, A. Durant, J. W. Ewert, A. Neri, W. I. Rose, D. Schneider, L. Siebert, B. Stunder, G. Swanson, A. Tupper, A. Volentik, and C. F. Waythomas (2009), A multidisciplinary effort to assign realistic source parameters to models of volcanic ash-cloud transport and dispersion during eruptions, *Journal of Volcanology and Geothermal Research*, 186 (1-2), 10-21.

Matoza, R. S., A. Le Pichon, J. Vergoz, P. Herry, J.-M. Lalande, H. Lee, I.-Y. Che, and A. Rybin (2011), Infrasonic observations of the June 2009 Sarychev Peak eruption, Kuril Islands: Implications for infrasonic monitoring of remote explosive volcanism, *Journal of Volcanology and Geothermal Research*, 200, 35-48.

Newhall, C. G., and S. Self (1982), The Volcanic Explosivity Index (VEI) – An Estimate of Explosive Magnitude for Historical Volcanism, *Journal of Geophysical Research-Oceans and Atmospheres*, 87(NC2), 1231-1238.

Pavolonis, M., and J. Sieglaff (2010), GOES-R Advanced Baseline Imager (ABI) Algorithm Theoretical Basis Document for Volcanic Ash (Detection and Height), *NOAA NESDIS Center for Satellite Applications and Research*.

Pavolonis, M. J., W. F. Feltz, A. K. Heidinger, and G. M. Gallina (2006), A daytime complement to the reverse absorption technique for improved automated detection of volcanic ash, *Journal of Atmospheric and Oceanic Technology*, 23(11), 1422-1444.

Prabaharan, D. J. (2002), Fear of Flying, *GIS User*, 50, 2.

Prata, A. J. (1989), Observations of Volcanic Ash Clouds in the 10-12 μm Window Using AVHRR/2 Data, *International Journal of Remote Sensing*, 10 (4-5), 751-761.

Prata, A. J., I. J. Barton, R. W. Johnson, K. Kamo, and J. Kingwell (1991), Hazard From Volcanic Ash, *Nature*, 354 (6348), 25-25.

Prata, A. J., and I. F. Grant (2001), Retrieval of microphysical and morphological properties of volcanic ash plumes from satellite data: Application to Mt Ruapehu, New Zealand, *Quarterly Journal of the Royal Meteorological Society*, 127(576), 2153-2179.

Rybin, A., M. Chibisova, P. Webley, T. Steensen, P. Izbekov, C. Neal, and V. Realmuto (2011), Satellite and ground observations of the June 2009 eruption of Sarychev Peak volcano, Matua Island, Central Kuriles *Bulletin of Volcanology*, 73 (9), 1377-1392.

Schneider, D. J., W. I. Rose, and L. Kelley (1995), Tracking of 1992 Eruption Clouds from Crater Peak Vent of Mount Spurr Volcano, Alaska, Using AVHRR, *U. S. Geological Survey Bulletin*, 2139, 27-36.

Searcy, C., K. Dean, and W. Stringer (1998), PUFF: A high-resolution volcanic ash tracking model, *Journal of Volcanology and Geothermal Research*, 80 (1-2), 1-16.

Skamarock, W. C., and J. B. Klemp (2008), A time-split nonhydrostatic atmospheric model for weather research and forecasting applications, *J. Comput. Phys.*, 227(7), 3465-3485.

Sparks, R.S.J., Bursik, M.I., Carey, S.N., Gilbert, J.S., Glaze, L.S., Sigurdsson, H., Woods, A.W., (1997), *Volcanic Plumes*. John Wiley & Sons, Chichester.

Steensen, T. and Webley, P. (2012), Qualitative Analysis of Input Parameters for Satellite-Based Quantification of Airborne Volcanic Ash, *Geoscience and Remote Sensing Symposium (IGARSS), 2012 IEEE International* , Pages 2982 – 2985, 10.1109/IGARSS.2012.6350799.

Steensen, T., M. Stuefer, P. W. Webley, G. Grell and S. Freitas (2013), Qualitative comparison of Mount Redoubt 2009 volcanic clouds using the PUFF and WRF-Chem dispersion models and satellite remote sensing data, *J. Volcanol. Geotherm. Res.*, 259, 238-247, doi:10.1016/j.jvolgeores.2012.02.018.

Stuefer, M., Freitas, S. R., Grell, G., Webley, P. W., Peckham, S., and S. A. McKeen (2013), Inclusion of Ash and SO₂ emissions from volcanic eruptions in WRF-CHEM: Development and some applications, *Geoscientific Model Development*.

Stunder, B. J. B., J. L. Heffter, and R. R. Draxler (2007), Airborne volcanic ash forecast area reliability, *Weather and Forecasting*, 22, 1132-1139.

University of Wisconsin (2013), McIDAS User's Guide, Version 2010.2. Available at http://birch.ssec.wisc.edu/mcidas/doc/users_guide/2010.2/app_d-8.html, last accessed on July 25, 2013.

Urai, M., and Y. Ishizuka (2011), Advantages and challenges of space-borne remote sensing for Volcanic Explosivity Index (VEI): The 2009 eruption of Sarychev Peak on Matua Island, Kuril Islands, Russia, *Journal of Volcanology and Geothermal Research*, 208 (3-4), 163-168.

Webley, P. W., B. J. B. Stunder, and K. G. Dean (2009), Preliminary sensitivity study of eruption source parameters for operational volcanic ash cloud transport and dispersion models - A case study of the August 1992 eruption of the Crater Peak vent, Mount Spurr, Alaska, *Journal of Volcanology and Geothermal Research*, 186(1-2), 108-119.

Webley, P. W., T. Steensen, M. Stuefer, G. Grell, S. Freitas, and M. Pavolonis (2012), Analyzing the Eyjafjallajökull 2010 eruption using satellite remote sensing, lidar and WRF-Chem dispersion and tracking model, *Journal of Geophysical Research-Atmospheres*, 117.

Wen, S. M., and W. I. Rose (1994), Retrieval of sizes and total masses of particles in volcanic clouds using AVHRR bands 4 and 5, *Journal of Geophysical Research-Atmospheres*, 99 (D3), 5421-5431.

4.9 Figures

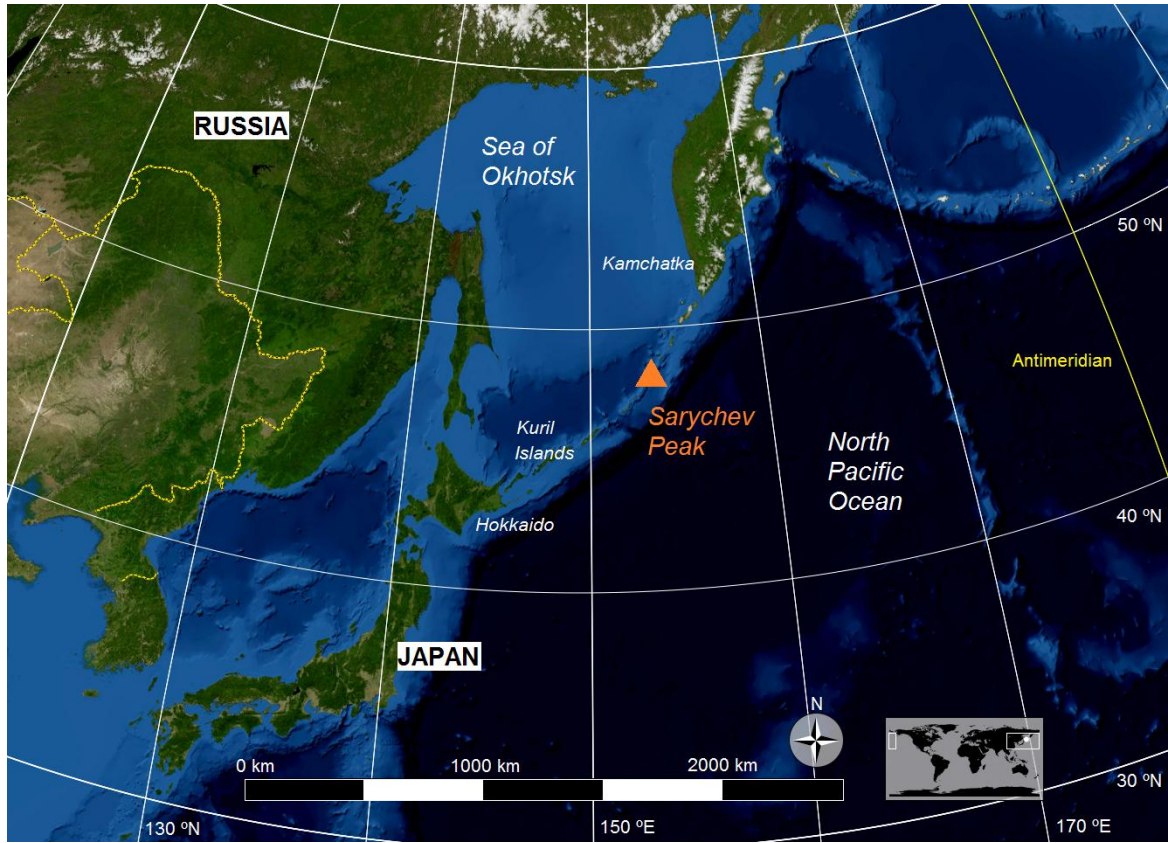


Figure 4.1: Location of Sarychev Peak volcano in the Kuril Islands, Eastern Russia. Courtesy of Marble, the KDE Education Project.

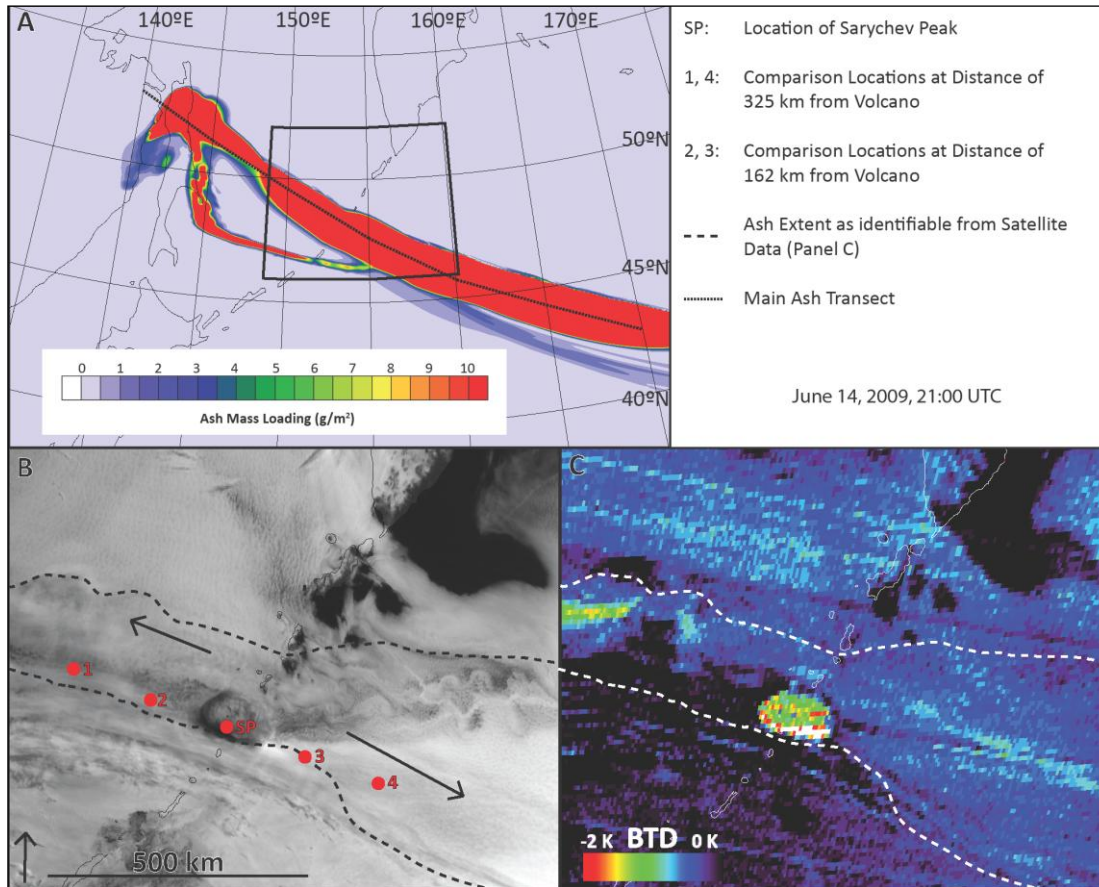


Figure 4.2: Spatial extent of the ash clouds on June 14, 2009, at 21:00 UTC in the Weather Research and Forecast Model with online Chemistry (WRF-Chem, A), in the 0.55 - 0.8 μm channel of the Multifunctional Transport Satellite (MTSAT) with the sample locations for the ash comparison between satellite and model data (B) and the difference between MTSAT's channels IR1 (10.3 - 11.3 μm) and IR2 (11.5 - 12.5 μm) to highlight the ash (Brightness Temperature Difference [BTD] method; C). Geographic locations of the sample locations are listed in Table 4.2. Event 16 can be seen at the vent (Location 'SP') while dispersing ash from previous events is identifiable especially to the west around location '1'. Note the meteorological cloud coverage that prevents volcanic ash below to be detected by satellites. The dashed lines represent the ash extent. The Box in Panel A shows the subset chosen for the analysis (B and C).

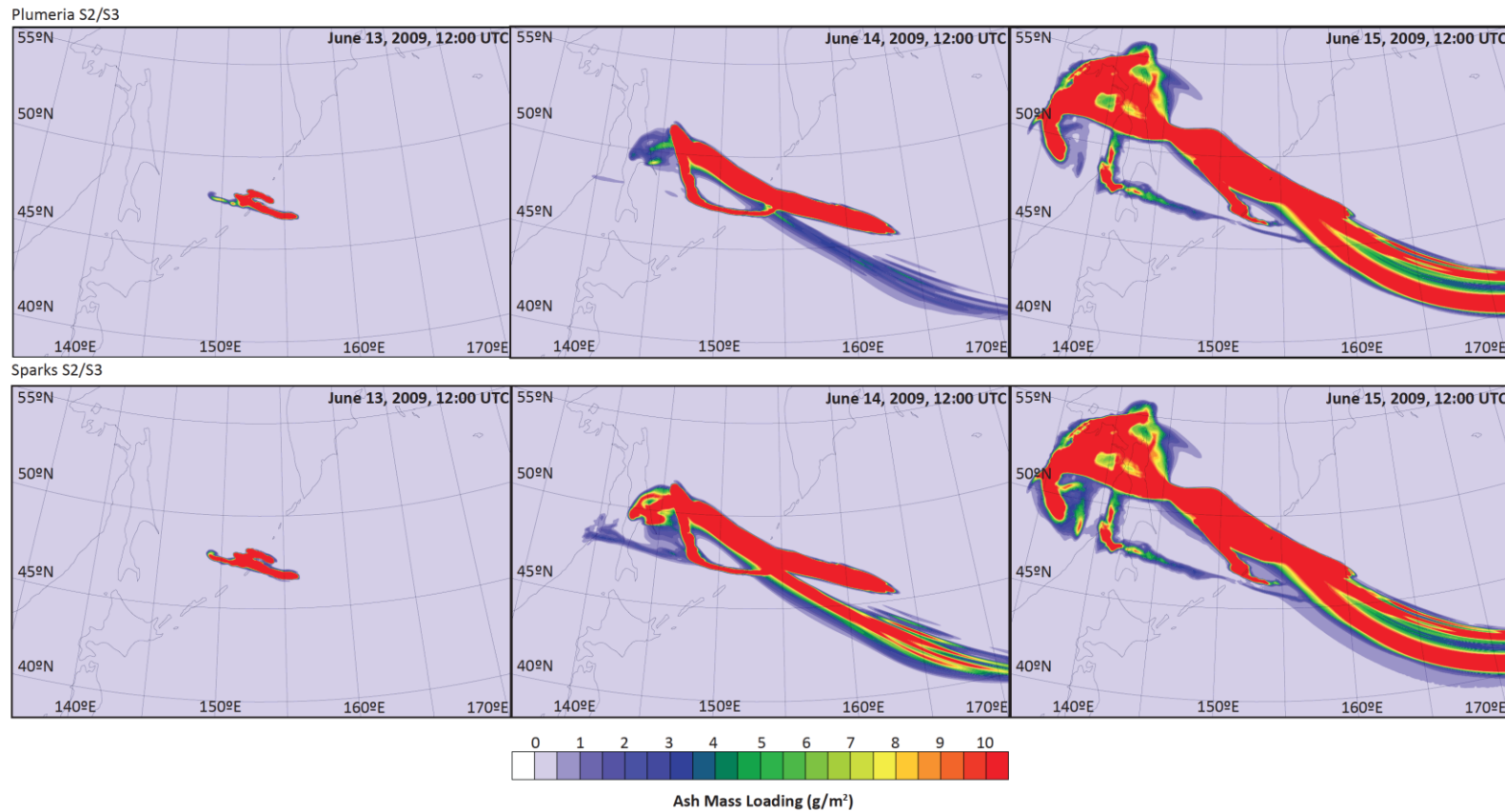


Figure 4.3: Ash dispersion predicted by the Weather Research and Forecast model with online Chemistry (WRF-Chem) using the Plumeria and Sparks-defined eruption rates and the particle size distribution S2/S3 (Table 4.3). The Sparks-defined eruption rate causes an increase in ash extent and mass loading during the earlier stages of the eruption while both model runs show similar results on June 15, 2009.

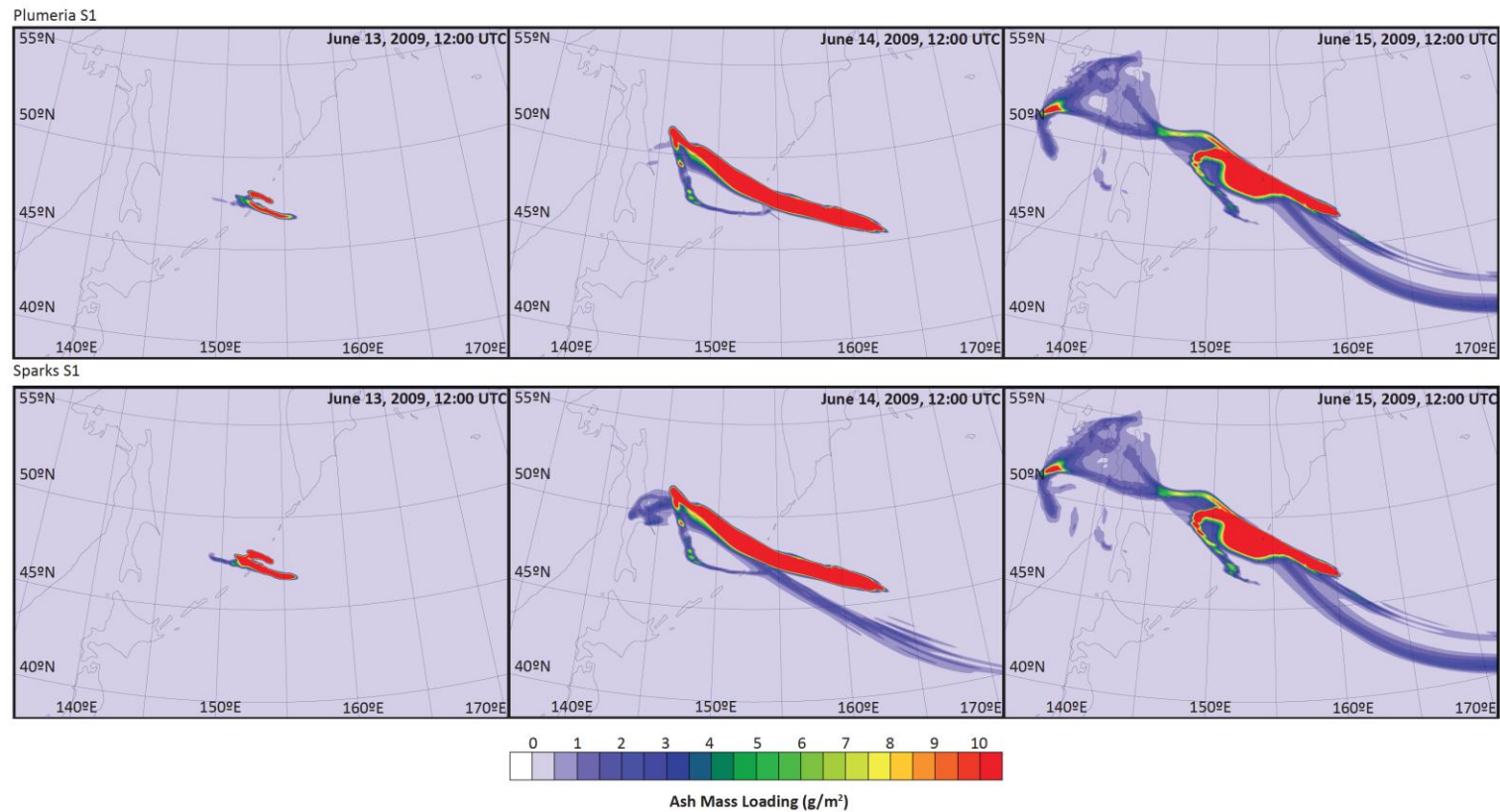


Figure 4.4: Ash dispersion predicted by the Weather Research and Forecast model with online Chemistry (WRF-Chem) using the Plumeria and Sparks-defined eruption rates and the particle size distribution S1 (Table 4.3). The Sparks-defined eruption rate causes an increase in ash extent and mass loading during the earlier stages of the eruption while both model runs show similar results on June 15, 2009.

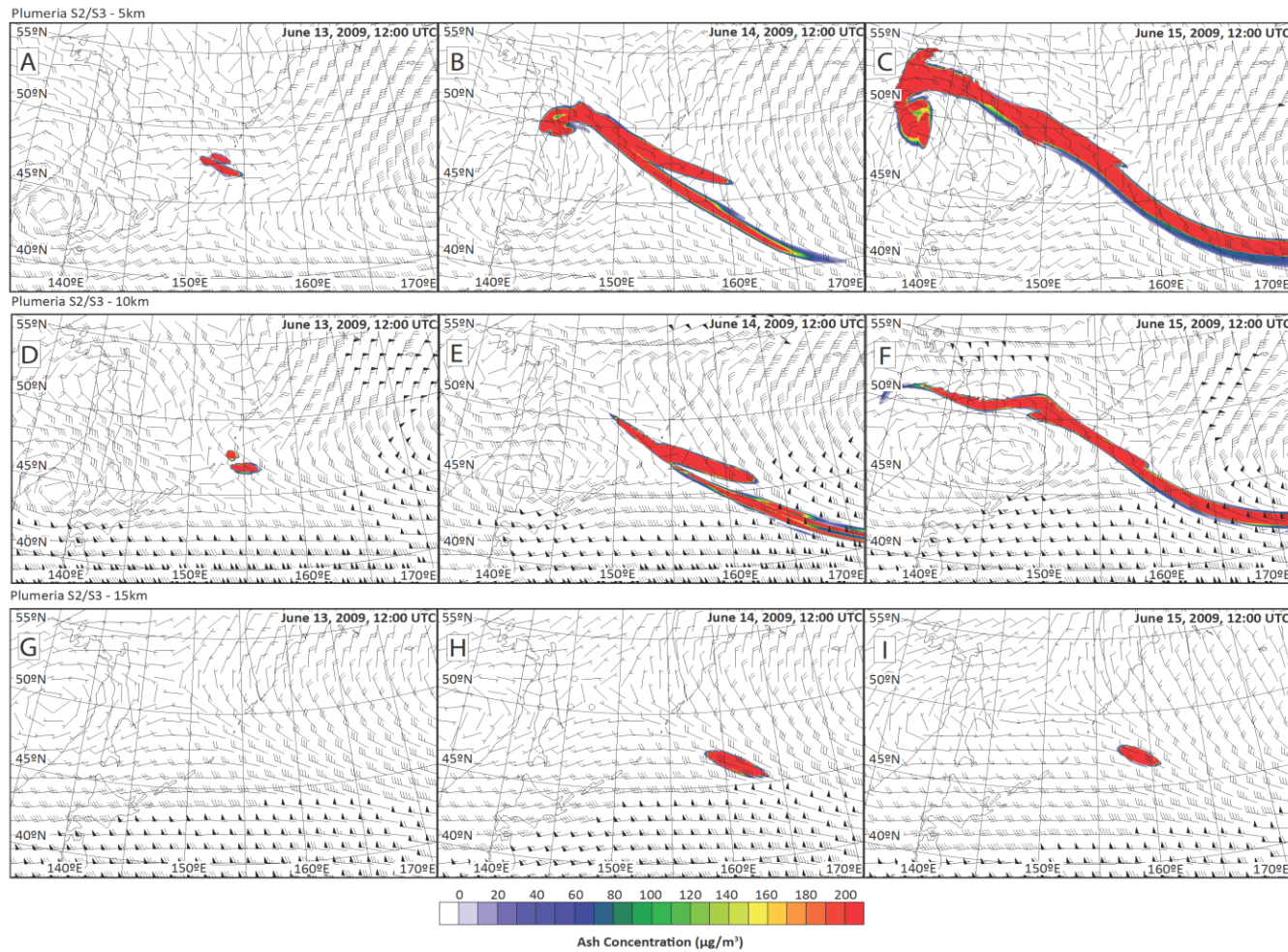


Figure 4.5: Ash concentration and dispersion predicted by the Weather Research and Forecast Model with online Chemistry (WRF-Chem) at different altitudes. A low-pressure system over Japan advects portions of the lower ash (5 and 10 km above sea level) towards the Sea of Okhotsk while the remaining ash at those altitudes and the entire ash at 15 km above sea level is caught in strong trans-Pacific winds.

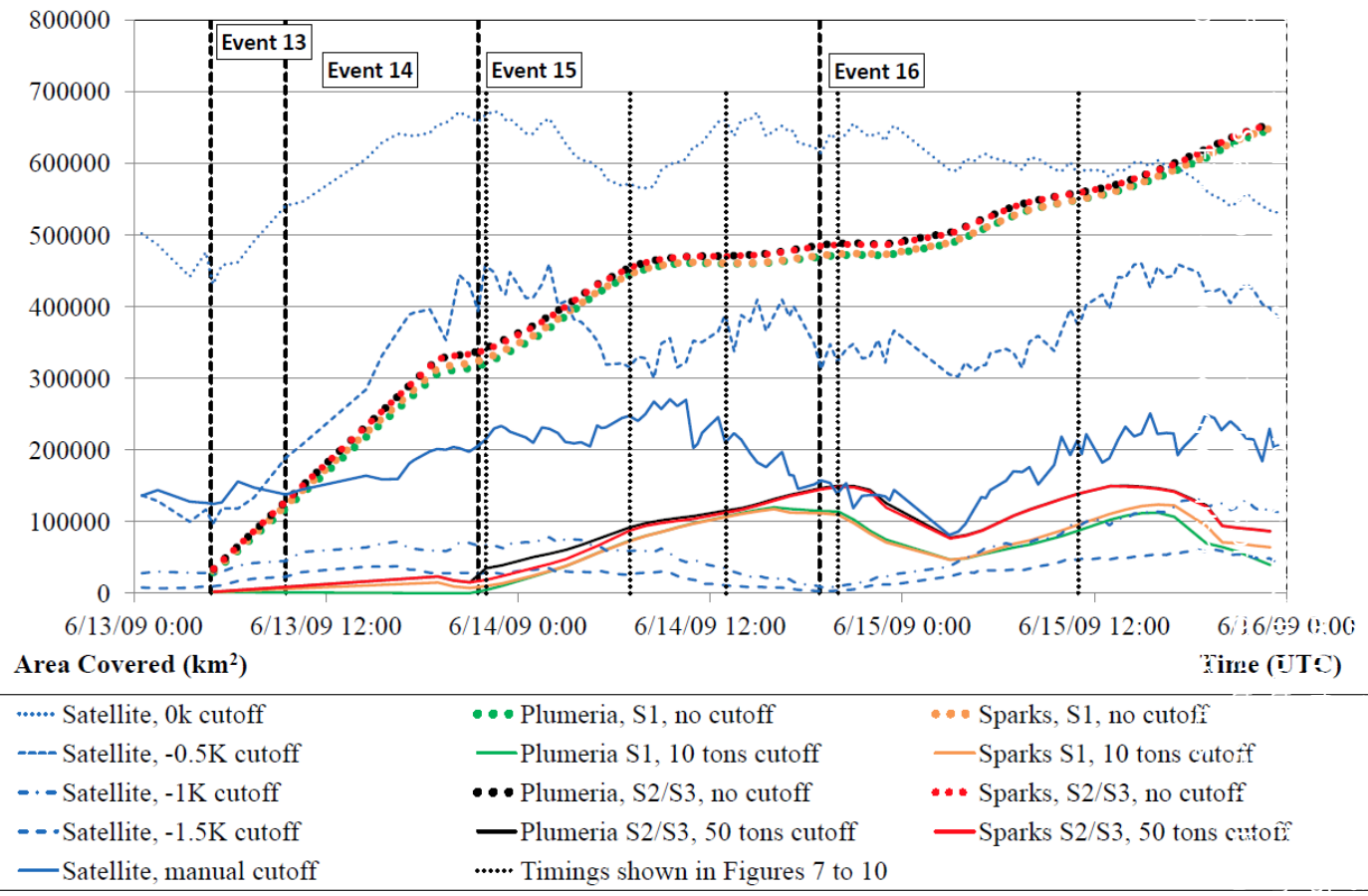


Figure 4.6: Qualitative spatial comparison of ash inundation between model and satellite results during June 13 - 16, 2009 over the domain studied (see Figure 4.2A). Computed ash from WRF-Chem is shown (without and with the best-fit cutoff) for all four combinations of eruption model and particle size distribution. The satellite-derived ash expansion is displayed for the BTD cutoffs of ranging from 0 K to -1.5 K in the reverse absorption images as well as for the manually outlined ash extent with the BTD cutoff of 0 K. Snapshots at indicated timings of ash extent based on both approaches can be seen in Figure 4.4. See text for details and explanations.

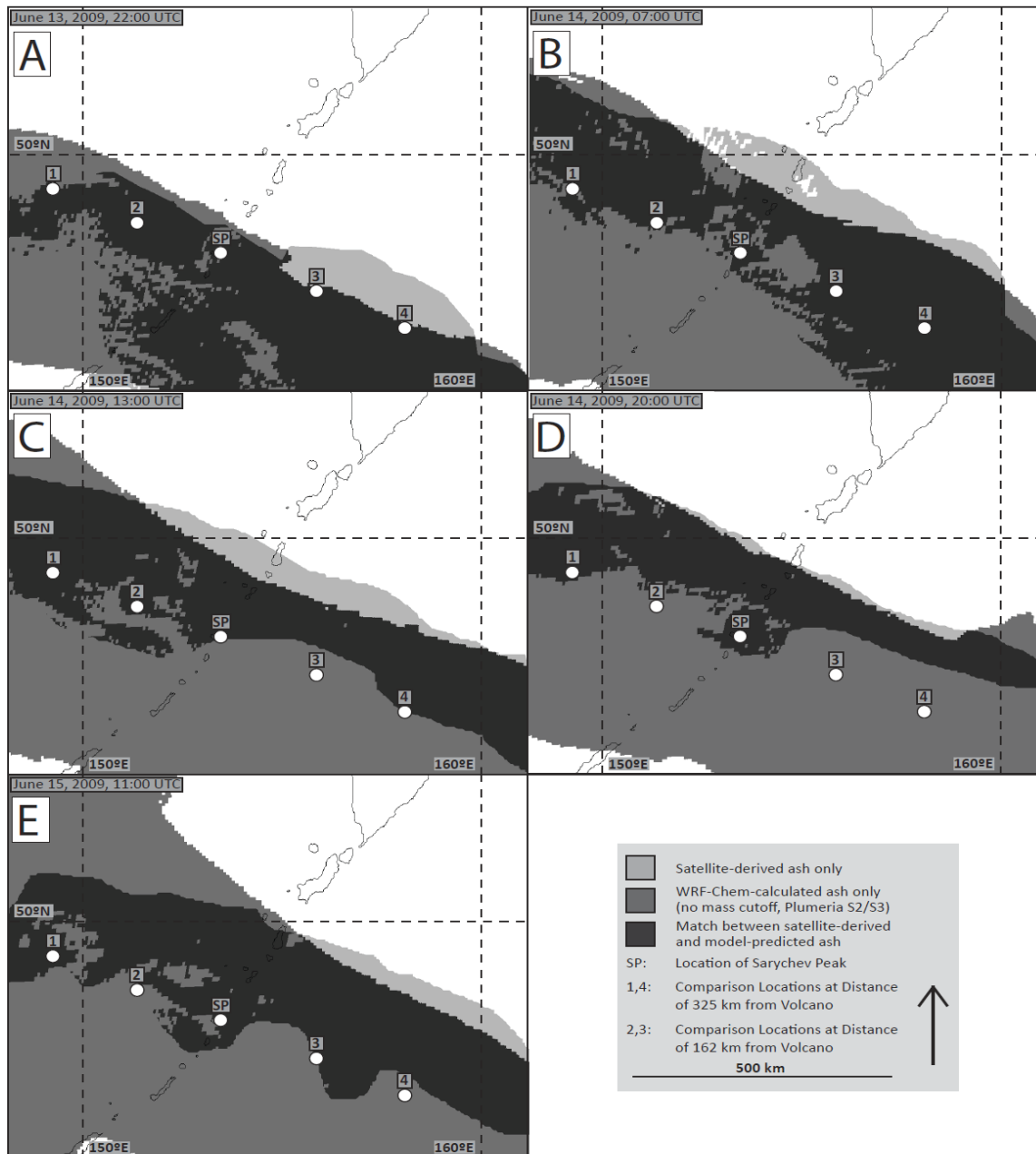


Figure 4.7: Selected timings of ash extent as derived by satellite data (light gray), calculated by WRF-Chem (Plumeria S2/S3) without a mass cutoff (dark gray) and the match of the two data sets (black). Especially in the earlier stages of the eruption (A – C), a closer match between satellite and model data is visible while the model over predicts towards later events (D and E). Gaps in the satellite-derived ash extent are a result of to meteorological cloud coverage.

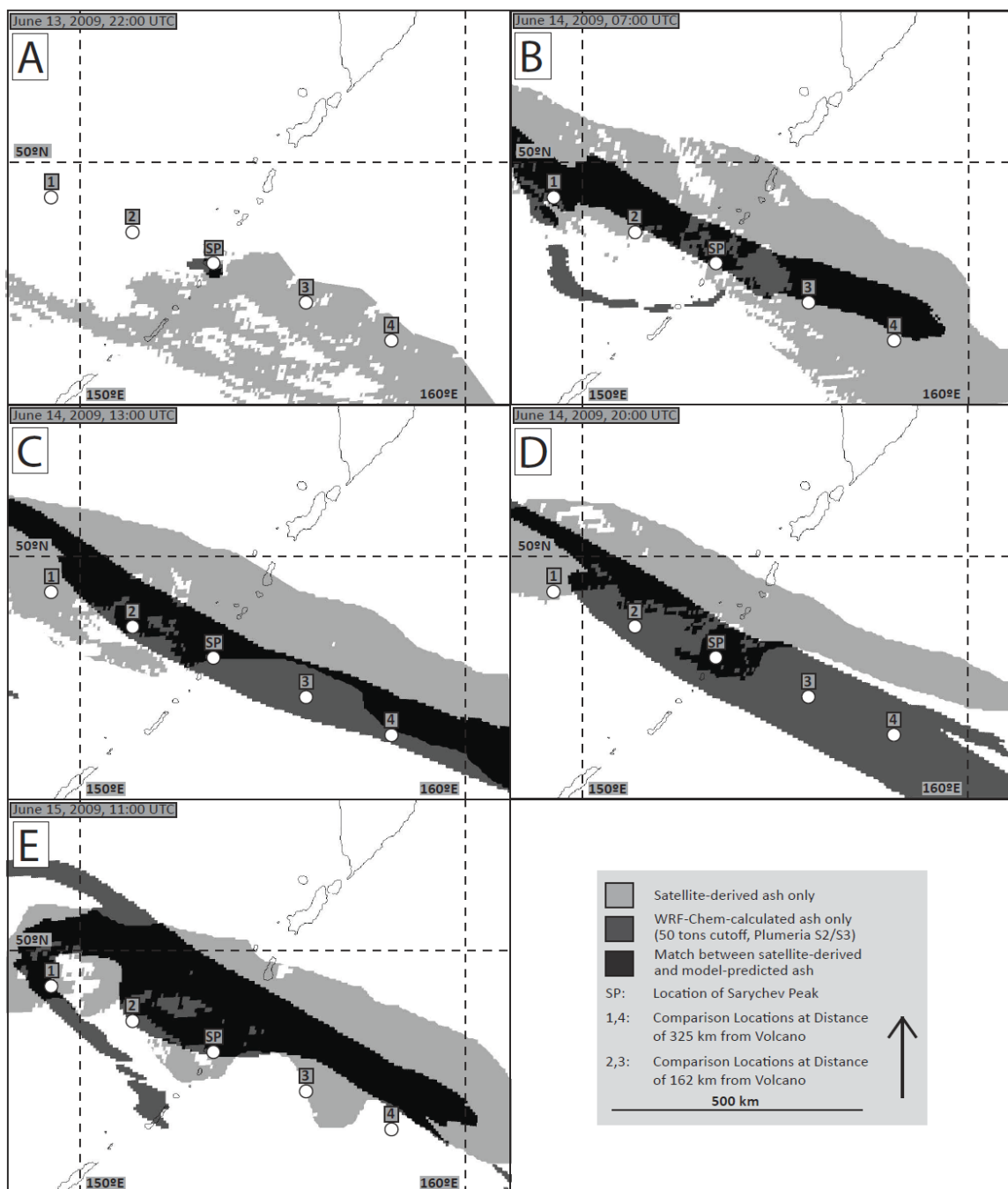


Figure 4.8: Selected timings of ash extent as derived by satellite data (light gray), calculated by WRF-Chem (Plumeria S2/S3) with a mass cutoff of 50 tons (dark gray) and the match of the two data sets (black). Especially in the earlier stages of the eruption (A – C), the satellite data over predicts the ash extent compared to WRF-Chem, while in later stages (D – E) a closer, albeit sometimes offset, match is shown.

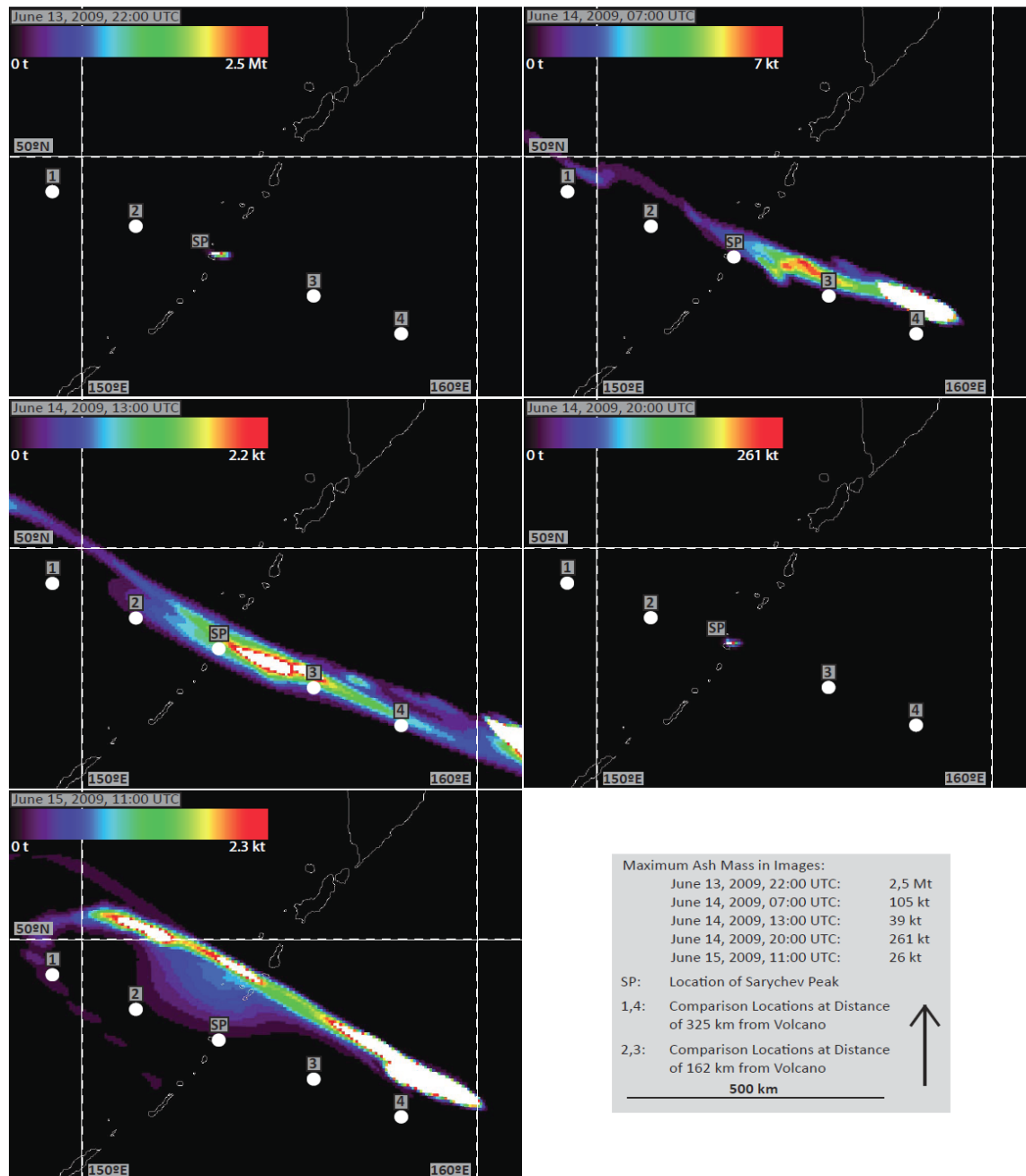


Figure 4.9: Selected timings of ash masses calculated by the WRF-Chem model using the Plumeria eruption rate and the particle size distribution S2/S3 (see Table 4.2 for details). A mass cutoff has not been applied but due to the 8-bit color scale, masses below $(1/2^8)$ of the highest value will be assigned background values. Image stretching has been applied to enhance features inside the dispersion, see text for further explanation.

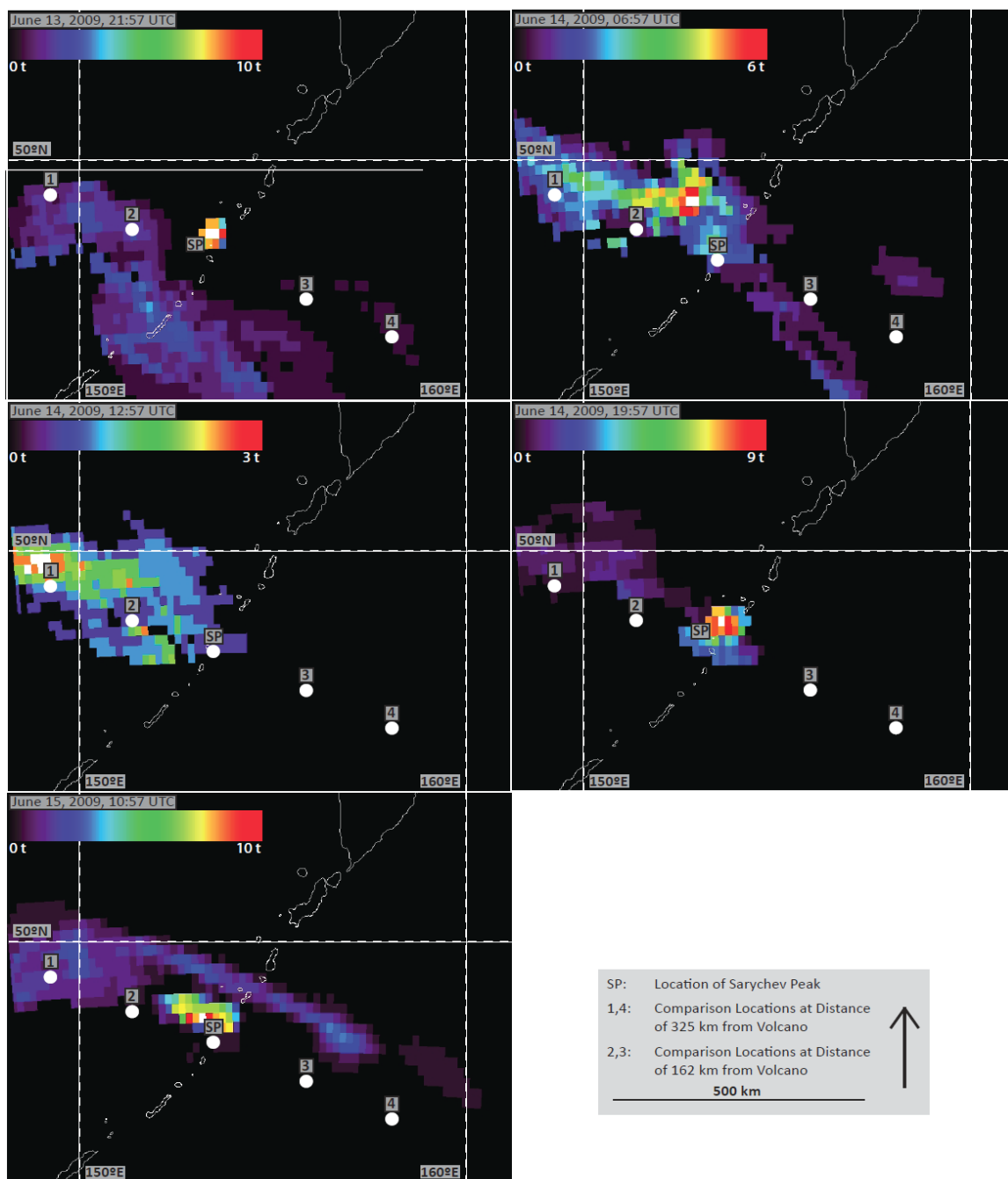


Figure 4.10: Selected timings of ash masses as calculated from satellite data. New eruptions can be seen at the vent (SP) at timings 21:57 UTC (June 13, 2009, A), 19:57 UTC (June 14, 2009, D) and 10:57 UTC (June 15, 2009, E). Dispersing ash can be seen dominantly to the northwest of Sarychev Peak with a lesser amount drifting to the southeast.

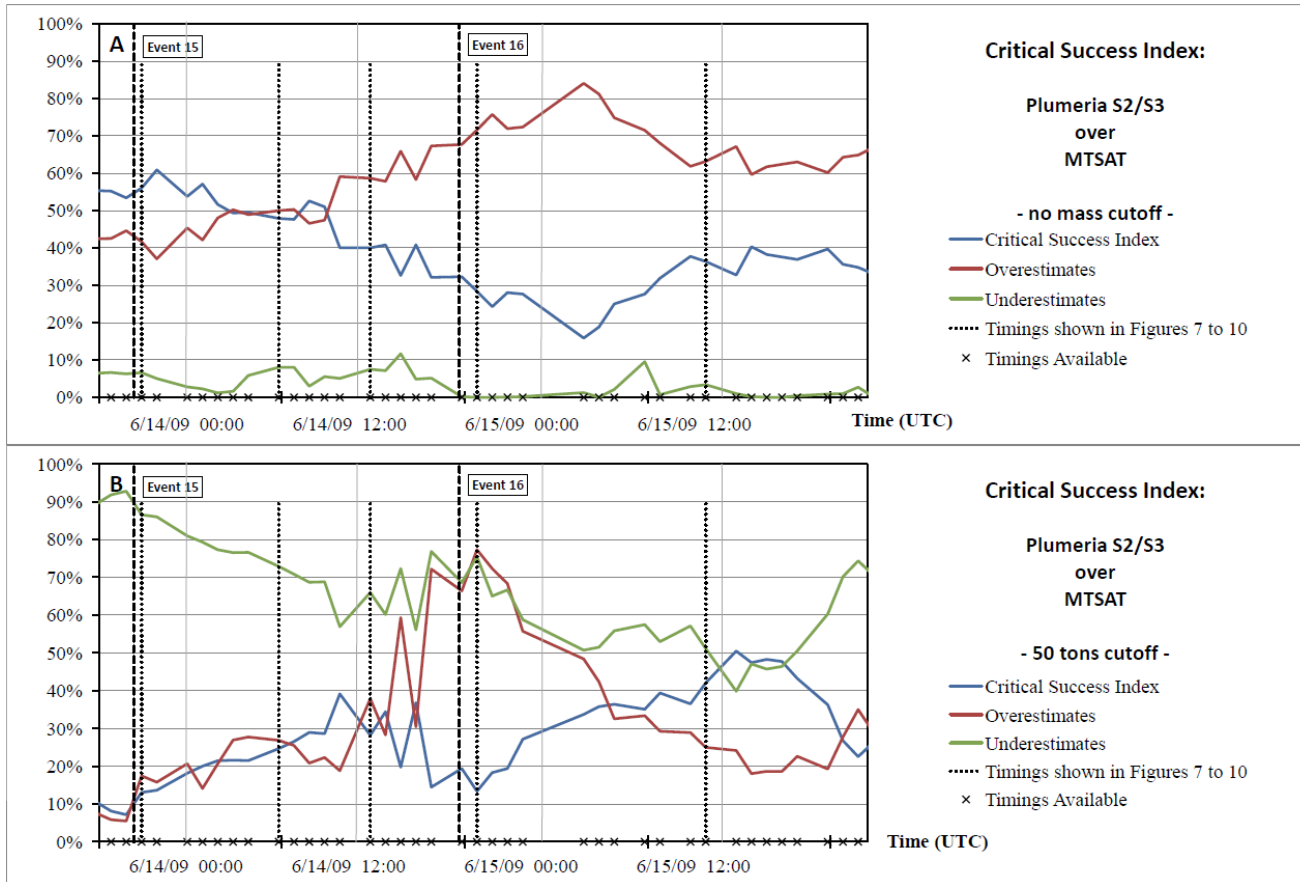


Figure 4.11: Quantitative spatial comparison of ash inundation between modeling and satellite retrieval results during June 13 (22:00 UTC) to 16 (00:00 UTC), 2009 over the domain studied. As the different model runs show very similar ash extents, the comparison shown here is between the Plumeria model run (S2/S3) with the satellite data (MTSAT: Multifunctional Transport Satellite) for runs without (Panel A) and with (Panel B) a threshold of 50 tons in the WRF-Chem data. Comparisons were made when satellite data and model outputs were obtained at the same time step. All timings used are marked in the

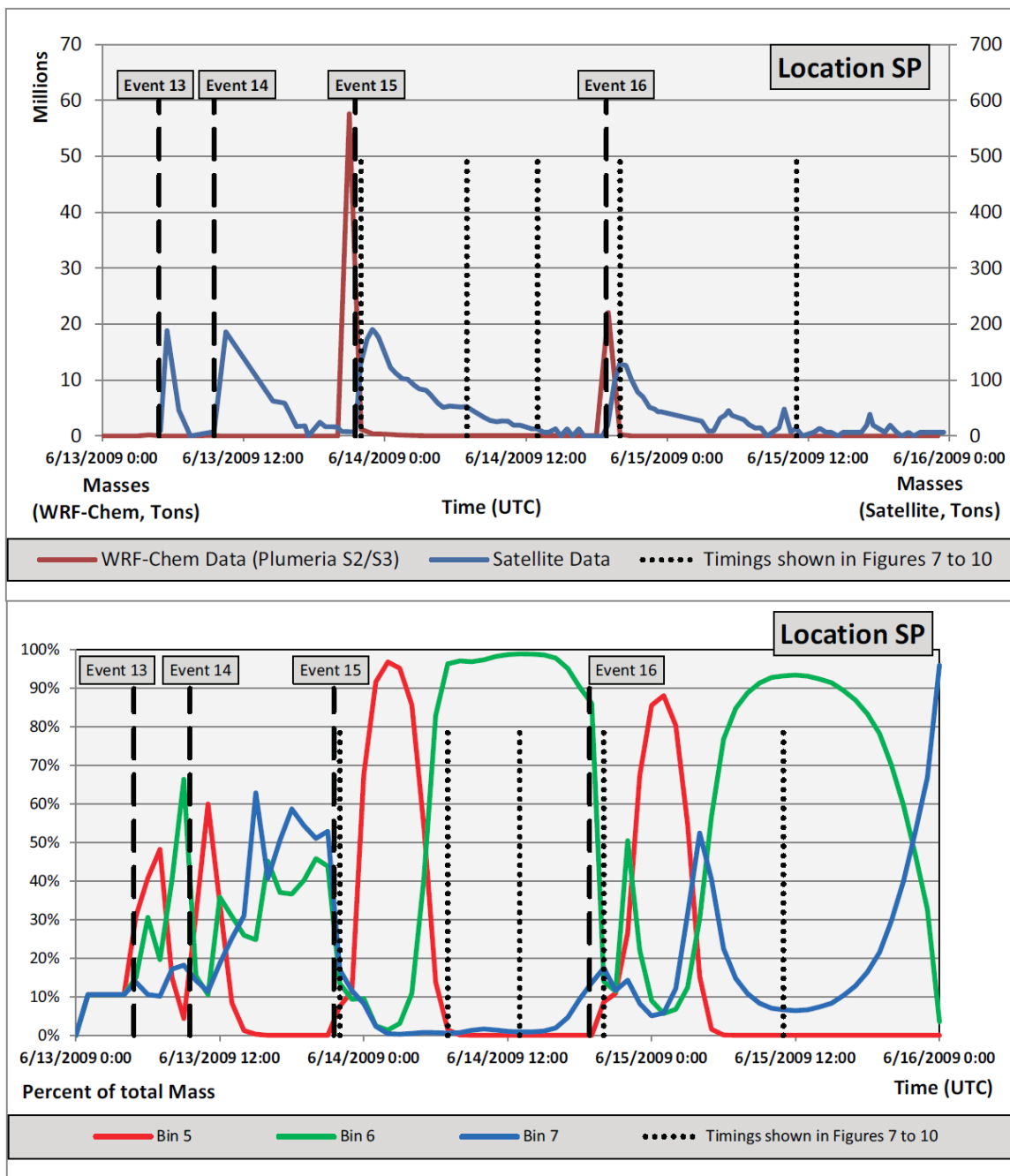


Figure 4.12A: For explanations see Figure 4.12E.

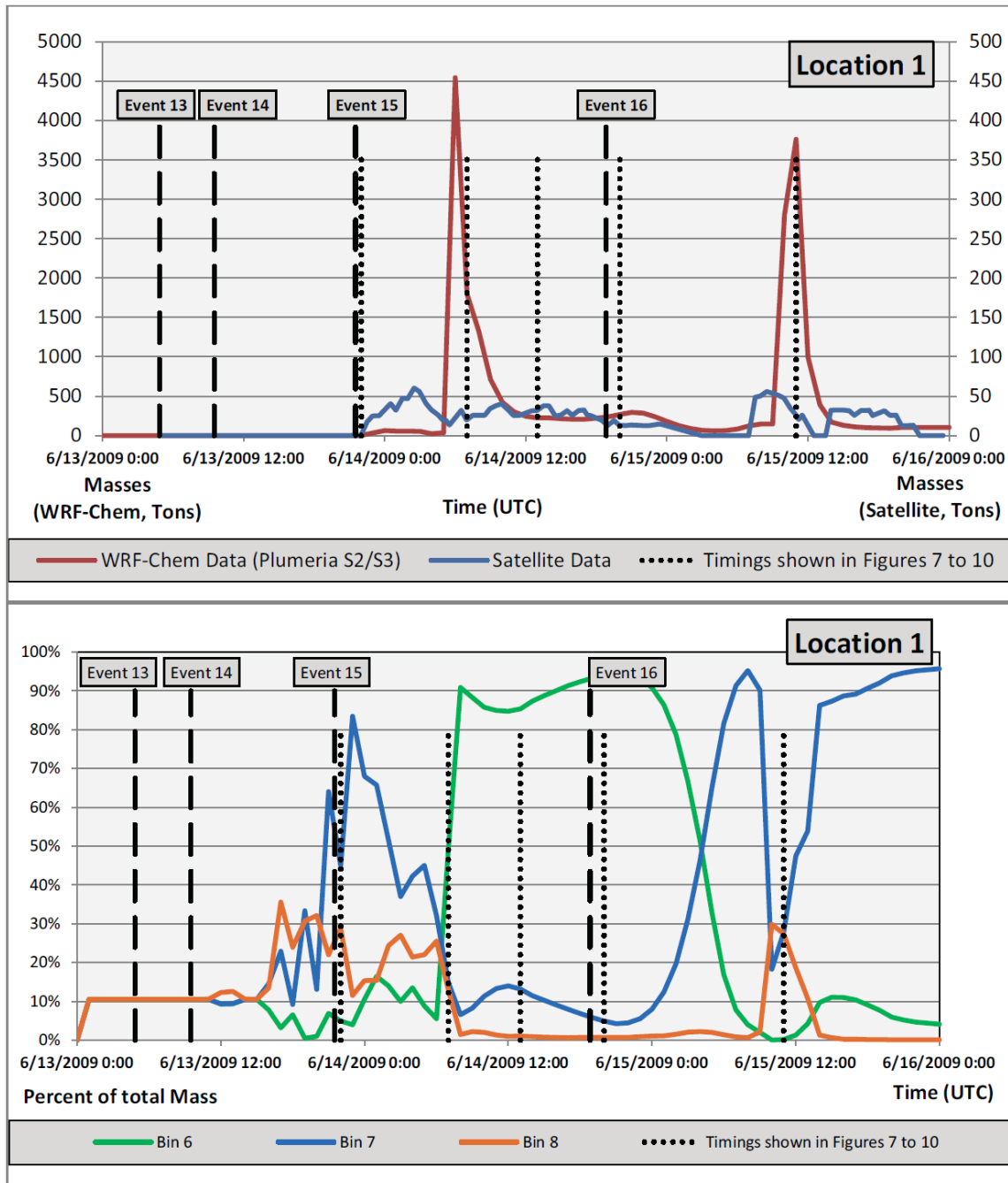


Figure 4.12B: For explanations see Figure 4.12E.

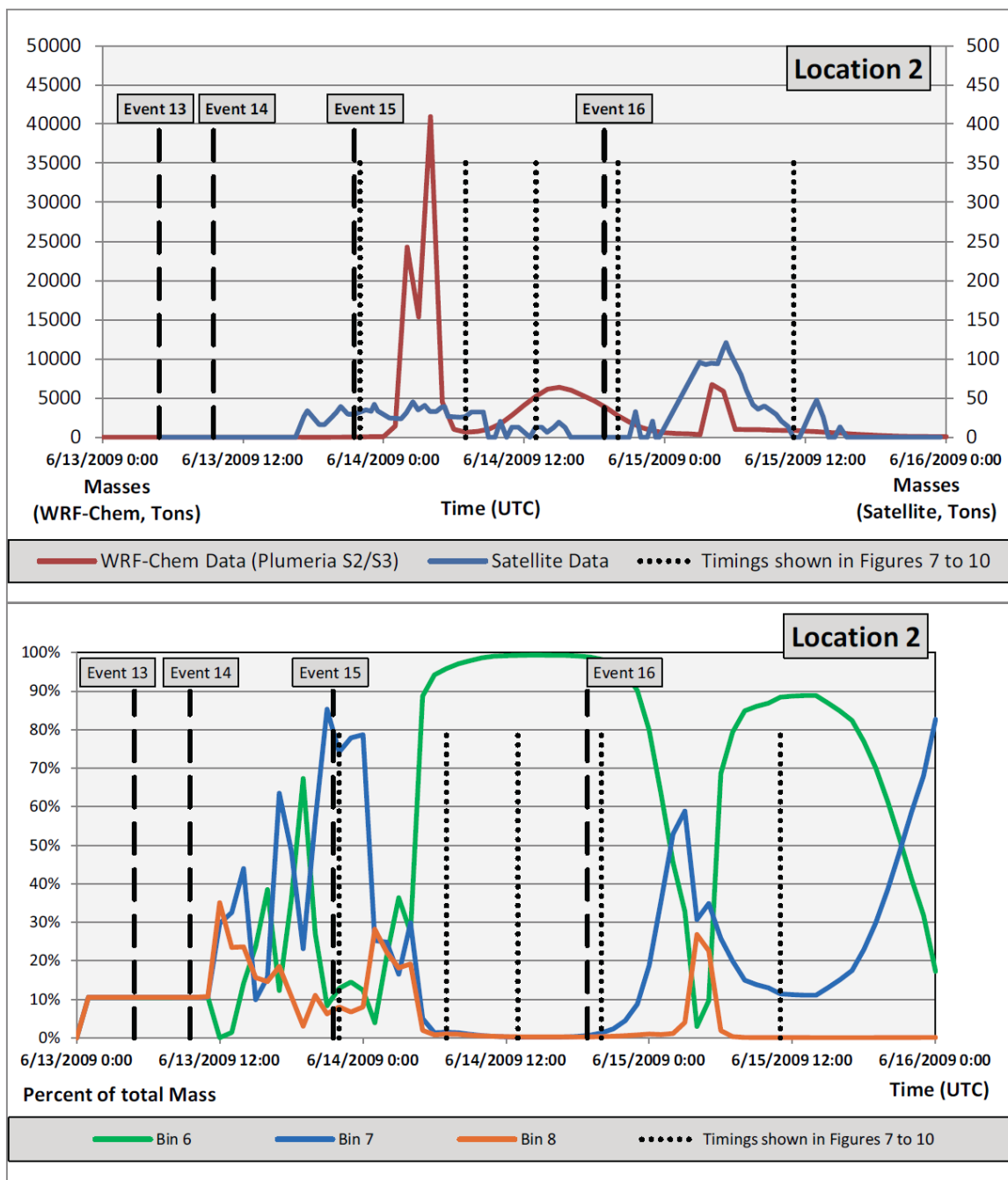


Figure 4.12C: For explanations see Figure 4.12E.

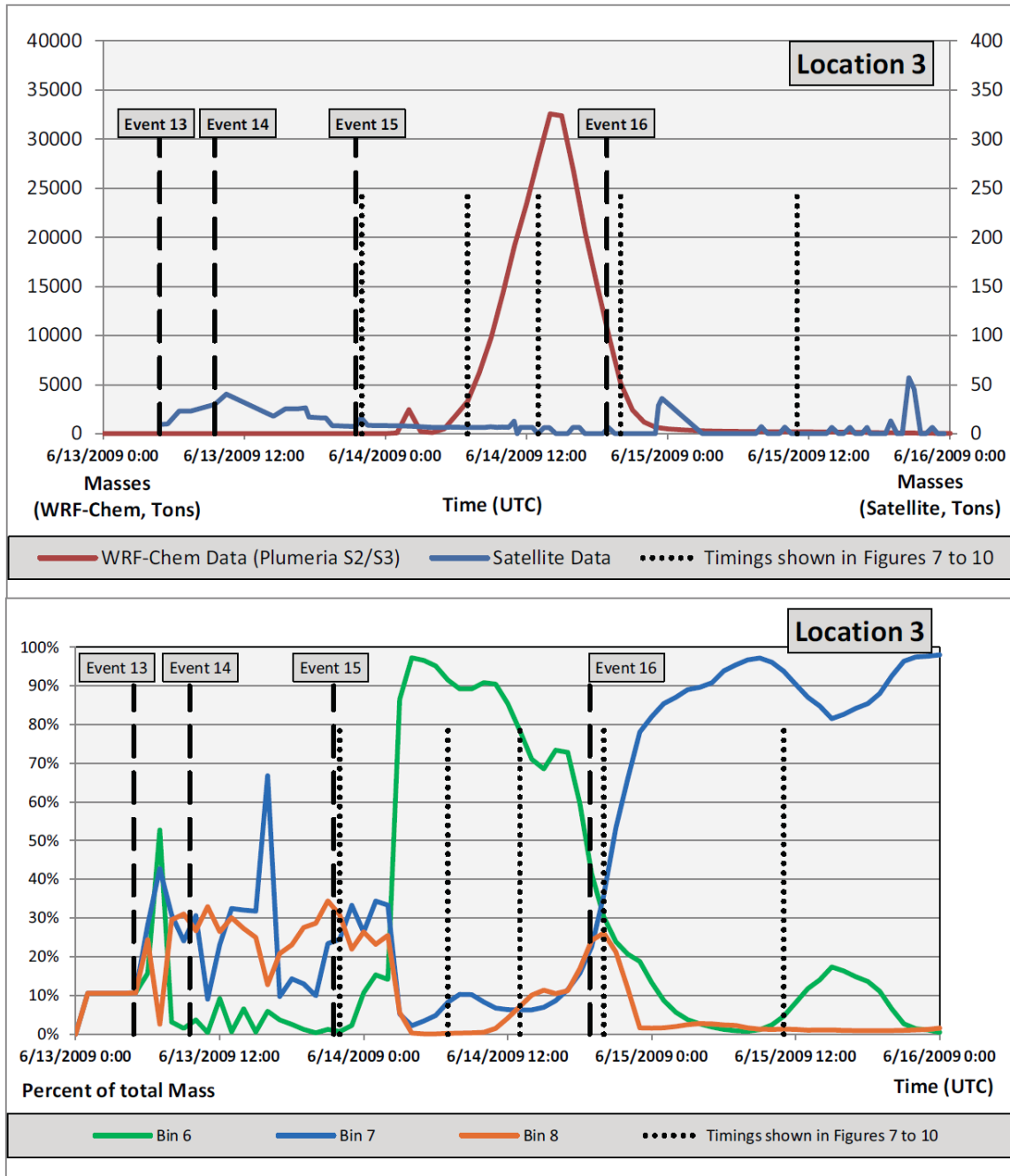


Figure 4.12D: For explanations see Figure 4.12E.

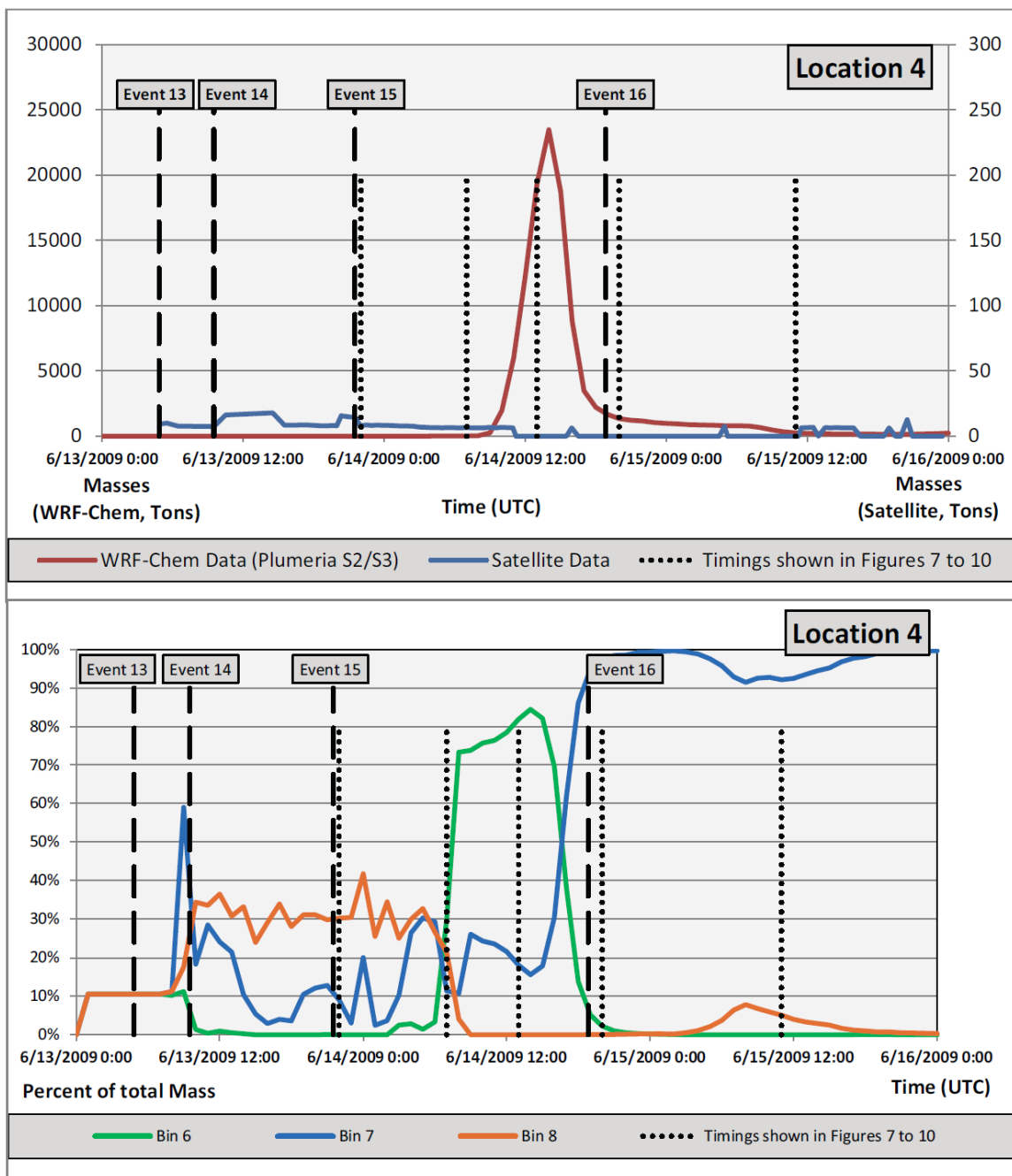


Figure 4.12E: Ash masses derived from satellite data and the WRF-Chem simulations at the five locations analyzed (Fig. 4.2). The upper panels in Figures 4.12A to 4.12E show a direct comparison between the derived masses in tons passing each location. Note the different scales on both the y-axes. For clarity, we only plotted the WRF-Chem results for the Plumeria S2/S3 runs. The lower panels show the percentages of the total masses passing the site from the three dominant WRF-Chem bins. Note the change from bins 5 to 7 (Figure 4.12A) to bins 6 to 8 (Figures 4.12B to E).

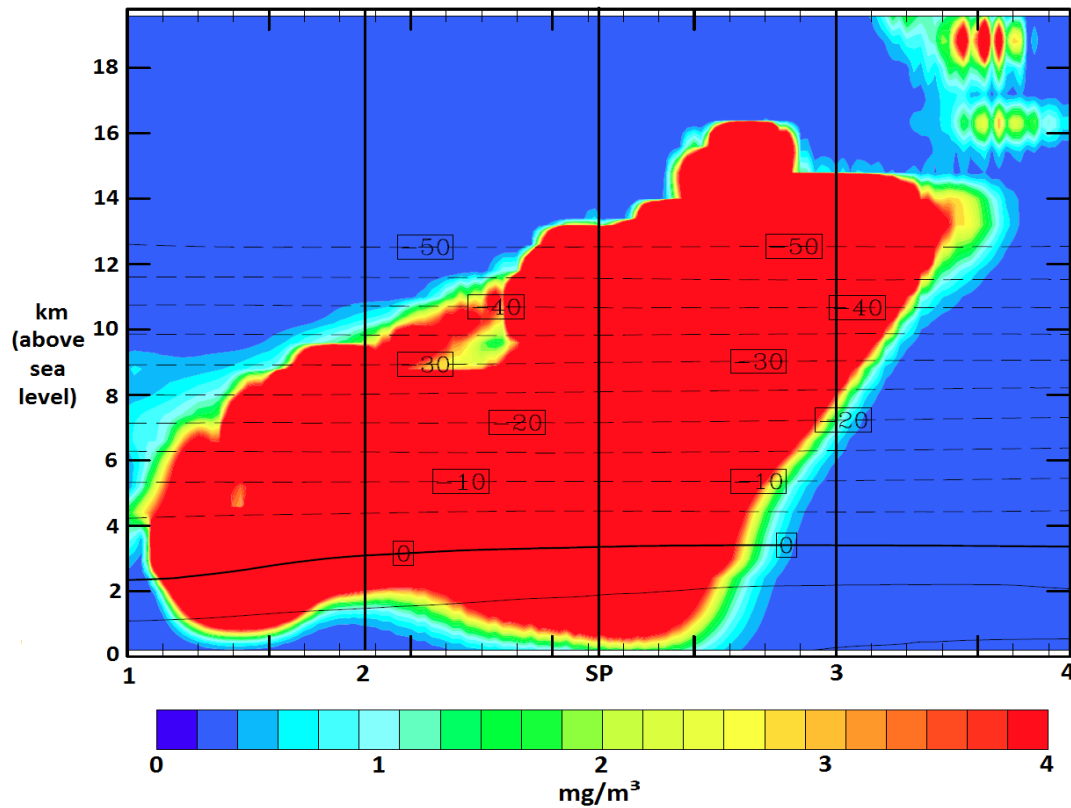


Figure 4.13: Vertical slice through the plume on June 14, 2009 at 07:00 (UTC) ranging from location '1' to '4' (see Table 4.2 for coordinates). The total thickness of the ash burden at locations '1' to '3' is greater than 500 m and, as such, should be visible in satellite imagery given meteorological cloud conditions don't prevent this and the particles in the column have an effective radius under $10 \mu\text{m}$. Numbers on the graph represent temperatures in Celsius. The color bar is chosen to represent 2 and 4 mg/m^3 , two values discussed as possible thresholds for ash concentration in the aviation community (ICAO, 2011).

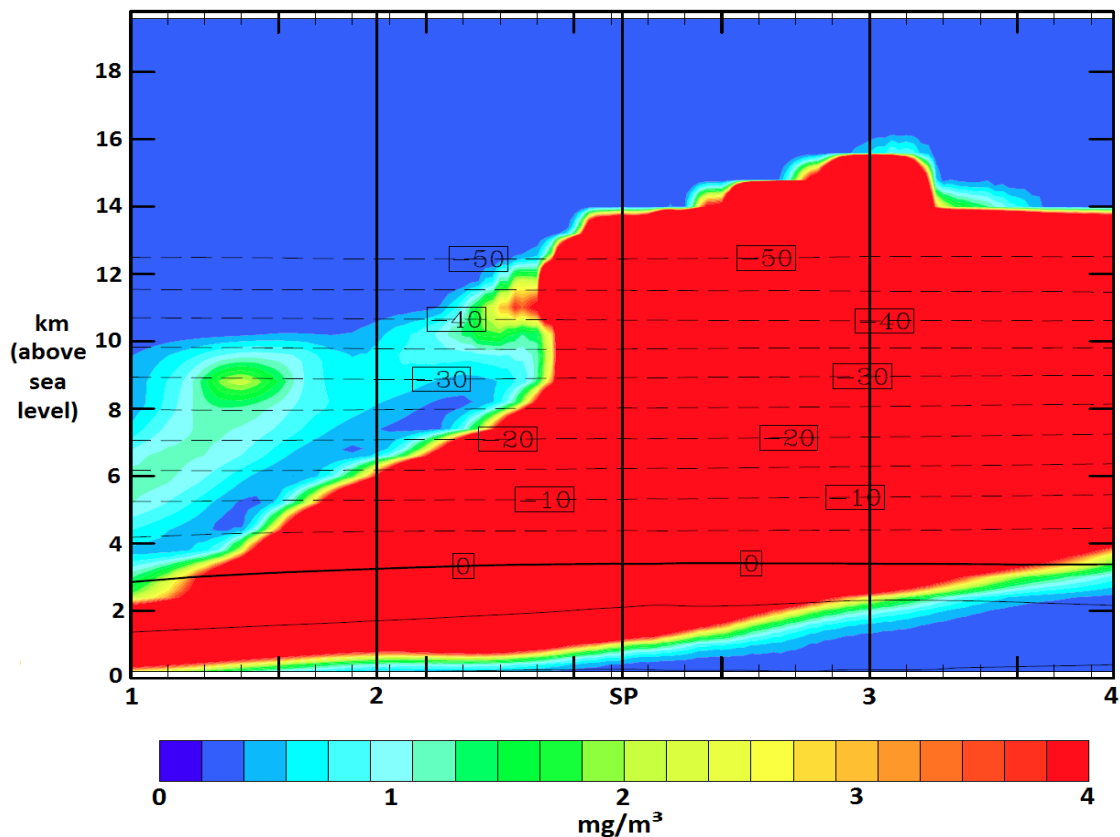


Figure 4.14: Vertical slice through the plume on June 14, 2009 at noon (UTC) ranging from location '1' to '4' (see Table 4.2 for coordinates). The total thickness of the ash burden at all locations is greater 500 m and, as such, should be visible in satellite imagery given meteorological cloud conditions don't prevent this and the particles in the column have an effective radius under $10\ \mu\text{m}$. Numbers on the graph represent temperatures in Celsius. The color bar is chosen to represent 2 and $4\ \text{mg/m}^3$, two values discussed as possible as thresholds for ash concentration in the aviation community (ICAO, 2011).

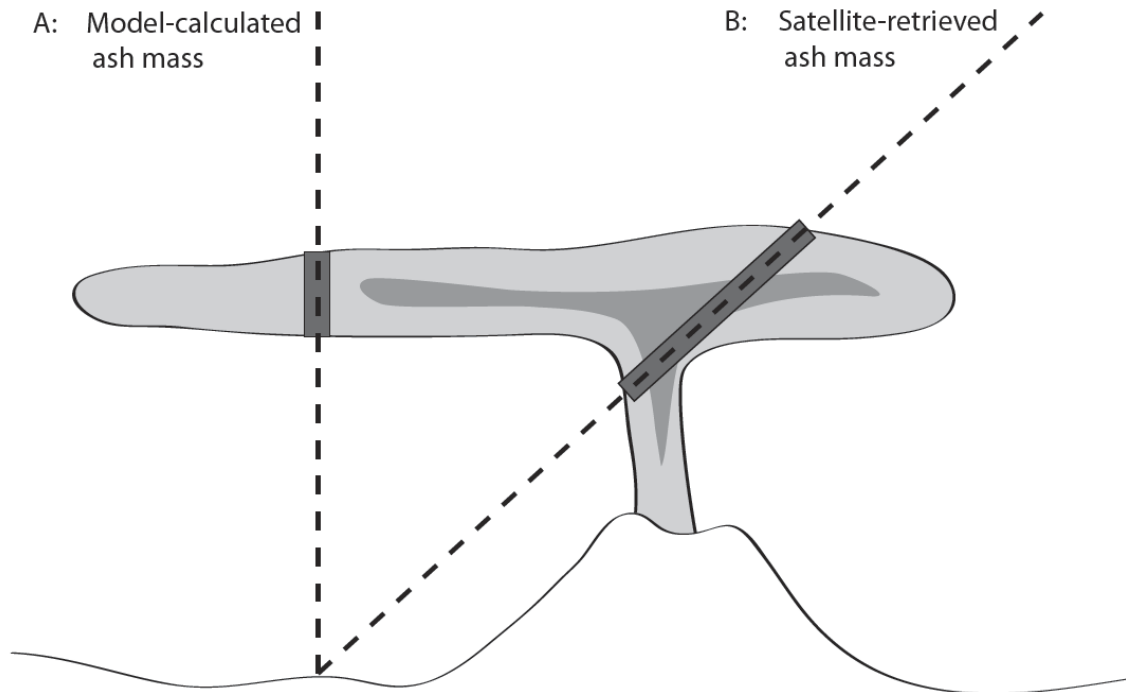


Figure 4.15: Diagram illustrating potential discrepancies between model calculations (A) and non-line-of-sight-corrected satellite retrievals (B). At any given point, the satellite will calculate the ash masses on a slanted angle while the model determines each point's location by summarizing the ash column vertically above. These two paths can not only differ in direction but also in length through the ash column (here depicted as dark rectangles) and encountered ash concentrations (here visualized as different shades of gray).

4.10 Tables

Table 4.1: Timings and heights of the 23 explosive events of the Sarychev Peak eruption of 2009. Plume heights (above sea level) and onsets are based on Levin et al. (2010), while the duration was derived from infrasound data by Matoza et al. (2011). We only included the duration if the given infrasound-derived onset falls within the range of ± 5 minutes from the satellite timing given by Levin et al. (2010).

Sarychev Peak, June 2009 Event No.	Day	Time	Plume Height	Duration
1	11-Jun	02:00 UTC	3 km	
2	11-Jun	07:00 UTC	4 km	
3	12-Jun	02:00 UTC	10 km	
4	12-Jun	04:00 UTC	6 km	13 minutes
5	12-Jun	07:57 UTC	12 km	
6	12-Jun	14:57 UTC	5 km	16 minutes
7	12-Jun	17:13 UTC	5 km	25 minutes
8	12-Jun	18:57 UTC	5 km	
9	12-Jun	22:15 UTC	5 km	20 minutes
10	12-Jun	23:30 UTC	6 km	
11	13-Jun	01:30 UTC	10 km	
12	13-Jun	04:30 UTC	10 km	
13	13-Jun	04:50 UTC	10 km	55 minutes
14	13-Jun	09:30 UTC	10 km	34 minutes
15	13-Jun	21:30 UTC	21 km	50 minutes
16	14-Jun	18:50 UTC	16 km	79 minutes
17	15-Jun	00:57 UTC	12 km	
18	15-Jun	05:15 UTC	5 km	
19	15-Jun	09:20 UTC	10 km	35 minutes
20	15-Jun	10:25 UTC	16 km	
21	15-Jun	10:55 UTC	10 km	
22	15-Jun	16:55 UTC	16 km	27 minutes
23	16-Jun	20:45 UTC	5 km	

Table 4.2: Parameters used for satellite and volcanic ash transport and dispersion analyses for the Sarychev Peak events 13 to 16. WRF-Chem = Weather Research and Forecast model with online Chemistry, VAR = Volcanic Ash Retrieval; WRF-Chem was run with two different eruption rates and two different particle size distributions, see text for details.

	Parameter	Unit	Event 13	Event 14	Event 15	Event 16	
General	Julian Date		164	164	164	165	
	Starting Time	UTC	04:50	09:30	21:30	18:50	
	Duration	min	55	34	50	79	
	Initial Height	km	10	10	21	16	
WRF-Chem	Erupted Volume	(a)	1.80×10^{-3}	1.11×10^{-3}	4.00×10^{-2}	2.02×10^{-2}	
		(b)	4.10×10^{-4}	1.93×10^{-4}	4.35×10^{-2}	1.45×10^{-2}	
	Eruption Rate	(a)	1.42×10^6	1.42×10^6	3.46×10^7	1.11×10^7	
		(b)	3.23×10^5	2.46×10^6	3.77×10^7	7.97×10^6	
	Mass fraction <63 μ m	(1)	%	1.9	1.9	1.9	1.9
		(2)	%	17.9	17.9	36.27	36.27
	Density	kg m^{-3}	2600	2600	2600	2600	
Spatial Resolution	km	5	5	5	5		
Vertical Plume Shape		Poisson-distribution with Height					
VAR	Cloud Top Temperature	K	213				
	Surface Temperature	K	269				
	Spatial Resolution	km	4.3				
	Reverse Absorption	K	0				
	Threshold		(ash outline manually-defined)				
	Specific Gravity of Ash	kg m^{-3}	2.6				
Refractive Index of Ash	11 μ m		2.14610+0.39891i				
	12 μ m		1.82854+0.12953i				
Refractive Index of Air		1.0					
Sample Locations (see Figure 2B)	Location SP		48.1°N		153.20°E		
	Location 1		49.3°N		149.05°E		
	Location 2		48.7°N		151.13°E		
	Location 3		47.5°N		155.23°E		
	Location 4		46.9°N		157.35°E		

a) Eruption rate calculated by the Sparks et al., (1997) Method

b) Eruption rate calculated by Plumeria (Mastin, 2007)

1) Standard particle size distribution as suggested by Mastin et al., (2009)

2) Tailored particle size distribution

Table 4.3: Particle size distributions based on the classification of Mastin et al. (2009). The default value for Sarychev Peak is S1 but based on the characteristics of the 2009 eruption, S2 is the best-fit for events 13 and 14, while events 15 and 16 are best represented by S3.

WRF-bins	#	S1	S2	S3
1 - 2 mm (Phi -1 - 0)	1	46.3	20.7	2.92
0.5 - 1 mm (Phi 0 - 1)	2	15.2	5.5	3.55
0.25 - 0.5 mm (Phi 1 - 2)	3	14.8	4.2	11.82
125 - 250 μm (Phi 2 - 3)	4	11.1	5.9	8.24
62.5 - 125 μm (Phi 3 - 4)	5	6.3	23.2	7.9
31.25 - 62.5 μm Phi (4 - 5)	6	3.1	11.7	13.02
15.625 - 31.25 μm (Phi 5 - 6)	7	1.3	10.9	16.28
7.8125 - 15.625 μm (Phi 6 - 7)	8	0.8	8.1	15.04
3.9065 - 7.8125 μm (Phi 7 - 8)	9	0.5	5.3	10.04
< 3.9065 μm (Phi > 8)	10	0.6	4.5	11.19

Chapter 5: Improvements on Volcanic Ash Quantification in the Puff Volcanic Ash Tracking and Dispersion Model and Satellite Thermal Infrared Remote Sensing Data¹

Abstract

In this study, advances in satellite to model comparisons of volcanic ash are analyzed. Following up on previous studies, a variable surface temperature per satellite pixel, based on numerical weather prediction data, is applied to volcanic ash retrievals to better quantify the ash masses in the atmosphere. Furthermore, the focus in this study is on a quantitative approach to compare model and satellite results based upon a simple 'Ash - No Ash' binary system, using two band thermal infrared (TIR) satellite data. For the model data, the Lagrangian Puff Volcanic Ash Transport and Dispersion (VATD) model is used. The volcanic ash retrieved mass data are analyzed both in the traditional model projection (i.e. vertically summed ash masses above given locations) as well as in the satellite-line-of-sight projection (i.e. summed from one location in a straight line towards the satellite). The case study focused upon is the eruption of Kasatochi Volcano in the Aleutian Islands, Alaska, during August 2008. Results reiterate that a quantification of ash masses is not easily performed with two band TIR data as

¹ Steensen, T., Webley, P, and Dehn, J. Improvements on Volcanic Ash Quantification in the Puff Volcanic Ash Tracking and Dispersion Model and Satellite Thermal Infrared Remote Sensing Data, in preparation.

meteorological cloud cover can intervene and subsequently no ash will be detectable in the satellite data, unless the ash is above the cloud cover and manually outlined perfectly or there is no cloud cover present. With a thick layer of clouds, this meteorological interference will alter the results. A binary 'Ash - No Ash' approach is considerably more promising for the two band data. It produces a better satellite-model match than a quantitative approach trying to derive absolute masses, as the extent of the ash is identifiable in satellite data with fewer assumptions than it needed in the calculation of the masses. This match can then be exploited for ash forecasting in a real-time setting. Finally, the change of projections (vertical - line-of-sight) in the model data has an effect on the position of the plume and, hence, on the comparison to satellite data. With 30 to 50 km spatial resolution in the modeled ash cloud from the numerical weather prediction model applied, these only needs to be taken into account if the spatial model resolution is finer than this offset or where the dispersing cloud is small relative to the modeled ash clouds concentration grid. This work provides improvements on near real time ash detection, which will be valuable for operational services for the aviation community.

5.1 Introduction

Satellite-based detection of volcanic ash in the atmosphere was first described qualitatively by Prata (1989). Using two satellite bands centered at 10.8 μm and 11.9

μm , respectively, Prata (1989) used the reverse absorption feature of silica ash located in the atmospheric window. As opposed to meteorological water, volcanic ash absorbs/scatters more radiation at lower wavelengths in this 10-12 μm atmospheric window, so that a difference of the two bands ($B_{10.8} - B_{11.9}$) brightness temperature data will yield a negative value if ash is present. Meteorological clouds, however, can obscure the results and it has been shown that they can also produce a falsely positive result (Pavolonis et al., 2006).

Wen and Rose (1994) built upon this method and developed a quantitative approach (Volcanic Ash Retrieval, VAR). With the difference of the brightness temperature bands described by Prata (1989) and some physical input parameters of the atmosphere and the ash, like surface and ash cloud top temperature and refractive indices of ash and air, Wen and Rose (1994) calculated the ash masses, the optical depth and the effective radii per pixel for volcanic clouds. This estimate from the VAR algorithm includes several uncertainties and assumptions including a thin homogenous ash layer parallel to the surface and no other scatterers in the satellite's line of sight (see Wen and Rose (1994) for a complete list). Furthermore, the input parameters for the volcanic ash mass retrievals are defined as default settings for the whole time series of images. Many of these values are hard to obtain (like air or particle density) if no field work can be performed. However, a small change can result in comparably high alterations in the

derived masses (Steensen and Webley, 2012), with the surface temperature (i.e. surface leaving radiance) being the most crucial variable.

In this paper, the work follows on from the previous studies of Steensen and Webley, (2012), Chapter 3 of this dissertation, and Steensen et al. (in review), Chapter 4 of this dissertation, and analyzes the eruption of Kasatochi Volcano (Aleutian Islands, Alaska, USA) with data acquired using the Geostationary Operational Environmental Satellite (GOES) located at 135°W and using the Puff VATD model (Searcy et al., 1998). A geostationary satellite was chosen for its reliability in coverage of the eruption both temporally and spatially. As opposed to previous scenarios, we vary the surface temperature per satellite pixel, as this is shown as being the most important variable in the ash retrieval in terms of accuracy (Steensen and Webley, 2012) as well as the projection of the dispersion model so that total masses are summed in the satellite's line of sight as opposed to vertically above the respective locations. See section 5.2 for further details on both techniques. The outcome from the analysis aims to provide improvements to global volcano monitoring and ash analyses utilizing a fusion of satellite and model data.

5.1.1 Kasatochi Location and its 2008 Eruption

Kasatochi is a stratovolcano in the Aleutian Islands of Alaska (USA, Fig. 5.1). In early August 2008, the volcano erupted in three different events sending ash up to 18 km above sea level (ASL) into the atmosphere (Waythomas et al., 2010). The onsets and durations of the different events were determined using seismic stations on nearby islands and satellite data. The plume heights were estimated using National Oceanic and Atmospheric Administration (NOAA) GOES and AVHRR (Advanced Very High Resolution Radiometer) data. This eruption was the first in recorded history. Tephra fallout was only mapped on neighboring islands and, hence, does not include distal deposits. The eruption and volcano parameters are summarized in Table 5.1.

5.2 Methodology

In this study, three previously-described enhancements suggested for better detection of airborne volcanic ash in satellite data are focused upon and their comparison and evaluation with VATD model data:

- a) Use of pixel-specific background temperatures in VAR;
- b) Comparison techniques of binary ash detection in model and satellite data, i.e. the 'Ash - No Ash' approach;

- c) Comparison of satellite data to VATD model data that has been projected in the satellite's line-of-sight (LOS).

5.2.1 Using Pixel-Specific Background Temperatures

The importance of the background temperature (derived from surface leaving radiance at thermal infrared wavelengths) has been outlined by Steensen and Webley (2012) in retrieving the total amount of ash in the atmosphere using the Volcanic Ash Retrieval of Wen and Rose (1994). A calculation of the sensitivities of all VAR input parameters showed that the Surface Temperature (T_s) has the strongest influence on the derived mass and can cause a $\pm 25\%$ change when assessed with an error bar of $\pm 2\%$.

Previously, a single T_s value has been estimated on a clear-sky pixel in the satellite scene and applied to all pixels in the whole time-series (e.g. Steensen et al., 2013). To estimate the per pixel T_s values in this study, the temperatures reported for the bottom layer in numerical weather prediction (NWP) global re-analysis atmospheric models is applied. While the temperature of the bottom layer of the atmosphere in the NWP model does not necessarily equal the true surface temperature, it is still an improvement over the previous method (as used in Chapters 2 and 4 of this dissertation) and takes into account regional changes of temperature.

In this project, data acquired from the National Centers for Environmental Protection (NCEP) is used. Their Global Forecast System (GFS) is available at spatial resolutions from 0.5 up to 2.5 degrees (NOAA, 2013). For the purpose of fast calculations, as needed in real-time assessments, but also relative accuracy, the spatial resolution of 1.0 degree was chosen. In addition, the traditional approach with one T_s value for the whole temporal and spatial sequence is also applied in the analysis. In this case, based on a clear-sky pixel, a T_s of 280 K was chosen. The spatial resolution here is dependent on the GOES pixel size at the respective location, which is about 4.4 km for the North Pacific region being focused upon in this study. All details regarding the atmospheric models used can be found in Table 5.2.

Since the NWP model has a different spatial resolution to the satellite data, each satellite pixel in the domain, specified in Figure 5.1, is assigned the closest T_s value of the NWP atmospheric model. This way, a T_s map is created with the same dimensions as the satellite data and so the calculated masses can be compared.

Furthermore, the surface temperature is assumed to be the sole radiance being emitted and being responsible for the signal received at the satellite. Any overlying meteorological clouds will obscure the signal. As the Aleutian Islands are a cloud-prone region and the cloud cover during the eruption was continuous (Waythomas et al., 2010), the real brightness temperature that generates a signal in the satellite data will be at least partially, or potentially entirely due to the clouds. If there are underlying

meteorological clouds that obscure the generally warmer surface, the calculated ash masses will be, at least partially, based on this colder signal and the derived ash masses will be lower. However, these are factors cannot be computed at this time and for this study a cloud-free sky is assumed. Taking into account the temperature of each NWP model layer would be required to fully resolve this issue.

To help identify the ash in the satellite data and to avoid a large misclassification of meteorological clouds as ash, the ash is outlined in the satellite data based on identification in the visible (where available) and infrared images (see Steensen et al., in review, for a previous application of this method; Chapter 4 of the dissertation). Since the analysis is limited to GOES data, the channels available are also limited, two bands in TIR, and a more detailed, multi-channel automated analysis (e.g. Pavolonis et al., 2006) was not possible. In this manual approach, only the pixels within this outline will be processed in VAR. With this, the area focused on in the satellite image is that defined as ash by the observer, while the other parts are ignored. This means that any areas of potential ash outside of the defined sub-image-area will not be included in the analysis. Without this method, a custom-defined threshold, commonly described as 0 K, is required for the band difference of $(B_{10.8} - B_{11.9})$ as described by Prata et al., 1989). This threshold changes according to the cloud cover so meteorological clouds, which can have a slight negative value (Wen and Rose, 1994), are not taken into account. However, any meteorological cloud coverage inside this region of interest will still be

processed and can result in a misclassification of as volcanic ash. To compare the different approaches used in this task, the maximum, minimum and mean ash load per m^2 in each time step with each method was determined. The trend over time was analyzed and compared to the Puff VATD modeled maxima, minima and mean ash masses for the same domain to determine the best approach.

Puff is a Lagrangian VATD model used for predicting volcanic ash movement, which has been described in detail by Tanaka (1991) and Searcy et al. (1998). It is initiated with a set number of particles, which are distributed using the Random Walk with a given data set of meteorological data. For this project, a set of eruption-specific input parameters as described in Table 5.3 with a spatial resolution of 10 km for the outputted ash concentration grid was used. The particle dispersion is calculated in space and time so that an estimate of the concentrations in the 4-dimensional domain is possible.

As the initial particle size distribution, the default values provided by Mastin et al. (2009) which give a fine ash amount ($< 63\mu\text{m}$) of 40% are used. The eruption rate used is based on equation 5.1, the formula provided by Sparks et al. (1997), where H = Height and Er = Mass eruption rate:

$$H = 1.67 \times \text{Er}^{0.259} \quad (5.1)$$

5.2.2 Comparison techniques of binary ash detection in model and satellite data

The maximum ash extent in the satellite BTM and VATD model data is measured in a simple binary approach. Here, there is no focus on absolute masses but rather if ash is present or not at a given location and time. For a quantitative comparison, the Critical Success Index (CSI) is applied. The CSI (Equation 5.2) was first described by Stunder et al. (2007) for volcanic ash and is a measure of the overall match between two areas. It is defined as the ratio between of the number of pixels belonging to both data sets (A) over the total amount of pixels belonging only to one (B) or both data sets (A+B), see equation 5.2:

$$CSI = \frac{A}{A+B} \quad (5.2)$$

As a follow-up, the satellite and model excess values (SE and ME, respectively) are introduced. The SE (Equation 5.3) is defined as the ratio of the satellite-detected ash extent that does not correlate with the VATD model results ($B_{\text{satellite}}$) over the cumulative area (A+B). Accordingly, the ME (Equation 5.4) is defined as the ratio between the VATD model-predicted areas that are not detected in the satellite data (B_{model}) over the cumulative area (A+B).

$$SE = \frac{B_{\text{Satellite}}}{A+B} \quad (5.3)$$

$$ME = \frac{B_Model}{A+B} \quad (5.4)$$

$$\text{With } B = B_model + B_satellite \quad (5.5)$$

The advantage of using these values, in addition to the CSI, is that the excess area of VATD model results and satellite detected data in relation to the entire possible ash area is defined. With this, the satellite data or the model results are not assumed to be truth but rather analyzed on how both compare with each other to find the ideal case where the CSI will be '1' and, hence, the SE and ME values will be '0' as the sum of the three values always equals '1' (Equation 5.6):

$$CSI+SE+ME=1 \quad (5.6)$$

5.2.3 Correction of the VATD model results to the satellite's line-of-sight

A general discrepancy can occur between satellite detected ash clouds and VATD model results based on the projection used: VATD models generally show values vertically integrated above a given location, while satellite retrievals always show values measured at an angle which can significantly change the geometry of the observation (Fig. 5.2; Steensen et al., in review). To estimate the offset caused by a non-LOS-corrected model run, the original VATD model results in terms of spatial extent at given timings during the Kasatochi eruption with equivalent data, are compared to those adjusted to the satellite's LOS.

The line-of-sight is calculated based on trigonometric rules with a GOES satellite height of 35,790 km above sea level (ASL) for each pixel assuming a spherical Earth with a radius of 6378 km. At any given height interval for the VATD model, the closest new coordinate pair is determined following the satellite's LOS. Since GOES is geostationary, there is no need to account for a movement of the satellite during the temporal range. The final cumulative ash mass is then projected to the original pixel to mimic the ash's location in a satellite image resulting in a north shift of the ash, since the eruption occurred north of the satellite's latitudinal location. The offset between true-vertical plume and south-shifted (along LOS) plume will be analyzed quantitatively with the CSI. In addition, the analysis for the LOS data implements the previously defined excess values SE (representing the amount the satellite-LOS-corrected ash extend exceeds the non-LOS-corrected one) and ME (representing the amount that is classified as ash only when the model sums the ash masses vertically).

5.3 Results

5.3.1 Satellite-Model Comparison 1: Mass Loading

Mass retrievals in the satellite remote sensing data and VATD model results differ significantly. Figure 5.3 shows the maximum, minimum and mean mass loading values for the whole eruption series as determined by VAR with the respective input values for

T_s , as well as for Puff. The mass loading for the Puff VATD model runs show values up to 450 kg/m^2 . The maximum values show clear peaks when the new ash is released from a new event during the Kasatochi eruption. The minima and mean values, on the other hand, appear insignificant compared to the maximum ash load.

The VAR-derived values, on the other hand, show mass loadings up to about 25 g/m^2 . In addition, the maximum values vary little over time, whereas the mean and minimum ash mass loadings of the scene decline over time. In all three cases, the universal surface temperature generally causes lower mass loadings and a less detailed trend than the VAR runs using a pixel-specific surface temperature show.

5.3.2 Satellite-Model Comparison 2: Spatial Extent

Focusing solely on the Puff VATD model results, the ash disperses to the southeast of the volcano towards Canada (Fig. 5.4). While initially at 14 and 18 km ASL (Fig. 5.4A), as determined by the input heights for the respective events, the ash cloud spans a vertical column from the surface up to 20 km ASL, the model's highest vertical layer. In the early stages of dispersion (August 8, 2008, Day 221), the cloud consists of two defined parts, offset to each other, one at higher-altitudes (about 11 to 20 km ASL, yellows to reds in Figure 4.5B) and another at a lower altitudes (0 to 11 km ASL, greens to blues in Fig. 5.4B). While the ash at higher altitudes is later-on (August 9, 2008, Day 222) caught up in a vortex, the lower altitude ash expands longitudinally towards the northeast and

southwest (Fig. 5.4C). Only after 72 hours of dispersion (at the end of August 10, 2008, Day 223), the Puff VATD model results show ash at an altitude of between 4 and 14 km ASL leave the vortex to be advected towards the Canadian mainland (Fig. 5.4D).

When comparing the extent of the ash cloud as manually identified in the satellite data and processed in VAR with the extent computed by the Puff VATD model, Fig. 5.5, an almost identical behavior can be seen until 12:00 UTC on Day 222 (August 9, 2008).

Thereafter, while the Puff-predicted ash steadily increases in spatial extent, the satellite-derived spatial coverage largely decreases over time. At the end of the chosen temporal domain, the model extent reaches 300,000 km², while only 25,000 km² is identifiable in the satellite data, Fig. 5.5.

Taking a closer look at the areas depicted as ash in the satellite data as well as the model runs reveals a less defined comparison than Figure 5.5 suggests (see Fig. 5.6). In the first two panels (Fig 5.6A and B), the satellite's furthest ash extent is west of the model's prediction furthest extent but still shows an overlap, while the eastern arm of the model's ash extent is not detected in the satellite data. 24 hours later (Fig. 5.6C), both approaches show a similar shape of the ash extent but Puff additionally predicts extensions to the northwest and the southeast of the main body. Towards the end of the chosen temporal domain for this study (Fig. 5.6D), the model's prediction significantly extends the satellite's data detected ash cloud. The satellite derived ash

cloud location only inhabits the core part of the Puff-calculated ash dispersion and does not show any ash moving across Canada.

The quantitative comparison of these extents is shown in Figure 5.7. The CSI, the percentage of overlap in both models, varies between under 10% in the beginning of Day 221 (August 8) and at the end of Day 223 (August 10) and up to 60% for the middle stages of ash dispersal. The excess area of the satellite (SE) surges briefly to over 40% towards the end of August 8, 2008 (Day 221) before it decreases slowly to 0% during Day 223 (August 10). The model over-prediction (ME) has maxima of over 90% during Day 221 (August 8) and at the end of Day 223 (August 10). In between, when the CSI values are at maximum, the ME has decreased to its minimum of about 22%.

5.3.3 Model Projections: Vertical vs. Corrected for Satellite Angle

The offset of the original model-determined ash extent to the satellite-LOS-corrected view is shown in Figure 5.8. Both extents agree to a large percent but the vertically-summed ash is projected a few pixels to the southeast of the LOS-corrected view. With a spatial resolution in the outputted ash concentration grids in the Puff VATD model predictions of 10 km; this offset comes to a shift of the ash by 30 to 50 km. In the eastern part of the domain, this becomes a more northern shift. The quantitative analysis of this offset shows CSI values over 80% for the whole time series after an initial

increase from about 50% during the events, Fig. 5.9. The SE and ME values are low and remain mostly below 10% and, during the later stages of the eruption, below 5%.

5.4 Discussion

5.4.1 Satellite-Model Comparison 1: Mass Loading

The direct comparison between ash amounts in Puff VATD model results and satellite data is problematic. The Puff VATD model results show a decline of the maximum amount over time after the eruption ended, while the satellite data shows an average value of 24 g/m^2 as the maximum for almost the entire sequence (Figure 5.3). However, mean and minima mass loading values show a similar trend as the VATD model does, albeit without the dominant spikes at the initiation of new events and with considerably lower mass loadings. Figure 5.6 reveals that the manually applied ash mask (the combined area of red and white) is largely continuous, therefore meaning that most pixels were classified as ash. Since the Puff VATD model-predicted ash extent is not a perfect match and the SE values are up to 30% for first 36 hours, with the exception of the very beginning (Fig. 5.7), and the cloud coverage was continuous (Waythomas et al., 2010), it is fair to assume that some meteorological clouds were misclassified as volcanic ash. Since most of these clouds pass the VAR threshold for ash, as seen by the largely continuous area in Figure 5.6, the retrieved values are partly non-volcanic.

Meteorological clouds can show a slight negative value in the temperature difference method as described by Prata (1989), Wen and Rose (1994) and Pavolonis et al. (2006). This slight negative value is also commonly associated with the highest masses in ash clouds, i.e. as ash clouds change from spectrally opaque in thermal infrared to semi-transparent and detectable by standard BTM data. This explains the relative constant maximum value based on satellite data when Puff VATD model shows a decline over time.

The large discrepancy between model and satellite data can be explained by the sensitivity of the ash retrieval. As opposed to VATD model runs, which calculate and forecast the entire range of particles unless otherwise specified (see Steensen et al., in review, for an example), VAR is most sensitive to volcanic ash whose effective radii are below 4 μm (Wen and Rose, 1994). The larger and heavier particles, especially dominant at the beginning of each new event, won't be picked up by satellite data.

5.4.2 Satellite-Model Comparison 2: Spatial Extent

The spatial extent comparison revealed excess values for both the satellite detected data and the Puff VATD model results as seen in Figures 5.6 and 5.7. The SE values can be explained by the heavy cloud cover as described by Waythomas et al. (2010). A clear signal of the ash did not always exist and the identifiable ash was tracked in the BTM data. For this reason, there is an area of a satellite overestimate to the west of the Puff

VATD model-calculated ash (Fig. 5.6B). This is the area where satellite ash was previously observed and, to the best of our knowledge, still existed.

The areas where the Puff VATD model over-predicted the satellite data (green in Fig. 5.6), is almost exclusively in the east, i.e. the front of the dispersing cloud. Comparing these locations with Figure 5.4 reveals them to be the lowest altitude portions of the ash with elevations below 12 km ASL. This suggests that the ash could have been covered by meteorological clouds at this altitude and therefore not be detected in the satellite data. Alternatively, the wind speeds in the NWP model used by the Puff VATD model could be different from reality and so the Puff VATD model dispersed the ash too far to the east.

In Figure 5.6D the satellite only detects a relatively small ash extent, where the Puff VATD model shows a large area encompassing the satellite's extent to all sides. Comparison to Figure 5.4 reveals that this was ash at altitudes of 18 km ASL and above but not the entire area up to 20 km ASL. This suggests that the satellite data could well identify the highest parts of the ash cloud until the ash's concentration became too thin to be detectable in the BTM data at the sensor.

There are some assumptions to be considered with this analysis. For instance, all layers of the ash cloud, most crucially the top and bottom layers, have a mass associated with them that is directly derived from the initial vertical distribution at the vent. For the lack

of better data, a poisson distribution was assumed for the initialization of the Puff VATD model. If this is incorrect, lower altitude portions of the projected plume and dispersing cloud, like the low-altitude extensions in Figure 5.4C or even the middle part reaching Canada in Figure 5.4D, might be either more pronounced or even non-existent.

Another assumption is in the meteorological NWP data used. A fine spatial resolution less than 1.0 degree provides more detailed results but is also more time-intensive to run. For real-time detection and monitoring of ash clouds, a default resolution needs to be used that is readily available. Hence, the resulting plume structure and match to satellite data would differ.

5.4.3 Model Projections: Vertical vs. Corrected for Satellite Angle

The comparison between the default model projection and the satellite-LOS-corrected extent shows an offset of 30 to 50 km to the southeast for the default projection during the majority of the ash dispersion. The direction is towards the satellite sensor. Since GOES is located geostationary at 135°W, the corrected areas will be further away from the sensor as the same ash will be projected away from it vertically above the ground point (see also Fig. 5.2 for clarification). This projection is responsible for the northwest shift (and north shift in the eastern part of the domain) of the LOS-corrected extents.

The displacement amount of 30 to 50 km is relatively small compared to the overall extend of the ash for this eruption of Kasatochi volcano. It is an offset that can easily be unnoticeably in coarser spatial resolutions, but needs to be taken into account if small-scale observations with fine resolutions are discussed, when the ash cloud is small relative to the modeled ash cloud concentration grid, or when the data is compared to other satellite, airborne or ground-based data. An important guideline is to assess the size of the ash extent compared to the spatial resolution of the VATD model and the calculated offset. If the offset is similar or larger than the extent of the cloud and can be detected with the given VATD model spatial resolution, a line-of-sight correction should be applied. In this large domain, however, it only shows some significance early on where CSI values are below 50%, Figure 5.9, and it does not show a significant improvement as the dispersing cloud grows as is underlined by the higher CSI values as the cloud disperses and low ME and SE values in Figure 5.9.

5.5 Conclusions

Kasatochi volcano erupted in 2008 providing an excellent time series dataset to carry out an assessment of the best methods to compare satellite detected ash clouds and volcanic ash transport and dispersion models results. This work shows some limitations of current volcano monitoring and possible improvements for the future. As stated in previous studies (Prata, 1989; Wen and Rose, 1994; Pavolonis et al., 2006; Steensen et

al., 2013), the cloud cover is a major obstacle for ash identification. While in this study the ash cloud was manually outlined to avoid a large amount of meteorological clouds and make use of the two band TIR data, some remaining clouds still influenced the results (Fig. 5.4).

Similarly, the meteorological clouds also deteriorated the CSI, ME and SE values (Figs. 5.6 and 5.7). A more defined manual outline of the assumed ash in the satellite data is currently the only way to improve these values with the given data set using two band TIR data. An automatic threshold-based ($B_{10.8} - B_{11.9}$) classification of the whole scenes will result in a large misclassification of meteorological features and an omission of volcanic ash due to a lowered cutoff value (see Steensen et al., in review, for further information on the manual ash outline). Further work could include examining for contiguous pixels as to identify the cloud rather than erroneously measured negative BTD pixels as well as comparing the two band TIR data to time-coincident, multi-spectral data sets.

The analysis of the different projections of the model-determined ash extent (default vs. satellite-LOS) has shown a high CSI value indicating that the projections are comparably similar. The calculated offset of 30 to 50 km is especially important for small-scale observations and in point-to-point comparisons. In addition, a coarser VATD model concentration grid may result in the inability to identify such an offset.

Future work should focus primarily on the delineation of ash in satellite images, either manually, using automated cutoffs or more advanced algorithms with multi-spectral satellite data. A more detailed user interpretation of the data is useful, focusing on extent, likely propagation, and cloud cover that can obscure results. Since meteorological clouds will affect the retrieved values, a binary approach (i.e. 'Ash - No Ash') is the most consistent way to analyze the ash's location, irrespective of ash masses and works well for two band TIR data. Incorporating different data sets where possible, such as masses from different sensors or ground observations, will further enhance the user interpretation and classify the detection limits of the satellite data. Comparison to VATD model data to further understand the ash movement is essential and should use the CSI value defined by Stunder et al., (2007) as well as the here-defined excess values ME and SE.

In addition, a detailed knowledge of the eruption behavior (i.e. plume height, shape, vertical distribution) is important, but not easily available. This data can change the plume dispersal but when compared to satellite data, as seen in the comparison between Figures 5.4 and 5.6, a detailed knowledge of the height of plume particles is more important. If dispersing clouds have a very low altitude, satellites are not likely to identify them clearly, especially in cloudy regions like the North Pacific.

This work has shown that a quantitative comparison between volcanic ash in satellite and model data is not always ideal. Quantities derived from satellite images have inherent uncertainties, while a binary approach (Ash - No Ash) shows a more promising result with the two band TIR data. Important for a binary approach is a good outline of the ash in the satellite imagery. With limited satellite bands as shown here, the best way is to do this manually taking into account data from the visible, where available, and infrared bands. A correction for the line-of-sight in the model data also shows promising results and moves the ash, in our case, 30 to 50 km to the north, an offset that can prove important for aviation. Coupling satellite measurements of an ash cloud location with VATD model simulations is necessary for aviation safety and hazard assessment, but one needs to be aware of the complexity and uncertainties that can occur before being able to make a complete hazard assessment and mitigate the risk.

5.6 Acknowledgements

This publication is the result in part of research sponsored by the Cooperative Institute for Alaska Research with funds from the National Oceanic and Atmospheric Administration under cooperative agreement NA080AR4320751 with the University of Alaska.

5.7 References

Mastin, L. G., M. Guffanti, J. W. Ewert, and J. Spiegel (2009), Preliminary Spreadsheet of Eruption Source Parameters for Volcanoes of the World, edited by United States Department of the Interior and United States Geological Survey.

National Oceanic and Atmospheric Administration (NOAA, 2013), <http://www.nco.ncep.noaa.gov/pmb/products/gfs/>, last accessed on July 25, 2013.

Pavolonis, M. J., W. F. Feltz, A. K. Heidinger, and G. M. Gallina (2006), A daytime complement to the reverse absorption technique for improved automated detection of volcanic ash, *Journal of Atmospheric and Oceanic Technology*, 23(11), 1422-1444.

Prata, A. J. (1989), Observations of Volcanic Ash Clouds in the 10-12 μm Window Using AVHRR/2 Data, *International Journal of Remote Sensing*, 10(4-5), 751-761.

Searcy, C., K. Dean, and W. Stringer (1998), PUFF: A high-resolution volcanic ash tracking model, *Journal of Volcanology and Geothermal Research*, 80(1-2), 1-16.

Sparks, R.S.J., Bursik, M.I., Carey, S.N., Gilbert, J.S., Glaze, L.S., Sigurdsson, H., Woods, A.W., (1997), 720 Volcanic Plumes. John Wiley & Sons, Chichester.

Steensen, T. and Webley, P. (2012), Qualitative Analysis of Input Parameters for Satellite-Based Quantification of Airborne Volcanic Ash, *Geoscience and Remote Sensing Symposium (IGARSS), 2012 IEEE International*, Pages 2982 – 2985, 10.1109/IGARSS.2012.6350799.

Steensen, T., M. Stuefer, P. Webley, G. Grell, and S. Freitas (2013), Qualitative comparison of Mount Redoubt 2009 volcanic clouds using the PUFF and WRF-Chem dispersion models and satellite remote sensing data, *Journal of Volcanology and Geothermal Research*, 259, 235-247, doi:10.1016/j.jvolgeores.2012.02.018.

Steensen, T, P. W. Webley, and M. Stuefer (In Review), Quantitative Comparison of Volcanic Ash Observations in Satellite-Based Remote Sensing Data and WRF-Chem Model Simulations.

Stunder, B. J. B., J. L. Heffter, and R. R. Draxler (2007), Airborne volcanic ash forecast area reliability, *Weather and Forecasting*, 22, 1132-1139.

Tanaka, H. (1991), Development of a Prediction Scheme for Volcanic Ash Fall From Redoubt Volcano, Alaska, *U. S. Geological Survey Bulletin*, 2047, 283-291.

Waythomas, C. F., W. E. Scott, S. G. Prejean, D. J. Schneider, P. Izbekov, and C. J. Nye (2010), The 7-8 August 2008 eruption of Kasatochi Volcano, central Aleutian Islands, Alaska, *Journal of Geophysical Research-Solid Earth*, 115.

Wen, S. M., and W. I. Rose (1994), Retrieval of sizes and total masses of particles in volcanic clouds using AVHRR bands 4 and 5, *Journal of Geophysical Research-Atmospheres*, 99(D3), 5421-5431.

5.8 Figures

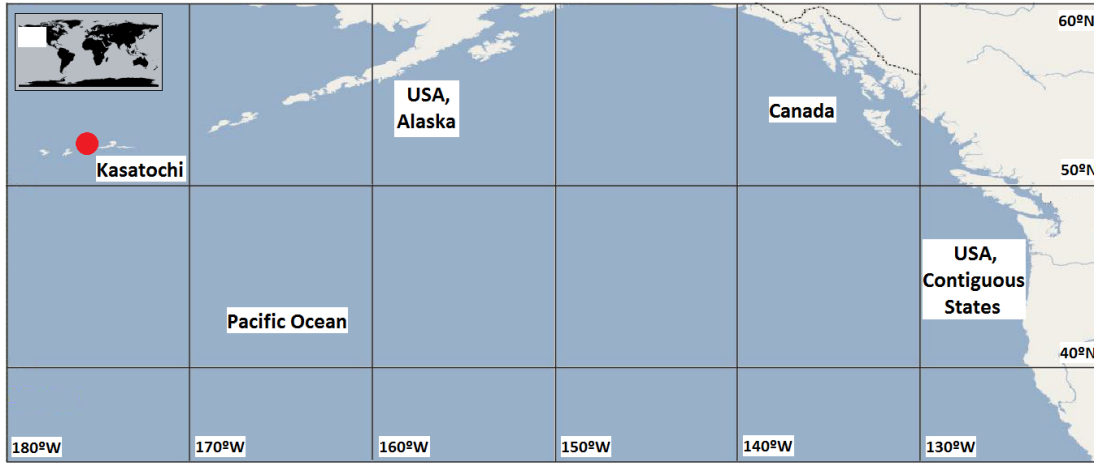


Figure 5.1: Location of Kasatochi Volcano in relation to Alaska, Canada and the Contiguous United States. The map shows the northeast Pacific Ocean, the area the ash from Kasatochi's 2008 eruption affected. Map courtesy of Marble, the KDE Education Project.

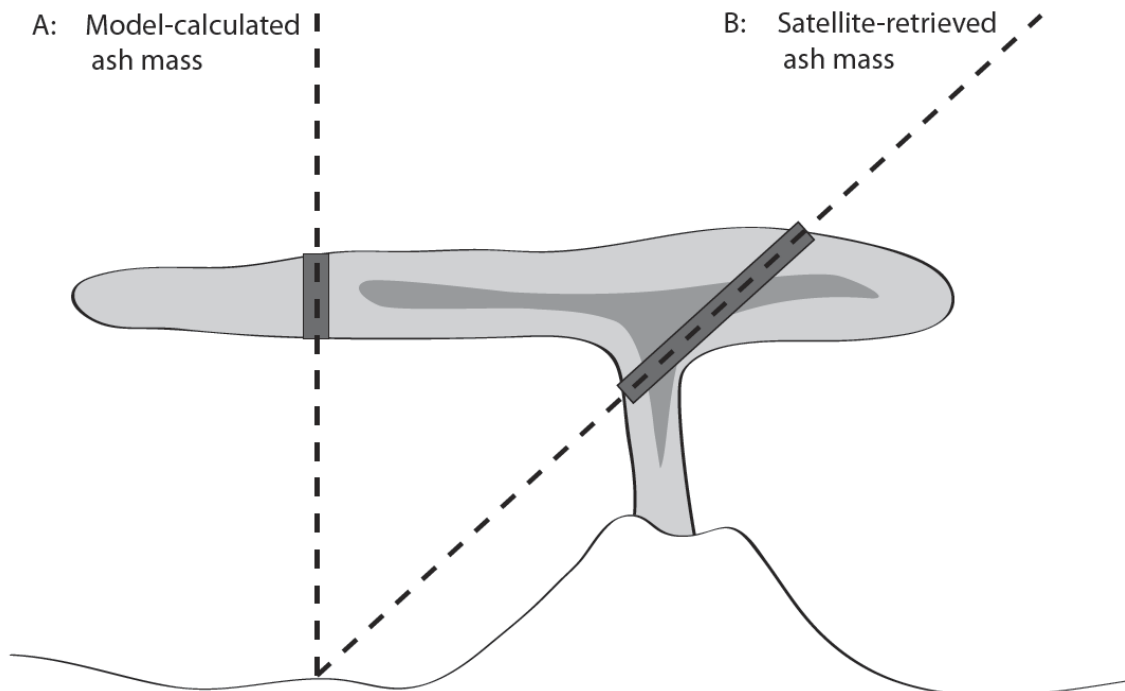


Figure 5.2: Schematic illustrating potential discrepancies between model calculations (A) and satellite retrievals (B). At any given point, the satellite will calculate the ash masses on a slanted angle while the model determines each point's location by summarizing the ash column vertically above. These two paths can not only differ in direction but also in length through the ash column (here depicted as dark rectangles) and encountered ash concentrations (here visualized as different shades of gray); Figure taken from Steensen et al. (in review).

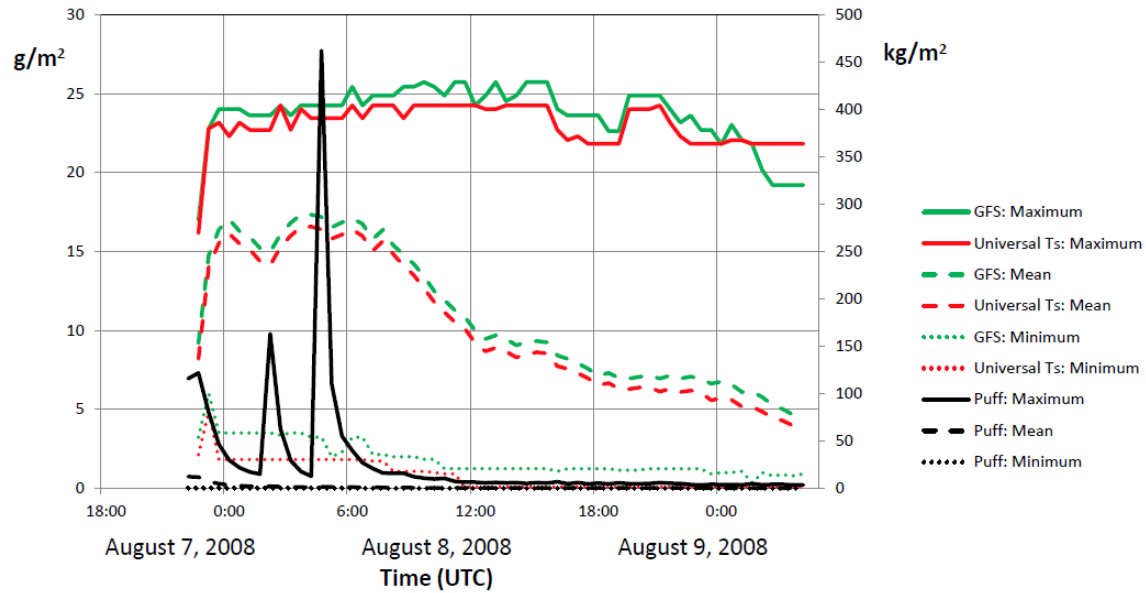


Figure 5.3: Maximum, mean and minimum ash mass loadings as calculated by the Puff model and as determined by satellite using a universal surface temperature (T_s) for all pixels and a pixel-by-pixel adjusted T_s value based on the Global Forecast System (GFS) in the Volcanic Ash Retrieval (VAR). While the Puff runs (black, right axis) show the expected decline in ash maxima, VAR calculations (green and red, left axis) show a comparably constant value over time for the maximum values and a similar decline for the mean and minimum values. The universal T_s lowers the retrieved mass compared to the pixel-based T_s . Puff runs show a mass loading considerably higher than the satellite data set.

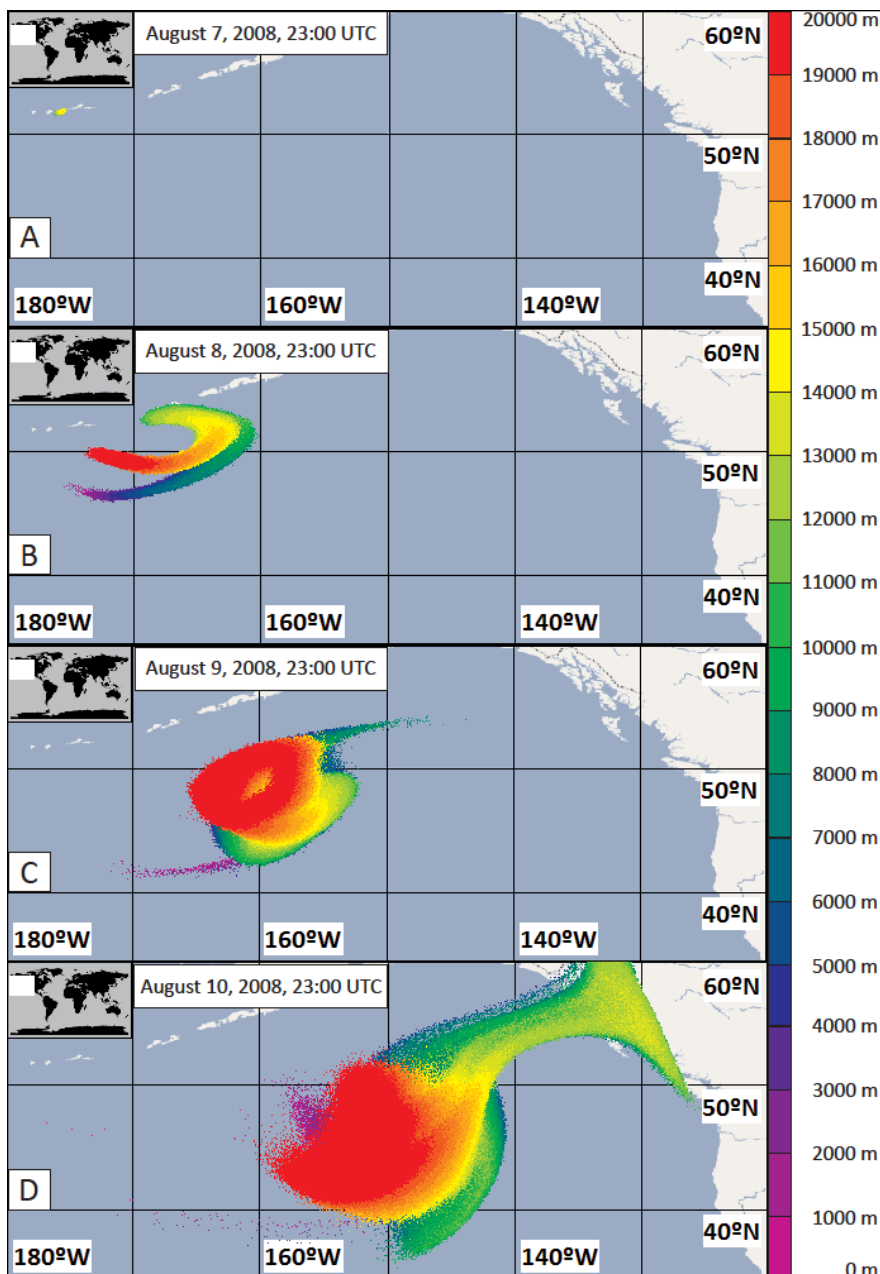


Figure 5.4: Extent and height analysis of the Puff ash dispersion for the first 74 hours after the eruption of Kasatochi at 23:00 UTC on Day 220 (August 7, A), Day 221 (August 8, B), Day 222 (August 9, C) and Day 223 (August 10, D). The ash can be seen drifting eastwards towards Canada while spanning the vertical column from ground level to 20 km above sea level (ASL). After 74 hours (Panel D), ash at altitudes between 4 and 14 km ASL are shown leaving the main vortex being advected towards across Canada. All heights depicted here are ASL.

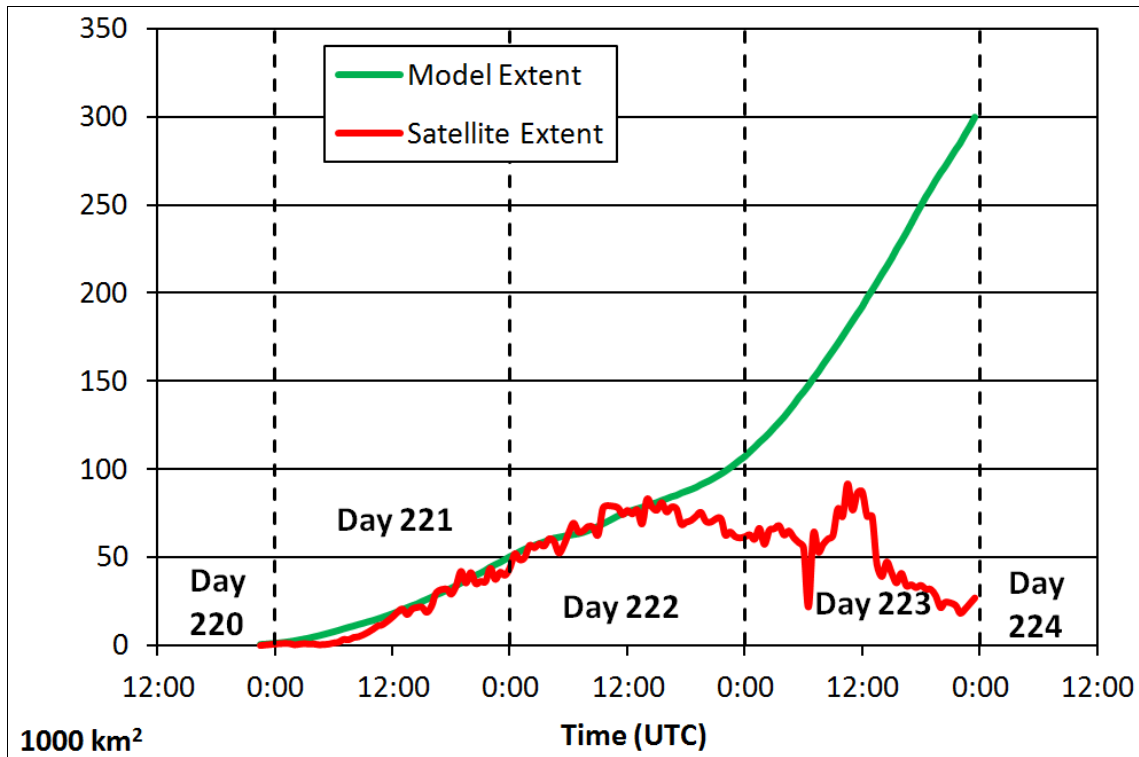


Figure 5.5: Preliminary extent comparison between Puff VATD model results and satellite detected volcanic ash data during dispersion. While both graphs follow a similar trend at the beginning, the model's extent is notably higher towards the end than that of the satellite.

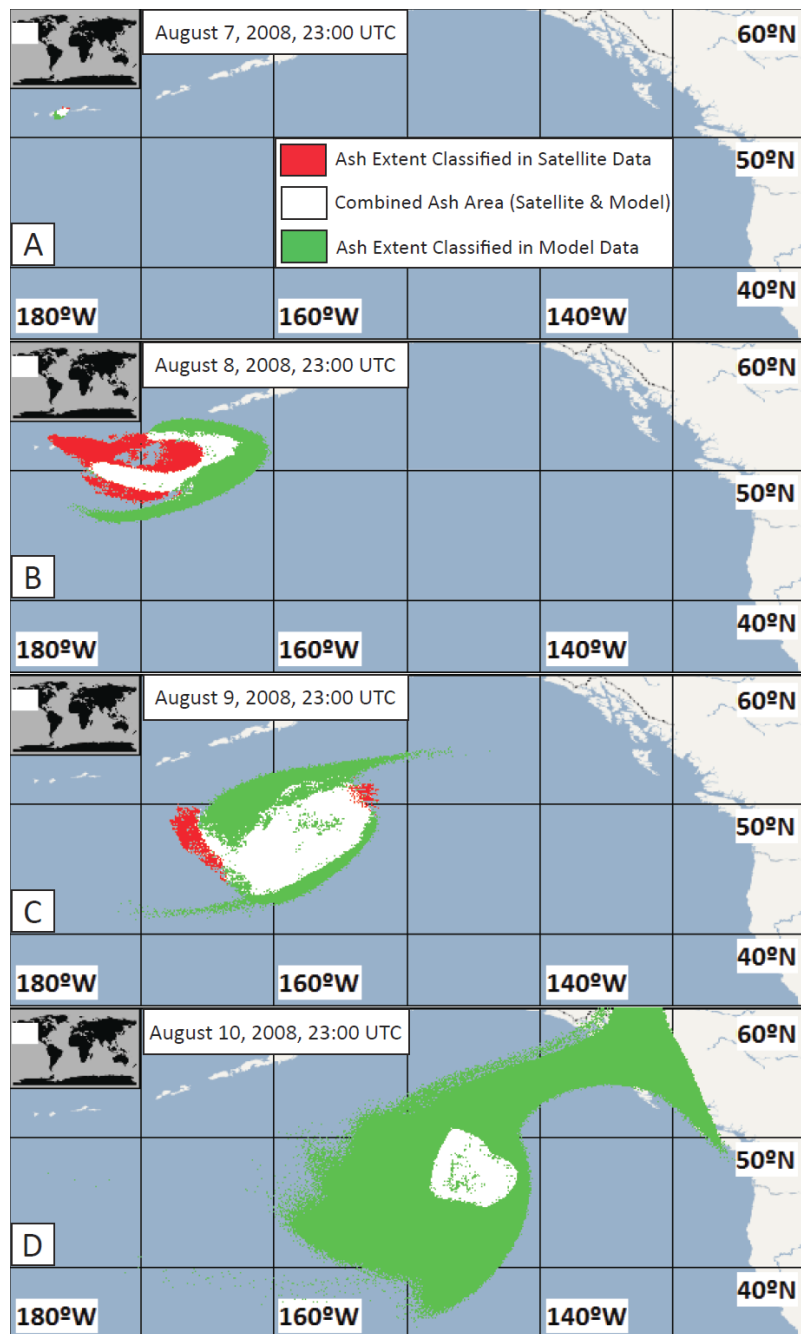


Figure 5.6: Direct comparison of the ash extent as identified in satellite data and calculated by Puff at 23:00 UTC on Day 220 (August 7, A), Day 221 (August 8, B), Day 222 (August 9, C) and Day 223 (August 10, D). At the beginning, the satellite data suggests ash to the west of the model, whereas in the later stages of the eruption, the model determines ash being distributed across Canada, which is not seen in the satellite data.

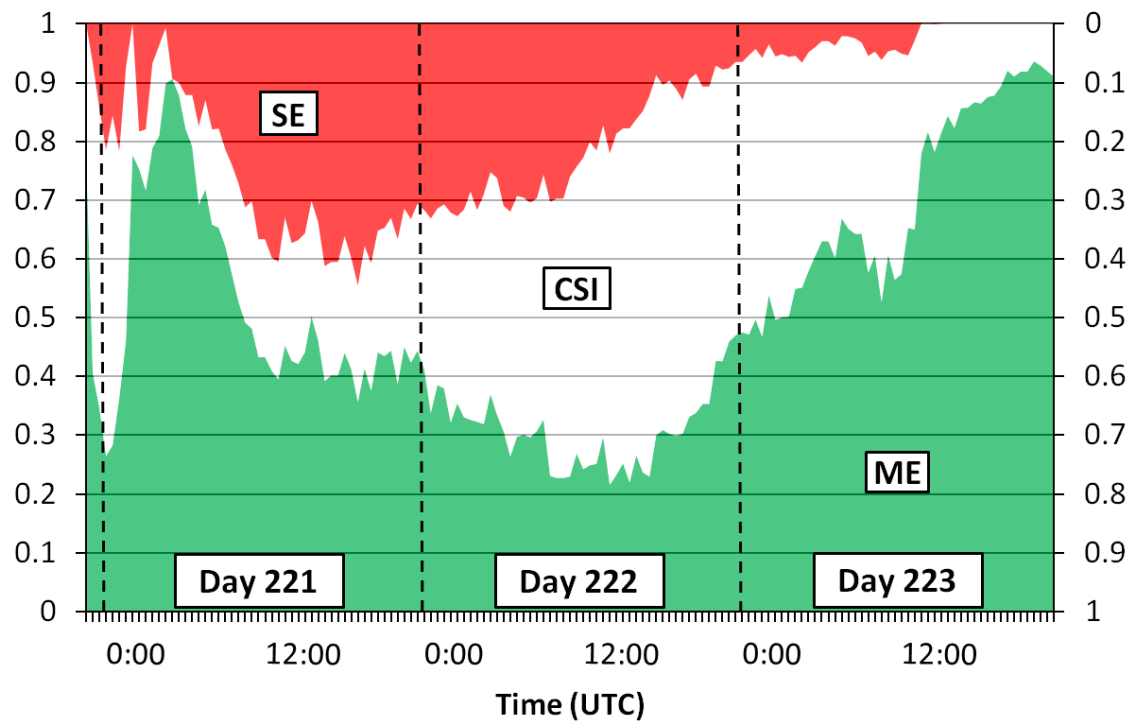


Figure 5.7: Critical Success Index (CSI), Model Excess (ME) and Satellite Excess (SE) values for the ash extent comparison between satellite data and Puff VATD model. A CSI of 1 would be the ideal case, with ME and SE values of 0. Here, the ME values are generally larger than the SE ones. The CSI reaches its maximum during Day 222 (August 9) and decreases again towards the end.

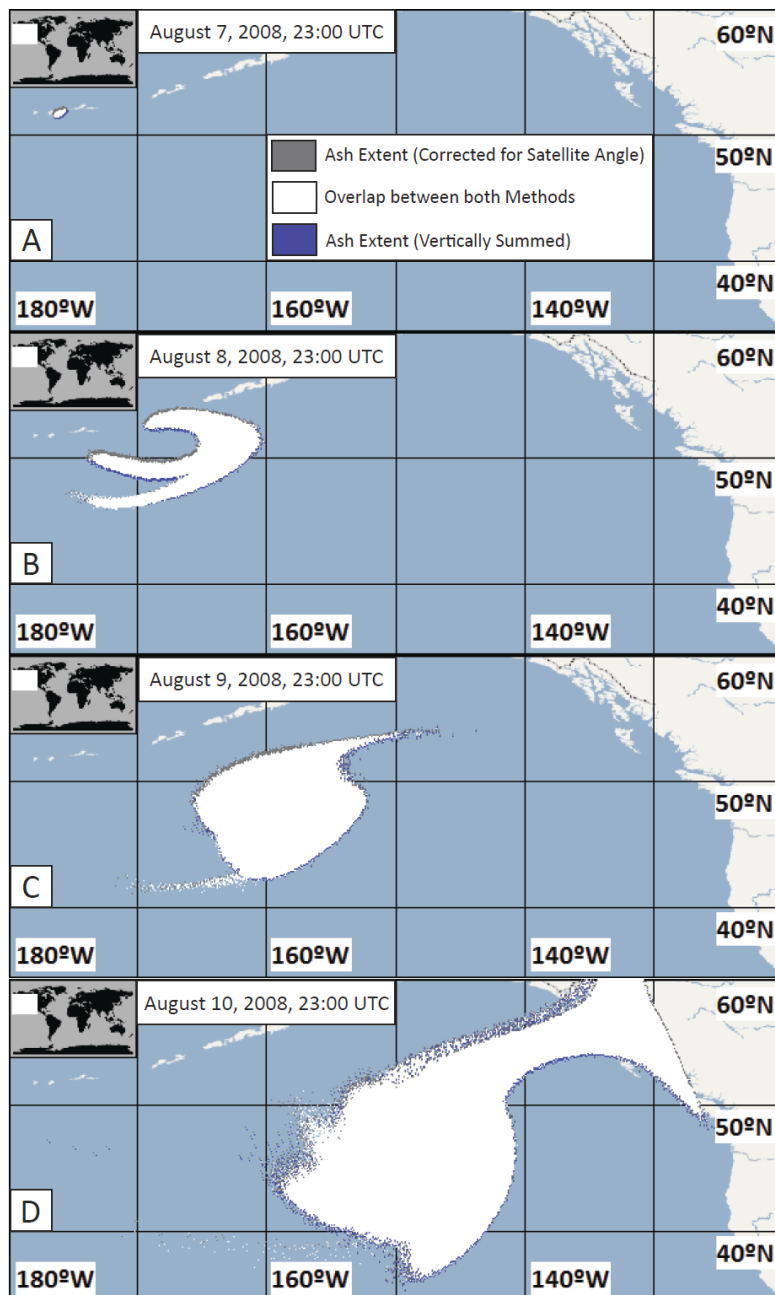


Figure 5.8: Direct comparison of the Puff VATD modeled ash extent using the default vertical summation versus the projection to the satellite's line-of-sight at 23:00 UTC on Day 220 (August 7, A), Day 221 (August 8, B), Day 222 (August 9, C) and Day 223 (August 10, D). The offset of the two areas is a few pixels, representing about 30 to 50 km, with the default projection to the southeast of the adjusted one. Both extents show a good match.

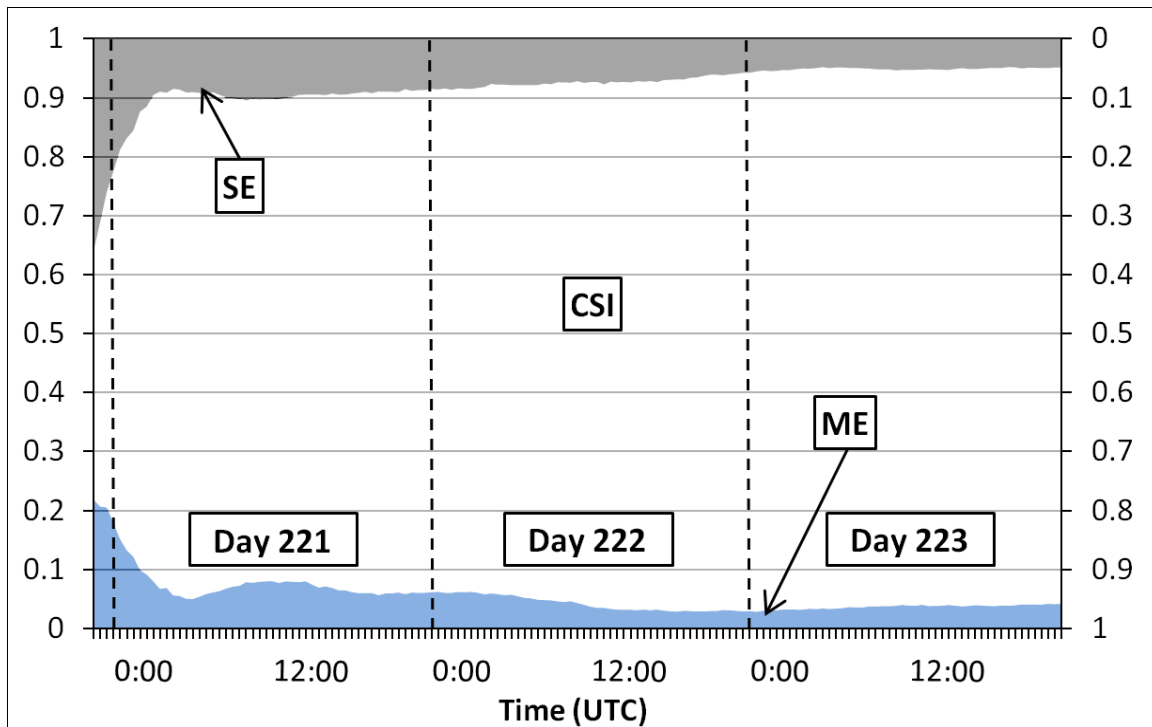


Figure 5.9: The quantification of the comparison between default and adjusted model projections shows very high numbers of the Critical Success Index (CSI) while the excess values for the default model projection (ME) and the satellite-LOS-corrected one (SE) are well below 10%.

5.9 Tables

Table 5.1: Volcano and eruption specifics as determined by seismic and satellite observations of the 2008 Kasatochi eruption (Waythomas et al., 2010).

Location	52.177°N		175.508°W		
Height	314 m above sea level				
	Date	Julian Date	Time	Height	Duration
Event 1	7-Aug-08	220	22:01 UTC	14 km	60 min
Event 2	8-Aug-08	221	01:50 UTC	14 km	30 min
Event 3	8-Aug-08	221	04:35 UTC	18 km	30 min

Table 5.2: The atmospheric numerical weather prediction model used to calculate pixel-specific surface temperatures with the respective characteristics as well as the universal surface temperature used for comparison with the other default parameters needed for the Volcanic Ash Retrieval. GFS=Global Forecast System.

Pixel-Specific Surface Temperature		
	Spatial Resolution	Coverage
GFS	1 degree	global

Universal Surface Temperature	
Spatial Resolution	4.4 km
Surface Temperature	280 K
Cloud Top Temperature	220 K
Specific Gravity of Ash	2.6 kg m ⁻³
Refractive Index of Ash	2.14610+0.39891i (11 μm)
	1.82854+0.12953i (12 μm)
Refractive Index of Air	1.0

Table 5.3: Input parameter for the Puff Volcanic Ash Transport and Dispersion runs. Detailed timings are listed in Table 5.1. NCAR= National Center for Atmospheric Research.

Start Time	22:00 UTC
Start Date	7-Aug-08
End Time	05:00 UTC
End Date	8-Aug-08
Number of Separate Events	3
Vertical Particle Distribution	Poisson
Wind Model	NCAR
Number of Particles	100,000
Eruption Rate	Sparks et al., 1997
Particle Size Distribution	Mastin et al., 2009
Amount of Fines (<63 μ m)	40%

Chapter 6: Conclusions

Volcanic ash clouds can be a major hazard for the aviation community and subsequent ash fall can pose a serious risk for infrastructure and human health. Satellite data can provide one instant in time and volcanic ash dispersion and transport models can forecast their movement, but these need to be validated/calibrated with the observations. The previous Chapters of this dissertation have outlined the advances and limitations of current airborne ash monitoring techniques. The Redoubt case study (Chapter 2) shows that a qualitative comparison between Eulerian and Lagrangian model results with remote sensing satellite data is advantageous as they complement each other by eliminating uncertainties. These uncertainties include the hindrance of meteorological clouds when detecting ash in satellite images and the uncertainty of model input parameters like vertical particle distribution or wind patterns. Chapter 2 also outlines the need to quantitatively analyze the ash dispersion to reach consensus about the quality of the satellite to model comparison and, hence, about the extent of the airborne ash.

To reach quantitative results, i.e. ash masses, the Volcanic Ash Retrieval (VAR) has been used (Wen and Rose, 1994). Chapter 3 analyzes the input parameters to quantitatively assess the most crucial factor for ash mass determination. The work showed that uncertainties in the surface temperature have the strongest influence on the derived

mass and, if possible, this value should be assessed on a pixel basis. Additionally, Chapter 3 shows that a set of parameters can be varied together to still achieve the same result. This means that one variable can be deliberately underestimated to counteract an overestimation of another variable (Figure 3.3). The percentages of those under- and over-estimates can be derived from Figure 3.2 where the resulting misrepresentation of the mass must add up to '0' to retrieve the correct value.

However, VAR calculations are subject to uncertainties based on meteorological cloud cover. To improve the retrieval, a new approach to manually outline ash clouds in satellites, when using two band thermal infrared (TIR) data, has been developed in Chapter 4, which was compared to the Eulerian Weather Research and Forecast Model with online Chemistry (WRF-Chem). Simultaneously, this chapter highlights uncertainties with model input data and how they affected the comparison.

Chapter 5 ties together the previous chapters by combining the need for a quantitative comparison between satellite and model data (Chapter 2) with the importance of a pixel-based approach to derive masses in VAR (Chapter 3) and the methodology of manually outlining a dispersing ash cloud in satellite data to enhance the retrievals (Chapter 4). It is suggested that, despite the improved values from pixel-based input parameters, the best results are achieved in a quantitative approach comparing the maximum ash extents in satellite and model data for two band TIR data. Deriving ash masses directly from the two band data has inherent uncertainties and these can then

propagate into the comparison. The four main conclusions drawn from this dissertation are outlined below:

1. To assess the volcanic ash dispersion in the atmosphere, a combination of satellite data and Volcanic Ash Transport and Dispersion (VATD) model calculations is needed that can take into account both qualitative and quantitative comparisons to achieve the best results.
2. For the quantitative ash evaluation based on the VAR (Wen and Rose, 1994), a pixel-based surface temperature should be used based on available data sets.
3. The model projection of the ash masses needs to be adjusted for the satellite's line-of-sight (LOS). This is especially important in smaller eruptions, where the offset is large relative to the ash extent.
4. Because of meteorological cloud coverage, lack of more data at other spectral ranges in the TIR (outside the two band data approach used here) and the lack of availability for accurate input parameters, results from the VAR can have a large level of uncertainty in the quantitative mass determination, and so a simpler 'Ash – No Ash' binary approach with the quantitative evaluation of the overlap based on the Critical Success Index (Stunder et al., 2007) and the Model and Satellite Excess

Values (ME and SE, respectively, Steensen et al., in prep.) is favorable over a direct ash mass quantification and comparison.

6.1 Necessity of Satellite – VATD Intercomparisons

Volcanic ash emissions are mapped and analyzed routinely using satellite data and VATD model predictions. Both approaches have inherent strengths but also weaknesses (Steensen et al., 2013). Satellite data provide a snapshot of the actual cloud's location but their accuracy depends on different assumptions, such as there being a lack of meteorological cloud coverage and the translucency of the ash to infrared radiation (see Fig. 2.2). In addition, the passive sensor satellite data measures thermal radiant temperatures along its LOS. This can change the interpreted properties of the cloud, since these will vary when compared to that identifiable in a vertical setting.

The identification of VATD model ash mass loading/concentration results, on the other hand, remains unaffected by meteorological properties, such as overlying clouds. The VATD model results accuracy, however, depends on the precision of the input parameters. Depending on the model type, the range of required input parameters changes; Lagrangian models, for example, do not require a pre-defined spatial domain whereas Eulerian models do. General input parameters needed for ash dispersion are (1) the vertical shape of the plume (poisson-, exponentially or linearly distributed); (2) the eruption duration and, if ash masses are calculated, (3) the particle size

distributions. Determining these factors during an eruption, or even afterwards, is often very difficult, thus, limiting the accuracy of the models used (Steensen et al., in review).

Due to these inherent advantages and disadvantages of VATD model data, a fusion of model and satellite approaches is recommended. Keeping in mind the respective limitations, a more precise estimate of the locations and, if necessary, quantity of the airborne ash can be achieved.

6.2 Importance of Pixel-Based Values for the Surface Temperature in VAR

To quantify airborne volcanic ash masses, Wen and Rose (1994) developed the VAR algorithm based on previous work by Prata (1989) identifying a negative brightness temperature difference (BTD) in consecutive infrared bands (e.g. $BT_{10.8\mu\text{m}} - BT_{12.0\mu\text{m}} < 0$ with BT_x =Brightness Temperature at the band located at wavelength X). This approach estimates the ash masses in any volcanic plume or cloud as well as the respective optical depths and effective radii per pixel. However, in order for this estimate to be correct, a range of input parameters has to be assessed *a priori*. Furthermore, different initial assumptions, like the lack of meteorological clouds, have to be met as well. A full list of all assumptions can be found in Wen and Rose (1994).

The parameters needing to be assessed *a priori* include several location-specific estimates such as the surface and cloud top temperature in each pixel and the refractive indices of ash and air. Steensen and Webley (2012) published a detailed analysis of

these parameters and their respective sensitivities to alter the retrieved masses, if assessed inaccurately. Their results, as described in Chapter 3, indicate that the surface temperature (i.e. surface leaving radiance in thermal infrared) shows the greatest potential to influence the calculated ash masses (Figure 3.2). An offset of 2 % in the measured surface temperature can already alter the derived mass by 25 %. The other parameters, though important, do not change the results this significantly.

As detailed data on the surface temperature are not always readily available, the value for the surface temperature has often been set to a default value for the whole satellite image and the entire time series (e.g. Steensen et al., 2013). Choosing pixel-specific surface temperatures based on meteorological data will change the results significantly (Steensen et al., in prep.). As seen in Figure 5.3, the approach using a default surface temperature can yield lower masses and more variability in the time series than the pixel-based surface temperature method. When quantifying ash masses, this can be a crucial offset and needs to be taken into account.

6.3 Improvements of LOS-Projections of VATD Model Data

One of the inherent differences between VATD model projections and satellite analysis is the LOS. While the VATD models generally show units summed up vertically above given locations, satellites only have the ability to analyze in their LOS. To compare model

and satellite data, regardless of quantitative and qualitative approaches, this offset needs to be taken into consideration.

Calculations using a geostationary satellite with the assumption of a spherical Earth have shown that this offset causes the modeled ash extent to be projected away from the satellite after the LOS correction with an offset of 30 to 50 km (Figure, 5.8; Steensen et al., in prep.). While such an offset is relatively small compared to an ash cloud extending several thousands of kilometers, as shown in Chapter 5 for Kasatochi Volcano, it becomes important for smaller eruptions and their detection in satellite imagery. This can be seen in the low CSI values as the Kasatochi ash cloud developed and grew in size (see the early stages in Figure 5.9). Furthermore, due to such an offset, the surface temperature necessary for a quantitative assessment of the ash masses can change if the pixel-based approach is chosen. Since spatial resolutions of VATD models vary, this offset only needs to be considered if the applied model resolution is at least as fine as the error introduced by not correcting for the line-of-sight.

6.4 Advantages Using a Binary ‘Ash – No Ash’ Approach as Opposed to a Quantitative Mass Estimate for two band Thermal Infrared data

As previously mentioned, a quantitative mass estimate using VAR requires a range of input parameters, often hard to assess in real time or even for research purposes after the respective eruptions. Additionally, VAR assumes that the volcanic ash is the only

scattering property in the atmosphere with a universal thickness stretching horizontally. To optimize the ash cloud detection, a reduction of uncertainties is needed to allow for a more qualitative approach. To achieve this for two band TIR data, the 'Ash - No Ash' binary approach has been outlined in Steensen et al. (in review) and Steensen et al. (in prep.).

This binary method avoids the direct quantification of ash masses and focuses on the ash extent, which is quantitatively compared between VATD model results and satellite data. An important factor for this technique is the outline of volcanic ash in satellite images. This is performed manually based on data in the visible wavelength, where available, and infrared bands when an automated approach as suggested by Pavolonis et al. (2006) is unavailable, due to a lack of the additional bands in the relevant parts of the TIR spectrum. Another advantage of a manual outline is the incorporation of different data sets. While VATD models generally calculate the ash dispersion over all particle sizes, ash retrievals are sensitive to effective radii below 4 μm . Using different data sets like *in-situ* observations (sampling, pilot reports) or other remote sensing data sets (ground-, air- or space-borne), this limitation can be addressed. Then volcanic ash, known to exist at a given location, although undetectable by satellite data due to detection limits or meteorological cloud coverage, can be identified.

Within the manually-defined outline of the ash extent from the two band TIR satellite data, VAR can be run to eliminate all pixels with a positive BTM and to create an improved ash mask. Since no absolute masses are calculated, the input values for VAR are of less importance, as long as the BTM remains negative. The remaining pixels are considered to be the total extent of the volcanic ash in that satellite image. This approach has the advantage of being able to utilize the BTM threshold of 0 K described by Prata (1989) as opposed to a lower threshold for the whole image to avoid meteorological artifacts (Pavolonis et al., 2006), which also eliminated ash pixels.

The total satellite ash extent is then compared to the model extent using the Critical Success Index (CSI; equation 5.2; Stunder et al., 2007) and the Satellite and Model Excess Values (equations 5.3 and 5.4; Steensen et al., in prep.). This technique does not take either the satellite data or the VATM model results as the truth but evaluates both against each other. With all values adding up to 1, a direct comparison can be achieved where a larger CSI means a better match (see Figs. 5.7 and 5.9).

For operational purposes of volcanic ash detection, tracking and predicting, this method reduces the effect of uncertainties that the direct mass quantification can have on real-time operational analysis due to its ability to be performed without evaluation of input parameters. It has, however, the limitation that, without using additional data sets, the detection is reduced to small particles, i.e size ranges detectable by the two band BTM data. This method will also enhance the model to satellite comparison as these values

can work as guidance for model accuracy with high CSI and low ME/SE values representing a better match between observed and modeled ash extent. The limitation, depending on available satellite bands, is the experience of the observer when outlining the ash cloud in the satellite data. Due to the necessity of this, the 'Ash – No Ash' approach can only be semi-automated. With the addition of more bands in the TIR that can assist in fully classifying if the detected pixels are volcanic ash, it is possible to determine the likelihood volcanic ash being present (see Pavolonis et al., 2013).

Depending on the eruption and the available model and satellite data, an additional LOS correction for the VATD data can be performed. This will further improve the comparison by increasing the CSI and reducing the ME and SE values. To further develop this methodology, a more detailed manual outline in satellite images needs to be developed or multi-spectral methods explained in Pavolonis et al. (2006) need to be applied. As of now, this heavily relies on the experience of the interpreter while studying available visible and infrared images of the eruption as well as tracking the ashes over time. It is also possible to do a secondary analysis of the manually defined area to eliminate all pixels with a positive brightness temperature difference to limit the analysis of meteorological clouds. Historic eruptions can also help to outline areas of less likelihood. In addition, combining the two band TIR data along with multi-spectral data can assist in defining the most likely ash pixels in the two band data.

A deterministic quantitative mass estimate to compare satellite and model results is not recommended, when using the two band TIR satellite data such as AVHRR (Advanced Very High Resolution Radiometer), GOES (Geostationary Operational Environmental Satellite) or MTSAT (Multifunctional Transport Satellite). A range of uncertainties occurs starting from inherent assumptions in VAR over the error bars affiliated with often-best-guessed values for the input parameters for the retrieval to similar uncertainties in Eulerian and Lagrangian model inputs. To be able to successfully compare such values, these uncertainties have to be limited or clearly identified requiring *in-situ* measurements and a newly developed Volcanic Ash Retrieval, with defined probabilities of ash occurrence.

Using the 'Ash – No Ash' approach, on the other hand, can limit many of these uncertainties, when using two band TIR data. With the CSI, ME and SE values, a quantitative comparison between satellite remote sensing data and model results can be achieved. This will enhance the capability to determine ash extents in an operational environment for any TIR satellite data acquired, in addition to being able to further the research in developing better analyses techniques for satellite remote sensing data and for Eulerian and Lagrangian VATD models.

6.5 Future Work

The advances in this work also outline areas of further research. There are inherent uncertainties in VATD model and VAR input parameters as well as assumptions in the basic VAR code. At the current point of research, these assumptions and uncertainties limit the retrieval of accurate ash masses when satellite bands are limited to two TIR channels and the binary 'Ash – No Ash' approach is favorable over the large error bar that accompanies the absolute deterministic mass retrievals. Future research as well as more *in-situ* sampling, where necessary and feasible, should address these limitations.

In addition, both VATD models used in this work don't take account of particle aggregation. This is an inherent aspect of ash dispersion as aggregation accelerates the fallout process based on Stoke's Law. Since satellite retrievals will be subject to actual particle sizes, the VATD model calculations need to address aggregation to be able show a comparable ash extent as well as retrieved mass.

The manual ash outline in the 'Ash – No Ash' approach is important with a limited range of satellite bands but when more bands in the TIR spectrum are available, an automated approach should be applied (e.g. Pavolonis et al., 2006) to assess uncertainties introduced by the manual outlining. Furthermore, the backgrounds in the case studies used here are comparably homogenous in terms of surface temperature as the ash was mainly dispersed over the ocean. A larger surface temperature difference (e.g.

mountainous terrain), temperature inversions (e.g. in Arctic/Antarctic settings) or also the presence of large amount of water vapor (e.g. tropical regions) or mineral dust (e.g. deserts) can significantly alter the results. These scenarios should be taken into account when applying the 'Ash – No Ash' approach on a global setting. Keeping those limitations in mind for future research, this approach can be implemented as fast near real time determination of ash extents in the case of a volcanic eruption to help the aviation community to more accurately determine the safety of the flight corridors.

6.6 Final Thoughts

This dissertation has provided a novel approach to compare satellite-retrieved data sets to VATD model results. With limited satellite TIR bands and uncertain input parameters for ash retrievals and VATD models, a quantitative deterministic comparison cannot be accomplished easily. The 'Ash - No Ash' approach requires a manual analysis of satellite data sets to outline area, where volcanic ash is detected. Additional data sets (e.g. direct observations or other remote sensing data) can be included to further enhance the accuracy of the ash outline. Due to this manual aspect, this method, in its current form, can only be run semi-automatically and, hence, also needs a trained observer for operational purposes. The actual time spent on outlining the ash extent can be minimized to allow for near real-time observations.

To quantify ash masses when advanced satellite retrievals from multi-spectral TIR data are not available due to limited satellite TIR bands, the input parameter accuracy needs to be considered and, where appropriate, improved. Default parameters can yield significant misrepresentations of the derived masses as shown by Steensen and Webley (2012). Furthermore, the Volcanic Ash Retrieval by Wen and Rose (1994) used in this dissertation is a good first-order quantification tool but due to the range of the associated assumptions (e.g. lack of meteorological clouds, spherical particles) its accuracy is limited. This is similar for VATD models where a lack of aggregation (Puff and WRF-Chem) and wet deposition (Puff) relatively increase the mass loading during dispersion. These limitations, together with a detection limit of volcanic ash in satellite data due to meteorological cloud coverage and large effective radii, are the main obstacles when working with volcanic ash detection and forecasting and have been highlighted throughout this dissertation.

Another option to increase the reliability of volcanic ash detection is to step away from deterministic measurements. With the high uncertainty of input parameters and the assumptions in VAR and VATD models, a probabilistic approach with the full spectrum of potential input parameters can provide different levels of likelihood of volcanic ash in the atmosphere as explained in Webley and Steensen (2013). With such an ensemble of VAR results, the best match to the modeled ash cloud can be identified.

Similarly, Pavolonis et al. (2013) calculate uncertainty ratios to accompany their retrievals. These ratios represent the level of confidence in the retrieved parameter at the given pixel. However, they require measured radiances at bands centered around 11, 12, and 13.3 μm . While the first two bands are common on all meteorological satellites, the band located at 13.3 μm is not available in all sensors. Only newer instruments like VIIRS (Visible Infrared Imager Radiometer Suite), SEVIRI (Spinning Enhanced Visible and Infrared Imager), MODIS (Moderate-resolution Imaging Spectroradiometer) and ABI (Advanced Baseline Imager) are equipped with this band. As newer sensors are developed and more channels in the TIR become available in geosynchronous and polar orbiting settings, probabilistic ash retrievals with likelihood of ash detected will become more used in operational settings. Coupling these with probabilistic simulations from VATD models such as those in Bursik et al. (2012), using methods such as the CSI applied in this dissertation, will then allow the observer a sense of the likelihood of ash occurrence, the measure of ash masses and then the reliability of the model simulations for the further dispersing cloud.

6.7 References

Bursik, M., M. Jones, S.A. Carn, K. Dean, A. Patra, M. Pavolonis, E.B. Pitman, T. Singh, P. Singla, P. Webley, H. Bjornsson, and M. Ripepe (2012), Estimation and propagation of volcanic source parameter uncertainty in an ash transport and dispersal model: application to the Eyjafjallajökull plume of 14-16 April, 2010, *Bulletin of Volcanology*, 74(10), 2321-2338.

Pavolonis, M. J., W. F. Feltz, A. K. Heidinger, and G. M. Gallina (2006), A daytime complement to the reverse absorption technique for improved automated detection of volcanic ash, *Journal of Atmospheric and Oceanic Technology*, 23(11), 1422-1444.

Pavolonis, M. J., A. K. Heidinger, and J. Sieglaff (2013), Automated retrievals of volcanic ash and dust cloud properties from upwelling infrared measurements, *Journal of Geophysical Research: Atmospheres*, 118(3), 1436-1458.

Prata, A. J. (1989), Observations of Volcanic Ash Clouds in the 10-12 μm Window Using AVHRR/2 Data, *International Journal of Remote Sensing*, 10(4-5), 751-761.

Steensen, T. and P. W. Webley (2012), Qualitative Analysis of Input Parameters for Satellite-Based Quantification of Airborne Volcanic Ash, *Geoscience and Remote Sensing Symposium (IGARSS), 2012 IEEE International*.

Steensen, T., M. Stuefer, P. Webley, G. Grell, and S. Freitas (2013), Qualitative comparison of Mount Redoubt 2009 volcanic clouds using the PUFF and WRF-Chem dispersion models and satellite remote sensing data, *Journal of Volcanology and Geothermal Research*, doi:10.1016/j.jvolgeores.2012.02.018.

Steensen, T, P. W. Webley, and M. Stuefer (In Review), Quantitative Comparison of Volcanic Ash Observations in Satellite-Based Remote Sensing Data and WRF-Chem Model Simulations.

Steensen, T., P. W. Webley and J. Dehn, Improvements on Volcanic Ash Quantification in the Puff Volcanic Ash Tracking and Dispersion Model as Satellite Thermal Infrared Remote Sensing Data, in Prep.

Stunder, B. J. B., J. L. Heffter, and R. R. Draxler (2007), Airborne volcanic ash forecast area reliability, *Weather and Forecasting*, 22, 1132-1139.

Webley, P. W., and T. Steensen (2013), Operational Volcanic Ash Cloud Modeling: Discussion on Model Inputs, Products, and the Application of Real-Time Probabilistic Forecasting, in *Lagrangian Modeling of the Atmosphere*, edited, pp. 271-298, American Geophysical Union.

Wen, S. M., and W. I. Rose (1994), Retrieval of sizes and total masses of particles in volcanic clouds using AVHRR bands 4 and 5, *Journal of Geophysical Research-Atmospheres*, 99(D3), 5421-5431.